

SOLUTION-PROCESSABLE ORGANIC SEMICONDUCTING MATERIALS FOR
PHOTOVOLTAIC APPLICATIONS

By

JIANGUO MEI

A DISSERTATION PRESENTED TO THE GRADUATE SCHOOL
OF THE UNIVERSITY OF FLORIDA IN PARTIAL FULFILLMENT
OF THE REQUIREMENTS FOR THE DEGREE OF
DOCTOR OF PHILOSOPHY

UNIVERSITY OF FLORIDA

2010

© 2010 Jianguo Mei

To my wife, our soon-to-come son, and my parents

ACKNOWLEDGMENTS

I would like to thank my advisor Dr. John R Reynolds. After four years of practicing “wet” chemistry in the lab, I am still optimistic and enthusiastic about what I am doing, for which he deserves a lot of credit. He has been a good advisor, wise listener and generous supporter. He made my experience at UF enjoyable and helped shape me in many aspects. As a teaching coordinator for his Organic Chemistry class, he taught me how to make and grade an exam, organize an office hour and communicate with students. As a researcher in the lab, he trained me how to properly write a technical report and a grant, draft a cover letter and a manuscript, review a scientific paper and give a public presentation. As an individual person, I gratefully benefited from the dedication and caring nature he demonstrated. He was always there to advice and support when it came to my career development.

I would also like to thank the members of my committee, Prof. Kirk S. Schanze, Prof. Daniel R. Talham, Prof. Ronald K. Castellano, Prof. Franky So, and Prof. Jiangeng Xue, for contributing their valuable time and expertise to my education at the University of Florida. I also wish to thank Prof. Ken Wagener for the many thoughtful pieces of advice and stimulating discussions he has given over the years, and for his efforts to create an excellent environment in the Butler Polymer Laboratory.

I am also grateful to my many collaborators who have contributed to the projects I have carried out at UF. Dr. Kirk Schanze, Dr. Young-Gi Kim, Dr. Katsu Ogawa, Dr. Nathan Heston and Dr. Jarrett Vella contributed significantly to my very first project on platinum-acetylide low bandgap polymers. Dr. Schanze has been a passionate supporter and on my reference list since then. Dr. Nathan Heston, Dr. Svetlana Vasilyeva, Dr. Michael F Durstock (AFRL) and Christopher A Bailey (AFRL) helped to develop the project on the vinylene-linked donor-acceptor conjugated polymers. Dr. Bernard Kippelen, Dr. Shree Prakash Tiwari, Dr. Hyeunseok

Cheun and Jaewon Shim at Georgia Tech contributed to the projects on small molecule-based field-effect transistors and organic solar cells. Dr. Franky So, Dr. Jegadesan Subbiah and Dr. Kaushik Roy Choudhury in Department of Material Science and Engineering at UF have worked on polymer-based devices together with me. And I also wish to thank Dr. Franky So for his insightful advice, hospitality and willingness to serve as my reference. Dr. Ronald Castellano made great efforts to the project on self-assembled amphiphilic cruciform shaped oligothiophenes. I also thank him for the valuable advice and serving as a reference.

I am deeply indebted to my two Reynolds group collaborators: “GRIT fellow” Romain Stalder and “GRIT fellow” Kenneth Graham. We have worked together on a number of projects, and our collaborations still keep moving ahead. I would also like to thank Brian Atiken in the Wagener group. We have worked closely together on regioregular electroactive polyolefins, the “first” collaboration between the two groups.

Many people have been influential in my development as a graduate student. My master’s degree advisor Prof. Shaoming Yu at the Hefei University of Technology encouraged and brought me into the scientific field. With his unselfish support and encouragement I was able to step out and make my move to the States. Prof. Steven P Nolan at the University of New Orleans was actually the first one who trained me as a chemist. Knowing that I would transfer to UF one year later, he still accepted me into his group, and provided me with various training opportunities. In his group, I, formerly trained as a chemical engineer, was trained by a number of experienced chemists, including Dr. Oscar Navarro, Dr. Roy A. Kelly, III, Dr. Natalie M. Scott, Dr. Nicolas Marion, Dr. Rohit Singh. I still remembered when Dr. Kelly showed me how to use a cannula to transfer liquids under inert atmosphere and Dr. Singh demonstrated the proper way to make a TLC spot.

After joining the Reynolds group, many people contributed to my work and made my stay at UF a pleasant journey of learning. I am grateful for the help and advice over the years from Dr. Stefan Ellinger, Dr. Prasad Taranekar, Dr. Robert Brookins, Dr. Timothy Steckler, Dr. Ryan Walzack, Dr. Nathan Heston, Dr. Aubrey Dyer, Dr. Svetlana Vasilyeva, Dr. Dan Patel, Dr. Mike Craig, Dr. Chad Amb, Dr. Pierre Beaujuge and Pengjie Shi. I also thank the younger generation of the Butler Lab members, Ken Graham, Romain Stalder, David Liu, Frank Arroyave, Yuying Wei, Bora Inci, Brian Atiken and Paula Delgado for their service and friendship. Special thanks go to Coralie Richard for occasionally bringing me her delicious home-made cookies.

I would also like to show my appreciation to Cheryl Googins, Gena Borrero and Sara Klossner for their great service, which made everything easy and convenient. Additionally, I will take this opportunity to thank George and Josphine Butler. I have enormously benefited from the environment and facility brought by their generous gifts. I am also grateful for the Butler Polymer Award funded by the Butler Foundation.

Finally, I would like to thank my parents Shixin Mei and Jinhua Zhu, and my wife, Yanrong Wu for their unconditional support and love. I am extremely indebted to my wife, who is carrying our first baby hundreds of miles away and asks little from me while I am working to prepare this dissertation. We are looking forward to the future and our soon-to-come son.

TABLE OF CONTENTS

| | <u>page</u> |
|--|-------------|
| ACKNOWLEDGMENTS | 4 |
| LIST OF TABLES..... | 10 |
| LIST OF FIGURES | 11 |
| LIST OF ABBREVIATIONS..... | 19 |
| ABSTRACT..... | 21 |
| CHAPTER | |
| 1 INTRODUCTION | 24 |
| 1.1 Organic Semiconducting Materials | 24 |
| 1.1.1 Inorganic and Organic Semiconducting Materials..... | 25 |
| 1.1.1.1 Conductivity..... | 26 |
| 1.1.1.2 Polaron, bipolaron and soliton | 28 |
| 1.1.1.3 The width of energy bands..... | 32 |
| 1.1.1.4 Charge carrier, charge transport, mobility and charge trap..... | 32 |
| 1.1.2 P-, N-type and Ambipolar Semiconducting Materials..... | 35 |
| 1.1.3 Molecular and Polymeric Semiconducting Materials..... | 36 |
| 1.2 Bandgap Engineering..... | 38 |
| 1.2.1 Bandgap Control | 39 |
| 1.2.2 The Donor-Acceptor Approach..... | 40 |
| 1.3 Photovoltaic Devices | 42 |
| 1.3.1 Silicon-Based Solar Cells..... | 43 |
| 1.3.2 Organic Solar Cells | 47 |
| 1.3.3 Bilayer Organic Solar Cells | 53 |
| 1.3.4 Bulk Heterojunction Organic Solar Cells | 54 |
| 1.3.4.1 Polymer/PCBM bulk heterojunction solar cells..... | 55 |
| 1.3.4.2 Polymer/polymer bulk heterojunction solar cells | 62 |
| 1.3.4.3 Molecular bulk heterojunction solar cells | 64 |
| 1.3.4.4 Organic-inorganic hybrid solar cells | 66 |
| 1.3.5 Tandem Bulk-heterojunction Solar Cells..... | 68 |
| 1.4 Objectives of this Dissertation | 69 |
| 2 EXPERIMENTAL METHODS AND CHARACTERIZATIONS | 71 |
| 2.1 Materials Characterization | 71 |
| 2.1.1 Structural Characterization | 71 |
| 2.1.2 Molecular Weight Characterization | 71 |
| 2.1.3 Thermal Characterization..... | 72 |
| 2.1.4 Electrochemical Characterization | 72 |

| | |
|---|------------|
| 2.1.5 Optical Characterization..... | 72 |
| 2.1.6 Morphology Characterization by Atomic Force Microscopy | 73 |
| 2.1.7 Single Crystal X-ray Diffraction..... | 74 |
| 2.1.8 2-D wide-angle X-ray scattering | 75 |
| 2.2 Bulk Heterojunction Solar Cells | 75 |
| 2.3 Charge Mobility Measurements | 77 |
| 3 LOW BAND GAP PLATIMUN-ACETYLIDE POLYMERS FOR PHOTOVOLTAIC APPLICATIONS | 80 |
| 3.1 Introduction..... | 80 |
| 3.2 Synthesis of Platinum-acetylide Model Complexes and Polymers | 85 |
| 3.3 Structural Characterizations..... | 89 |
| 3.4 Photophysical and Electrochemical Studies | 91 |
| 3.4.1 Photophysical Studies | 91 |
| 3.4.2 Electrochemical Studies | 98 |
| 3.5 Solar Cells..... | 101 |
| 3.5.1 Optical Properties and Hole Mobility of Polymer Films | 101 |
| 3.5.2 Solar Cell Studies | 103 |
| 3.7 Mechanism and Energetics of Charge Separation in the Pt-polymer/PC ₆₁ BM Blends .. | 106 |
| 3.6 Conclusion | 110 |
| 3.7 Experimental Details | 112 |
| 4 VINYLENE-LINKED DONOR-ACCEPTOR POLYMERS FOR PHOTOVOLTAIC APPLICATIONS | 122 |
| 4.1 Introduction..... | 122 |
| 4.2 Synthesis of P3HTV and PTVBT | 125 |
| 4.3 Structural Characterizations and Optical Studies | 127 |
| 4.4 Electrochemical and Spectroelectrochemical Studies | 130 |
| 4.5 Organic Solar Cells..... | 133 |
| 4.6 Conclusion | 135 |
| 4.7 Experimental Details | 136 |
| 5 DIKETOPYRROLOPYRROLE-BASED SEMICONDUCTING MATERIALS FOR PHOTOVOLTAIC APPLICATIONS | 144 |
| 5.1 Introduction..... | 144 |
| 5.2 Diketopyrrolopyrrole-based Amphiphilic Oligothiophene..... | 147 |
| 5.2.1 Synthesis of DPP-1 | 147 |
| 5.2.2 Structural Characterization, Optical and Electrochemical Studies | 149 |
| 5.2.3 Thermal Analysis, Polarized Light Microscopy and X-ray Analysis | 152 |
| 5.2.4 Morphology Studies | 156 |
| 5.2.5 Organic Field-Effect Transistors and Molecular Heterojunction Solar Cells.... | 158 |
| 5.3 Diketopyrrolopyrrole-based Hydrogen-bonded Amphiphilic Oligothiophenes | 161 |
| 5.3.1 Synthesis of DPP-OH-n (n = 0, 1, 2 and 3) and DPP-TEG | 162 |
| 5.3.2 Structural Characterization, Optical and Electrochemical Studies | 164 |

| | |
|---|------------|
| 5.3.3 Thermal Analysis | 167 |
| 5.4 Thermally Cleavable DPP-Based Low Bandgap Polymer | 169 |
| 5.5 Conclusion | 177 |
| 5.6 Experimental Details | 178 |
| 6 ISOINDIGO-BASED SEMICONDUCTING MATERIALS FOR PHOTOVOLTAIC APPLICATIONS | 190 |
| 6.1 Introduction..... | 190 |
| 6.2 Isoindigo-based Oligothiophenes | 191 |
| 6.2.1 Synthesis of Isoindigo-Based Oligothiophenes | 191 |
| 6.2.2 Structural Characterization, Optical and Electrochemical Studies | 194 |
| 6.2.3 Molecular Bulk-Heterojunction Solar Cells..... | 196 |
| 6.3 Molecular Engineering in Isoindigo-based Oligomers..... | 199 |
| 6.3.1 Synthesis of Isoindigo-Based Oligomers | 199 |
| 6.3.2 Structural Characterization, Optical and Electrochemical Studies | 200 |
| 6.3.3 Thermal Analysis | 207 |
| 6.3.4 Field-Effect Transistors and Molecular Bulk-Heterojunction Solar Cells..... | 208 |
| 6.4 Isoindigo-Based Polymers with Di-block Solubilizing Groups | 212 |
| 6.4.1 Synthesis of Isoindigo-Based Polymers with Biphasic Solubilizing Groups ... | 213 |
| 6.4.2 Structural Characterization, Optical and Electrochemical Studies | 214 |
| 6.4.3 Current-Voltage Measurements | 220 |
| 6.5 N-type Isoindigo-Based Conjugated Polymers | 222 |
| 6.5 Conclusion | 227 |
| 6.6 Experimental Details | 228 |
| 7 PERSPECTIVES AND OUTLOOK | 241 |
| LIST OF REFERENCES | 247 |
| BIOGRAPHICAL SKETCH | 265 |

LIST OF TABLES

| <u>Table</u> | | <u>page</u> |
|--------------|--|-------------|
| 1-1 | Photovoltaic data of representative high performance OPVs | 61 |
| 3-1 | Photophysical properties of model compounds and polymers | 92 |
| 3-2 | Photophysical properties of M3, M4, M5, P3, and P4 in ODCB | 98 |
| 3-3 | Electrochemical properties of model compounds and polymers | 101 |
| 3-4 | I-V characteristics of P1/PC ₆₁ BM photovoltaic devices..... | 105 |
| 3-5 | Summary of <i>I-V</i> characteristics of polymer/PC61BM OPVs | 106 |
| 5-1 | Summary of DPP-1 based OFET devices..... | 159 |
| 5-2 | Electrochemical energy levels and gaps of DPP-OH-n (n = 1-4) from DPV | 167 |
| 5-3 | Photovoltaic performance of PDPP/PC ₇₁ BM solar cells with different blend ratio..... | 175 |
| 5-4 | Transport properties of PDPP-Boc and PDPP polymer and their blends with PC ₇₁ BM in a ratio of 1:2 | 176 |
| 6-1 | Solid state optical and electrochemical properties and calculated energy levels..... | 196 |
| 6-2 | Performance of I-1/I-2:PC60BM solar cells before and after annealing | 197 |
| 6-3 | Electrochemically determined HOMO and LUMO energy levels of IsoI-N, IsoI-O and IsoI-S (by CV and by DPV). | 206 |
| 6-4 | Bottom-Gate Top-Contact OFET Characteristics of IsoI-N, IsoI-O, and IsoI-S..... | 210 |
| 6-5 | Performance of IsoI-N/IsoI-O/IsoI-S:PC ₆₁ BM solar cells..... | 212 |
| 6-6 | Zero-field hole mobility in PIsoI _{AM} -1, PIsoI _{AM} -2 and PIsoI _{AM} -3, derived from fitting J-V data to the trap-free single-carrier SCLC model | 221 |
| 6-7 | Electrochemically determined energy levels and gaps of PIsoI-C16 and PIsoI-BT- C16 by DPV..... | 226 |

LIST OF FIGURES

| <u>Figure</u> | <u>page</u> |
|--|-------------|
| 1-1 One silicon atom has been replaced by a) a pentavalent antimony atom, and b) a trivalent aluminum atom | 27 |
| 1-2 a) Band gaps of metals ($E_g \sim 0$ eV), semiconductors ($E_g < 3$ eV) and insulator ($E_g > 3$ eV); b) illustration of the energies involved in a molecular ionization process; c) schematic illustration of the one-electron energy levels for an organic molecule in its ground –state electronic configuration adopting: the equilibrium geometry of the ground state (left) and the equilibrium geometry of the first ionized state; d) schematic illustration of the band structure of a polymeric chain in the case of a vertical ionization process (left) and the formation of a polaron (right). E_{IP-v} is the vertical ionization energy, E_{rel} , the relaxation energy gained in the ionized state, E_{dis} the distortion energy to be paid in the ground state in order that the molecule adopts the equilibrium geometry of the ionized state, E_{IP-d} , the ionization energy of the distorted molecule | 29 |
| 1-3 a) Spectroelectrochemical experiments monitoring the formation of ionic states, namely polarons (radical-cations) and bipolarons (dication), upon progressive increase of an electrical bias in an oxidation process; b) progressive doping of poly(3,4-propylenedioxythiophene) (For simplicity, OH tails are omitted). | 31 |
| 1-4 Charge mobilities in different semiconductors and the necessary mobilities for their relevant applications | 34 |
| 1-5 a) The schematic diagram of the energy distribution of localized electronic states in the energy gap between the HOMO and LUMO bands (Adapted from Ref. 30 with permission); b) Distribution of HOMO and LUMO levels in disordered organic semiconducting materials..... | 35 |
| 1-6 a) representative p-type organic semiconducting materials; b) representative n-type organic semiconducting materials; c) representative ambipolar semiconducting materials | 37 |
| 1-7 a) Simplified diagram of the buildup of energy band of conjugate polymer chain; b) Illustration of the nondegenerate ground states of polythiophene as a representation for all aromatic conjugated polymers; c) the origin of bandgap..... | 39 |
| 1-8 Schematic illustration of donor-acceptor interaction. The HOMO of the donor segment interacts with the HOMO of the acceptor segment to yield two new HOMOs for the D-A polymer, so does LUMO levels. After the electrons redistribute themselves from their original non-interacting orbitals to the new hybridized orbitals of the polymer, a higher lying HOMO and a lower lying LUMO are formed. This leads to a narrowing of the optical band gap. | 41 |
| 1-9 a) Representative electron-deficient units; b) Representative electron-rich units. | 42 |

| | | |
|------|---|----|
| 1-10 | a) Representation of a silicon-based p-n heterojunction solar cell under short circuit conditions, illustrating the built-in electric field that exists in the depletion region near the p-n junction and the direction of current flow upon irradiation with light; b) The density of charge carriers in n-type doping, p-type doping and depletion region..... | 44 |
| 1-11 | Current-voltage characteristic of a silicon solar cell for dark and light conditions with illustration of the fill factor (<i>FF</i>), showing the open circuit voltage (<i>V_{oc}</i>), the short circuit current (<i>I_{sc}</i>), and the voltage and current at the maximum power point..... | 45 |
| 1-12 | a) Schematic representation of the irradiation geometry; b) Comparison of the solar spectrum under AM0 and AM1.5 conditions. | 47 |
| 1-13 | a) Energy diagram showing three possible arrangements of the lowest singlet (S_1), triplet (T_1), and charge transfer (CT) excited states relative to the singlet ground state (S_0) for D–A blends: Type I represents D–A blends in which photoinduced electron transfer (PET) is absent because the CT state is situated at an energy higher than the lowest S_1 state. Types IIa and IIb show situations in which PET does occur: with (Type IIa) and without (Type IIb) charge recombination to the lowest T_1 state (CRT). Note that E_g and E_T represent the lowest energies of $E_g(D)$ or $E_g(A)$, and $E_T(D)$ or $E_T(A)$, respectively; b) Jablonski diagram with energies of E_g , E_T , E_{CT} , $ E_{HOMO}(D) - E_{LUMO}(A) $ and eV_{oc} relative to the ground state (rounded to a tenth of an eV). The double headed arrow between V_{oc} and E_g indicates the minimum energy difference for which efficient PET is expected and that between V_{oc} and E_T the minimum energy difference that prevents CRT..... | 50 |
| 1-14 | A schematic sketch of electronic processes in an organic photovoltaic device..... | 52 |
| 1-15 | a) The original Tan cell; b) a solution processed polymer-polymer bilayer device. | 53 |
| 1-16 | Bulk heterojunction solar cells with different compositions: a) polymer/ PCBM; b) polymer/polymer; and c) small molecule/PCBM. | 54 |
| 1-17 | Representative p-type conjugated polymers with power conversion efficiency over 4% in blend of fullerene derivatives | 57 |
| 1-18 | Donor and acceptor combinations used in all-polymer solar cells | 63 |
| 1-19 | Solution-processable p-i-n three layered molecular bulk heterojunction solar cells based on TBP and SIMEF..... | 65 |
| 1-20 | a) Energy-level diagram showing the HOMO and LUMO energies of each of the component materials; b) the device structure (right) and TEM cross-sectional image (left) of the polymer tandem solar cell. Scale bars, 100 nm (lower image) and 20 nm (upper image). | 68 |
| 2-1 | AFM images of self-assembled DPP-based nanowires on mica (10 x 10 μm scan size): a) amplitude image, and b) height image. | 74 |

| | | |
|------|---|-----|
| 2-2 | Four possible FET architectures (in cross-section): a) top contact, b) bottom contacts, c) top contacts/top gate, d) bottom contacts/top gate..... | 79 |
| 3-1 | Structures of Pt-acetylide model compounds and polymers..... | 83 |
| 3-2 | Synthesis of M-1, M-2, P-1 and P-2: a) tributyl(thiophen-2-yl)stannane, Pd(PPh ₃) ₂ Cl ₂ , THF, 76 %; b) NBS, DMF, 92%; c) trimethylsilylacetylene, Pd(PPh ₃) ₂ Cl ₂ , CuI and iPr ₂ NH-THF, 90%; d) K ₂ CO ₃ , MeOH, 97%; e) trans-Pt(PBu ₃) ₂ Cl ₂ , CuI and piperidine-CH ₂ Cl ₂ ; f) <i>trans</i> -Pt(PBu ₃) ₂ Cl ₂ , TBAF, CuI and piperidine-CH ₂ Cl ₂ | 86 |
| 3-3 | Synthesis of compound 3-12: a) fuming H ₂ SO ₄ -HNO ₃ , 39 %; b) tributyl(thiophen-2-yl)stannane,Pd(PPh ₃) ₂ Cl ₂ , THF, 76 %; c) Iron-acetic acid, 65 %; d) tetradecane-7,8-dione, p-TSA, CHCl ₃ , 79 %. e) NIS, CHCl ₃ , 87 %; f) trimethylsilylacetylene, Pd(PPh ₃) ₂ Cl ₂ , CuI and iPr ₂ NH-THF, 84 %;..... | 87 |
| 3-4 | Synthesis of M-3, M-4, M-5 and P-3: a) 1 eq <i>trans</i> -Pt(PBu ₃) ₂ Cl ₂ , TBAT, CuI and Et ₃ N-CH ₂ Cl ₂ ;b) 5eq <i>trans</i> -Pt(PBu ₃) ₂ Cl ₂ , TBAT, CuI and Et ₃ N-Ch ₂ Cl ₂ ; c) CuI and Et ₃ N-CH ₂ Cl ₂ | 87 |
| 3-5 | Synthesis of P-4: a) CuI and Et ₃ N-CH ₂ Cl ₂ | 88 |
| 3-6 | ³¹ P-NMR spectra of model complexes of 3-13, 3-14, and 3-15. | 89 |
| 3-7 | MALDI-TOF mass spectra of P1 and P2..... | 91 |
| 3-8 | Absorption and emission spectra of a) M-1 and P1, and b) M-2 and P2..... | 93 |
| 3-9 | Transient absorption difference spectra of a) M-1and b) P1. Excited at 550 nm with 5 ns pulses. Spectra obtained with an initial 60 ns delay and with succeeding 1 μ s delay increments. Arrows indicate the direction of change of spectra with increasing delay time..... | 96 |
| 3-10 | Fluorescence emission quenching of M-1by PC ₆₁ BM. The legend shows the concentration of PC ₆₁ BM in solution, and the plot in the inset shows the Stern-Volmer plot of I ⁰ /I vs. [PC ₆₁ BM]..... | 97 |
| 3-11 | UV-vis absorption spectra of P1, P3, and P4..... | 98 |
| 3-12 | Cyclic voltammograms of a) M-1, b) P1, c) M2, and d) P2 in CH ₂ Cl ₂ with 0.1 M TBAPF ₆ as supporting electrolytes, scanned at 100 mV/s. Potentials are referenced to Fc/Fc ⁺ as an internal standard. | 100 |
| 3-13 | I-V characteristic curves of a) P1/PC ₆₁ BM and b) P2/PC ₆₁ BM photovoltaic cells under AM 1.5 simulated solar irradiation (100mW·cm ⁻²) | 104 |
| 3-14 | External quantum efficiencies and absorption spectra of a) P1/PC ₆₁ BM blend, and b) P2/PC ₆₁ BM. | 106 |

| | | |
|------|---|-----|
| 3-15 | Energy level diagram for P1..... | 108 |
| 4-1 | Chemical structures of P3HTV, PTVBT and bisTVBT | 124 |
| 4-2 | Synthesis of regioregular poly(3-hexylthienylenevinylenes) (P3HTV). a) NBS, DMF, 88%; b) acrylic acid, Pd(OAc) ₂ , P(o-tol) ₃ , Et ₃ N-CH ₃ CN-THF, 95%; b) NBS, LiOAc, CH ₃ CN-H ₂ O, 48%. | 125 |
| 4-3 | Synthesis of PTVBT and bisTVBT. a) 1) C ₈ H ₁₇ Br, Mg, Et ₂ O; 2) Ni(dppf)Cl ₂ , Et ₂ O, reflux, 88% b) 4,4,4',4',5,5,5',5'-octamethyl-2,2'-bi(1,3,2-dioxaborolane) [Ir(OMe)COD] ₂ -dtbpy Heptane, 50 °C, 81%; c)Pd(OAc) ₂ , P(o-tol) ₃ ,Et ₃ N, CH ₃ CN-THF, reflux, 65%; d) NBS, LiOAc, CH ₃ CN-H ₂ O, rt, 60%; e) Pd ₂ (dba) ₃ ,P(o-tyl) ₃ ,Et ₄ NOH, toluene-water, 60 °C, 87%; f) 2-(3,4-diocetylthiophen-2-yl)-4,4,5,5-tetramethyl-1,3,2-dioxaborolane, Pd ₂ (dba) ₃ , [(^t Bu ₃)PH]BF ₄ , CsF, THF-water, rt, 86%; | 127 |
| 4-4 | ¹ H-NMR spectra of bisTVBT in deuterated chloroform (top) at room temperature and PTVBT in deuterated tetrachloroethane at 100 °C..... | 128 |
| 4-5 | IR spectra of bisTVBT and PTVBT | 128 |
| 4-6 | Absorption spectra of bisTVBT and PTVBT in THF..... | 130 |
| 4-7 | a) Differential pulse voltammetry of PTVBT on a platinum working electrode in 0.1M TBAP/PC solution with a step time of 0.02 s, a step size of 2 mV, and amplitude of 100 mV; b) Cyclic voltammetry of PTVBT on a platinum working electrode (0.02 cm ²) in 0.1M TBAP/PC solution at 50mV s ⁻¹ | 131 |
| 4-8 | Spectroelectrochemistry of PTVBT spray cast on ITO/glass from 3 mg/mL solution of the polymer in toluene in 0.1M TBAP/PC between 0.2 and 0.85V in 50mV steps (vs Fc/Fc ⁺). The thick line corresponds to the neutral state of the polymer at 0.2 V. | 132 |
| 4-9 | a) A.M. 1.5 <i>J-V</i> characteristics of devices with varied PTVBT/PC ₆₁ BM weight percentages; b) A.M. 1.5 Efficiencies measured from cells of differing PTVBT-PC ₆₁ BM weight percentages and also differing active layer thicknesses; c) IPCE of a representative device..... | 134 |
| 4-10 | Tapping mode atomic force microscopy images of spin coated blend films from solutions of varying PTVBT:PCBM weight ratios. The z-scale factor is 20..... | 135 |
| 5-1 | Chemical structure and model of DPP-1. | 147 |
| 5-2 | Synthesis of DPP-1. a) potassium <i>tert</i> -butoxide, <i>tert</i> -amyl alcohol, 95 °C, ~30%; b) 1-bromo-2-(2-(2-methoxyethoxy)ethoxy)ethane, potassium carbonate, DMF, 46%; c) NBS, chloroform, 61%; d) tributyl(5'-dodecyl-2,2'-bithiophen-5-yl)stannane, Pd ₂ (dba) ₃ , P(o-tyl) ₃ , THF, 49%..... | 148 |
| 5-3 | ¹ H-, and ¹³ C-NMR of DPP-1 in CDCl ₃ | 150 |

| | | |
|------|--|-----|
| 5-4 | a) Absorption and emission of DPP-1 in toluene; b) absorption of DPP-1 (2.2×10^{-5} M) in NMP, DCM, THF and DME; c) the images of DPP-1) in NMP, DCM, THF and DME | 151 |
| 5-5 | a) Cyclic voltammetry, and b) differential pulse voltammetry of DPP-1 measured in a 0.1M solution of TBAPF ₆ /DCM (scan rate 25mV/s) vs Ag/Ag ⁺ ($E_{Fc/Fc}^+ = E_{Ag/Ag}^+ + 0.16$ V) | 152 |
| 5-6 | Differential scanning calorimetry thermograms. a) DPP-1, b) PC ₆₁ BM, and c) DPP-1 and PC ₆₁ BM mixture (1:1, wt %). | 153 |
| 5-7 | a) Polarized optical microscope (POM) images of DPP-1 under 170 °C at two different angels; b) Snapshots of the directed growth of a DPP-1 plastic phase as viewed by POM at 170 °C after shearing (pictures taken at 5 s intervals and the arrow indicates the shearing direction); c) POM images of DPP-1 under 80 °C, and d) RT | 154 |
| 5-8 | Diffraction patterns obtained from DPP-1 at 170, 80, and 50 °C..... | 155 |
| 5-9 | a) tapping mode AFM image ($20 \times 20 \mu\text{m}$, 250 nm in height) of DPP-1 as deposited from THF-hexane onto mica. b) UV-vis spectra of DPP-1 in methylcyclohexane (2.2×10^{-5} M, at 30 °C) recorded at 45 s intervals;..... | 157 |
| 5-10 | Tapping mode AFM images ($5 \times 5 \mu\text{m}$) with z-height line scan profiles of DPP-1 drop-cast from chlorobenzene (2.2×10^{-4} M) on mica. Solvent evaporation times are a) 3.5 min, b) 5 min and c) 8.5 min..... | 157 |
| 5-11 | a) Output and b) transfer characteristics of a representative DPP-1 field-effect transistor device | 159 |
| 5-12 | a) <i>J-V</i> characteristics and b) external quantum efficiencies of a representative DPP-1 : PC ₆₁ BM photovoltaic device before and after annealing at 90 °C | 160 |
| 5-13 | Molecular structures of DPP-OH-n and DPP-TEG. | 161 |
| 5-14 | Synthesis of donor building blocks for DPP-OH-n. a) C ₁₂ H ₂₅ Br, K ₂ CO ₃ , DMF, 60 °C, 94%; b) 4,4,4',4',5,5,5',5'-octamethyl-2,2'-bi(1,3,2-dioxaborolane), Ir[OMe(COD)] ₂ , heptane, 80 °C, 91%; c) 2-bromothiophene, Pd ₂ (dba) ₃ , P(o-tyl) ₃ , aqueous Et ₄ NOH, toluene, 98%; d) 2-bromobithiophene, Pd ₂ (dba) ₃ , P(o-tyl) ₃ , aqueous Et ₄ NOH, toluene, 71%; e) 2-bromoterthiophene, Pd ₂ (dba) ₃ , P(o-tyl) ₃ , aqueous Et ₄ NOH, toluene, 72%; f) 4,4,4',4',5,5,5',5'-octamethyl-2,2'-bi(1,3,2-dioxaborolane), Ir[OMe(COD)] ₂ , heptane, 80 °C, 50%; g) 4,4,4',4',5,5,5',5'-octamethyl-2,2'-bi(1,3,2-dioxaborolane), Ir[OMe(COD)] ₂ , heptane, 80 °C, 50%; h) 4,4,4',4',5,5,5',5'-octamethyl-2,2'-bi(1,3,2-dioxaborolane), Ir[OMe(COD)] ₂ , heptane, 80 °C..... | 162 |
| 5-15 | Synthesis of 3,4,5-tris(dodecyloxy)phenylboronic acid. a) K ₂ CO ₃ , C ₁₂ H ₂₅ Br, DMF, 90°C, 24h, 85%; b) NaNO ₂ , HNO ₃ , H ₂ O, CH ₂ Cl ₂ , rt, 3h, 90%; c) hydrazine, graphite, | |

| | | |
|------|--|-----|
| | EtOH, 110 °C, 24h, 88%; d) NaNO ₂ , HCl, H ₂ O, 0 °C and then KI, rt, 12h, 49%; e) nBuLi, THF, -78 °C followed by B(OMe) ₃ , -78 °C and HCl, H ₂ O, 80%..... | 163 |
| 5-16 | Synthesis of DPP core for DPP-OH-n. a) Et ₃ N, CH ₂ Cl ₂ , rt, 95%; b) 5-1 , K ₂ CO ₃ , DMF, 90°C, 24h, 42%; c) NBS, chloroform, then HCl, H ₂ O, rt, 60%..... | 164 |
| 5-17 | ¹ H-NMR spectra of DPP-C12, DPP-TEG and DPP-OH-2..... | 164 |
| 5-18 | Absorption spectra of DPP-OH-n (n = 1-4) in CH ₂ Cl ₂ and their optical images | 166 |
| 5-19 | DSC thermograms of DPP-C12, DPP-TEG and DPP-OH-2..... | 168 |
| 5-20 | DSC thermograms of DPP-OH-n (n=1, 2 3 and 4)..... | 169 |
| 5-21 | Thermal transition of PDPP-Boc | 170 |
| 5-22 | a) di-tert-butyl dicarbonate, DMAP, THF, rt, 60%; b) NBS, CHCl ₃ , rt, 77%; c) ProDOT-Sn2, Pd ₂ (dba) ₃ , P(o-tyl) ₃ , toluene, 85 °C, 85%..... | 170 |
| 5-23 | a) Weight loss of PDPP-Boc as a function of temperature; b) Absorption spectra of PDPP-Boc in solution, thin-film before and after cleavage; c) Crystal structure for compound 5-15 | 171 |
| 5-24 | a) Weight loss of N, N' -bis-(<i>tert</i> -butoxycarbonyl)-DPP as a function of temperature (rate, 10 °C min-1; onset, 163.6 °C; midpoint, 177.7 °C; end point 191.8 °C; step height, 40.7%); b) Ultraviolet-visible absorption spectra of a 1.5- μ m-thick p - hydroxy-polystyrene film containing 40% N, N' -bis-(<i>tert</i> -butoxycarbonyl)-DPP, spin-coated (yellow) and after 2 min at 180 °C (red); c) Schematic illustration of the hydrogen-bonding network of DPP. | 172 |
| 5-25 | Cyclic voltammograms and differential pulse voltammograms of PDPP-Boc. | 173 |
| 5-26 | The J-V curve of a DPP polymer solar cell under AM 1.5 conditions with a blend ratio of a) 1:1, b) 1:2, and c) 1:3. | 174 |
| 6-1 | Chemical structures of I-1, and I-2. | 191 |
| 6-2 | Synthetic scheme of isoindigo building blocks. a) con HCl (<i>cat.</i>), acetic acid, reflux, > 95%; b) RBr, K ₂ CO ₃ , DMF, 100 °C. | 192 |
| 6-3 | Synthetic scheme of mono-functionalized isoindigo building block. a) <i>conc.</i> HCl (<i>cat.</i>), acetic acid, reflux, > 95%; b) RBr, K ₂ CO ₃ , DMF, 100 °C. | 193 |
| 6-4 | Synthesis of I-1, and I-2. a) Pd ₂ (dba) ₃ , P(o-tyl) ₃ Et ₄ NOH, toluene, 85 °C, 83% and 57% for I-1, and I-2, respectively. | 193 |
| 6-5 | UV-vis spectra of I-1 and I-2 in solution and in thin-film..... | 194 |

| | | |
|------|--|-----|
| 6-6 | Cyclic voltammetry of I-1 (left) and I-2 (right) measured in a 0.1 M solution of TBAPF ₆ /DCM (scan rate 25 mV/s) vs Fc/Fc ⁺ | 195 |
| 6-7 | J-V characteristics of I-1/I-2:PC ₆₁ BM solar cells under 100 mW/cm ² white light illumination annealed at 100 °C for 20 min. | 197 |
| 6-8 | AFM height images of I-1:PCBM (50:50) spin-coated from chlorobenzene a) as cast, and b) annealed at 100 °C for 20 min; I-2:PCBM (60:40) spin-coated from chlorobenzene c) as cast, and d) annealed at 100 °C for 20 min. All images are 1 x 1 um with 5 nm height scales. RMS surface roughness values of the AFM images are 0.15 nm, 0. 98 nm , 0.14 nm , and 0.95 nm from left to right..... | 198 |
| 6-9 | Chemical structures of IsoI-N, IsoI-O and IsoI-S..... | 199 |
| 6-10 | Synthesis of IsoI-N, IsoI-O and IsoI-S. a) Pd ₂ (dba) ₃ , P(o-tyl) ₃ Et ₄ NOH, toluene, 85 °C, 88%, 92%, and 84% for IsoI-N, IsoI-O and IsoI-S, respectively. | 200 |
| 6-11 | ¹ H-NMR spectra of IsoI-N, IsoI-O and IsoI-S including a) the full spectra and the aromatic regions of b) IsoI-N, c) IsoI-O, and IsoI-S..... | 201 |
| 6-12 | UV-vis spectra of IsoI-N, IsoI-O and IsoI-S a) in solution, and b) in thin-film. | 203 |
| 6-13 | Temperature-dependent UV-vis spectra of a) IsoI-N, b) IsoI-O and c) IsoI-S. | 204 |
| 6-14 | Cyclic voltammograms (scan rate = 50 mV/s) and differential pulse voltammetry (step size of 2 mV and step time of 0.1 seconds) of IsoI-N, IsoI-O and IsoI-S in 0.1 M TBAPF ₆ -CH ₂ Cl ₂ electrolyte solution. a) CV of IsoI-N; b) DPV of IsoI-N; c) CV of IsoI-O; d) DPV of IsoI-O; e) CV of IsoI-S; f) DPV of IsoI-S..... | 205 |
| 6-15 | a) Repetitive scan electropolymerization of 5 mM IsoI-N on ITO in 0.1 M TBAPF ₆ /DCM ; b) UV-Vis spectra of IsoI-N in CH ₂ Cl ₂ and electropolymerized Poly(IsoI-N) on ITO | 206 |
| 6-16 | Thermogravimetric analysis of a) IsoI-N, b) IsoI-O and c) IsoI-S. | 207 |
| 6-17 | DSC thermograms of a) IsoI-N, b) IsoI-O and c) IsoI-S (kJ mol ⁻¹ , unit in parendissertation after transition temperature) | 208 |
| 6-18 | a) Output and b) transfer characteristics of a representative IsoI-S field-effect transistor device processed from chloroform solution..... | 210 |
| 6-19 | J-V characteristics of IsoI-O/IsoI-S:PC ₆₁ BM solar cells | 212 |
| 6-20 | Polymer structures of PIsoI _{AM} -1, PIsoI _{AM} -2 and PIsoI _{AM} -3. | 213 |
| 6-21 | Synthesis of IsoI _{AM} building blocks and PIsoI _{AM} . a) K ₂ CO ₃ , DMF, 100 °C; b) Pd ₂ (dba) ₃ , P(o-tyl) ₃ , toluene, 85 °C..... | 214 |
| 6-22 | GPC traces of PIsoI _{AM} -1, PIsoI _{AM} -2 and PIsoI _{AM} -3 | 215 |

| | | |
|------|---|-----|
| 6-23 | UV-vis spectra of PIsoI _{AM} -1, PIsoI _{AM} -2 and PIsoI _{AM} -3 in thin film..... | 216 |
| 6-24 | Temperature-dependent UV-Vis spectra of a) PIsoI _{AM} -1; b) PIsoI _{AM} -2; c) PIsoI _{AM} -3; and d) PIsoI _{AM} -1, PIsoI _{AM} -2 and PIsoI _{AM} -3 in dichlorobenzene at 95 °C..... | 217 |
| 6-25 | Cyclic voltammetry of a) PIsoI _{AM} -1; b) PIsoI _{AM} -2; c) PIsoI _{AM} -3 measured in a 0.1M solution of TBAPF ₆ /ACN vs Fc/Fc ⁺ | 218 |
| 6-26 | Differential pulse voltammetry of a) PIsoI _{AM} -1; b) PIsoI _{AM} -2; c) PIsoI _{AM} -3 measured in a 0.1M solution of TBAPF ₆ /ACN vs Fc/Fc ⁺ | 218 |
| 6-27 | 2D wide-angle X-ray scattering of PIsoI _{AM} -1, PIsoI _{AM} -2 and PIsoI _{AM} -3..... | 220 |
| 6-28 | a) Experimental dark current densities for hole-only devices of PIsoI _{AM} -1, PIsoI _{AM} -2 and PIsoI _{AM} -3 as a function of the effective electric field; b) Experimental dark current densities for electron-only devices of PIsoI _{AM} -1, PIsoI _{AM} -2 and PIsoI _{AM} -3 as a function of the effective electric field..... | 221 |
| 6-29 | Polymer structures of PIsoI-C16 and PIsoI-BT-C16..... | 223 |
| 6-30 | Synthesis of PIsoI-C16 and PIsoI-BT-C16. a) Pd(dppf)Cl ₂ , KOAc, 1,4-dioxane, 80 °C, 75%; b) Pd ₂ (dba) ₃ , P(o-tyl) ₃ Et ₄ NOH, toluene, 85 °C, 95% and 93% for PIsoI-C16 and PIsoI-BT-C16, respectively..... | 224 |
| 6-31 | ¹ H-NMR spectrum of compound 6-11..... | 224 |
| 6-32 | Differential pulse voltammetry of PIsoI-C16 and PIsoI-BT-C16. Electrochemical reduction and oxidation of the films on a platinum button was carried out in 0.1 M TBAPF ₆ /ACN supporting electrolyte using Ag/Ag ⁺ reference electrode (calibrated against Fc/Fc ⁺) and a platinum flag as the counter electrode..... | 225 |

LIST OF ABBREVIATIONS

| | |
|------------------------------------|---|
| ACS | American Chemical Society |
| AFM | Atomic Force Microscopy |
| BTD | 2,1,3-benzothiadiazole |
| CRT | Charge recombination to triplet |
| CST | Charge separated state |
| CT | Charge transfer |
| CV | Cyclic voltammetry |
| DMF | Dimethylformamide |
| DPP | Diketopyrrolopyrrole |
| D-A-D | Donor-Acceptor-Donor |
| dppf | 1,1'-diphenylphosphino-ferrocene |
| DPV | Differential pulse voltammetry |
| Fc/Fc ⁺ | Ferrocene/Ferrocenium |
| FF | Fill factor |
| GPC | Gel permeation chromatography |
| J _{sc} | Short current density |
| MALDI | Matrix assisted laser desorption/ionization |
| NBS | N-bromosuccimide |
| OPVs | Organic photovoltaics |
| OLEDs | Organic light-emitting diodes |
| OFETs | Organic field-effect transistors |
| Pd ₂ (dba) ₃ | Trisbenzylidene acetone dipalladium (0) |
| PCE | Power conversion efficiency |
| PCBM | [6,6]-phenyl-C ₆₁ -butyric acid methyl ester fullerene |

| | |
|----------|--|
| PDI | Polydispersity index |
| PET | Photoinduced electron transfer |
| P3HT | Poly(3-hexylthiophene) |
| PTV | Poly(thienylene vinylene) |
| SCLC | Space-charge limited current |
| TBAF | Tetrabutylammonium fluoride |
| TBAT | Tetrabutylammonium triphenyldifluorosilicate |
| THF | Tetrahydrofuran |
| V_{oc} | Open circuit voltage |

Abstract of Dissertation Presented to the Graduate School
of the University of Florida in Partial Fulfillment of the
Requirements for the Degree of Doctor of Philosophy

**SOLUTION-PROCESSABLE ORGANIC SEMICONDUCTING MATERIALS FOR
PHOTOVOLTAIC APPLICATIONS**

By

Jianguo Mei

August 2010

Chair: John R. Reynolds
Major: Chemistry

This dissertation documents our efforts in the development of solution-processable organic semiconducting materials for photovoltaic applications. The operation of organic solar cells generally involves the following processes: light absorption, exciton generation and diffusion, charge separation and transport, as well as charge collection. Thus, the organic molecules and polymers reported are designed to meet one or more criteria imposed by these processes for the purpose of understanding fundamental aspects and potentially achieving high performance photovoltaic materials.

Incorporation of heavy transition metals into polymer backbones theoretically imparts the resulting metallated conjugated polymers with longer triplet exciton lifetimes, and less geminate recombination compared to pure hydrocarbon conjugated polymers when used as active materials in bulk-heterojunction solar cells. Toward this end, a family of platinum-acetylide polymers with bandgaps ranging from 1.4 to 2.0 eV has been developed. Extensive photophysical on the polymers and their blends with PCBM (phenyl-C₆₁-butyric acid methyl ester) revealed that although a triplet excited state is produced following light absorption, it is too low in energy to undergo photoinduced electron transfer with PCBM. It is suggested that the

photovoltaic response of the solid materials arises due to charge separation from the singlet state of the polymers.

The second part of this dissertation deals with a general approach to prepare a class of vinylene-linked donor-acceptor low bandgap conjugated polymers. By using a simple sequence of Heck coupling, Hunsdiecker decarboxylation bromination and Suzuki coupling, we were able to prepare a vinylene-linked thiophene-benzothiadiazole polymer (PTVBT). By removing the torsion and planarization of polymer backbones, PTBVT shows a red shift (~ 20 nm) in its absorption in comparison to its parent analogue.

Using diketopyrrolopyrrole (DPP) as an electron acceptor, amphiphilic discrete oligomers that can self-assemble into highly ordered nanostructures for organic field-effect transistors (OFETs) and molecular bulk-heterojunction solar cells (OPVs) were studied. Charge mobility as high as $4 \times 10^{-3} \text{ cm}^2 \text{V}^{-1} \text{s}^{-1}$ was obtained from OFET measurement and PCEs of 0.7% were reported with a high fill factor of 0.58 in molecular BHJ solar cells with PCBM as an electron acceptor. A DPP-based thermocleavable polymer was also prepared and OPVs based on this polymer demonstrated an enhanced PCE of 1.44% upon cleavage.

In chapter 6, isoindigo was introduced as an electron acceptor in π -conjugated materials. Isoindigo-based oligothiophenes were prepared and used as donor materials in molecular bulk-heterojunction OPVs and power conversion efficiencies up to 1.85% were achieved. Three isoindigo-based polymers were synthesized to validate the hypodissertation that charge mobility in conjugated polymers can be enhanced via enforcement of π - π interactions by means of introducing biphasic solubilizing groups. The results from SCLC modeling of J-V characteristics of single-carrier diodes are consistent with the hypodissertation presented where a nearly 10-fold increase in hole mobilities was observed for polymers with biphasic solubilizing group. In

addition, a facile approach to isoindigo-based n-type conjugated polymers was also reported, in which the LUMO level as deep as -4.1 eV and deep HOMOs of ~6.0 eV were found. These polymers can be considered as an alternative to commonly used acceptors such as PCBM derivatives currently employed in polymer-based solar cell devices

CHAPTER 1

INTRODUCTION

1.1 Organic Semiconducting Materials

Organic semiconducting materials have been focus of inquiry in the development of potential low-cost, large-area, flexible and light-weight optoelectronic devices, such as light-emitting diodes,¹ solar cells,² field-effect transistors,³ organic lasers,⁴ and electrochromics.⁵ Compared with their widely known inorganic counterparts; mainly silicon, germanium and metal oxide semiconductors, organic semiconducting materials present some intrinsic merits. For instance, materials properties can be fine tuned via structural modifications that can be easily achieved through intelligent molecular design. Solution-processing can be realized for low cost and large-area devices via numerous techniques (spin-coating, spray coating, ink-jet printing, roll-to-roll printing and Langmuir layer-by-layer assembly, etc).⁶⁻⁸ The low processing temperature, combined with the mechanical flexibility of organic materials, provides great opportunities to access flexible integrated circuits, electronic paper (or fabric), and foldable organic electronics.⁹⁻¹⁰

To chemists, physicists, materials scientists and electrical engineers who currently work in this field, the question then simply becomes how to turn these great visions and perspectives into reality. Arguably the most important merit of organic semiconducting materials lies in the ability to impart functionality by rational molecular design with chemists' synthetic capabilities. The aspect of materials and electrical engineering is also an indispensable component of the successful development of 21st century organic electronics. The performance of these sophisticated electronics depends not only on the intrinsic properties of the organic semiconducting materials, but also the device configuration and the technique to assemble the devices. In addition, understanding the operation principles is a prerequisite in order to achieve

sustainable development in organic devices. In a word, synergetic efforts from different disciplines are required for the realization of reliable and high-performance opto-electronics using organic materials. The first step would be to learn from the success of inorganic semiconductors and understand the unique features of organic materials. Therefore, this chapter will address this critical issue by making comparisons of inorganic semiconductors and organic semiconducting materials, followed by categorizing them by either structure or function to present the intrinsic features of organic materials. The subsequent section will then address some basics in organic semiconducting materials such as the origin of the bandgap. After having the information on the materials side, the discussion will then move to device fabrication and physics. A variety of devices will be covered and an emphasis will be put on organic photovoltaics (OPVs). Finally, the central topic of this dissertation will be discussed; approaches to design solution-processible organic semiconducting materials for photovoltaic applications, and the principles for constructing these materials.

1.1.1 Inorganic and Organic Semiconducting Materials

Recently, there has been an increasing debate as to whether the next generation semiconductors, organic semiconducting materials, will replace or be a viable alternative to silicon in the electronic industry. To set aside whether it is a valid claim or not, however, it is always important for organic semiconductor to learn from the success of inorganic semiconductor in electronic industry. This section is intended to present a condensed collection of concepts in modern solid state theory, primarily developed for inorganic materials, to explore the applicability of these concepts in organic semiconductors, and to make a comparison between the two types of materials.

1.1.1.1 Conductivity

Conductivity (σ) is defined as the charge transported across a unit cross-sectional area per second per unit electric field, and can be written as:

$$\sigma = zen\mu \quad (1-1)$$

where z is ion charge per elemental charge, e is elemental charge, n is the concentration and μ is mobility.

The conductivity is thus proportional to the amount of charge (zen) and to the velocity of charge transport (μ) in a field, where ze represents a net charge of electronic charges for each carrier. If it is assumed to travel under unit electric field, the velocity is called the mobility μ . Conductivity also shows anisotropic nature in organic materials, because the mobility μ is usually different with adapting different spatial orientations.

The major breakthrough in conductance of organic semiconducting materials came from the discovery in 1977 that polyacetylene could be made highly conducting, $\sim 10^3 (\Omega \text{ cm})^{-1}$, from its intrinsic conductivity, $\sim 10^{-5} \Omega^{-1} \text{ cm}^{-1}$, by exposing it to oxidizing or reducing agents.¹¹ The room temperature conductivity of doped polyacetylene is therefore comparable with their inorganic counterparts (polymers), for instance polysulfur nitride $(\text{SN})_x$, whose conductivity is in the order of $10^3 (\Omega \text{ cm})^{-1}$ (also to be compared with $5 \times 10^6 (\Omega \text{ cm})^{-1}$ for copper). It must be stressed that the metallic character of $(\text{SN})_x$ is an intrinsic property of the material, related with the presence of one unpaired electron for each S-N unit. As a result, the highest occupied molecular orbitals are only half-filled. Since there is no forbidden gap (see section 1.1.1.3 for discussion of this term) between the highest occupied and lowest unoccupied levels, the electrons can move freely under an applied electric field to give rise to an electrical conductivity. In most organic semiconducting materials, they have closed-shell, meaning all the electrons are paired. Doping is required to bring up the conductivity as observed in polyacetylene.¹¹

The doping mechanism in π -conjugated organic films differs from that of inorganic semiconductors. In order to get conductivities approaching the metallic range, high doping levels are typically required, as high as 20% in the case of polyacetylene when it is doped by iodine.¹¹⁻¹³ This is in sharp contrast with inorganic semiconductors where doping levels are several orders of magnitude lower.

In inorganic semiconductors, the conductivity can be intrinsic or extrinsic. Any conductivity from intrinsic semiconductors is due to electrons acquiring sufficient energy to cross the forbidden gap. The energy can be supplied from thermal, photon or electrical field excitation. Excitation of electrons into the conduction band in an intrinsic semiconductor leaves behind holes in the valence band. That is to say excitation of an intrinsic semiconductor creates two charge carriers.

Extrinsic conductivity is due to lattice defects, resulting from lattice imperfections or impurities. For instance, one silicon atom has been replaced by a pentavalent antimony atom or trivalent aluminum atom, as illustrated in Figure 1-1. The former leads to one free electron, called n-doped. It presents n-type conductivity. The latter creates an electron vacancy, namely a hole. This type of material is called p-type and gives rise to p-type conduction.

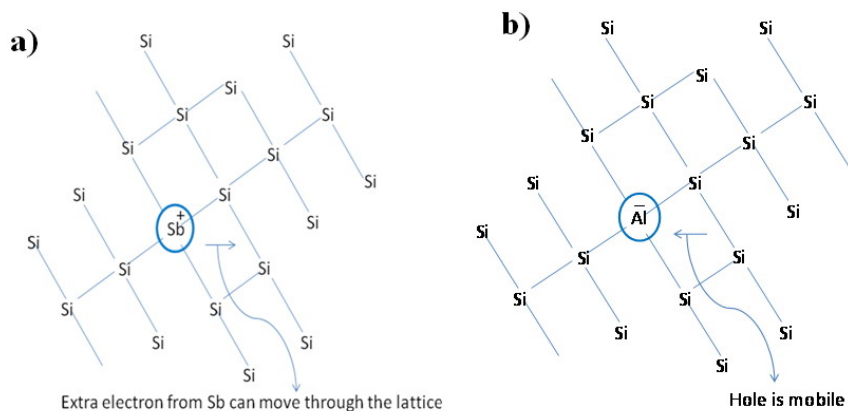


Figure 1-1. The origin of extrinsic conductivity. One silicon atom has been replaced by a) a pentavalent antimony atom, and b) a trivalent aluminum atom.

In organic semiconductors, optical absorption can lead to formation of spatially localized electrically neutral electron-hole pairs (called excitons). The exciton binding energy that holds electron-hole pairs is typically high around ~0.5 eV in organic materials.¹⁴ Exciton motions are not affected by an electrical field, since they are neutral species. In order to generate an electrical current, excitons are required to be split to generate free charge carriers. This feature herein leads to a different operation mechanism in organic solar cells. More analysis will be given in section 1.4.

Initially, high conductivity observed in doped organic semiconductor was ascribed to the formation of unfilled electronic bands, resulting from electrons being removed from the top of the valence band for p-doping or being added to the bottom of conduction band for n-doping.¹⁵ This is in analogy to the mechanism of charge generation mechanism in doped inorganic semiconductors. The validation of this theory was questioned when unpaired electrons were not observed in doped polyacetylene, polypyrrole and poly(*para*-phenylene), etc. Instead, polaronic models and disordered charge-transport mechanisms are consistent with the experimental findings.¹⁶⁻¹⁸

1.1.1.2 Polaron, bipolaron and soliton

In a conjugated molecule (polymer), the interaction of a unit cell with all its neighboring units lead to the formation of electronic bands.¹⁹ The highest occupied molecular orbitals (HOMO) form the valence band and the lowest unoccupied molecular orbitals (LUMO) create conduction band. The width of the forbidden band, namely energy gap (bandgap), between the valence band and conduction band determines the intrinsic electrical properties of a material as illustrated in Figure 1-2a. Upon doping, high conductivity can be observed in organic materials. As discussed in section **1.1.1.1.**, however, conductivity in highly doped organic materials does

not seem to be associated with unpaired electrons but rather with spinless charge carriers, characteristic of formation of bipolarons.

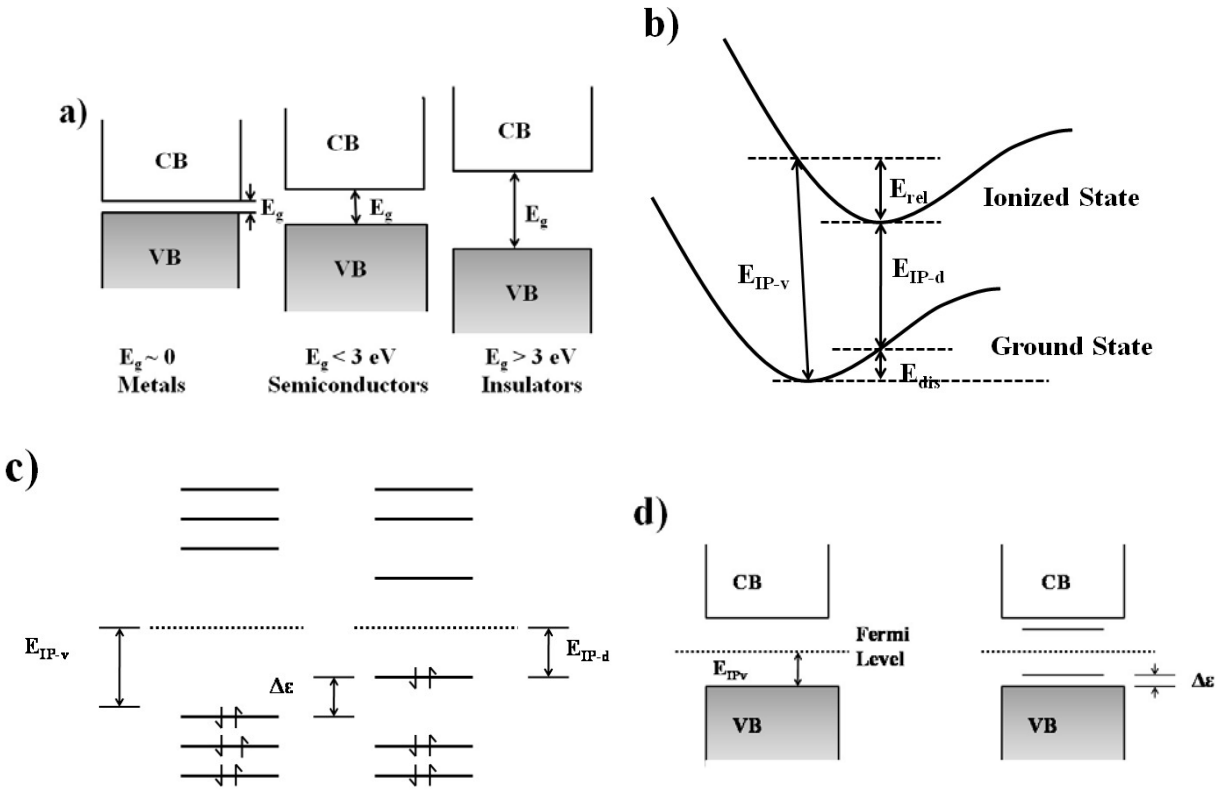


Figure 1-2. a) Band gaps of metals ($E_g \sim 0$ eV), semiconductors ($E_g < 3$ eV) and insulator ($E_g > 3$ eV); b) illustration of the energies involved in a molecular ionization process; c) schematic illustration of the one-electron energy levels for an organic molecule in its ground-state electronic configuration adopting: the equilibrium geometry of the ground state (left) and the equilibrium geometry of the first ionized state; d) schematic illustration of the band structure of a polymeric chain in the case of a vertical ionization process (left) and the formation of a polaron (right). $E_{\text{IP-v}}$ is the vertical ionization energy, E_{rel} , the relaxation energy gained in the ionized state, E_{dis} the distortion energy to be paid in the ground state in order that the molecule adopts the equilibrium geometry of the ionized state, $E_{\text{IP-d}}$, the ionization energy of the distorted molecule (Adapted from Ref. 19 with permission).

It is helpful to elucidate doping process in order to understand this phenomenon. In organic molecules, it is usually the case that the equilibrium geometry in the ionized state is different than in the ground state, e.g., benzenoid-like geometry in ground state *vs* quinoid-like geometry in the ionized state. Figure 1-2b shows an ionization process of a molecule (polymer). There are

two possible pathways, a vertical ionization process and a distorted ground-state ionization process. In the former process, an energy E_{IP-d} has to be initially paid for ionized states by keeping the geometry of a ground state. Through relaxing down to the bottom of the potential energy surface of the first (lowest) ionized state, a relaxation energy E_{rel} can be gained back and the ionized state reach its equilibrium geometry. The second pathway involves the molecule adapting the equilibrium geometry of the ionized states in its ground state via a lattice distortion. In this case, this distortion leads to an upward shift of the HOMO level and a down shift of the LUMO level, as illustrated in Figure 1-2b. Only E_{IP-d} is required to proceed to the ionized states. In organic materials, the latter case is energetically favored and leads to the localization of the charge on the chain through a local distortion of the lattice. This process produces the localized electronic states in the gap due to a local upward shift $\Delta\varepsilon$ of the HOMO and down shift of the HOMO (Figure 1-2c). With the removal of an electron from a polymer chain upon oxidation, we lower the ionization energy by an amount of $\Delta\varepsilon$ (Figure 1-2d). If $\Delta\varepsilon$ is larger than the distortion energy E_{dis} , this charge localization process will be favored compared to the band process. We say a polaron is created. In chemical terminology, the polaron is a radical ion with spin number of half. These electronic states can be called polaronic states with a lattice distortion. When a second electron is removed from the polymer chain, a bipolaron is created. A bipolaron is defined as a columbically bound pair of charges with the same sign. In case of p-type doping, the bipolaron in the gap are empty, the bipolarons are thus spinless. With the increase of doping level, polaron becomes bipolaron on the polymer chain, and eventually bipolaron bands are formed. This evolution is consistent with ESR measurements, where the ESR signals grow, saturate, decrease and eventually vanish. The optical spectra upon doping provide additional information on this evolution. Figure 1-3 shows spectroelectrochemical experiments upon

progressive increase of an electrical bias in an oxidation process, monitoring the formation of polarons and bipolarons on a donor-acceptor conjugated polymer.²⁰ At very high p-doping level, the absorption completely moves towards near-IR region with the depletion of visible absorption. This can be explained by the broadening of the bipolaron states in the forbidden gap upon increasing the voltage (doping level) and eventually the merging of the lower and upper bipolaron bands with the valence and conduction band, respectively. For the polymers with small bandgap in their neutral state (< 2.0 eV), this process can result in a conventional metallic-like conduction mechanism (band theory).

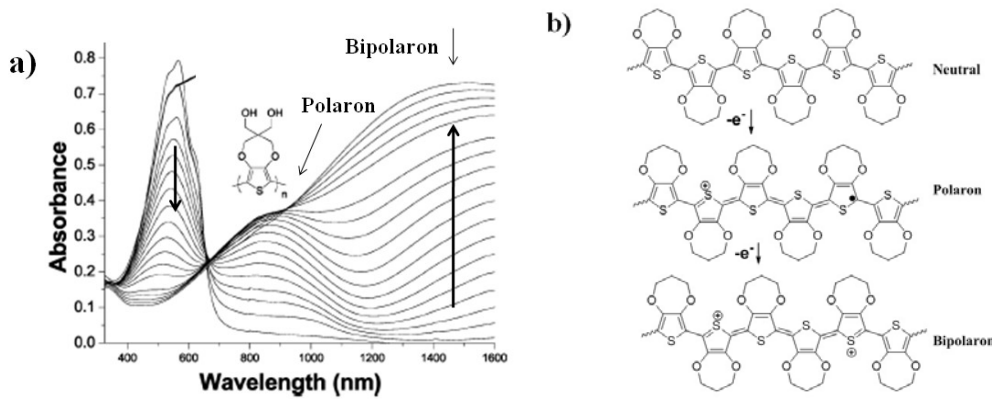


Figure 1-3. a) Spectroelectrochemical experiments monitoring the formation of ionic states, namely polarons (radical-cations) and bipolarons (dication), upon progressive increase of an electrical bias in an oxidation process; b) progressive doping of poly(3,4-propylenedioxothiophene) (For simplicity, OH tails are omitted, adapted from Ref 20. with permission).

A soliton is a charge associated with a boundary and has the properties of a solitary wave which can propagate without deformation and dissipation.¹⁹ Therefore, it requires a degenerate ground state within the polymer. *trans*-Polyacetylene is such a polymer.²¹ Other than this unique polymer, most polymers we encounter (e.g., polythiophene, polypyrrole) have a non-degenerate ground state. The charge-carrying states are polaronic, and differ significantly in energy to the HOMO and LUMO edges of the neutral polymer. More details about soliton can be found elsewhere.²²⁻²³

1.1.1.3 The width of energy bands

In inorganic solids, atoms are covalently bonded in an ordered high density crystal lattice. The strong interactions of massive atoms lead to considerably wide energy bandwidths for both valence and conduction band, much wider than $k_B T$ ($k_B T$ is the product of the Boltzmann constant, k , and the temperature). At RT, $k_B T$ is about 0.025 eV). Organic semiconductors, e.g., molecular crystals and conjugated polymers, are considered as disordered materials. They have weak crystal lattices, held together by van der Waals forces.¹⁴ The interaction among the adjacent cell units is therefore weak, resulting in a narrow intermolecular bandwidth (smaller compared to $k_B T$). In other words, electronic structure of an organic solid preserves that of a molecule or a single polymer chain. This has a pronounced influence on charge transport in organic solids. For instance, the population of thermally excited charge carriers from valence band to conduction band is exceedingly low. The validity of band theory, e.g., band transport, is thus problematic in most conjugated organic molecules and polymers, except for the case of some highly crystalline high-mobility organic films, such as single crystals of rubrene or pentacene.²⁴ Instead, charge-carrier mobilities move around by a hopping mechanism between localized states in organic semiconductors.²⁵ Therefore, they are inherently low, with typical values of $<10^{-2} \text{ cm}^2/\text{Vs}$.²⁶

1.1.1.4 Charge carrier, charge transport, mobility and charge trap

Both electron and hole are effective charge carriers. A hole is the region of space from which a negative charge has been removed. A prime parameter in determining the successful use of organic compounds as the active layers in optoelectronic devices is the mobility of these charge carriers within the materials. This parameter controls, for example, the switching speed of field effect transistors, the intensity of light-emitting diodes, and the separation of charge in photovoltaic cells. Since the organic systems have a closed-shell configuration, the charge

carriers are thus either injected into the organic semiconductors from the electrodes or generated with photo-induced charge separation within the materials at the interface between electron-donor and electron acceptor components. Also to be noted, pristine films of π -conjugated molecules and polymers, other than their doped forms, are used in most devices.

As mentioned in the previous section, band transport is often not valid in organic materials. As a matter of fact, conjugated molecules and polymers are known to transport via a thermally activated hopping-type mechanism, which depends on the interplay between the intrinsic features of the individual molecule and polymer chain and their relative orientations and solid state packing.¹⁸ There are two major mechanisms proposed for charge transport in disordered organic materials. In the systems where the electron-phonon interaction and the polaron effect are significant, e.g., small molecules, Marcus theory provides a good estimation for charge transfer between polaronic states of different molecules.²⁷ For the systems with weak electron-phonon coupling, phonon-assisted hopping mechanism can be accountable for the charge transfer among localized active energy sites (Many models have been developed to describe the hopping mechanisms).^{18,27}

The mobility μ can be expressed as in the presence of an external electric field:

$$\mu = v/E \quad (1-2)$$

where v is the velocity of the charges and E is the amplitude of the applied field. Charge mobilities can be measured experimentally by a variety of techniques.²⁸ Many factors affect charge carrier mobility, such as molecular packing, the presence of impurities, charge-carrier density, electric field, temperature and pressure. Compared to band transport in inorganic materials, the thermally assisted hopping mobility in disordered organic materials is many orders of magnitude lower (typically less than $10^{-2} \text{ cm}^2 \text{V}^{-1} \text{S}^{-1}$ as compared to $10^2 \text{ cm}^2 \text{V}^{-1} \text{S}^{-1}$ of Si single

crystal).²⁹ Figure 1-4 shows the rough charge mobilities in different semiconductors and the necessary mobilities for their relevant applications.

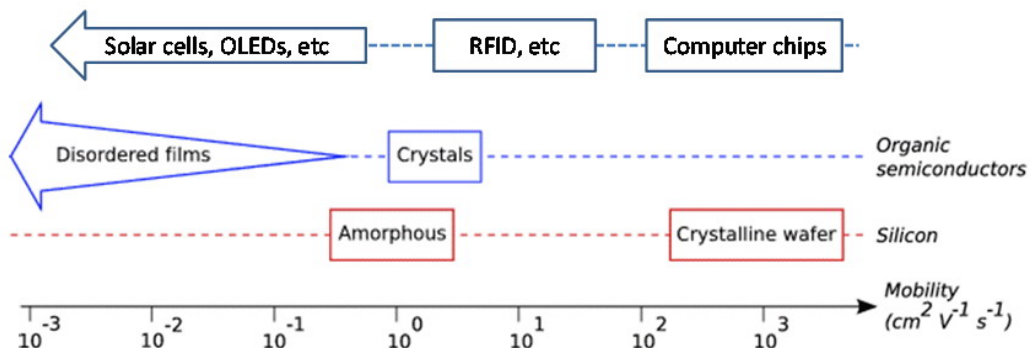


Figure 1-4. Charge mobilities in different semiconductors and the necessary mobilities for their relevant applications

Charge carriers and mobilities are accompanied by charge traps, the localized energy states where a charge carrier will be retained temporally or permanently.¹⁸ In other words, once a carrier is trapped, one of two events will eventually take place: either the carrier acquires sufficient energy, usually by means of a lattice interaction, to climb out of the trap and rejoin the conduction band after a specific retention period, or it recombines by attracting a carrier of opposite sign. More specifically in the former case, if the energies of localized states are separated from the mobility edge by more than a few $k_B T$, the states act as deep traps: once trapped in deep traps, the charge carriers have to be released by thermal excitations or photoexcitations. On the other side, trap states with energies within a few $k_B T$ of the mobility edge are characterized as shallow trap; after being trapped for a characteristic time (τ_{trap}), the charges can be thermally activated and released to the band without applying external forces.

Electron traps are localized states below the conduction band edge and hole traps are the ones above valence bands. In organic materials the width of the bands is usually very small, less than $k_B T$, therefore HOMO and LUMO are typically used to replace the valence and conduction

bands, respectively. The density of states (DOS) in organic thin films can be represented by a Gaussian-like distribution of localized molecular orbitals of individual molecules as shown in Figure 1-5.³⁰⁻³¹ The charge transport is dominated by the hopping processes between localized energy states. There is no distinguishing line between a charge trap energy state and a charge transport state, which are both temperature-dependent. The origin of trap states can result from impurities, structural defects, geminate pairs, as well as self trapping polarons and biporalons. The more detailed discussions on charge traps and their measurements are out of the scope of this dissertation and can be found elsewhere.³²⁻³³

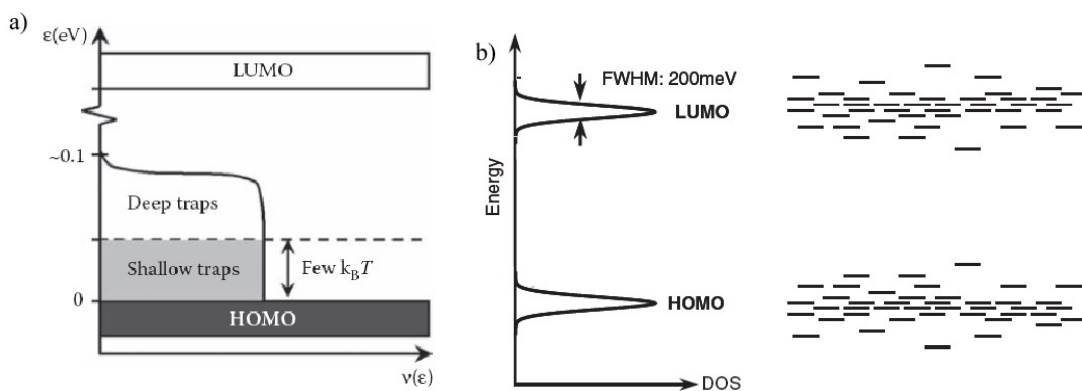


Figure 1-5. a) The schematic diagram of the energy distribution of localized electronic states in the energy gap between the HOMO and LUMO bands (Adapted from Ref. 30 with permission); b) Distribution of HOMO and LUMO levels in disordered organic semiconducting materials (Adapted from Ref 31 with permission)

1.1.2 P-, N-type and Ambipolar Semiconducting Materials

P-type semiconducting materials can stabilize positive charges and transport holes; while n-type materials are the ones that can stabilize negative charges and transport electrons. Ambipolar semiconductors are the combinations that they can transport both charge carriers. Currently, the majorities of conjugated small molecules and polymers are used as p-type materials in organic electronic devices. In photovoltaic devices, these p-type conjugated

materials are also called electron donors. A few representative solution processable p-type materials are listed in Figure 1-6a.³⁴⁻³⁶

Research in the field of solution processable n-type materials (in particular n-type conjugated polymers) lags behind, compared to the existence of hundreds of p-type semiconductors. In the case of OFET devices, one of the most challenging tasks is to overcome the stability obstacle for n-channel materials. Only a handful of n-type materials have been reported with fairly good electron mobility under ambient conditions. Besides, little is currently known about electron transport and field-effect mobility of electrons in polymeric semiconductors. With the successful development of high-mobility p-type materials, n-type conductors have recently drawn increasing attention due to the potentials to couple with p-type materials and make all-polymer complementary circuits. Figure 1-6b shows some of advanced solution processable n-type semiconducting materials.³⁷⁻⁴⁰

Ambipolar semiconducting materials also attract a growing interest as active materials.⁴¹⁻⁴⁸ Ambipolar semiconductors support both hole and electron accumulation. The transistors thereof can operate in pure p-type mode, in pure n-type mode or in a mode where hole and electron accumulations coexist. Ambipolar materials imparted by this dual nature are suitable for the fabrication of complementary integrated circuits based on a single organic semiconductor. This can provide substantial processing advantages over CMOS-type logics (CMOS stands for complementary metal-oxide semiconductor) using on two organic semiconductors, one of p-type and the second of n-type. Figure 1-6c exhibits a couple of examples that have been implemented in ambipolar logics.^{41,49}

1.1.3 Molecular and Polymeric Semiconducting Materials

Molecular semiconducting materials in this dissertation refer to those materials that have a well-defined molecular structure. Polymeric materials simply refer to conjugated polymers.

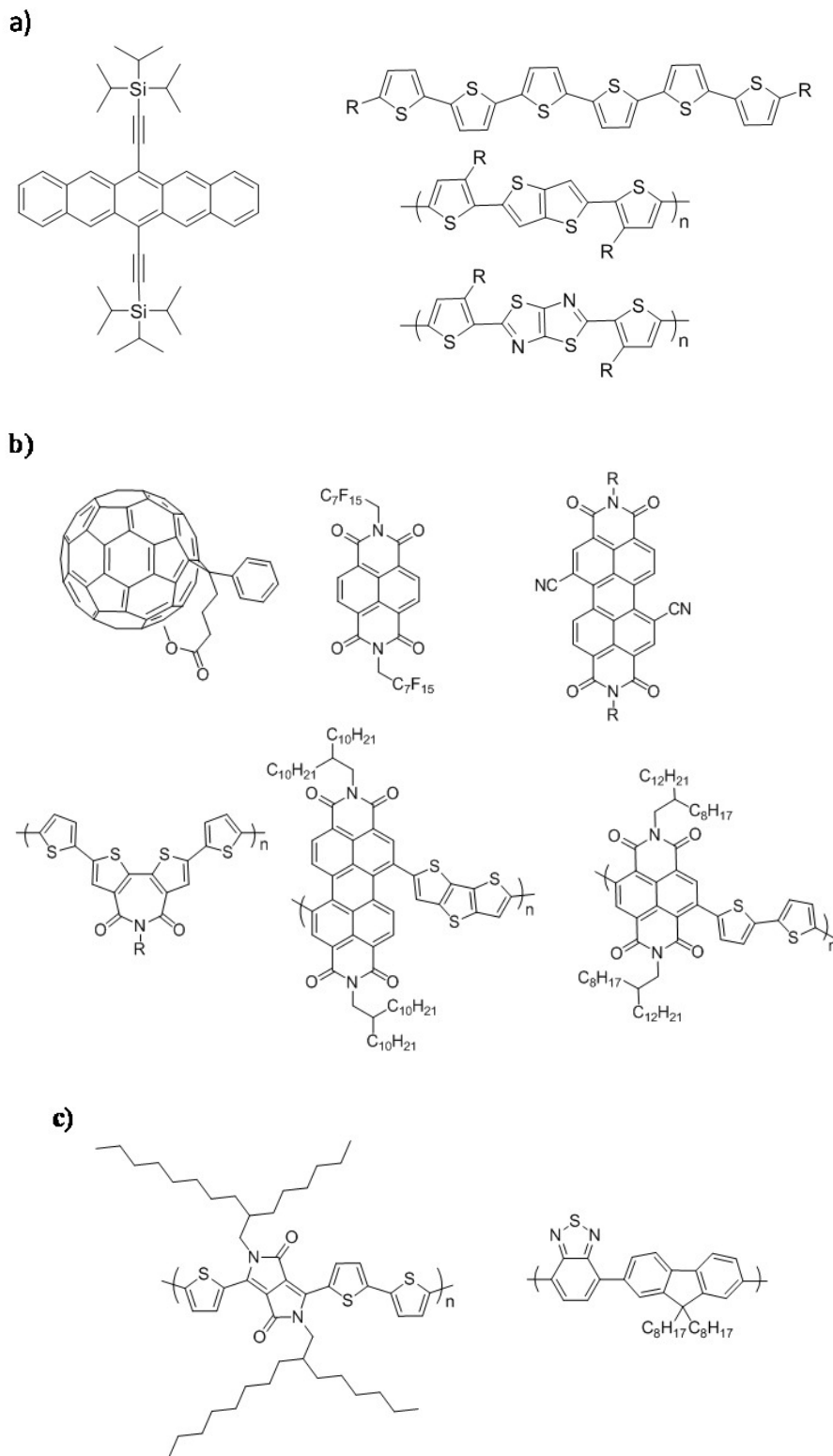


Figure 1-6. a) representative p-type organic semiconducting materials; b) representative n-type organic semiconducting materials; c) representative ambipolar semiconducting materials.

Both molecular and polymeric materials have been extensively studied.^{2,50} They have their own intrinsic advantages and disadvantages regarding their use as active materials in organic electronic devices. As far as molecular semiconductors are concerned, their monodisperse nature with well-defined chemical structures imparts no end-group contaminants and little batch-to-batch variations beyond impurities to these materials. Much existing knowledge and techniques in the field of small molecules can be applied to purify them and obtain electronic grade materials. In addition, the physical and electronic properties of molecular materials can be much more easily controlled, even at molecular level. However, the use of solution processing to obtain high-quality thin-films can be problematic.

Polymeric materials, on the other hand, have an excellent thin-film formation capability and mechanical flexibility. They can also be functionalized and modified with great freedom. The biggest disadvantage for polymeric materials is lack of efficient and effective purification techniques that can produce high purity materials. Trace amounts of metal catalyst residue trapped inside the polymer matrix can be detrimental to the device performance. It is worth mentioning that recycling gel permeation chromatography (GPC) has recently been used to obtain high purity polymers.⁵¹

1.2 Bandgap Engineering

An advantage for working with organic materials is that there are countless numbers of them. Compared with inorganic semiconductors, they are easy to modify or design entirely from the scratch. This implies that their properties, e.g., absorption, emission and charge transport, can be customized for specific applications. The focus in the previous section (1.1) has been to consider the collective properties of organic semiconductors (e.g., charge transport) as solid state materials. In this section, attention will be given to understand and control the fundamental properties of conjugated polymers and molecules, such as bandgap and energy levels.

1.2.1 Bandgap Control

The band structure of conjugated polymers results from the interactions of π -orbitals of the repeat unit through the entire chain, exemplified in Figure 1-7a. The energy difference between valence band and conduction band is defined as the bandgap. The presence of bandgap is mainly caused by bond length alternation, a product of Peierls instability, as shown in Figure 1-7b. As a matter of fact, most conjugated polymers have non-degenerate ground states between aromatic and quinoid forms (An exception is polyacetylene). Although bandgap is mainly dependent on bond length alternation, it is also affected by other factors, including planarity, substitution, aromaticity and interchain interaction, as sketched in Figure 1-7c.⁵²

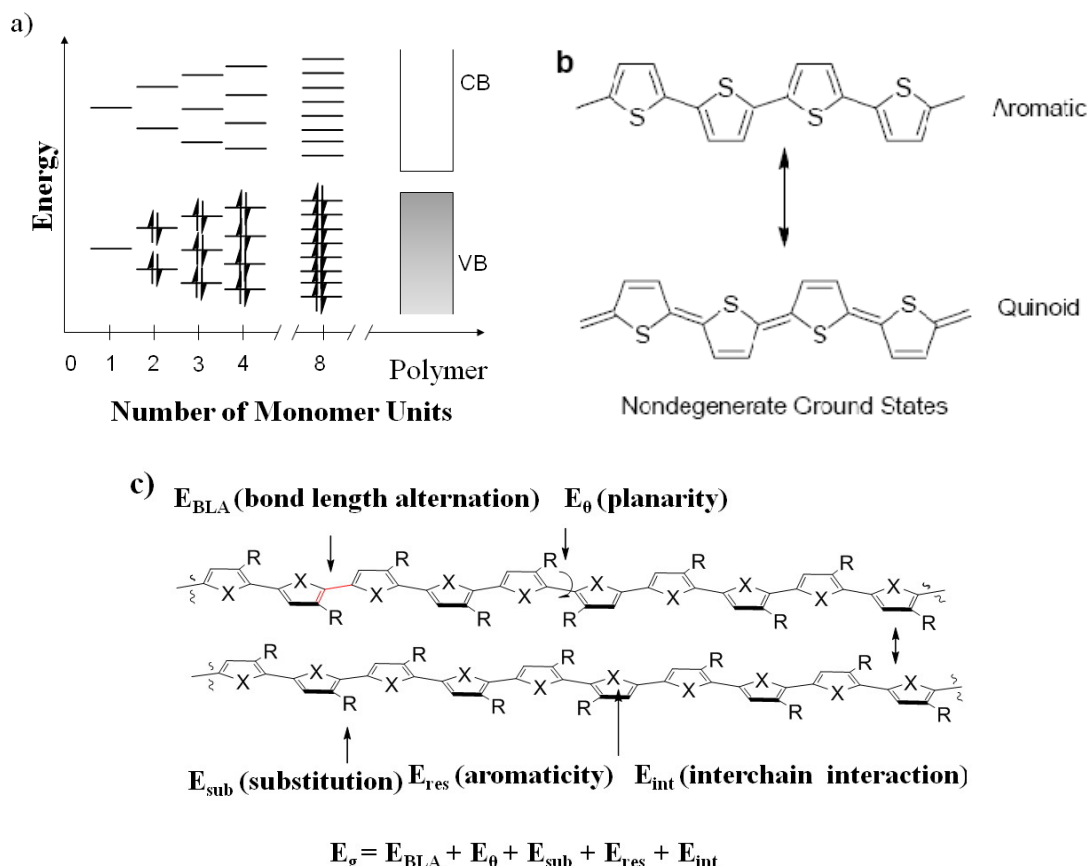


Figure 1-7. a) Simplified diagram of the buildup of energy bands of a conjugate polymer chain; b) Illustration of the nondegenerate ground states of polythiophene as a representation for all aromatic conjugated polymers; c) the origin of bandgap.

Specifically, E_{BLA} is related to the difference in bond length between the single and double bonds. The donor-acceptor approach is probably the most effective tool to reduce the energy gap and will be discussed in the next section. E_θ is correlated to the torsion angle between the two adjacent repeat units, usually caused by steric interactions between the rings. To use a linkage such as a double bond or a triple bond can decrease the torsion and enhance the planarity, resulting in a smaller bandgap. E_{sub} is caused by electron-donating or electron-withdrawing effects of substituents. For instance, an electron-donating substituent, (for example, an alkoxy group), will raise the HOMO level while an electron-withdrawing group, (such as a cyano group), will lower the LUMO level. In practice, peripheral substituents (R in Figure 1-7c) are often introduced to increase the solubility of the (otherwise intractable) polymer. These passive substituents also affect E_{int} through their influence on morphological properties of the polymer. E_{res} is connected to the aromatic resonance energy (Dewar Resonance Energy, DRE). The DRE for benzene, thiophene, pyrole and furan are 22.6, 6.5, 5.3 and 4.3 kcal/mole, respectively.⁵³ The higher this value, the larger the bandgap of the corresponding polymer has. a high DRE value disfavors delocalization. E_{int} is determined by intermolecular interactions and can be affected by many factors, including the aforementioned substituent effects. Strong interchain π - π interactions can reduce torsion angle and thus reduce the bandgap. These five correlated parameters all have influence on energy level and bandgap of conjugated polymers (molecules). To achieve the desired energy levels and bandgaps typically require tuning one or more these parameters.⁵²

1.2.2 The Donor-Acceptor Approach

The donor-acceptor approach, also known as the push-and-pull method, is based on the incorporation of electron-rich unit (donor) and electron-deficient unit (acceptor) in an alternating fashion along the polymer backbone. Through the introduction of push-pull driving forces to favor electron delocalization and the formation of quinoid mesomeric structures ($D-A \leftrightarrow D^+ = A^-$)

over the conjugated main chain, the BLA can be significantly reduced. This effectively leads to a compressed bandgap. Photoinduced intramolecular charge transfer (ICT) correlated with the highlying HOMO of the donor unit and the low-lying LUMO of the acceptor unit can also account for the reduced optical band gap.² Figure 1-8 shows the principle of the donor-acceptor concept.⁵⁴ Here it can be seen that a hybridization of HOMO and LUMO energy levels of the donor and the acceptor results in the formation of the compressed band gap. One experimental characteristic of an ICT absorption band is its sensitivity to solvent polarity. In general, the energy required for excitation decreases as the solvent polarity increases. The donor-acceptor approach has been by far the most successful synthetic tool to control energy levels and bandgaps while avoiding the necessity of controlling interchain effects or generating insoluble, rigidly planar polymer backbones. A soluble and stable conjugated polymer with bandgap as low as 0.5 eV has been prepared within this group, using bisbenzothiadiazole as an acceptor and dithienopyrrole as a donor.⁴⁴

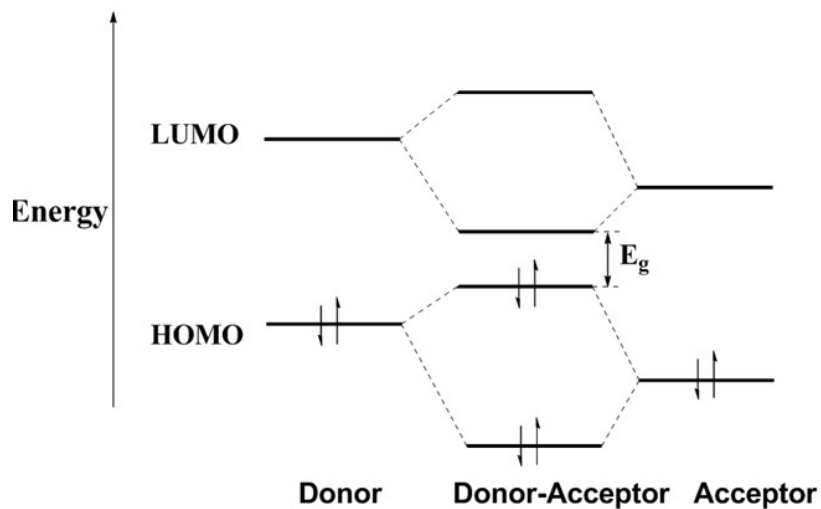


Figure 1-8. Schematic illustration of donor-acceptor interaction. The HOMO of the donor segment interacts with the HOMO of the acceptor segment to yield two new HOMOs for the D-A polymer, so does LUMO levels. After the electrons redistribute themselves from their original non-interacting orbitals to the new hybridized orbitals of the polymer, a higher lying HOMO and a lower lying LUMO are formed. This leads to a narrowing of the optical band gap (Adapted from Ref. 54 with permission).

We noticed there is one exception that is poly(isothianaphthene). Its bandgap is estimated to be ~ 1 eV, and it is nearly 1 eV lower than that of poly(thiophene) (~ 2 eV).⁵⁵ This is simply realized by stabling quinoid structures without adapting donor-acceptor approach.

Figure 1-9a shows a set of representative electron-deficient aromatic cores that have been used as acceptors in the literature.⁵⁶⁻⁵⁸ A series of commonly-used electron-rich moieties are provided in Figure 1-9b.⁵⁹⁻⁶⁰ In addition, more and more new electron-rich and electron-deficient aromatic heterocyclic compounds are currently developed for the purpose of designing materials for optoelectronic applications.⁶¹ The numerous combinations of donors and acceptors have built a rich library of conjugated polymers (molecules) and therefore specified properties may be tailored by judicious choices of donor and acceptor moieties.

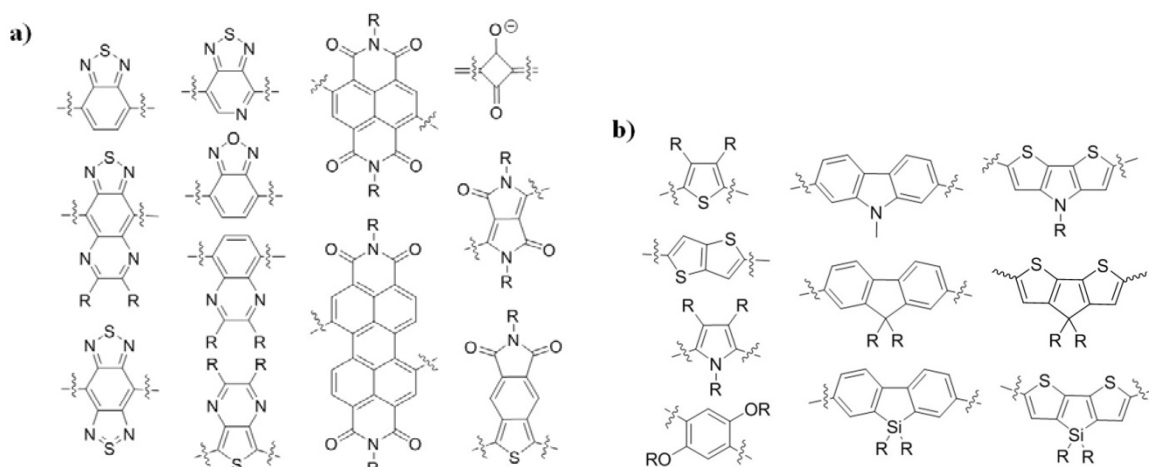


Figure 1-9. a) Representative electron-deficient units; b) Representative electron-rich units.

1.3 Photovoltaic Devices

With increasing energy demand for human activities and the gradual depletion of non-renewable fossil-based fuels, the search for renewable energy becomes increasingly important, if not critical. Renewable energy, from abundant natural sources, e.g., sunlight, geothermal heat, tide and wind, can be used with little or no adverse effects to the environment and no concerns of depletion.

Solar energy is the energy from solar radiation can be regarded as clean and renewable energy. There are two principle types of solar energy: active and passive.⁶² In this dissertation, we focus on active solar energy; relying on the generation of electricity from solar irradiation. The device operated in such transformation is therefore called photovoltaic device (solar cell). Based on the functional (light-absorbing) materials in these devices, photovoltaic devices can be further categorized into inorganic and organic (OPV) technologies. In the following sections, a brief introduction will be given to silicon-based solar cells, including their operating mechanism and some important parameters that define the performance of such a device. An extensive description of OPVs will be subsequently provided, including their operating mechanism and device configuration. The problems and challenges of these devices will be addressed in the discussions. It is worth mentioning that the research-cell efficiencies are different than the module efficiencies. A module is composed of a series of solar cells that are connected and encapsulated. In reality, module efficiency is much lower than the single cell efficiency.

1.3.1 Silicon-Based Solar Cells

The first silicon-based solar cell was invented by Russel Ohl at Bell Laboratory in 1941. There have been many approaches to improve the efficiency of this technology over the years, such as textured front surfaces for enhanced light absorption, extremely thin cells with back-surface reflectors for internal light trapping through total internal reflection, and passivated cell surfaces to reduce losses due to recombination effects.⁶³ The highest measured efficiency for a large-area (i.e., 5 inch²) crystalline silicon solar cell stands at 21.5%. Due to the defects associated with the grain boundaries, the best polycrystalline silicon (p-Si) solar cell efficiencies stand at 19.8%. Amorphous silicon thin-film solar cells have been reported around 13% with multi-junction architecture.

The standard silicon solar cell is also called a p-n junction solar cell, as shown in Figure 1-10a. A p-n junction is formed where the doping status is abruptly switched from p-type to n-type at the interface. At the p-n junction interface, free electrons from the n-type side will move to fill the holes from the p-type side. The net outcome is creating a region that is deficient of majority charge carriers and is known as a depletion region (Figure 1-10b). Additionally there is a built-in electric field resulting from generation of a net positive charge on the n-type side of the depletion region and a net negative charge on the p-type side of the depletion region.

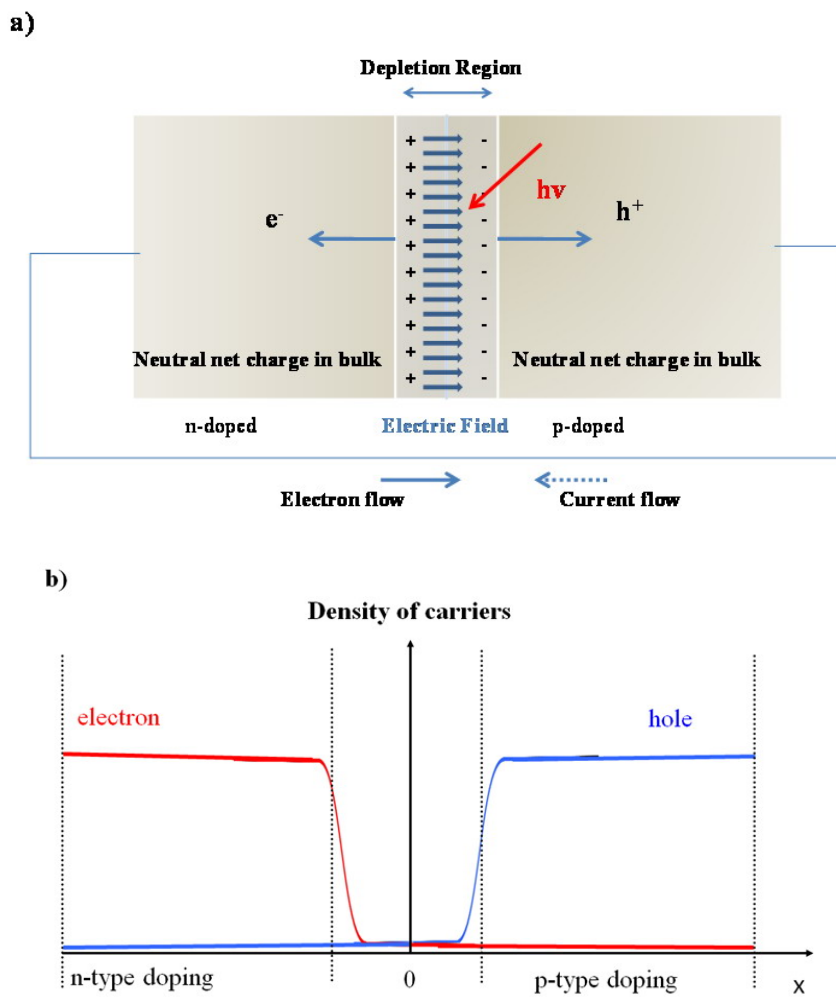


Figure 1-10. a) Representation of a silicon-based p-n heterojunction solar cell under short circuit conditions, illustrating the built-in electric field that exists in the depletion region near the p-n junction and the direction of current flow upon irradiation with light; b) The density of charge carriers in n-type doping, p-type doping and depletion region.

Upon irradiation, an electron is excited from valence band to conduction band when the absorbed energy from incident photons is larger than the bandgap. An electron-hole pair is formed at the interface with relatively weak columbic interactions (< 0.05 eV), which can be fully dissociated into a free electron and hole with the assistance of thermal activation. In the field of a built-in potential across the depletion region, electrons are swept toward the n-type region, and holes are swept toward the p-type region. If the heterojunction is connected to an external circuit, a current will be measured flowing in the reverse bias sense, from p to n, and the resulting current will be the combination of the photocurrent and the equilibrium current (which in solar cell terminology is often called the dark current).

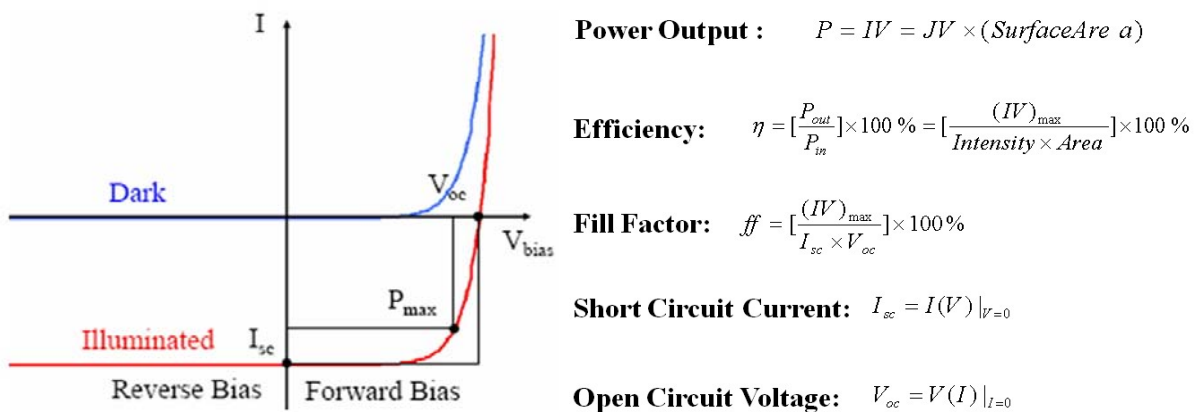


Figure 1-11. Current-voltage characteristic of a silicon solar cell for dark and light conditions with illustration of the fill factor (FF), showing the open circuit voltage (V_{oc}), the short circuit current (I_{sc}), and the voltage and current at the maximum power point.

The important characteristics of defining a solar cell are listed in Figure 1-11. The value of the current is called the short-circuit current when the bias voltage is zero. It is the current that results from the direct connection of the p-side and n-side with a wire (short-circuited), while the device is under illumination. The open circuit voltage is the value of the voltage where the device is illuminated, but not

connected. The point of maximum power is indicated where the product of I and V on the curve is maximum. The fill factor is defined as the maximum power divided by the product of the open circuit voltage and the short circuit current. The efficiency of the device is determined by the ratio of the maximum output power of the device to the input power from the incident photons.

External quantum efficiency (EQE), defined as the ratio of charges extracted from a device to the number of incident photons (Eq. 3), is the key benchmark of solar cell performance. The significance of this characteristic is that it is a single-wavelength measurement that indicates the number of photogenerated charge carriers (electrons) produced by a photon of a given energy. When the EQE is examined as a function of wavelength, a photocurrent action spectrum is obtained that determines the relative contribution of various spectral regions (and thus the materials absorbing in those regions) to the overall photocurrent generated in the device.

$$EQE(\%) = \left[\frac{\#Photons}{\#Electrons} \right] \times 100 = \left[\frac{0.124 \times I_{sc} (\mu A/cm^2)}{\lambda(nm) \times P_{in} (W/cm^2)} \right] \quad (1-3)$$

Internal quantum efficiency, *i.e.* the ratio of charges extracted from a device and the number of photons absorbed by the active layer, provides a useful way to isolate electronic loss mechanism from light coupling and parasitic absorption losses in a solar cell.

In order to evaluate the solar cell performance under the same standard, it is necessary to define the radiation sources. Figure 1-12a illustrates three conditions where the solar radiation interacts with different air mass (AM0, AM1 and AM1.5G). The letters AM stand for air mass and indicate the amount of atmosphere through which the radiation passes. AM0 indicates the radiation passes through zero air mass and is therefore used for outer space. AM1.5 represents light that travels through approximately one and a half earth atmospheres, where the States and Europe are approximately located when the sun light hits the surface. Figure 1-12b shows the relationship of AM0 and AM1.5G radiation. Here it can be seen that the atmosphere reduces the

intensity of solar radiation in general, especially in the UV region. Additionally, atmospheric components such as water, carbon dioxide, oxygen, ozone, and methane, introduce several characteristic absorption bands into the spectrum. If the total amount of energy is summed over the frequency range the intensity of light outside the earth's atmosphere is about 1.35 KW/m^2 . A similar sum for AM1.5 radiation results in about 890 W/m^2 . For a standard reporting, an intensity of 1 KW/m^2 is usually selected for a solar simulator.

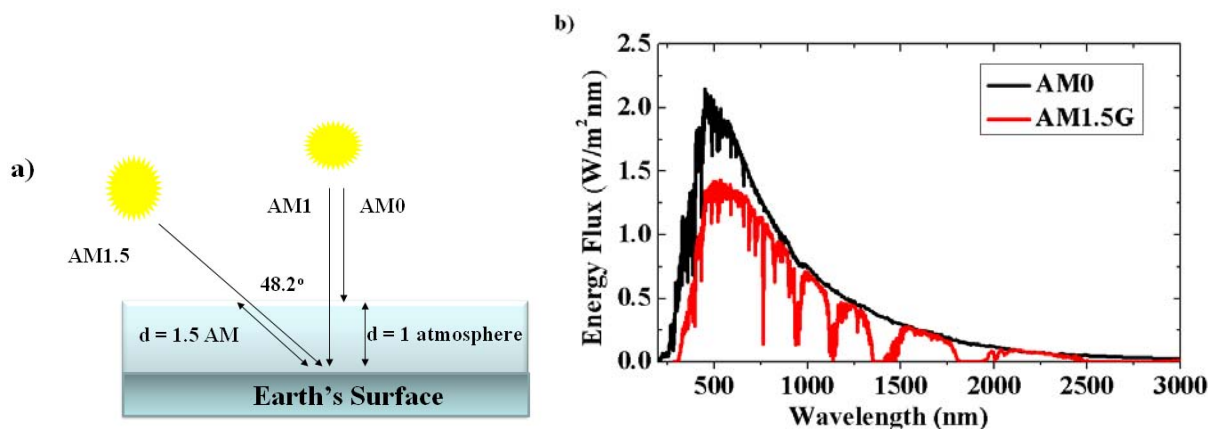


Figure 1-12. a) Schematic representation of the irradiation geometry; b) Comparison of the solar spectrum under AM0 and AM1.5 conditions.

Other than silicon semiconductors, group III-V semiconductors, such as CdTe, GaAs and CuInSe₂, have also drawn considerable attention for developing the third generation of inorganic photovoltaics, aimed at reducing thermal and optical losses in the devices. Significant improvements have been made and more information can be found elsewhere.⁶⁴⁻⁶⁶

1.3.2 Organic Solar Cells

Organic semiconducting materials have gained momentum for implementation in photovoltaic devices over the past few years in the context of increase demand for renewable energy. Since the inception of a molecular bilayer thin-film organic solar cell by Tang (with PCE over 1%),⁶⁷ several concepts have evolved using different device configurations, including small molecule-small molecule bilayer,⁶⁸ conjugated polymer-conjugated polymer bilayer,⁶⁹

small molecule-conjugated polymer bilayer,⁷⁰ small molecule-small molecule bulk heterojunction,⁷¹⁻⁸³ small molecule-polymer bulk heterojunction,⁸⁴ all-polymer bulk heterojunction,^{40,85-107} as well as combinations of organic-inorganic hybrid systems.¹⁰⁸⁻¹²¹ No matter what device configurations are, all OPVs share something in common that is the excitonic character of their optical properties. Optical excitation in organic materials results in the formation of a spatially confined electron-hole pair (Frenkel type exciton), as mentioned free charge carriers are generated in the case of conventional inorganic semiconductors. The exciton binding energy is usually large, on the scale of 0.5 eV and above (note: less than 0.025 eV for silicon-based semiconductors).¹⁴ This value is much larger than the thermal activation energy and therefore the formation of heterojunction between electron-donor material and electron-acceptor material is necessary to dissociate the exciton into free electron and hole carriers.

Below, a full description of electronic and optical processes that take place during the operation of an organic solar cell will be presented in the order of photoinduced charge separation (optical absorption and exciton formation, exciton migration, exciton dissociation at the donor-acceptor interface), charge carrier transport and charge collection electrodes.

Conjugated materials typically have large absorption extinction coefficients in the range of $10^5 \text{ L mol}^{-1} \text{ cm}^{-1}$, resulting from the large wave function overlap between the electronic ground state and the lowest excited state. The high absorptivities enable efficient light harvesting even in thin films with thickness of 100-200 nm for organic materials. As mentioned earlier, π -conjugated material presents strong electron-vibration coupling. Once promoted to an electronic excited state, the excited system relaxes down to the bottom of the potential energy surface of the lowest excited state and the whole excited state reaches equilibrium geometry. A new exciton is

generated in this event. This process is associated with certain energy loss, especially in low bandgap conjugated polymer systems.

The neutral exciton will then diffuse randomly within the materials. Typically, the exciton diffusion length, defined by diffusion coefficient and exciton life time ($L = (Dt)^{1/2}$), is in the order of 10-20 nm (highly crystalline pentacene:C₆₀ device has shown an exciton diffusion length as high as 71 nm).¹²² In order to generate free charge carriers, the exciton has to reach the donor and acceptor heterojunction before it decays back to the ground state. It thus requires the length (thickness) of individual phase (either donor or acceptor phase) should be comparable to exciton diffusion length. This is the major drawback for bilayer organic devices.

Upon reaching the donor-acceptor interface, exciton is now able to dissociate into an electron and a hole. It is rather complicated event. At the present, no clear picture has emerged to describe the exciton dissociation at the molecular level. A two-step mechanism has been proposed to interpret this event. Initially, an excitonic state at the interface evolves into a charge-transfer state (D⁺/A⁻), which then either recombines to the ground state or dissociates into free charge carriers via a charge-separated state.

A closer look at the role of the charge transfer state at donor-acceptor interface and its relationship with open circuit voltage (V_{oc}) has been given by Janssen (Figure 1-13).¹²³ In their analysis, the energy difference between electrochemical bandgap and optical bandgap is introduced to estimate so called “effective optical HOMO (E_{HOMO}^{Opt}) and LUMO (E_{LUMO}^{Opt}) energies of the individual donor and acceptor materials in thin films. They are derived from E_{ox} and E_{red} and using the value of -5.23 eV for Fc/Fc⁺ versus vacuum level¹²³:

$$E_{HOMO}^{Opt} = -5.23eV - eE_{ox} + 1/2(E_{cv}^{sol} - E_g) \quad (1-4)$$

$$E_{LUMO}^{Opt} = -5.23eV - eE_{red} - 1/2(E_{cv}^{sol} - E_g) \quad (1-5)$$

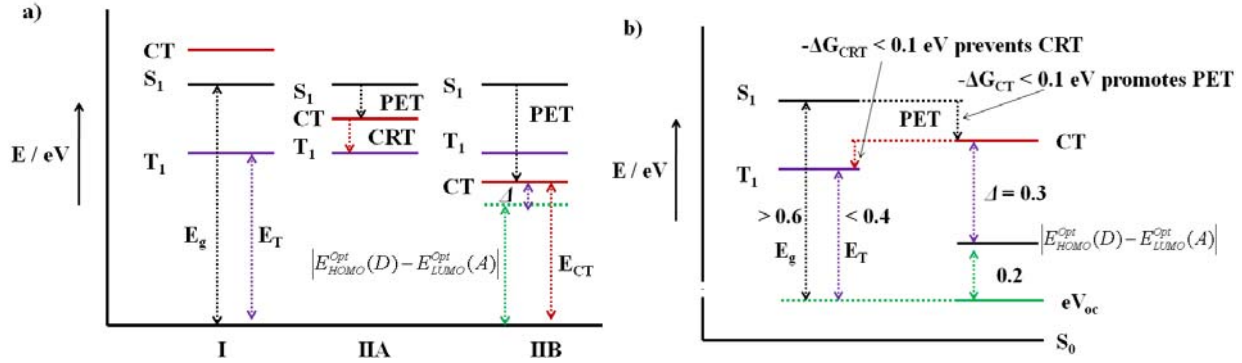


Figure 1-13. a) Energy diagram showing three possible arrangements of the lowest singlet (S_1), triplet (T_1), and charge transfer (CT) excited states relative to the singlet ground state (S_0) for D–A blends: Type I represents D–A blends in which photoinduced electron transfer (PET) is absent because the CT state is situated at an energy higher than the lowest S_1 state. Types IIa and IIb show situations in which PET does occur: with (Type IIa) and without (Type IIb) charge recombination to the lowest T_1 state (CRT). Note that E_g and E_T represent the lowest energies of $E_g(D)$ or $E_g(A)$, and $E_T(D)$ or $E_T(A)$, respectively; b) Jablonski diagram with energies of E_g , E_T , E_{CT} , $|E_{\text{HOMO}}^{\text{opt}}(D) - E_{\text{LUMO}}^{\text{opt}}(A)|$ and eV_{oc} relative to the ground state (rounded to a tenth of an eV). The double headed arrow between V_{oc} and E_g indicates the minimum energy difference for which efficient PET is expected and that between V_{oc} and E_T the minimum energy difference that prevents CRT. (Adapted from Ref. 123 with permission)

The energy level of the intermolecular charge transfer (CT) state at the donor-acceptor interface can be accordingly described as:

$$E_{\text{CT}} = |E_{\text{HOMO}}^{\text{opt}}(D) - E_{\text{LUMO}}^{\text{opt}}(A)| + \Delta \quad (1-6)$$

Where Δ is a term that describes a Coulomb force responsible for higher energy in CT state than in charge separated (CS) state. By the same argument, the driving force for photoinduced electron transfer (PET), ΔG_{CT} , and the driving force for charge recombination to triplet state (CRT), ΔG_{CRT} , can also correlate to this coulomb term, as follows:

$$\Delta G_{\text{CT}} = |E_{\text{HOMO}}^{\text{opt}}(D) - E_{\text{LUMO}}^{\text{opt}}(A)| - E_g + \Delta \quad (1-7)$$

$$\Delta G_{\text{CRT}} = E_T - |E_{\text{HOMO}}^{\text{opt}}(D) - E_{\text{LUMO}}^{\text{opt}}(A)| - \Delta \quad (1-8)$$

Three statements from the semi-experimental analysis are 1) a minimal energy loss of 0.6 eV ($E_g - eV_{\text{oc}}$) in organic heterojunction solar cells, 2) a minimal driving force of 0.1 eV for PET

process and 3) the considerations of charge recombination into triplet states when there is a large gap between singlet state and triplet state.

Once the charges (electron and hole) are separated from each other, they will move to their respective electrodes via hopping in a typically disordered system. As a result, the charge-mobilities, as described earlier, strongly rely on the local morphology and can vary over several orders of magnitude from “ordered” crystalline organic materials (10^{-3} - $1 \text{ cm}^2 \text{ V}^{-1} \text{ s}^{-1}$) to highly disordered amorphous conjugated polymers ($\sim 10^{-6}$ - $10^{-3} \text{ cm}^2 \text{ V}^{-1} \text{ s}^{-1}$).

Upon reaching the electrode/organic layer interfaces, charges are efficiently collected in most cases. It is noted that the efficiency of the charge collection process can not simply be determined from the work function of the isolated electrode and the ionized potential of donor materials or electron affinity of acceptor materials. With the close proximity between organic layers and electrodes, implications, e.g. interfacial charge-density redistribution, geometry modifications and even chemical reactions, will have strong influence the alignment of the organic frontier orbitals and the electrode Fermi level.

Figure 1-14 sketches the electronic processes above mentioned in OPVs. The solid line represents a favorable process; while the dotted line indicates a recombination event. Step 1 involves light absorption to generate an exciton. A geminate recombination event is accompanied as indicated by step 2. If the exciton can safely drift to the D-A interface, a process called exciton dissociation will occur and free charge carriers are generated in step 3. The generated hole and electron will face two choices. The charge carriers can either hop along their own domain to the electrodes as shown in step 4, or dilapidate via charge recombination as indicated in step 7. While the free charge carriers move to the electrode, there is still a possibility that a charge recombination event can occur as demonstrated in step 8. If the charge

carriers survive, a hole will even reach the anode and an electron will hit the cathode. These are called effective charge carriers. As many people point out, the optimization of OPVs is a fine balancing act among the various competing event. For instance, the presence of an interfacial dipole at the D-A interface will likely improve the open circuit voltage (V_{oc}), but also reduce the driving force for exciton dissociation. For photovoltaic material point of view, alternating donor and acceptor low bandgap conjugated polymers have been used extensively to harvest long-wavelength sunlight. The low-lying LUMO in these conjugated materials will decrease the likelihood of charge separation and the high-lying HOMO will reduce the open circuit voltage. There are many more trade-off events in the whole process. Clearly, it is important to bear in minds that careful balances and collective understanding of all electronic processes is a prerequisite step to design materials for high performance OPVs.

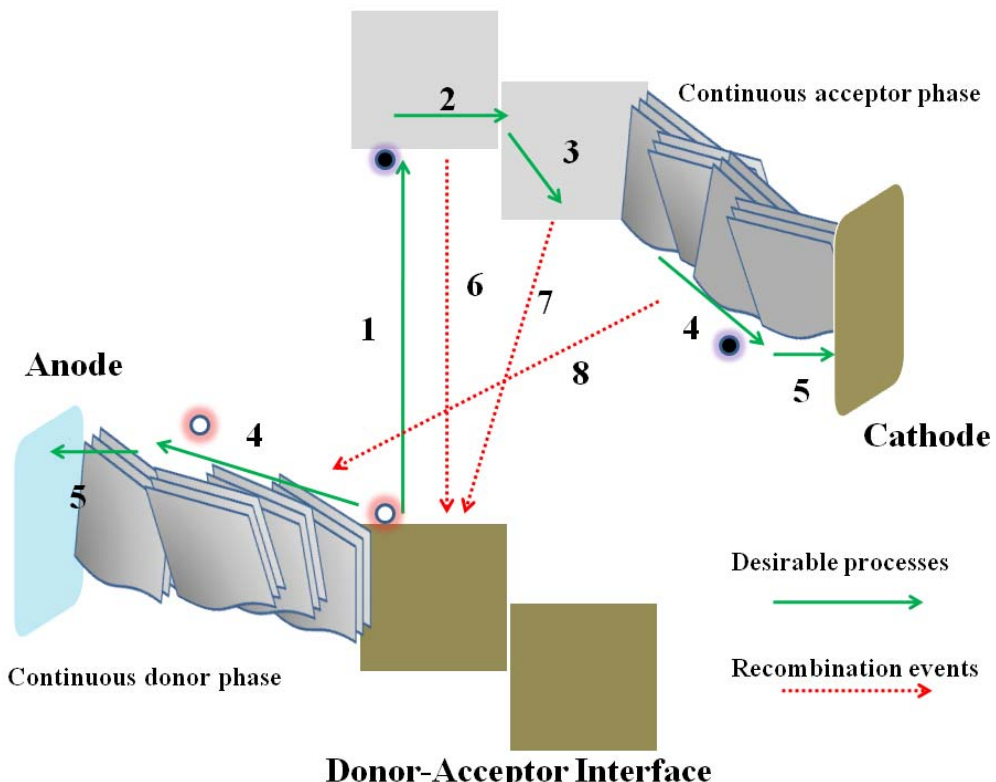


Figure 1-14. A schematic sketch of electronic processes in an organic photovoltaic device.

1.3.3 Bilayer Organic Solar Cells

A bilayer heterojunction solar cell with a layer of vacuum-deposited copper phthalocyanine (CuPc) as a donor and a layer of vacuum-deposited perylene tetracarboxylic derivative (PV) as an acceptor reported by Tang in 1986 embarked a new era in the development of organic-based photovoltaic devices (Figure 1-15a), even though quite a few studies had previously been performed using single layer configuration. In this seminal work, an open circuit voltage (V_{oc}) of 0.45 V, a short circuit current (I_{sc}) of 2.3 mA/cm², a high fill factor of 0.65 and a PCE of 0.95% were obtained on a typical device illuminated under AM2 (it means the efficiency should be higher under standard AM1.5).⁶⁷ Many efforts have been made to improve the performance of vacuum-deposited bilayer solar cells. Currently, the state-of-the-art such organic solar cells have reached PCEs over 4%, claimed by Xue and Forrest, et al.⁶⁸

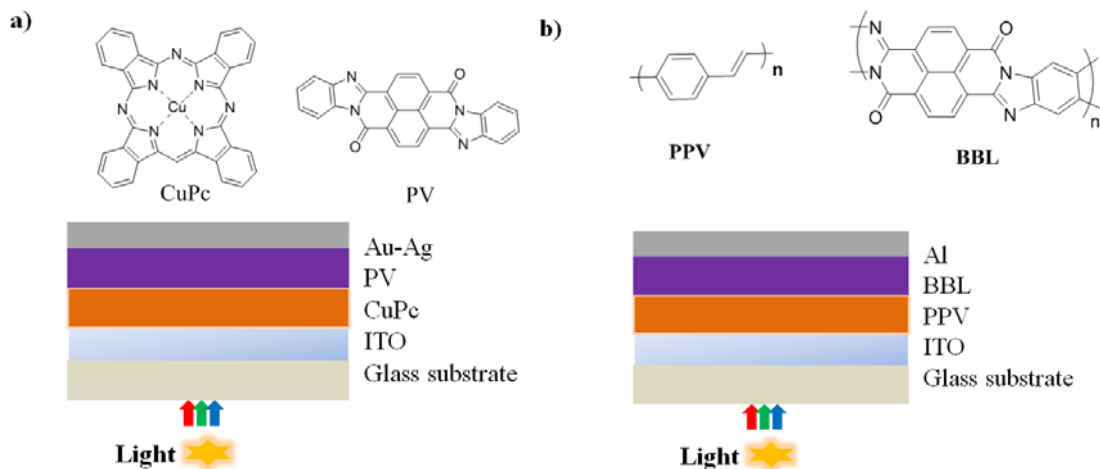


Figure 1-15. a) The original Tan cell; b) a solution processed polymer-polymer bilayer device.

Conjugated polymer-based bilayer devices have also drawn certain interests. These devices have been made by either laminating donor (p-type) layer and acceptor (n-type) layer or placing a p-type polymer layer and then adding n-type materials such as fullerenes, semiconductor nanocrystals, or conjugated polymers via incompatible processing conditions. For instance, Jenekhe et al. reported the solution processed polymer-polymer bilayer solar cells using the p-

type poly(p-phenylene vinylene) (PPV) and the n-type conjugated ladder polymer poly(benzimidazobenzophenanthroline ladder) (BBL) (Figure 1-15b).⁶⁹ In their devices, PPV thin films were spin coated from the sulfonium precursor solution in methanol, followed by heating in vacuum at 250 °C for 1 h. On top of the resulting PPV thin film a layer of BBL was spin coated from its solution in GaCl₃/nitromethane and decomplexed by immersing in deionized water for 8 h to remove the gallium chloride. In Jenekhe's report, they found that the device performance is highly dependent on layer thickness. A 40% drop from 49% to 10% in IPCE at maximum point was observed when BBT layer thickness increased to 75 nm from 50 nm. This highlights the tradeoff between optical length and exciton diffusion length, that is the created exciton in the donor (acceptor) phase may not reach D-A interface due to the presence of thick donor (acceptor) phase (a large optical layer). This leads to the loss of absorbed photons and external quantum efficiency. The fundamental conflict has pushed researchers to explore other potential device configurations. Up to this point, less efforts have been put forth to develop high performance bilayer devices, even though this configuration is still frequently used to diagnose and identify whether charge transfer can occur between new donor and acceptor material.

1.3.4 Bulk Heterojunction Organic Solar Cells

Three types of bulk heterojunction organic (BHJ) solar cells will be addressed in this section, as shown in Figure 16, namely polymer/PCBM, polymer/polymer and molecular BHJ solar cells.



Figure 1-16. Bulk heterojunction solar cells with different compositions: a) polymer/ PCBM; b) polymer/polymer; and c) small molecule/PCBM.

1.3.4.1 Polymer/PCBM bulk heterojunction solar cells

Sariciftci, et al. reported efficient photoinduced electron transfer (PET) in a conjugated polymer-fullerene (Buckminsterfullerene, C₆₀) composite in 1992.¹²⁴ In this report, a time scale of 45 fs PET was observed from a conjugated polymer to fullerene, several orders of magnitude faster than any photoexcitation radiative decay or back electron transfer in the process. Consequently, the quantum efficiency of charge separation in such a composite can approach unity. The tendency for fullerene to crystallize in organic solvents and on surfaces, however, leads to unfavorable phase separation in the composite. This implies charge carriers do not have the necessary channels to reach the electrodes. Hence, efficient solar cells are still not achievable in this context.

The conceptually new photovoltaic device, namely bulk heterojunction (BHJ) solar cell, was demonstrated by Wudl, Heeger and coworkers in 1995, simply using the blend of poly(2-methoxy-5-(2'-ethyl-hexyloxy)-1,4-phenylene vinylene) (MEH-PPV) and a fullerene derivative ([6,6]-phenyl-C₆₁-butyric acid methyl ester, PC₆₁BM) (Figure 1-16a).¹²⁵ The replacement of fullerene with more soluble and less symmetrical PCBM decreases the formation of large fullerene clusters, and instead increases the possibility to form a D-A interpenetrating network in the composite. Thus this network with a large conjugated polymer-fullerene interfacial area and the appropriate phase domain size, at least in one-dimension comparable to the exciton diffusion length, enables the required compromise between optical length and exciton diffusion length, as mentioned in the discussion of bilayer heterojunction solar cells. In other words, the absorbing sites in the blend are most likely within exciton drifting length to the D-A interface. Meantime, efficient hole and electron transport can also be realized with the likelihood of the formation of bicontinuous donor and acceptor network in such a blend. It is also noted that the fast PET can effectively improve the photostability of the conjugated polymers, due to the fast quenching of

the highly reactive excited states and thus the reduction of any possible photooxidation associated with oxygen and water, etc. In addition, the use of a single active layer greatly simplify the solution processing, a great advantage over solution-processed bilayer devices.

Since then, many efforts have been put forth to design new soluble π -conjugated polymers as donor material for BHJ solar cells, where fullerene derivatives are primarily used as electron acceptor, e.g. PC₆₁BM and PC₇₁BM. Figure 1-17 shows a list of conjugated polymers from which PCE over 3% have been achieved in blend with either PC₆₁BM or PC₇₁BM.

Regioregular Poly(3-hexylthiophene) (RR-P3HT) is perhaps the most investigated conjugated polymer in the field of BHJ solar cells. RR-P3HT has HOMO and LUMO levels at -5.2 and -3.2 eV, respectively, with an optical bandgap of \sim 2.0 eV. Using RR-P3HT as donor and PC₆₁BM as acceptor with the device structure of Glass/ITO/P3HT:PC₆₁BM/TiO_x/Alumina, BHJ solar cells have been able to exhibit EQE of 75% and PCE up to 5%.¹²⁶ Unfortunately, the success of RR-P3HT has not been repeated in other homo-conjugated polymers. The high efficiency of RR-P3HT/PC₆₁BM devices may result from a unique microcrystalline lamellar stacking in the blends. Sariciftci et al. has studied a series of regioregular poly(3-alkylthiophenes), with butyl, hexyl, octyl, decyl and dedecyl as solubilizing groups. They observed that chain lengths longer than eight carbons facilitate diffusion rates of PC₆₁BM in the blend during the thermal annealing.¹²⁷ This leads to unfavored phase separation and thereby lowers the device performance. From this study, it is reasonable to conclude that the passive solubilizing chains also affect the optical and electronic properties of a conjugated material and hence its performance in a device.

In the course of studying RR-P3HT/PC₆₁BM BHJ solar cells, people have learned many useful processing techniques to improve device performance. It has been demonstrated that

device performance based on RR-P3HT/PCBM can be dramatically enhanced by careful selection of processing solvent,¹²⁸ solvent vapor annealing,¹²⁹ thermal annealing,¹³⁰ and the addition of high-boiling point additives.¹³¹ (Note: the additive effect was first reported in the blend of PCPDTBT.¹³²) These strategies are now widely applied in other conjugated polymer-based BHJ solar cells.

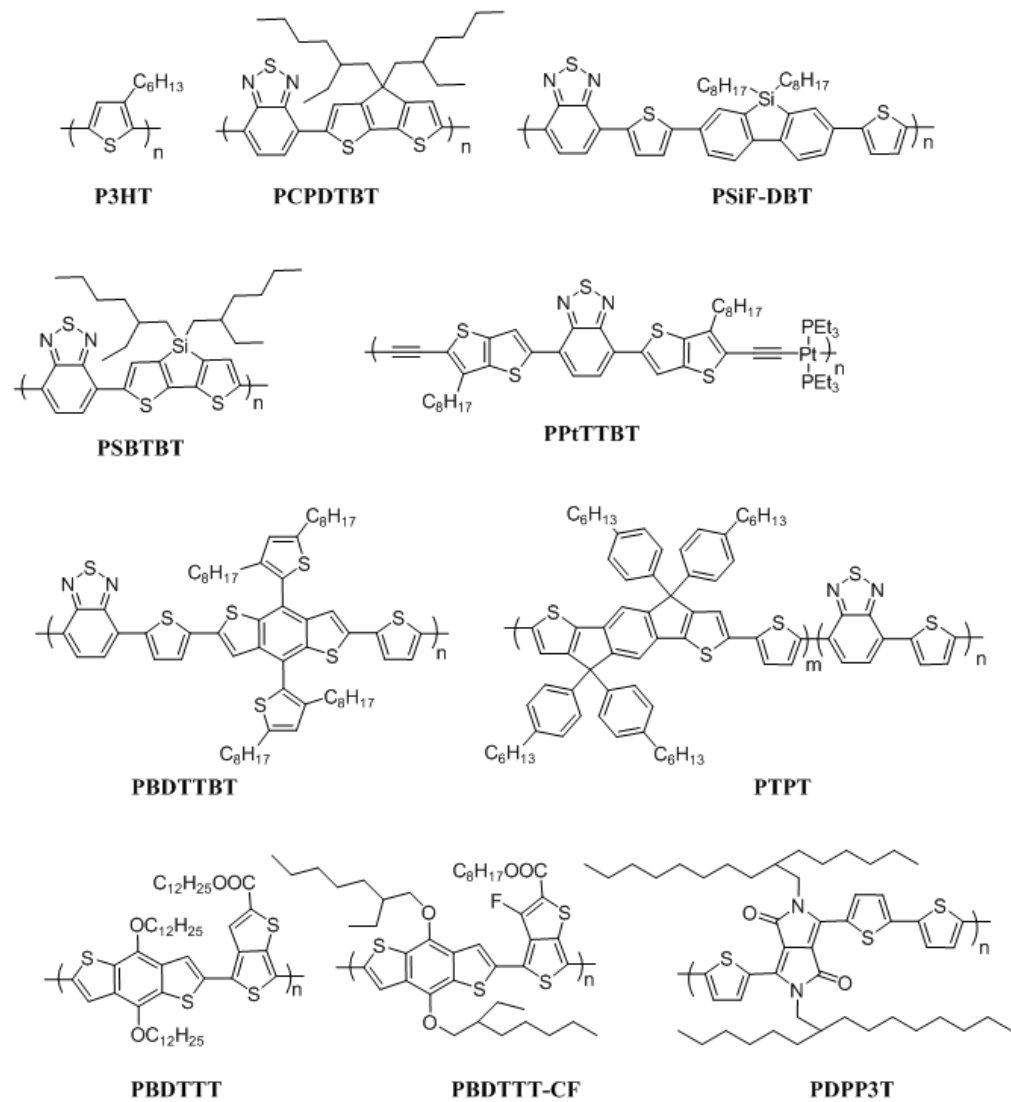


Figure 1-17 Representative p-type conjugated polymers with power conversion efficiency over 4% in blend of fullerene derivatives

It is arguable that the further improvement of PCEs in RR-P3HT/PCBM cells is hindered by its relatively large band gap (~ 1.9-2.0 eV). That is to say a RR-P3HT/PCBM blend only

absorbs lights with wavelength shorter than 650 nm, at best about 22.4% of total amount of photons under AM 1.5G. It is therefore important to design polymers that can harvest more photons from the available sunlight. It also needs to consider that narrowing bandgap will consequently cause a decrease in open circuit voltage and thus a decrease in PCE. Through a careful estimation, an optical bandgap of 1.4 eV will be ideal for polymer/PCBM BHJ solar cells provided the appropriate energy offset is present.¹³³⁻¹³⁴ We are proud to point out the Reynolds group was among the first one to provide an analysis on this issue.¹³⁴ In practice, an optimal bandgap of 1.3 to 1.8 eV has been reported for conjugated polymers as the active absorbing materials blended with PCBM in high performance BHJ solar cells. A few examples are listed below to illuminate the common features that these polymers share.

PCPDTBT is donor and acceptor alternating conjugated polymer. It possesses an optical bandgap (E_g^{opt}) of 1.4 eV (absorption onset 890 nm), and an electrochemical band gap (E_g^{echem}) of 1.7 eV with a HOMO level of -5.3 eV and a LUMO level of -3.6 eV.¹³⁵ This polymer is the first low bandgap polymer with highly efficient photovoltaic response in near-IR region and has a PCE of 3.2% blended with PC₇₁BM (a PEC of 2.7% blended with PC₆₁BM). The V_{oc} is typically at 0.65 V; the highest observed values approach 0.7 eV. With the addition of small amount alkanedithiols in the solvent, PCPDTBT/PC₇₁BM devices have shown PCEs up to 5.5%, with V_{oc} of ~0.62, J_{sc} of ~16.2 mA cm⁻², and FF of ~0.55.¹³² The role of dithiols is to alter the bulk heterojunction morphology.¹³⁶⁻¹³⁷

PSiF-DBT is a 2,7-silafluorene (SiF) and 4,7-di(2'-thienyl)-2,1,3-benzothiadiazole (DBT) alternating polymer with an optical bandgap of 1.8 eV. The HOMO level from electrochemical measurements was -5.4 eV. In blend with PC₆₀BM, the optimized PSiF-DBT BHJ solar cells exhibited a PCE up to 5.4 %, a large V_{oc} of 0.9 V, a J_{sc} of 9.5 mA cm⁻², and a FF of 0.51.¹³⁸

Noticeably, no thermal or solvent annealing was performed on these devices. In addition, this combination is also the first low bandgap polymer with a PCE over 5%.

PSPTPB is a combination of PCPDTBT and PSiF-DBT from the material design point of view. From the study of Psi-DBT, it has shown Si atom has a pronounced effect on the device performance. Yang et al. therefore replaced the bridge carbon atom in cyclopentadithiophene (CPDT) with silicon atom and obtained poly[(4,4'-bis(2-ethylhexyl)dithieno[3,2-b:2',3'-d]silole)-2,6-diyl-alt-(2,1,3-benzothiadiazole)-4,7-diyl] (PSPTPB). ⁵⁹ The HOMO and LUMO levels are -5.1 and -3.3 eV measured by cyclic voltammetry (Note: these values are calculated using -4.8 eV as ferrocene/ferrocenium standard versus vacuum level. It can be converted to -5.4 and -3.6 eV for a comparison reason, since -5.1 eV as ferrocene/ferrocenium standard versus vacuum level is used in this dissertation). The optical band gap (E_g^{opt}) of 1.45 eV is very similar to that of PCPDTBT. The photovoltaic device with a structure of ITO/PEDOT-PSS/PSBTBT: PCBM /Ca /Al showed a maximum PEC up to 5.1%, with a V_{oc} of 0.68V, a J_{sc} of 12.7 mA cm⁻², and a FF of 0.55.

PPtTTBT is a metallated polymer with an E_g^{opt} of 1.8 eV. HOMO and LUMO levels are -5.1 and -3.3 eV, respectively.¹³⁹ The best solar cell performance is based on the PPtTTBT and PC₇₁BM blend and yields an open circuit voltage (V_{oc}) of 0.79, a short circuit current (J_{sc}) of 10.1 mA cm⁻², a FF of 0.51, and a PCE of 4.13% under simulated AM 1.5 G illumination. In an early report, Wong et al. using a similar polymer as a donor and PC₆₁BM as an acceptor demonstrated PCEs up to ~5%, with EQEs as high as 87% at 570 nm.¹⁴⁰ Serious doubts, however, have been raised, suggesting that the reported efficiencies are significantly overestimated (In chapter 3, more details will be given).¹⁴¹ Nevertheless, the concept of designing materials that demonstrate triplet excitons is still interesting, as demonstrated in PPtTTBT.

PBDTTBT is different from most of linear donor-acceptor type conjugated polymers in that it possesses a cross-conjugation segment in its donor. This polymer has three absorption bands, a distinction from a two-band donor-acceptor system, and therefore absorbs broadly from 300 to 700 nm with an E_g^{opt} of 1.75 eV. PBDTTBT presents HOMO and LUMO levels of -5.6 and -3.7 eV (after correction), respectively. The HOMO level is about 0.3 eV deeper than PSPTPB and PCPDTBT.¹⁴² The deeper HOMO level leads to a higher V_{oc} of 0.9 V, an expected result, considering the difference between the HOMO level of a donor and the LUMO level of PCBM. PCEs up to 5.66% have been obtained from the PBDTTBT-based device, with a V_{oc} of 0.92 V, a J_{sc} of 10.7 mA cm⁻², and a fill factor (FF) of 0.58, which is one of the highest PCEs for single-active-layer OPVs.

PTPT is perhaps the only existing random donor-acceptor copolymer that exhibits efficient photovoltaic response, with EQE as high as 63% at 540 nm and over 50% for a broad range. The PTPT/PC₇₁BM cell has highest AM1.5G PCE of 4.4%, with a V_{oc} of 0.81 V, a J_{sc} of 10.2 mA cm⁻², and a FF of 0.53.¹⁴³ The devices also showed encouraging stability after encapsulation under ambient conditions, where only 15% loss was observed after two months storage in air.

It is interesting to notice that all the high performance D-A conjugated polymers mentioned above contain benzothiadiazole as an acceptor. Thieno[3,4-b]thiophene (TT) and diketopyrrolopyrrole (DPP) are the two other known acceptors being used in D-A conjugated polymers that demonstrate their applicability in high performance solar cells.

PBDTTT and its derivatives are benzo[1,2-*b*:4,5-*b'*]dithiophene (BDT) and Thieno[3,4-*b*]thiophene (TT) alternating polymers, with HOMO levels from -5.20 to -5.5 eV, and LUMO levels from -3.6 to -3.8 eV.¹⁴⁴⁻¹⁴⁶ The PBDTTT-CF₃/PC₇₁BM-blend BHJ solar cells prepared from chlorobenzene (CB), show a V_{oc} of 0.76 V, a J_{sc} of 10.2 mA cm⁻², a FF of 0.51, which

corresponds to a PCE of 3.92%. Upon using a mixture of chlorobenzene (CB) and 1,8-diodooctane (DIO) (97:3 by volume) as a co-solvent, the PCE of this blend is almost doubled to 7.4%, with a increase in J_{sc} to 14.5 mA cm^{-2} and a boost in FF to 0.69. This is the highest PCE in a polymeric solar cell reported up to date.¹⁴⁶

PDPP3T is an ambipolar conjugated polymer. Field-effect transistors based on PDPP3T exhibit nearly balanced electron and hole mobilities of 0.01 and $0.04 \text{ cm}^2 \text{ V}^{-1} \text{ s}^{-1}$, respectively. The best cells obtained for PDPP3T/PC₆₁BM in a 1:2 weight ratio have a V_{oc} of 0.68 V, a J_{sc} of 8.3 mA cm^{-2} , and a FF of 0.67, yielding a PCE of 3.8%.⁴¹ The PCEs of the devices increase to ~4.7% due to a jump in photocurrent to 11.8 mA cm^{-2} , switching PC₆₁BM to PC₇₁BM. In addition, it needs to point that the EQE of the optimized device is still relatively low, about 35% on average. It can be ascribed to inefficient electron transfer, due to approaching the minimum offset of $eV_{oc} = E_g^{\text{opt}} - 0.6 \text{ eV}$ with V_{oc} of 0.65~0.68 V and a small optical bandgap of 1.3 eV.¹²³ An interesting observation for PDPP3T is that its molecular weights affect the performance of photovoltaic devices, but have little or no influence on charge mobilities.

Table 1-1. Photovoltaic data of representative high performance OPVs

| | V_{oc}/V | $J_{sc}/\text{mA cm}^{-2}$ | FF | E_g^{opt} | PCE (%) |
|-----------------|-------------------|----------------------------|------|--------------------|---------|
| RR-P3HT | 0.61 | 11.1 | 0.66 | 1.85 | 5.0 |
| PCPDTBT | 0.62 | 16.1 | 0.55 | 1.40 | 5.5 |
| PSiF-DBT | 0.90 | 9.5 | 0.51 | 1.82 | 5.4 |
| PSPTPB | 0.68 | 12.7 | 0.55 | 1.45 | 5.1 |
| PPtTTBT | 0.79 | 10.1 | 0.51 | 1.80 | 4.1 |
| PTPT | 0.81 | 10.2 | 0.53 | 1.76 | 4.4 |
| PBDTTBT | 0.74 | 14.5 | 0.69 | 1.62 | 7.4 |
| PDPP3T | 0.65 | 11.8 | 0.60 | 1.30 | 4.7 |

The photovoltaic data of some representative high performance OPVs are summarized in table 1-1. As one can see, the efficiencies for OPVs are steadily approaching the predicted values of 10~12%. Designing new polymers will still be the focus in realizing such a grand goal.

1.3.4.2 Polymer/polymer bulk heterojunction solar cells

Friend and Holmes reported the first all-polymer bulk-heterojunction solar cells in 1995, blending MEH-PPV as a donor with CN-PPV as an acceptor.¹⁴⁷ Compared to polymer/fullerene photovoltaic devices, all-polymer BHJ solar cells have several foreseeable advantages. In order to maximize PCEs of solar cells, it is necessary to absorb across the whole visible and near-IR solar spectrum. In a polymer/polymer blend, both donor and acceptor components contribute to harvest light. It is possible to make a complementary polymer pair that absorb across the field. Although PC₇₁BM provides enhanced absorption in the blue region (peak at *ca.* 500 nm) with respect to PC₆₁BM (peak at *ca.* 349 nm), it contributes little in the red and near-IR region in the case of polymer/fullerene systems. In addition, polymer Synthesis offers much higher versatility and flexibility than fullerene chemistry, as demonstrated in the development of polymer/fullerene solar cells. Thus, it enables the control the energy levels to a great extent. The energy offset between the LUMO level of a donor and the LUMO level of an acceptor can be pre-customized to obtain the highest possible V_{oc} that is dependent on the difference between the LUMO level of an acceptor and the HOMO level of a donor without sacrificing the driving force for charge transfer and separation.

Figure 1-18 shows some donor and acceptor polymer combinations used in all-polymer BHJ solar cells. The state-of-the-art all-polymer cells exhibit PCEs of 1.5-1.9%, using the combination ranging from POPT/MEH-CN/PPV,^{88,90} P3HT/F8BT,¹⁰⁰ M3EH-PPV/CN-ether-PPV to TVPT/PDIDTT.^{40,106} These efficiencies are significantly less than those of polymer/PCBM BHJ solar cells. The efficiency discrepancy has tentatively been attributed to the

lower electron mobility of most conjugated polymers compared to fullerene derivatives , which is consequently led by the poor phase segregation resulted from binary polymer demixing and the limited availability of n-type conjugated polymers.

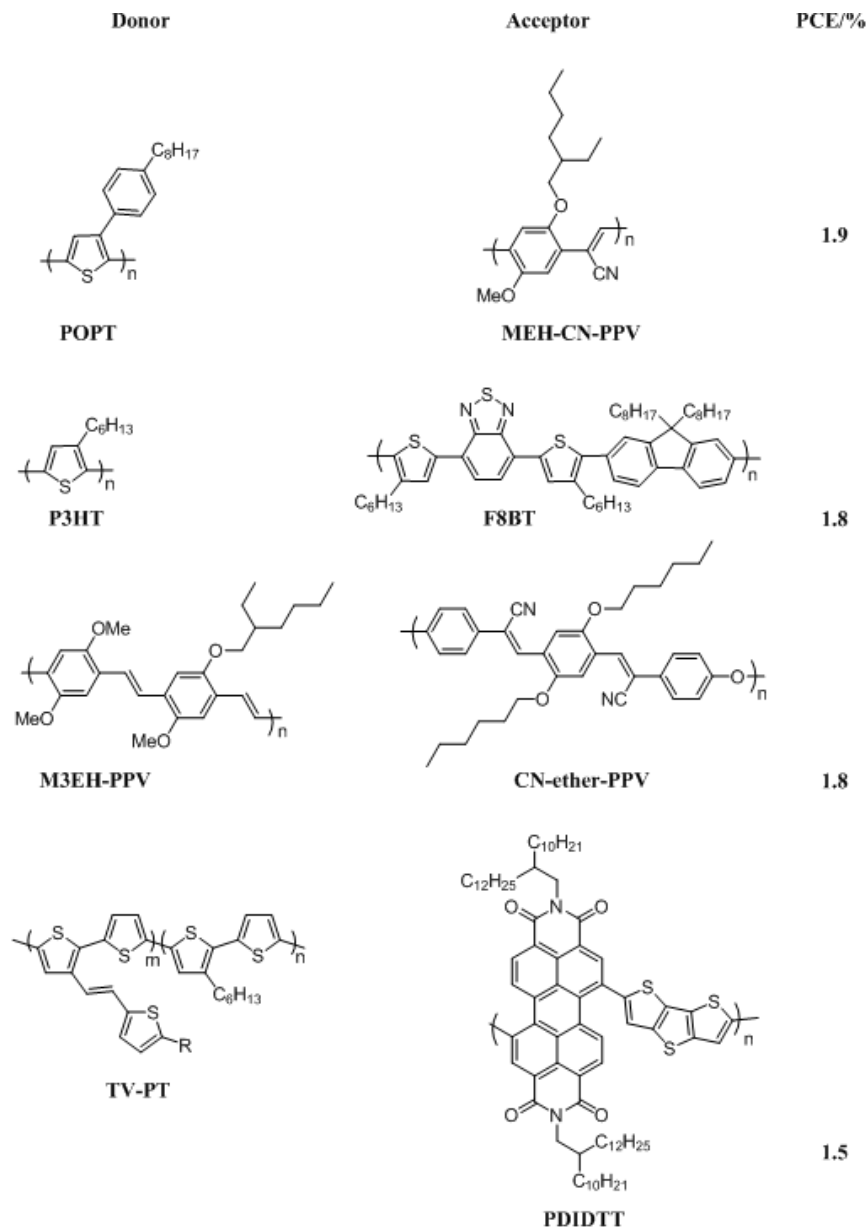


Figure 1-18 Donor and acceptor combinations used in all-polymer solar cells

Polymer blends have an intrinsic proclivity to demixing (phase separate) into their individual pure phase due to low entropy of mixing. There is no exception for rigid rod-like conjugated polymers. Binary random coil-like polymers and their demixing have been

extensively studied and are relatively well understood.¹⁴⁸⁻¹⁴⁹ Phase separation in conjugated polymers is instead much less understood, even though some demixing mechanisms, e.g. nucleation and growth of one phase in a surrounding phase, or by the process of spinodal decompositions, have been proposed based on what has been learned from random coil polymer systems. It also needs to be noted that these models are suitable for bulk phase separation, but may not be applicable to thin-film phase separation.⁹⁵ Nevertheless, people have applied these principles to control the phase separation process in order to obtain the characteristic domain size of 10-20 nm for photovoltaics. Certain progress has been achieved through techniques such as thermal annealing, and the use of mixed solvents.^{101,103}

Many efforts have been devoted to design p-type conjugated polymers, resulting in a large pool of p-type conjugated polymers. In contrast, the number of solution-processable n-type conjugated polymers is still limited, as mentioned in section 1.1.2. The available n-channel polymeric materials are still dominated by perylene diimide and naphthalene diimide-containing polymers.^{89,150-151} To design and prepare other n-type polymers with variable electron affinity, high electron mobility, and good ambient stability is thereby becoming the biggest challenge for all-polymer BHJ solar cells.

With the increased synthetic efforts and the better understanding of phase-separation for rigid-rod type polymers, all-polymer BHJ solar cells have the potential to push PCEs to higher levels in organic photovoltaics.

1.3.4.3 Molecular bulk heterojunction solar cells

Molecular bulk heterojunction (MBHJ) solar cells refer to photovoltaic devices based on monomeric semiconductors as the donor and the acceptor materials, and fullerene derivatives are still the dominant electron acceptors at this stage. Solution-processable MBHJ solar cells did not draw attention until 2006,^{74,152} about ten years after the debut of the polymer/PCBM and all-

polymer solar cells. Nevertheless, MBHJ solar cells have made significant progress in a few years,^{71,73,75-79,81-82} and the PCEs of a single layer device have climbed up to 4.4% in a recent report.⁸⁰ Matsuo and Nakamura et al. have recently reported a solution-processable three-layered p-i-n organic photovoltaic device using tetrabenzophorphyrin (TBP) as a molecular donor and silylmethyl[60]fullerene (SIMEF) as an electron acceptor (Figure 1-19).⁷² This device shows a PCE of 5.2%, a value that brings MBHJ solar cells into the family of the best performance BHJ solar cells that is usually composed of polymer/fullerene combinations. This study consolidates the need for further investigation of small molecules and new device configuration for development of efficient organic solar cells.

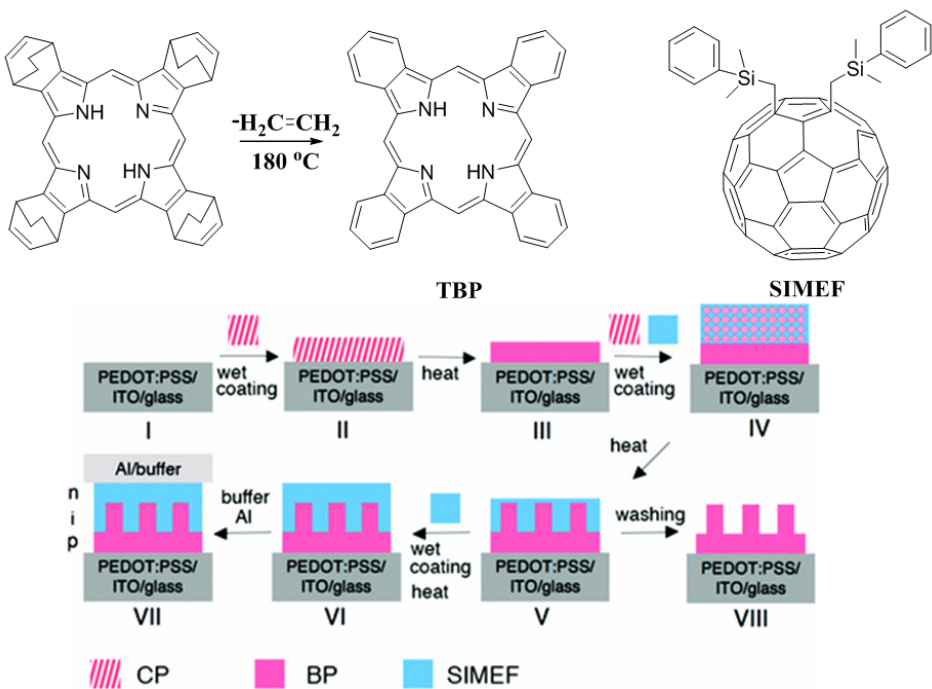


Figure 1-19. Solution-processable p-i-n three layered molecular bulk heterojunction solar cells based on TBP and SIMEF (Adapted from Ref. 72 with permission)

The knowledge accumulated in the development of polymer/fullerene solar cells has greatly facilitated the design of small molecules for MBHJ photovoltaic devices. On the other side, one also needs to realize that crystalline small molecules and semi-crystalline conjugated

polymers are two distinctive types of materials and have different phase separation behaviors.

To explore the solution-processing conditions and post-annealing techniques suitable for small molecule/fullerene blends becomes important and needs to be addressed in future study.

1.3.4.4 Organic-inorganic hybrid solar cells

Grätzel et al. in 1991 reported an efficient photovoltaic device based on organic dye molecules absorbed on TiO₂ nano-crystalline thin films, widely described as dye sensitized solar cells (DSSCs).¹¹⁶ This type of photovoltaic device differs from the later developed bulk-heterojunction solar cells, as they replace organic electron acceptors, e.g. fullerene derivatives, with inorganic TiO₂ nano-crystalline materials, and rely on liquid redox electrolytes to transfer charges from the dye molecules after charge separation. Other than its own significance as a new type of photovoltaic device,^{109,118-119} the study of DSSCs also stimulated the interest in organic-inorganic hybrid solar cells, because it has been proven that charge separation can be efficient at the hybrid interface in DSSCs.

The hybrid solar cells are of interest for several reasons. First, the energy gap of nanocrystals is a function of their particle size. For instance, the energy gap can be varied from 2.6 to 3.1 eV in CdS and from 2.0 to 2.6 eV in CdSe when changing the size from 6 to 2 nm.¹⁰⁸ Therefore, their absorption profile can be tuned in the visible region. This quantum size effect can also be applied to tandem solar cells. Second, the electron affinity of inorganic nanocrystals is usually significantly lower than organic conjugated polymers. In the case of widely used CdSe, its electron affinity ranges from 3.5 to 4.5 eV,¹¹³ suitable to function as acceptors in inorganic/polymer hybrid solar cells. Third, nanocrystals have a large surface area that can interact with polymers to lead to a nanoscale mixing, which is important for efficient charge separation. Last, but the most important, inorganic nanocrystals have high intrinsic carrier mobilities.

There are also some disadvantages for development of hybrid solar cells. Nanocrystals tend to coalescence into large particles by a process called “Ostwald ripening”,¹¹⁰ due to high surface tension. The surface of the nanocrystals is thereby typically capped by an organic ligand, which passivates the surface electronically. Greenham et al observed significant quenching of the luminance in the blend of polymer/CdSe when the nanocrystals surface is not coated with trioctylphosphineoxide (TOPO).¹¹² It is much less efficient quenching when the nanocrystals are coated with TOPO, which forms a barrier of 1.1 nm thickness between the nanocrystal core and the polymer. In addition, the ligand is also a barrier for transport of charges from one nanocrystal to the other. If such ligands are to be removed, it causes a different problem that electronic defects will be created at the interface when polymer has an intimate contact with the nanocrystal in the blend.

Since the first report on CdSe/MEH-PPV system, where PCE of 0.1% has been achieved,¹¹² hybrid solar cells have managed their way to obtain higher efficiencies. Alivisator et al. reported CdSe-nanorods/P3HT hybrid solar cells, for which a PCE of 1.7% has been achieved. Greenham used the high boiling solvent trichlorobenzene to process CdSe/MODO-PPV blends and obtained a vertical phase separation. In this device, the best PCE of 2.8%, on average 2.1%, has been obtained. By using a low bandgap polymer poly[2,6-(4,4-bis-(2-ethylhexyl)-4*H*-cyclopenta[2,1-*b*;3,4-*b'*]dithiophene)-*alt*-4,7-(2,1,3-benzothiadiazole)] (PCPDTBT) blended with CdSe nanocrystals, Dayal demonstrated a PCE of 3.1% for hybrid solar cells.

In order to continue to improve the PCEs of hybrid solar cells, a few issues require special attention. The ill-balanced charge carrier mobilities in the hybrid blends typically lead to the decreased EQE and fill factor. Further, the electronic defects on the nanocrystals surface

generate electron traps and hinder the efficient charge transport. It is thereby necessary to come up with a solution either chemically or physically to remove these traps. In addition, designing suitable conjugated polymers specifically for hybrid solar cells is also important to pursue higher efficiencies, considering high electron affinity in inorganic nanocrystals.

1.3.5 Tandem Bulk-heterojunction Solar Cells

In a single layer solar cell, a sizable portion of energy is inevitably lost. Photons with energy smaller than the bandgap of active materials will not be absorbed; while high energy photons will lose the excess energy via thermalization. One way to minimize the energy loss is to adapt tandem configuration, as demonstrated in small molecule heterojunction solar cells,¹⁵³ *i.e.* stack two cells in series with complementary wavelength absorption. Another feature of tandem cells is that their large open circuit voltage, in principle, is the sum of the individual subcells.

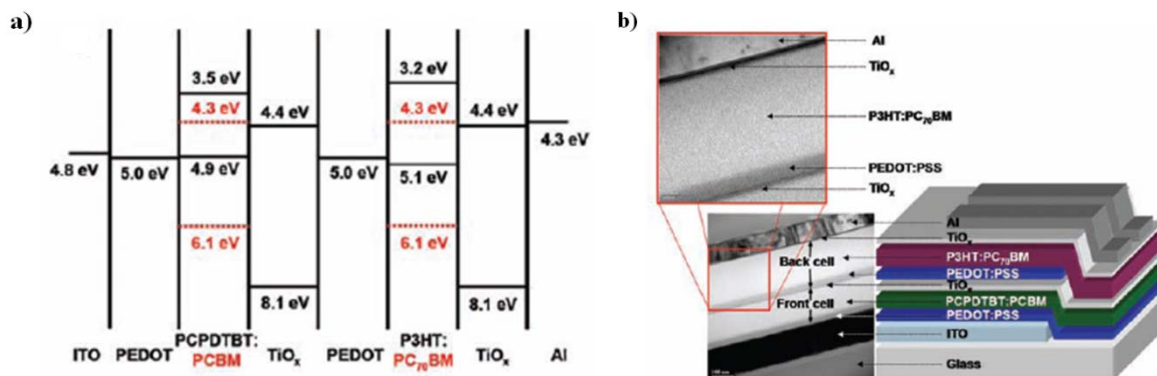


Figure 1-20. a) Energy-level diagram showing the HOMO and LUMO energies of each of the component materials; b) the device structure (right) and TEM cross-sectional image (left) of the polymer tandem solar cell. Scale bars, 100 nm (lower image) and 20 nm (upper image). (Adapted from Ref. 153 with permission)

Heeger et al. first reported tandem bulk-heterojunction solar cells with device structure as shown in Figure 1-20.¹⁵⁴ The PCPDTBT/PC₆₁BM single cell yields $J_{sc} = 9.2 \text{ mA/cm}^2$, $V_{oc} = 0.66 \text{ V}$, $FF = 0.50$, and $\eta = 3.0\%$, and the P3HT/PC₇₁BM single cell yields $J_{sc} = 10.8 \text{ mA/cm}^2$, $V_{oc} = 0.63 \text{ V}$, $FF = 0.69$, and $\eta = 4.7\%$. In a typical tandem cell, it gives $J_{sc} = 7.8 \text{ mA/cm}^2$, $V_{oc} = 1.24 \text{ V}$, $FF = 0.69$, and $\eta = 7.2\%$.

V , $FF = 0.67$, and $\eta = 6.5\%$. By using the similar strategy, Yang et al. have successfully demonstrated PSBTBT/P3HT/PC₇₁BM tandem cells.¹⁵⁵ And the optimal PCE of 5.84% has been obtained, compared to 3.77% for P3HT and 3.94% for PSBTBT individual cells. Janssen et al. showed that the combination of a wide bandgap material (PFTBT) and a small band gap polymer (PBBTDPP) for a tandem cell exhibited a PCE of 4.9%, with a large V_{oc} of 1.58 V. Brabec et al. estimated that a 15% tandem cell can be indeed achieved through care selection of the polymer pair and device structure.¹⁵⁶

Clearly, using a tandem configuration can be a very effective approach to improve the device performance. It also needs to be clear that introducing a large number of different layers via solution processing can be challenging and costly in such a tandem device. It is therefore important to reach a balance between processing and efficiency.

1.4 Objectives of this Dissertation

It is obvious that designing high performance organic semiconducting materials for photovoltaic applications is a challenging goal that requires delicate balance of all involved factors. It therefore becomes necessary to understand the underlying design principles and their consequent interplay, apply these interacting rules to material selection, and reconsolidate our comprehension on design criteria, so on and so forth. It is also important to point out that we use chemistry as a tool to make materials and develop new chemistry in this process.

In this dissertation, I intend to outline the field of organic semiconducting materials with a comparison with inorganic materials, and appraise the current status of various-types of organic solar cells. Chapter 2 introduces all the characterization tools and experimental setups. Chapter 3 focuses on a series of low bandgap platinum acetylide polymers with the intention to understand whether the introduction of triplet excitons will have an influence on solar cell performance. In chapter 4, a new approach has been demonstrated to prepare vinylene-linked donor-acceptor

conjugated polymers, and these low bandgap conjugated polymers have been tested in photovoltaic devices. Chapter 5 targets small molecules and polymers based on diketopyrrolopyrrole conjugated core and will describe how amphiphilic molecular design has been applied to achieving the first conjugated plastic crystal. In chapter 6, the preparation of a large number of donor-acceptor type small molecules and polymers is described using the newly designed electron-deficient isoindigo as acceptor core. This dissertation stops at chapter 7 with our perspectives for organic solar cells.

CHAPTER 2

EXPERIMENTAL METHODS AND CHARACTERIZATIONS

2.1 Materials Characterization

All reagents and starting materials were purchased from commercial sources and used without further purification, unless otherwise noted. The poly-(3,4-ethylenedioxythiophene)/poly(styrenesulfonate) (PEDOT-PSS) used was Baytron P VP Al 4083. PC₆₁BM was purchased from SES Research, Houston, TX. All procedures involving air- and moisture-sensitive reagents were performed using standard Schlenk techniques. 1,2-Dichlorobenzene (ODCB) was distilled from calcium hydride under a nitrogen atmosphere. Other anhydrous solvents were obtained from an anhydrous solvent system.

2.1.1 Structural Characterization

All ¹H NMR (300 MHz) and ¹³C NMR (75 MHz) spectra were recorded on a Varian Mercury 300 spectrometer. Chemical shifts for ¹H and ¹³C NMR were referenced to residual signals from CDCl₃ (¹H NMR δ = 7.25 ppm and ¹³C NMR δ = 77.23 ppm). Mass spectrograms were recorded on either a Finnigan MAT95Q Hybrid Sector (EI, HRMS) or a Bruker Reflex II (MALDI-TOF) mass spectrometer operated in linear mode with delayed extraction. Elemental analyses were carried out by Atlantic Microlab, Inc.

2.1.2 Molecular Weight Characterization

Gel permeation chromatography (GPC) was performed at 40 °C using a Waters Associates GPCV2000 liquid chromatography system with an internal differential refractive index detector and two Waters Styragel HR-5E columns (10 μm PD, 7.8 mm ID, 300 mm length) using HPLC grade THF as the mobile phase at a flow rate of 1.0 mL/min.

2.1.3. Thermal Characterization

Thermogravimetric analysis (TGA) was performed on TA Instruments TGA Q1000 Series using dynamic scans under nitrogen. Differential scanning calorimetry (DSC) analysis was performed using a TA Instruments Q1000 series equipped with a controlled cooling accessory (liquid nitrogen cooling system).

2.1.4 Electrochemical Characterization

Anhydrous TBAPF₆ salt, freshly distilled propylene carbonate (PC) and dichloromethane (DCM) were transferred to an argon-filled dry box (OmniLab model, Vacuum Atmospheres). Cyclic voltammetry (CV) and differential pulse voltammetry (DPV) studies were performed using an EG&G Princeton Applied Research model 273A potentiostat/galvanostat in an argon-filled dry box. Solution CVs were carried out in a 0.1M TBAPF₆/DCM solution at a scan rate of 25mV/s. Solid state DPVs were recorded in a 0.1M TBAPF₆/PC (ACN) solution from drop cast films on a platinum disk electrode, where platinum disk electrode (0.02 cm²), platinum flag and Ag/Ag⁺ electrode were the working, counter and reference electrodes respectively. All potentials are reported with respect to the potential of Fc/Fc⁺ redox couple (-5.1 eV vs. vacuum).¹⁵⁷

2.1.5 Optical Characterization

UV-vis spectra were recorded on a Varian Cary 500 Scan UV-vis-near-IR spectrophotometer. Solid state absorption spectra were recorded for films s with a PerkinElmer Lambda 25 UV-vis spectrometer. The oligomer films were spin coated on 1 x 1" PEDOT:PSS coated glass slides. Fluorescence spectra were recorded with an ISA SPEX Triax 180 spectrograph coupled to a Spectrum-1 liquid nitrogen cooled silicon charge coupled device detector.

Steady-state UV-visible absorption spectra were obtained on a Perkin-Elmer Lambda 25 dual beam absorption spectrometer using 1 cm quartz cells. Steady-state fluorescence emission

spectra were recorded on a SPEX TRIAX 180 spectrograph coupled with a Spectrum One CCD detector. Steady-state near-IR fluorescence spectra were recorded on SPEX-2 fluorescence spectrophotometer with an Indium-Gallium-Arsenide (InGaAs) detector. Fluorescence decays were obtained by time-correlated single photon counting on an instrument that was constructed in-house. A violet diode laser (405 nm, IBH instruments, Edinburgh, Scotland, pulse width 800 ps) was used as the excitation source. Transient absorption difference spectra were collected using a 2 mm path length cell on an apparatus described elsewhere.¹⁵⁸ Solutions were prepared in ODCB and purged with argon for 30 min before each measurement. The 3rd harmonic (355 nm) of a Continuum Surelite II-10 ND:YAG laser was augmented with a Continuum Surelite OPO Plus optical parametric oscillator to provide 550 nm laser pulses (10 mJ-pulse^{-1}) as the excitation source.

2.1.6 Morphology Characterization by Atomic Force Microscopy

Atomic force microscopy (AFM) was extensively used to characterize film morphology in this dissertation. Atomic Force Microscopy (AFM) relies on the repulsive or attractive forces between a finely pointed tip and the surface of a sample. There are 3 main modes of AFM which rely on different interactions between the atoms on the tip and the atoms on the sample. Tapping mode is the most commonly used mode of AFM, especially for our samples, due to its non-destructive nature vs. contact mode and higher resolution vs. non-contact mode. In tapping mode the tip oscillates and a set point amplitude is chosen. The tip is then scanned across the surface and the tip-sample height is constantly adjusted by the piezoelectric scanner to maintain the constant set point amplitude. In tapping mode the oscillation of the tip is driven by a small piezoelectric in the chip carrier. The difference between the oscillation of this piezoelectric and the oscillation of the tip is known as the phase shift. The phase shift can be used to construct an

image which provides information about the nature of the material or the sloping features present. If the surface is biphasic the phase shift will likely vary between materials and therefore regions of each material can be identified. The amplitude of the tip's oscillation can also be used to create an image. The amplitude will vary the most when the height of the surface changes more abruptly. This can be used to identify underlying features which may have been overshadowed in the height image. Figure 2-1 shows two AFM images obtained from our self-assembly studies on diketopyrrolopyrrole-based supramolecular nanostructures. These images are contributed by Kenneth Graham.

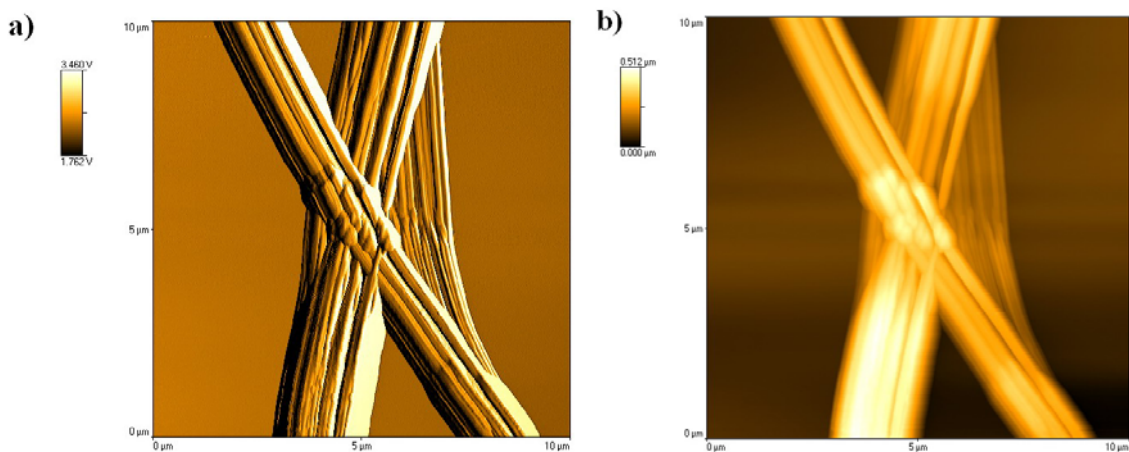


Figure 2-1. AFM images of self-assembled DPP-based nanowires on mica (10 x 10 μm scan size): a) amplitude image, and b) height image.

2.1.7. Single Crystal X-ray Diffraction

The crystals were submitted to the Center for X-ray Cryptography at UF. Data were collected at 173 K on a Siemens SMART PLATFORM equipped with A CCD area detector and a graphite monochromator utilizing MoK_α radiation ($\lambda = 0.71073 \text{ \AA}$). Cell parameters were refined using up to 8192 reflections. A full sphere of data (1850 frames) was collected using the ω -scan method (0.3° frame width). The first 50 frames were re-measured at the end of data collection to monitor instrument and crystal stability (maximum correction on I was < 1 %).

Absorption corrections by integration were applied based on measured indexed crystal faces. The structure was solved by the Direct Methods in *SHELXTL6*, and refined using full-matrix least squares. The non-H atoms were treated anisotropically, whereas the hydrogen atoms were calculated in ideal positions and were riding on their respective carbon atoms. A total of 158 parameters were refined in the final cycle of refinement using 2169 reflections with $I > 2\sigma(I)$ to yield R_1 and wR_2 of 4.85% and 12.26%, respectively.

2.1.8 2-D wide-angle X-ray scattering.

2-D wide-angle X-ray scattering (WAXS) experiments were performed at Max-Planck-Institute for Polymer Research. The fiber WAXS experiments were performed using a rotating anode (Rigaku 18 kW) Xray beam with pinhole collimation and a 2D Siemens detector. A double graphite monochromator for the Cu K α radiation ($\lambda = 0.154$ nm) was used. The fibers were prepared by filament extrusion using a home-built mini-extruder at elevated temperatures. The extrusion was performed for 0.7 mm thin fibers by a constant-rate motion. A $\theta - \theta$ Siemens D500 Kristalloflex with a graphite-monochromatized CuK α X-ray beam was used for the investigation of the structure in the thin film. The diffraction patterns were recorded in the 2θ range from 1 to 34° and are presented as a function of the scattering vector s ; with $s = (2 \sin \theta)/\lambda$ where 2θ is the scattering angle.

2.2 Bulk Heterojunction Solar Cells

Solar cells were fabricated on indium tin oxide (ITO) covered glass substrates (Delta Technologies, $Rs = 8-12 \Omega/\text{square}$). The ITO/glass substrates were etched by exposure to aqua regia vapor and subsequently cleaned in an ultrasonic bath for 15 min with aqueous sodium dodecyl sulfate (SDS, Fisher Scientific), de-ionized water (Milli-Q), acetone, and isopropanol. The substrates were then treated with oxygen plasma for 15 min in a Plasma Cleaner (HARRICK

PDC-32G). An aqueous PEDOT-PSS solution (Bayer Baytron P VP Al 4083) was spin coated at 4000 rpm onto the cleaned glass substrates and the resulting polymer film was dried under vacuum for 10 min at 150 °C. A solution of the photoactive material (P1 or P2 and PCBM, 1:4 weight ratio of polymer:PCBM) was prepared in toluene or *o*-dichlorobenzene with solids added at 1 – 2 % by weight. The solution of the photoactive materials was then spin-coated onto the PEDOT-PSS coated substrate in an inert atmosphere box (M-Braun) under argon, and the resulting films were dried under high vacuum overnight at room temperature. The thickness of the active layer was measured using a Dektak 3030 (Veeco Instruments Inc.) profilometer. (Each thickness reported in this study is the average of at least 3 different measurements on different regions of the film.) Aluminum (Al, 100 nm) was deposited by thermal evaporation on the photoactive layer. The active area of the devices was 0.25 cm². Note that the entire process of active layer spin-coating and electrode evaporation were carried out inside of the inert atmosphere glove box.

The current-voltage (I-V) characteristics were measured with a Keithley SMU 2400 source measurement unit under the illumination of AM 1.5 with an incident power density of 100 mW/cm² using a 150 W Xe arc lamp power supply (Oriel instruments). The external quantum efficiency of the photovoltaic devices was evaluated by measuring the incident photon to current efficiency (IPCE, %). For IPCE measurements, device pixels were irradiated with monochromatic light through an ISA H20 monochromator with a 75 W Xe arc lamp as a light source. The intensity of the source at each wavelength was determined using an energy meter (S350, UDT Instruments) equipped with a calibrated silicon detector (Model 221, UDT Instruments). The current response under short circuit conditions was then recorded for each pixel at 10 nm intervals using a Keithley 2400 SMU (positive lead to ITO and negative lead to

aluminum). The current-voltage (I-V) curve and IPCE plots were measured for at least three pixels, and the data represent the average of the three measurements. The measurements were performed in air without encapsulation.

2.3 Charge Mobility Measurements

Charge mobility is perhaps one of utmost important parameters in determining the applicability of organic semiconducting materials in photovoltaic applications. Typically, organic semiconducting materials (other than highly crystalline molecules, e.g. pentacene and rubrene) have low mobility ($<< 1 \text{ cm}^2 \text{V}^{-1} \text{s}^{-1}$). The method for measuring mobility of organic materials is therefore different from that of inorganic materials. In other words, the models developed for inorganic crystalline materials have to be modified before being applied to disordered organic materials. Quite a few suitable methods have been evolved over the past several decades to deal with organic materials, including time-of-flight method, analysis of steady-state trap-free space-charge limited current diodes (SCLC), modeling of $J-V$ characteristics from field-effect transistors (FET) and pulse radiolysis time-resolved microwave conductivity techniques. These methods have their own features and also present their challenges. In this dissertation, SCLC and FET methods are used to evaluate the mobilities of some newly prepared polymers and small molecules.

The applicability of the SCLC technique is built on the assumptions that ohmic contacts are present across semiconducting materials and metal electrodes, and only one type of charge carrier is present under the selected device construction. Therefore, one should be cautious to apply this model to analyze mobility of a material when these two assumptions are not granted. The sandwich device structure is rather simple, composed of two electrodes that have the same or very similar work function and one layer of organic semiconducting materials that can be either n- or p-type. When the material is n-channel, low-work function metal is chosen to create

an injection barrier for holes. For a hole-only device, typical for conjugated polymers, high-work function metal, e.g. gold and platinum, will be used as electrodes to create an injection barrier for electrons.

Charge mobility can be extracted from *J-V* characteristics of a device in dark. Typically, there are two regions in the *J-V* characteristics. At the low applied voltage, *J-V* characteristics show ohmic response. At the high applied voltage, the *J-V* characteristics exhibit space-charge limited current behavior because charge is injected only from one electrode. Under ohmic contact conditions, the current *J* is transport-limited instead of injection-limited and can be expressed as

$$J = 9/8 \varepsilon \mu_0 V^2 / d^3 \theta \quad (2-1)$$

In this equation, ε and d are permittivity and thickness of a material, respectively. Since SCLC diode construction is very similar with the photovoltaic configuration, this model is frequently used and very useful for determining charge mobility of a material that is for photovoltaic applications. It also needs to keep in mind that the mobility by this method is dependent on the third power of the film thickness. Inaccuracy of film thickness measurement will lead to a devastating deviation.

The FET technique is currently a common method to measure charge mobility in organic materials. There are four possible OFET architectures, including top contacts/bottom gate, top contacts/top gate, bottom contacts/bottom gate and bottom contacts/top gate. All four of these OFETs architectures are shown in Figure 2-2. In this dissertation, top contacts/bottom gate is chosen for its structure simplicity to evaluate the charge mobility.

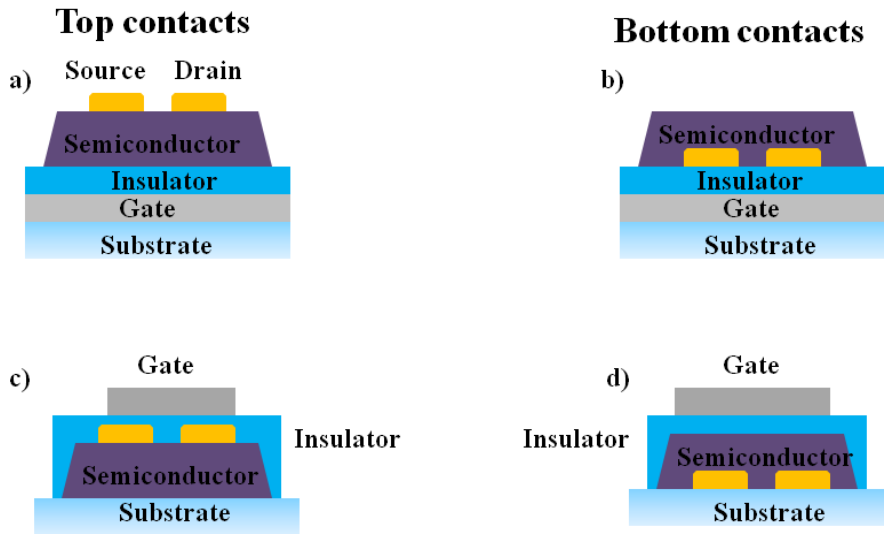


Figure 2-2. Four possible FET architectures (in cross-section): a) top contact, b) bottom contacts, c) top contacts/top gate, d) bottom contacts/top gate

The charge mobility can be extracted from $J-V$ characteristics of a FET device. In the linear and saturated regimes, it can be expressed as

$$I_{SD} = \frac{W}{L} \mu C (V_G - V_T) V_{SD} \text{ and } I_{SD} = \frac{W}{2L} \mu C (V_G - V_T)^2 \quad (2-2)$$

Here I_{SD} and V_{SD} denote the current and voltage bias between source and drain. V_G denotes the gate voltage and V_T is the threshold voltage at which the current starts to rise. C is the capacitance of the gate dielectric, and W and L are the width and length of the conducting channel.

The mobility resulting from the TFT measurements is often dependent on many other factors, other than the intrinsic mobility of a semiconducting material. The dielectric constant of the gate insulator greatly affects the mobility. The mobility is even sometimes gate-voltage dependent. In a word, it requires extra caution to make a comparison among mobilities values. Another notion is that in-plane mobility along a very thin channel is obtained in FET measurements, as opposed to vertical mobility. This makes FET mobility less applicable to photovoltaic devices, where the charges are perpendicular across the entire film.

CHAPTER 3
LOW BAND GAP PLATIMUN-ACETYLIDE POLYMERS FOR PHOTOVOLTAIC
APPLICATIONS

3.1 Introduction

Organic π -conjugated polymers and oligomers, due their potential in the development of plastic solar cells that are lightweight, mechanically flexible and low cost, have drawn significant attention as active materials in organic photovoltaic devices (OPVs).¹⁵⁹⁻¹⁶¹ Since the discovery of rapid and efficient photoinduced electron transfer from poly(2-methoxy-5-(2'-ethyl-hexyloxy)-*para*-phenylenevinylene (MEH-PPV) to C₆₀ in early 1990s,¹⁶²⁻¹⁶³ the use of fullerene derivatives as electron acceptors in OPVs has become ubiquitous. The so-called bulk-heterojunction OPVs have been most studied, using a single layer blend of a conjugated polymer and a fullerene derivative such as [6,6]-phenyl-C₆₁-butyric acid methyl ester (PC₆₁BM) or [6,6]-phenyl-C₇₁-butyric acid methyl ester (PC₇₁BM). In this type of device, appropriate phase segregation enables the formation of a bulk-heterojunction at the interface of the donor and acceptor components. Current state-of-the-art single layer conjugated polymer-based OPVs achieve power conversion efficiencies in the range of $\sim 7\%$, while the highest reported efficiency of 6.5% is for a tandem solar cell.^{144-145,164-171} Solar cells with optimized performance have been developed using P3HT/PC₆₁BM blends,¹⁷² and these cells feature nearly ideal photon-to-current quantum efficiency (IPCE) in the mid-visible region. However, to produce highly efficient OPVs light absorption by the active layer must be extended into the near-infrared region while at the same time preserving the high IPCE and open circuit voltage. In principle, the overall power conversion efficiency of the device is mainly determined by several individual efficiencies: light harvesting efficiency across the visible and near-infrared regions, exciton diffusion to the donor-acceptor interface, photoinduced charge separation, and the mobility of the charge carriers produced by photoinduced charge separation and charge collection.¹⁵⁹

In the Reynolds and Schanze groups there is an interest in exploring whether triplet excited states can be harnessed to increase the efficiency of charge generation in OPV active materials.¹⁷³⁻¹⁷⁴ In theory, there are several possible reasons why triplet states are expected to give rise to efficient charge generation. First, the long lifetime (up to the μ s time regime) of the triplet state (triplet exciton) may enhance the probability of exciton diffusion to a donor-acceptor interface.¹⁷⁵⁻¹⁷⁶ Second, quantum mechanical spin-restrictions prevent charge recombination in the geminate ion-radical pair produced as a result of photoinduced charge transfer from a triplet state precursor.¹⁷⁷ Conventionally, triplet states are not produced efficiently as a result of direct photo-excitation of most organic hydrocarbon π -conjugated materials. Therefore, in order to explore the effects of triplet states in OPVs, it is necessary to utilize materials that incorporate heavy atoms which give rise to efficient intersystem crossing by enhancing spin-orbit coupling.¹⁷⁸

Platinum acetylide oligomers and polymers have been widely studied because they represent a class of π -conjugated materials featuring high quantum efficiency for intersystem crossing (to produce the triplet excited states) following direct photo-excitation. This provides considerable insight into the electronic structure and the delocalization and dynamics of the triplet exciton.¹⁷⁹⁻¹⁸⁴ Platinum acetylides have also been used as the active materials in organometallic photovoltaic devices. An early example by Köhler and co-workers demonstrated that the photocurrent response of a blend of a platinum acetylide polymer and C₆₀ was enhanced relative to the pure polymer.¹⁸⁵ Evidence that the polymer triplet state was involved in charge generation came from the observation that C₆₀ only partially quenched the polymer's singlet emission (fluorescence) but completely quenched the triplet emission (phosphorescence). More recently, our group reported a photophysical and OPV device study that focused on active

materials consisting of blends of the platinum acetylide polymer p-PtTh and PC₆₁BM.¹⁷³⁻¹⁷⁴ Luminescence quenching and transient absorption spectroscopy indicate that photoinduced electron transfer (PET) from the p-PtTh triplet to PC61BM is efficient. Solar cells constructed using a 4:1 PC61BM/p-PtTh blend as the active material exhibit a peak IPCE of *ca.* 10% and an overall power conversion efficiency of 0.27%. While the IPCE of the p-PtTh/PC₆₁BM cells is respectable, the overall power conversion efficiency is limited because p-PtTh only absorbs blue light ($\lambda_{\text{max}} \approx 411$ nm), and consequently its absorption overlaps poorly with the solar emission spectrum.

In a natural continuation of our investigations utilizing the triplet excited state in OPVs, we sought to develop platinum acetylide polymers that absorb light strongly throughout the visible and near-IR regions. It was proposed that such materials would lead to more efficient photocurrent generation due to increased light harvesting efficiency while preserving the high quantum yield of intersystem afforded by the presence of the platinum heavy metal centers in the π -conjugated chain. In order to achieve this objective, we designed a series of polymers and model oligomers that feature π -conjugated segments of the type donor-acceptor-donor alternating with (or end-capped by) *trans*-Pt(PBu₃)₂-units (Figure 3-1). These materials were developed on the basis of prior work demonstrating that low bandgap polymers and oligomers can be prepared when the conjugated backbone consists of alternating repeat units that have electronic donor and acceptor properties.^{56,186-193} Three pairs of polymers and model oligomers, together with a copolymer, are the focus of the work presented herein. The first pair features a π -conjugated segment consisting of the 2,1,3-benzothiadiazole (BTD) acceptor moiety flanked on either side by 2,5-thienyl donor units (**M-1** and **P1**), whereas in the second pair the BTD unit is flanked by (3,4-ethylenedioxy)-2,5-thienyl donors (**M-2** and **P2**). Both oligomer/polymer

pairs absorb strongly throughout the visible region; however, because the ethylenedioxothiophene moiety is a stronger donor than thiophene, the latter oligomer/polymer pair has a correspondingly lower bandgap, and therefore harvests light more efficiently in the near-infrared region. The third pair use a much stronger acceptor [1,2,5]thiadiazolo[3,4-g]quinoxaline to replace 2,1,3-benzothiadiazole leading to a shift in the absorption maximum into the near-IR region. Combining the repeat units found in **P1** and **P3**, polymer **P4** absorbs across the entire visible and Near-IR regions.

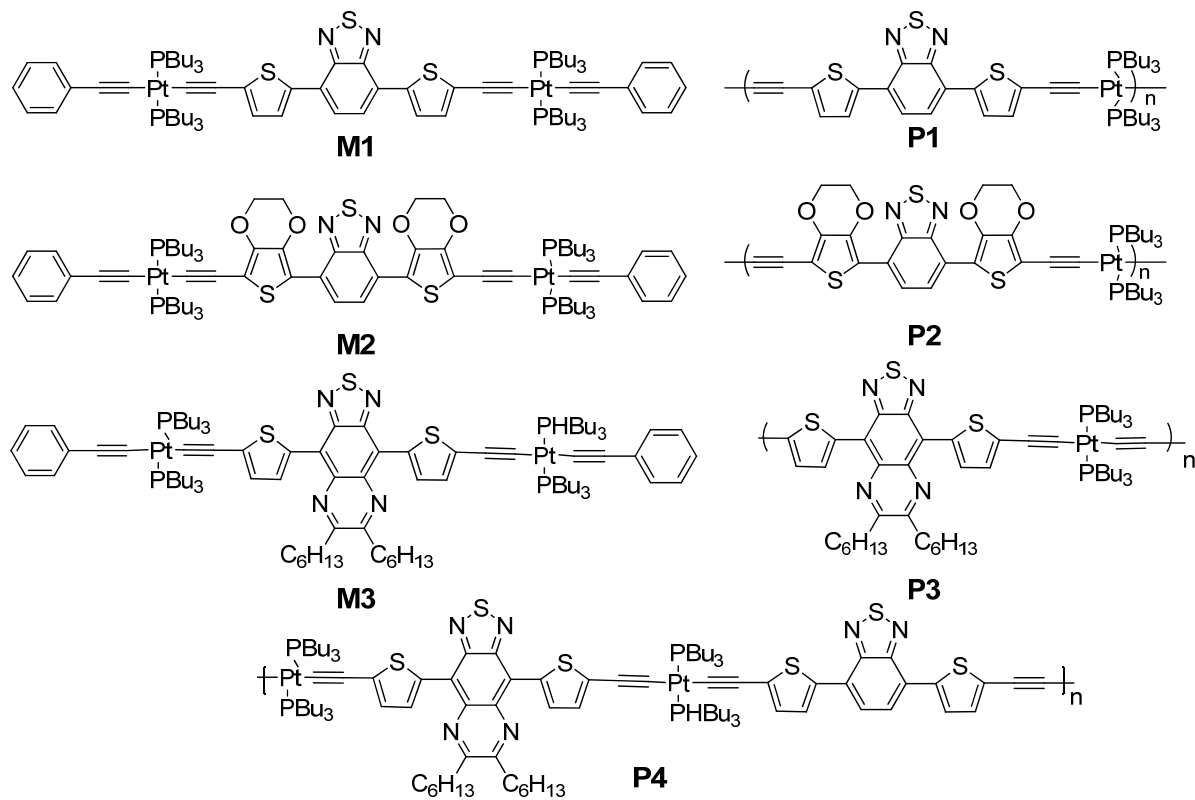


Figure 3-1. Structures of Pt-acetylide model compounds and polymers.

In this chapter a complete report of the syntheses as well as photophysical and electrochemical characterization of a set of low bandgap platinum-acetylide model complexes and polymers is provided. In addition, the ability of **P1** to undergo photoinduced electron transfer (PET) to PC_61BM from both the singlet and triplet excited state manifolds is also

investigated. Finally, OPVs based on blends of **P1/P2/P3/P4** with PC₆₁BM were characterized under monochromatic and simulated solar (AM1.5) illumination. The photophysical studies reveal that the materials undergo relatively efficient intersystem crossing. It was observed that the singlet state is quenched efficiently by PC₆₁BM, but the triplet state is not quenched, indicating that charge generation in the photovoltaic materials must ensue from the singlet manifold. A thermodynamic analysis of PET based on the electrochemical and spectroscopic data indicate that charge transfer from the singlet state of the low bandgap platinum acetylides is thermodynamically feasible but not favored from the triplet state. Nevertheless, the materials perform well when used in bulk heterojunction OPV devices. Operating under AM1.5 conditions, optimized devices exhibit an open circuit voltage (V_{oc}) of ~0.5 V, a short circuit current density (I_{sc}) of ~7.2 mA·cm⁻², and a fill factor of ~35%, which yields overall power conversion efficiencies of 1.1 to 1.4% for **P1**.

During the course of our studies, a report by Wong and coworkers appeared describing the fabrication and characterization of OPVs fabricated with blends of PC61BM and **P1**.¹⁹⁴⁻¹⁹⁵ The OPVs tested by Wong's group operate with remarkably high efficiency: a peak IPCE of 87% at 575 nm is reported and the overall efficiency of a cell operating under AM1.5 illumination is reported to be 4.93%.¹⁹⁴ It should be noted that the technical accuracy of these reported values have been examined by others as careful analysis of the results is required for these PV cells.¹⁹⁶⁻

¹⁹⁷ Our complete study provides an interesting and useful complement and contrast to the materials-oriented study by the Wong group, as we have fully characterized the photophysics, electrochemistry and photoredox properties of two structurally-related low bandgap platinum acetylide polymers, as well as characterizing their performance in bulk heterojunction OPV devices. An important point is that the devices characterized in our hands operate with lower

efficiency compared to the previous report.¹⁹⁴ Possible origins for this discrepancy in device performance are considered in our discussion. In addition, it is worth mentioning that our photovoltaic results are consistent with the observations from Jen¹³⁹ and Jenekhe.¹⁹⁸ All three of these reports are more in agreement with the theoretical simulation carried out by Janssen.¹⁴¹

3.2 Synthesis of Platinum-acetylide Model Complexes and Polymers

The general synthetic routes used to prepare **P1**, **M1**, **P2**, and **M2** are illustrated in Figure 3-2. Compound **3-2** was obtained in 59% by Stille coupling of dibromo-2,1,3-beozothidiazole (**3-1**) and 2-tributylstannylthiophene. Upon reacting compound **3-2** with N-bromosuccinimide in DMF, the precipitate was collected by suction filtration and washed with methanol to yield compound **3-3** in 90% yield. Trimethylacetylene moieties were installed on the both sides of **3-3** through the palladium-catalyzed Sonogashira reaction in high yields to give compound **3-4**, which is subsequently deprotected by the removal of TMS groups to give compound **3-5** in almost quantitative yield. Compound **3-5** was reacted with *trans*-Pt(PBu₃)₂Cl₂ in the presence of a catalytic amounts of CuI and piperidine in toluene to afford the polymer **P1** as a material that is soluble in THF, chloroform and toluene. The phenylethynyl end-capped model oligomer **M-1** was obtained in a good yield by reacting **3-5** with mono-capped phenylacetylene chloroditributylphosphine platinum complex in the presence of CuI as a catalyst. A similar strategy was used to prepare **P2** and **M-2** with a slight modification in the procedure. Specifically, due to the fact that removal of the trimethylsilyl protecting groups by reaction of **3-6** with tetrabutylammonium fluoride (TBAF) led to decomposition of the product, a methodology was adopted whereby **3-6** was deprotected *in situ*. Thus, reaction of **3-6** with TBAF in the presence of either *trans*-Pt(PBu₃)₂Cl₂ or mono-chloroplatinum complex afforded the expected products **P2** or **M2**, respectively.

The sequence to prepare **P3** and **M-3** is outlined in Figure 3-3. Nitration of **3-1** with a mixture of fuming sulfuric acid and fuming nitric acid led to compound **3-7**. Due to the existence of structural isomers, the purification of **3-7**, which is obtained in low yield, is extremely tedious and difficult.

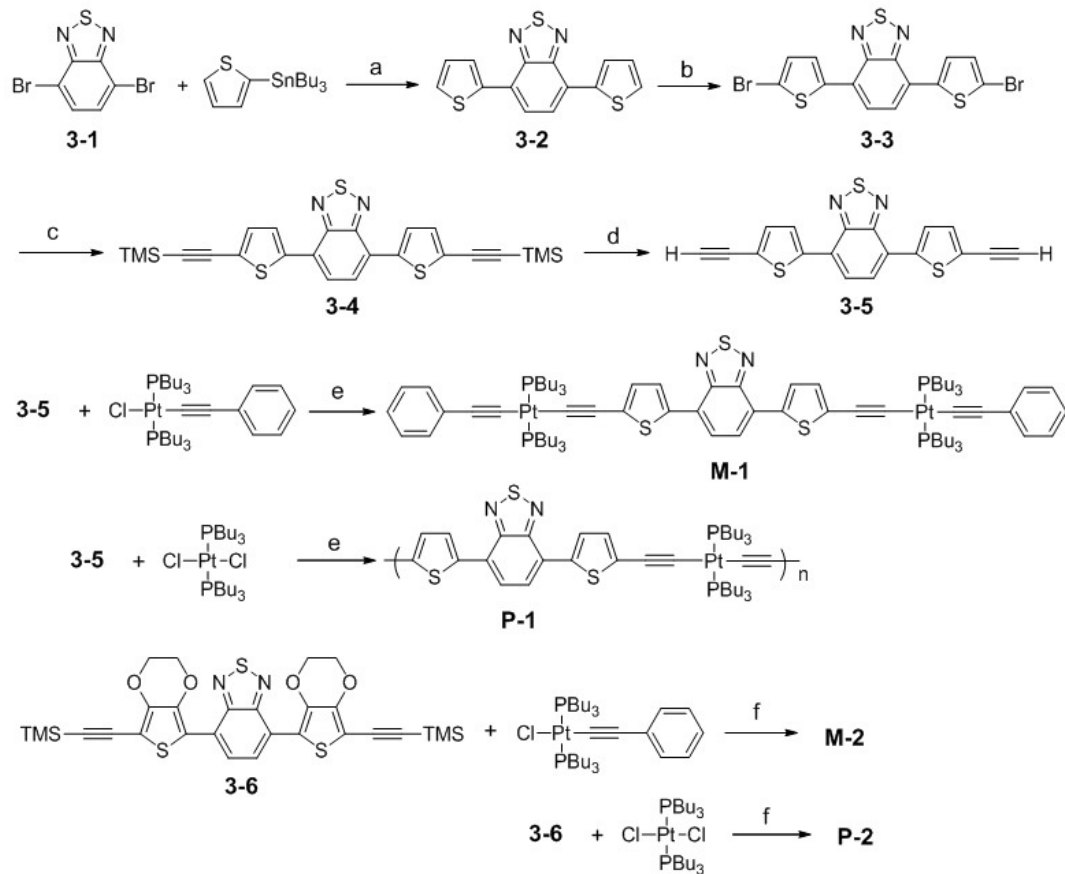


Figure 3-2. Synthesis of M-1, M-2, P-1 and P-2: a) tributyl(thiophen-2-yl)stannane, $\text{Pd}(\text{PPh}_3)_2\text{Cl}_2$, THF, 76 %; b) NBS, DMF, 92%; c) trimethylsilylacetylene, $\text{Pd}(\text{PPh}_3)_2\text{Cl}_2$, CuI and $i\text{Pr}_2\text{NH}$ -THF, 90%; d) K_2CO_3 , MeOH, 97%; e) trans- $\text{Pt}(\text{PBu}_3)_2\text{Cl}_2$, CuI and piperidine- CH_2Cl_2 ; f) trans- $\text{Pt}(\text{PBu}_3)_2\text{Cl}_2$, TBAF, CuI and piperidine- CH_2Cl_2 .

After successful installation of the flanking thiophene rings, compound **3-8** was reduced with iron powder in acetic acid. Ring closing was achieved via the acid-catalyzed condensation of compound **3-9** and tetradecane-7,8-dione yield compound **3-10** in high yield. Compound **3-12** was then obtained using a strategy similar to that employed for compound **3-4**.

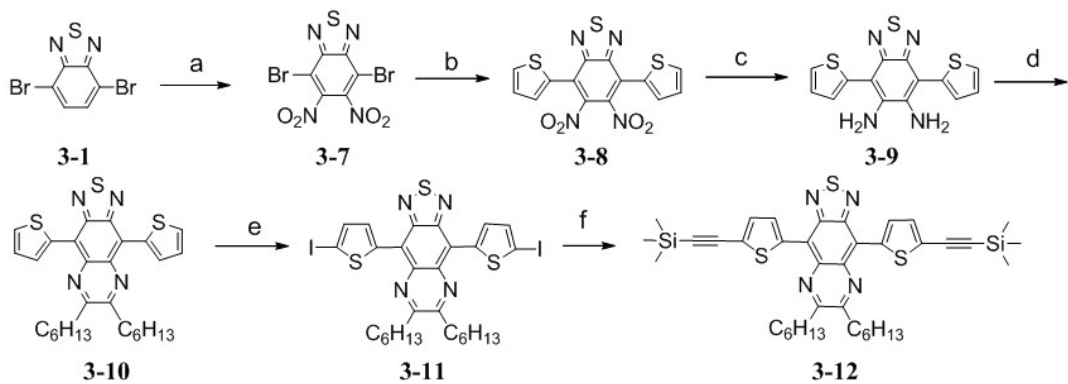


Figure 3-3. Synthesis of compound 3-12: a) fuming H₂SO₄-HNO₃, 39 %; b) tributyl(thiophen-2-yl)stannane, Pd(PPh₃)₂Cl₂, THF, 76 %; c) Iron-acetic acid, 65 %; d) tetradecane-7,8-dione, p-TSA, CHCl₃, 79 %. e) NIS, CHCl₃, 87 %; f) trimethylsilylacetylene, Pd(PPh₃)₂Cl₂, CuI and iPr₂NH-THF, 84 %;

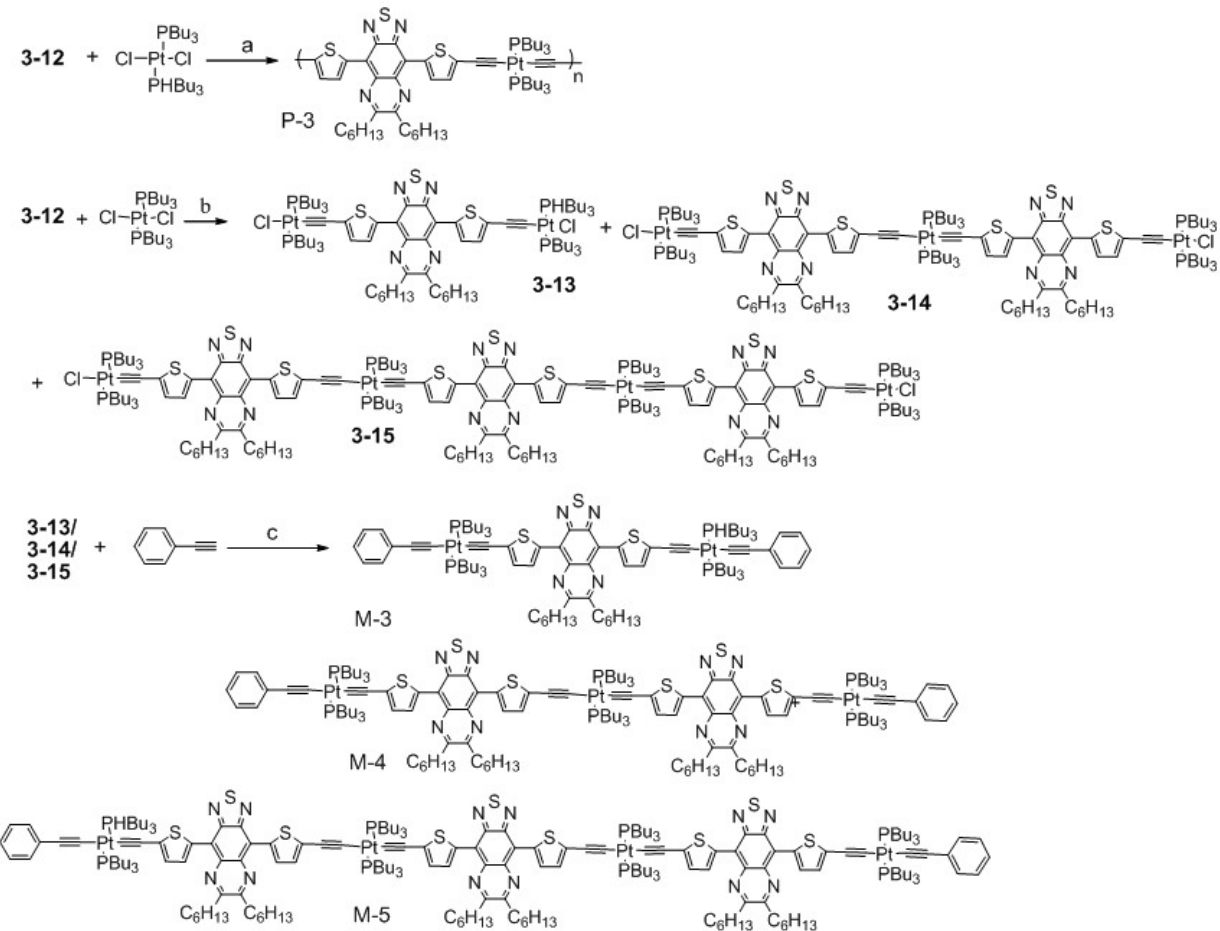


Figure 3-4. Synthesis of M-3, M-4, M-5 and P-3: a) 1 eq trans-Pt(PBu₃)₂Cl₂, TBAT, CuI and Et₃N-CH₂Cl₂; b) 5eq trans-Pt(PBu₃)₂Cl₂, TBAT, CuI and Et₃N-CH₂Cl₂; c) CuI and Et₃N-CH₂Cl₂.

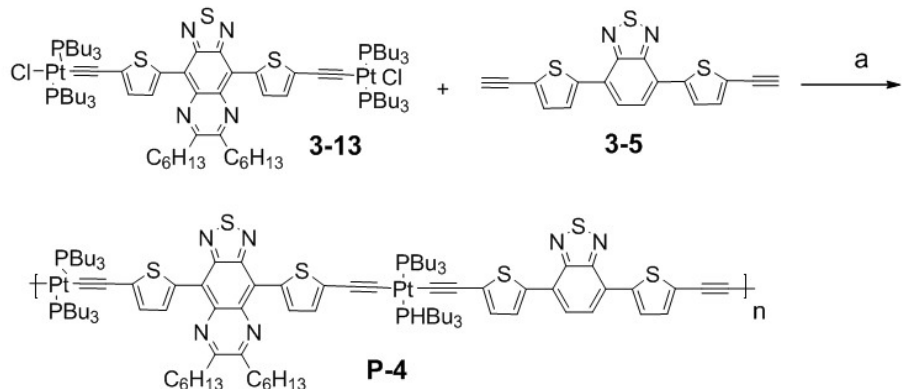


Figure 3-5. Synthesis of **P-4**: a) CuI and Et₃N-CH₂Cl₂.

With compound **3-12** in hand, we first attempted to remove the TMS protecting group.

Little success was achieved after a number of trials using standard deprotection methods including TBAF, TBAF-acetic acid, K₂CO₃-methanol, CsF, KF, and HF-pyridine. As mentioned for **P2**, TBAF used in the case of the preparation of **P2** leads to the decomposition of **3-12**. Therefore, in-situ deprotection and polymerization were carried out to obtain **P3**. A color change from deep blue to yellow upon addition of TBAF indicates the decomposition of compound **3-12**. It is likely caused by the basic nature of TBAF in solution. Fortunately, it was found that replacing TBAF with tetrabutylammonium triphenyldifluorosilicate (**TBAT**) can circumvent this problem as shown in Figure 3-4. **TBAT** is a commercially available white crystalline solid.

For the preparation of **M-3**, a different approach was taken than that used to make **M-1** and **M-2**. Compound **3-13** was instead prepared, which served two purposes. First, it was used to prepare **M-3** through a reaction with phenylacetylene. Additionally, compound **3-13** can react with compound **3-5** to yield **P4**, as shown in Figure 3-5. In the course of preparing **3-13**, compounds **3-14** and **3-15** were obtained as side products, which were then converted into **M-4** and **M-5**, respectively. This set of monomer, dimer and trimer provides a very good base to analyze the difference between oligomers and their corresponding polymer.

3.3 Structural Characterizations

The intermediate and model complexes **M-1**, **M-2**, **M-3**, **M-4**, and **M-5** were purified by silica gel column chromatography and the ^1H , ^{13}C , and ^{31}P NMR spectra of the isolated products are consistent with their molecular structures. As an example, Figure 3-6 shows the ^{31}P NMR spectra of **3-13**, **3-14**, and **3-15**. In compound **3-13**, there exists only one phosphine peak with two satellites, in accordance with the existence four equivalent phosphene ligands bound to each platinum atom. From the big coupling constant of 2230 Hz, we can also conclude that the two phosphene ligands are in a *trans*-conformation. In contrast, two peaks appear in the case of compound **3-14** and **3-15**. These peaks can be explained by the existence of two different phosphene ligands, which are situated at internal and terminal positions in the molecules. The polymer samples were purified by precipitation from CHCl_3 solution into methanol and then subjected to Soxhlet extraction with methanol, hexane, and CHCl_3 for further purification. The ^1H and ^{31}P NMR spectra of the polymers are in agreement with the structure of the materials. Further characterization information can be found at the end of this chapter.

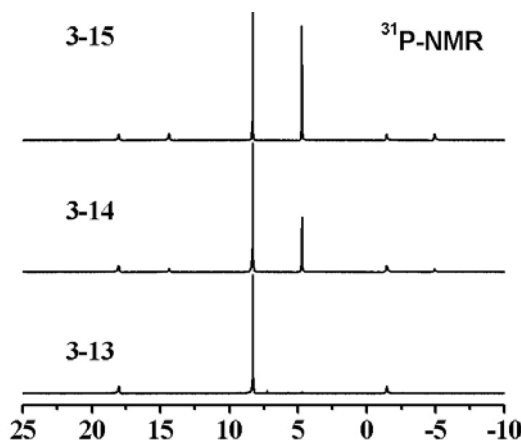


Figure 3-6. ^{31}P -NMR spectra of model complexes of **3-13**, **3-14**, and **3-15**.

Matrix assisted laser desorption-ionization (MALDI) mass spectroscopy was carried out on samples **P1** and **P2** in an effort to obtain additional information concerning the molecular weight

distribution of the polymers. This data is shown in Figure 3-7. The MALDI mass spectrometry was performed using DCTB ((2-[(2E)-3-(4-tert-butylphenyl)-2-methylprop-2-enylidene]malonitrile) as the matrix.¹⁹⁹ The **P1** MALDI mass spectrum exhibits peaks spanning from $m/z = 1,000\text{-}15,000$ with several ion series observed in the spectrum. Ions in each series are separated by 946 amu, which is consistent with the repeat unit structure of the polymer (see Scheme 1). Above $m/z = 4100$ there are two main series. The most intense is $[(AB)_n + 2]^+$. It is suspected that the residual mass of 2 amu could represent 2 hydrogen end groups. However, at this mass the accuracy of the instrument is insufficient to distinguish between linear compounds with 2 hydrogen end groups and cyclic compounds. $[(AB)_n + 302]^+$ is the other main series at higher masses. In contrast, the **P2** MALDI mass spectrum has ion series spanning only from $m/z 1,000\text{-}9,000$. This may result from high mass discrimination on the part of the instrument or polymer with low molecular weight. Ions in each series are separated by 1062 amu, consistent with the repeat unit structure of this polymer. Below $m/z 5000$, there are related series of $[(AB)_n + 672]^+$, $[(AB)_n + 764]^+$, and $[(AB)_n + 855]^+$. These series correspond to B(AB)_n polymers with 2 chlorine end groups, 1 chlorine/1 iodine end group, and 2 iodine end groups, respectively ($n = 1\text{-}5$). Above $m/z 5000$, the predominant series is $(AB)_n^+$ with $n=5, 6, 7, 8$. Interestingly, end groups of 2 chlorines, 1 chlorine/1 iodine, and 2 iodines, similar to the end groups in the lower mass series, do not exist. It should be noted that the iodine content could originate from the CuI catalyst).

Gel permeation chromatography (GPC) was performed on polymer samples using chloroform as the eluent and molecular weights are referenced to polystyrene standards. The GPC chromatogram of **P1** exhibits a relatively narrow molecular weight distribution with a number-average molecular weight (M_n) of 22 kDa and polydispersity index (PDI) of 1.97. By

contrast, **P2** exhibits a comparable M_n of 33 kDa, but the PDI of the polymer is unreasonably high. The broad PDI observed for **P2** is likely due to the fact that this polymer has a lower solubility and consequently tends to aggregate. This premise is supported by the observation that the PDI of **P2** obtained by GPC varies with the concentration of the solution used for the analysis. **P3** has a number-average molecular weight of 27 KDa and a PDI of 3.5. The broad PDI can be explained by the nature of in-situ deprotection and polymerization, which would be expected to give a large molecular weight distribution. In contrast, **P4** has a larger M_n of 35 KDa, but a smaller PDI of 2.6.

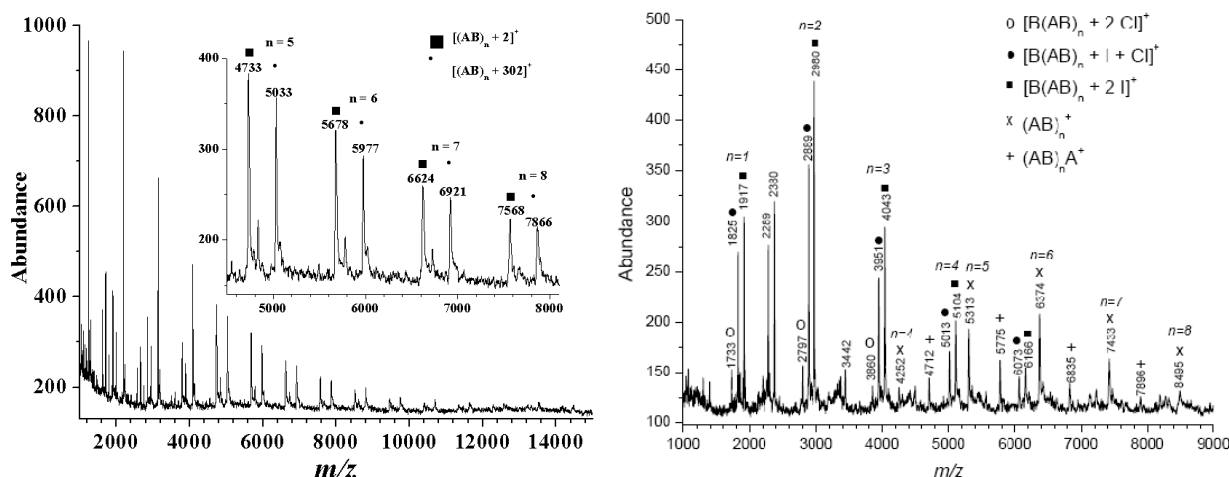


Figure 3-7. MALDI-TOF mass spectra of P1 and P2.

3.4 Photophysical and Electrochemical Studies

3.4.1 Photophysical Studies

The photophysical properties of the model compounds and polymers were characterized in THF solution. The absorption and photoluminescence spectra of the first two pairs are shown in Figure 3-8, and pertinent photophysical data are listed in Table 1. In general, all of the materials feature two primary absorption bands with one appearing in the near-UV or blue region of the visible spectrum and the second at lower energy with a wavelength maximum in the 550 – 650 nm region. Several features emerge upon close inspection of the absorption data. First, for each

model complex/polymer pair, the absorption band maxima are red-shifted for the polymers relative to the monomers. This feature suggests that there is some excited state delocalization in the polymers relative to the monomers. This effect may arise via molecular orbital delocalization via $d\pi-p\pi$ orbital overlap through the Pt centers.²⁰⁰ Alternatively, the red-shift may result from exciton interactions between adjacent π -conjugated chromophores in the polymer systems. A second feature is that the band maxima for **M-2** and **P2** are red-shifted significantly compared the band maxima for **M-1** and **P1**. This feature is consistent with the electrochemical bandgap calculations discussed later (Table 3-3), and results from the strong effect of the EDOT donor on raising the HOMO level in BTD-EDOT type compounds. The net result is that the presence of the strong EDOT donor lowers the band gap resulting in a substantial red-shift of both of the optical transitions. **P3** has a much stronger acceptor that pushes the absorption even more into near-IR region.

Table 3-1. Photophysical properties of model compounds and polymers

| Material ^a | $\lambda_{\text{max}}/\text{nm}$ | $\varepsilon/\text{cm}^{-1}\text{M}^{-1}$ | $\lambda_{\text{em}}/\text{nm}$ | Φ_f ^b | τ_f/ns | $\tau_{\text{TA}}/\mu\text{s}$ ^c | E_g/eV ^d |
|-----------------------|----------------------------------|---|---------------------------------|-----------------------|--------------------|---|------------------------------|
| M1 | 372 | 40,900 | 678 | 0.29 | 9.3 | 1.8 | 2.09 |
| | 549 | 28,400 | | | | | |
| M2 | 389 | 69,200 | 710 | 0.14 | 6.4 | 1.4 | 1.95 |
| | 596 | 43,800 | | | | | |
| P1 | 378 | 45,600 | 683 | 0.04 | 1.1 | 1.1 | 2.07 |
| | 563 | 43,600 | | | | | |
| | 408 | 55,300 | | | | | |
| P2 | 621 | 51,100 | 717 | 0.05 | 0.9 | 1.2 | 1.93 |
| | 405 | 46,900 | | | | | |
| P3 | 800 | 36,900 | 1010 | | | 0.16 | 1.30 |

(^a In THF. ^b Excited at 510 nm, calculated using Rhodamine B ($\Phi_f = 0.69$)^{ref201} in ethanol as an actinometer. ^c In ODCB. ^d Optical.)

All of the materials feature a broad, structure-less (red) photoluminescence that is Stokes-shifted relatively little from the lowest energy absorption band. Quantum yields and emission lifetimes are listed in Table 3-1. The photoluminescence decay lifetimes are in the range of a few nanoseconds, consistent with assignment of the photoluminescence to radiative decay from

the singlet excited state (fluorescence). Despite the general similarity of the fluorescence from the materials, there are several significant differences that emerge from close inspection of the data. First, the trends noted for the absorption maxima are mirrored in the fluorescence spectra. Specifically, the fluorescence maxima are red-shifted in the polymers compared to the corresponding monomers, and the fluorescence for the **M-2** and **P2** materials is red-shifted compared to the **M-1** and **P1** materials. The energy of the relaxed (fluorescent) singlet excited state (E_s) is estimated for each of the materials by using the onset wavelength for the fluorescence. The values are listed in Table 3-1 and they range from ~ 2.1 eV for the **M-1** and **P1** materials to ~1.95 eV for the **M-2** and **P2** materials. **P3** is much more red-shifted than **P1** or **P2** with an E_s of 1.3 eV.

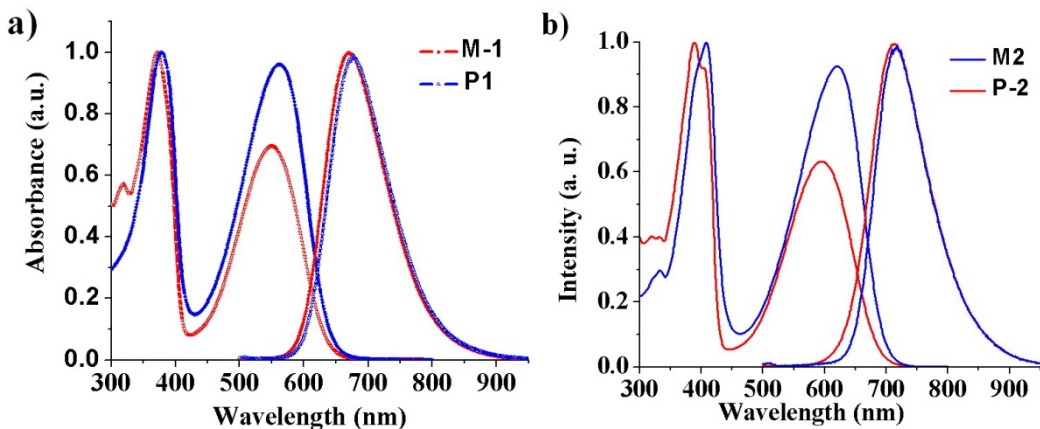


Figure 3-8. Absorption and emission spectra of a) M-1 and P1, and b) M-2 and P2.

The fluorescence quantum yields and lifetimes were determined for the materials in solution. The quantum yields are 3 – 5 times larger for the model complexes relative to the corresponding polymers. A similar trend is seen in the fluorescence lifetimes, which indicates that non-radiative decay is more efficient in the polymers. The more efficient non-radiative decay of the singlet state in the polymers likely arises from quenching sites (traps) in the polymers caused by interchain aggregation and also possibly by defects in the chain structure.

A key objective of this work is to explore the nature and photoactivity of the triplet states in low-bandgap platinum acetylide materials. The observation of moderately efficient fluorescence and fluorescence (singlet) lifetimes in the nanosecond range suggests that intersystem crossing in the BTD-Th and BTD-EDOT materials is not as efficient as has been observed in platinum acetylide materials that have been previously investigated where singlet lifetimes < 100 ps and triplet yields approaching unity have been reported.^{183,202} Nevertheless, as outlined below, there is clear evidence that photoexcitation of all of the materials leads to at least moderately efficient population of long-lived triplet states.

First, in efforts directed towards observing phosphorescence from the triplet states of the materials, a series of careful photoluminescence experiments was performed using a spectrometer equipped with a liquid nitrogen cooled InGaAs detector. Emission scans over the wavelength range of 0.85 – 1.5 μm were carried out with the samples in solution and solvent glass at room temperature and at 80 K, respectively. Unfortunately, in all cases no detectable phosphorescence emission could be observed. This result is consistent with the previous report of Wong and co-workers who also reported the absence of phosphorescence from **P1** in the near-infrared region.¹⁹⁴

Despite the inability to observe phosphorescence emission, clear evidence for the production of triplet states upon direct excitation of all of the materials was obtained by ns - μs time-resolved absorption spectroscopy. Specifically, as shown in Figure 3-9, following a 550 nm pulsed laser excitation degassed dichlorobenzene solutions of **M-1** and **P1** exhibit relatively strong transient absorption signals throughout the 350 – 800 nm region. The spectra are characterized by broad absorption over the entire visible region, peaking at ~700 nm, with negative (bleaching) bands that correspond to the ground state absorption of the BTD-Th

chromophore. For both materials the transient species giving rise to the absorption decays with $\tau \sim 1 - 2 \mu\text{s}$ and is consistent with assignment of the spectrum to the absorption of the triplet excited state. Close comparison of the spectra in Figure 3-9 shows that the transient absorption (ΔOD) is approximately 3 times larger for the model complex compared to the polymer. Given that the spectra were obtained on solutions having matched absorption (concentration) and the same laser power, this difference (although qualitative) suggests that the triplet yield is larger for the model complex compared to the polymer. Interestingly, this difference is consistent with the fluorescence yield and lifetimes, which indicate that the singlet state is quenched in the polymers. Apparently singlet quenching in the polymers leads to a reduction in the triplet yield. Time resolved absorption on the BTD-EDOT materials produced very similar results; i.e., a triplet state is observed with a lifetime in the microsecond range and the transient absorption is stronger for **M-2** compared to **P2** suggesting a higher triplet yield in the former. Moving to a lower bandgap **P3**, the lifetime measured from transient absorption experiments are in the range of tenths of microseconds.

Photoinduced electron transfer (PET) and charge separation is a key step in the mechanism by which photovoltaic cells convert optical energy to electrical power.^{159,162} As noted above, in a previous study we confirmed that the triplet state of a platinum acetylide polymer was active in photoinduced electron transfer by demonstrating that PC₆₁BM quenches the phosphorescence and, more importantly, by observing the products of PET via the time-resolved absorption spectroscopy.¹⁷³ Similar studies were conducted in the present investigation in order to probe the involvement of the triplet state in PET. Thus, transient absorption experiments were conducted with the platinum acetylide model complexes and the polymers in the presence of PC₆₁BM (conc. = 1 mM) in dichlorobenzene solution. These experiments showed that in every case

PC_{61}BM does not quench the triplet state, and ion radicals resulting from charge separation were not observed. These results conclusively demonstrate that for the BTD-Th and BTD-EDOT materials the triplet is not involved in charge separation. With even lower energy gap and low-lying LUMO levels, the triplet excited states on **P3** can not be quenched by PC_{61}BM . As a matter of fact, the triplet excited states are lower than the lowest lying LUMO of PC_{61}BM .

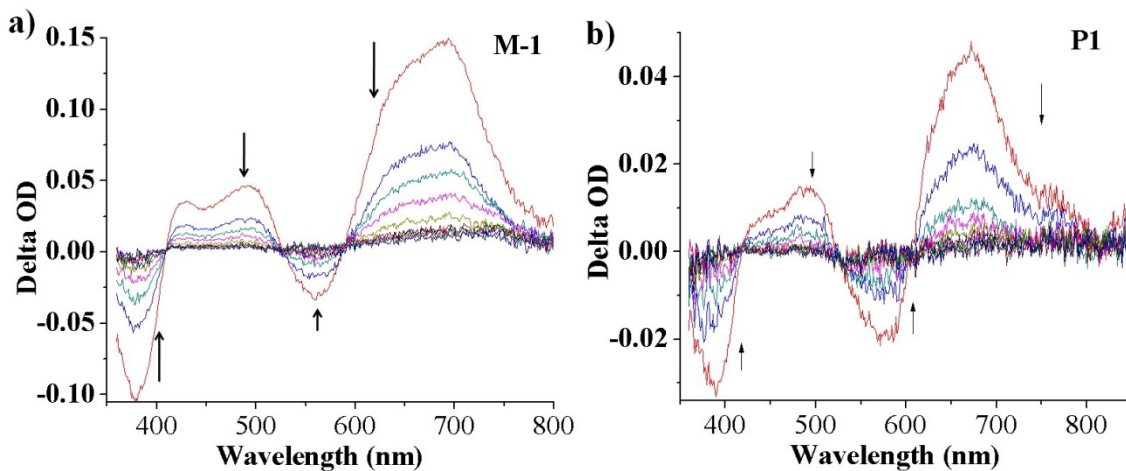


Figure 3-9. Transient absorption difference spectra of a) M-1 and b) P1. Excited at 550 nm with 5 ns pulses. Spectra obtained with an initial 60 ns delay and with succeeding 1 μs delay increments. Arrows indicate the direction of change of spectra with increasing delay time.

With the above results in hand, we turned to experiments designed to probe whether PC_{61}BM interacts with the singlet state. For each of the materials tested, addition of PC_{61}BM to dichlorobenzene solutions of the models (or polymers) was observed to quench the fluorescence efficiently. For example, Figure 3-10 shows the fluorescence spectrum of **M-1** in dichlorobenzene with PC_{61}BM added over the concentration range 0 – 2 mM. The inset illustrates the Stern-Volmer quenching plot, which is linear and affords a Stern-Volmer quenching constant $K_{\text{SV}} = 2.0 \times 10^3 \text{ M}^{-1}$. Given the relatively short fluorescence lifetime, the large K_{SV} value suggests that static quenching may be the dominant quenching pathway. In parallel quenching experiments it was observed that PC_{61}BM does not quench the lifetime of **M-1**.

1, a result which confirms that static quenching occurs. Taken together, the fluorescence quenching results suggest that addition of PC₆₁BM to **M-1** results in the formation of a ground state association complex.²⁰³⁻²⁰⁴ Similar results were obtained when quenching experiments were carried out using **M-2**, indicating that in this case as well, PET to PC₆₁BM only occurs from the singlet state, and that a ground state association complex is produced between the complex and PC₆₁BM in solution.

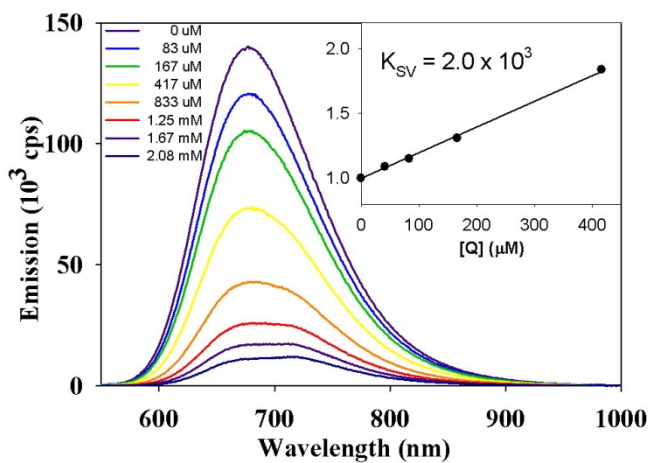


Figure 3-10. Fluorescence emission quenching of M-1 by PC₆₁BM. The legend shows the concentration of PC₆₁BM in solution, and the plot in the inset shows the Stern-Volmer plot of I^0/I vs. [PC₆₁BM].

The absorption and emission data for **M3**, **M4**, **M5**, **P3** and **P4** are summarized in Table 3-2. The model complexes and the polymers have very similar photophysical properties with all compounds having two band absorptions with maxima around 400 and 800 nm. Similarly, all exhibit a broad emission band in the near-IR region around 1010 nm. From the comparison of **M3**, **M4**, **M5** and **P3**, it is clear that electron delocalization does not extend beyond each repeat unit. In contrast, **P4** presents a three-band absorption pattern, as shown in Figure 3-11. Its absorption curve appears to be the sum of **P1** and **P3** suggesting the above-mentioned argument that the conjugation is limited within the each repeat unit.

Table 3-2. Photophysical properties of M3, M4, M5, P3, and P4 in ODCB

| Material | $\lambda_{\text{max}}/\text{nm}$ | $\epsilon/\text{cm}^{-1}\text{M}^{-1}$ | $\lambda_{\text{em}}/\text{nm}$ |
|-----------------|----------------------------------|--|---------------------------------|
| M3 | 396 | 56,100 | 1010 |
| | 797 | | |
| M4 | 401 | 110,300 | 1010 |
| | 799 | | |
| M5 | 403 | 157,000 | 1010 |
| | 800 | | |
| P3 | 405 | 46,900 | 1010 |
| | 800 | | |
| P4 | 398 | 74,900 | ~1010 |
| | 757 | | |

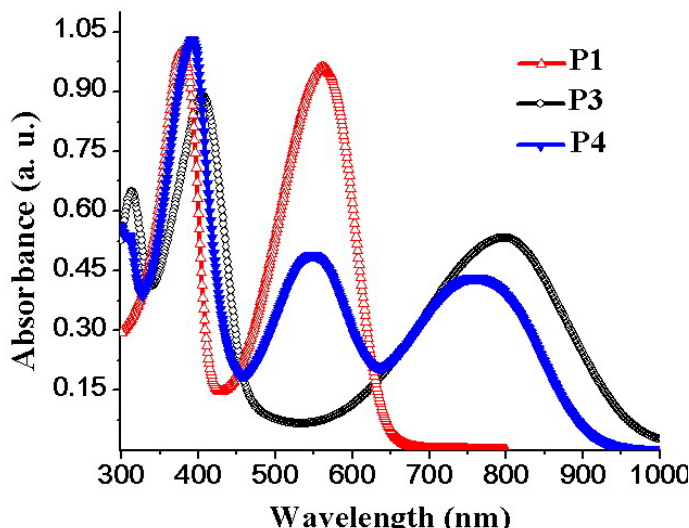


Figure 3-11. UV-vis absorption spectra of P1, P3, and P4.

3.4.2 Electrochemical Studies

Cyclic voltammetry (CV) and differential pulse voltammetry (DPV) were performed in order to characterize the accessible redox states of the compounds and to obtain the oxidation and reduction potentials for the redox processes. When combined with the photophysical data (*vide infra*) the electrochemical potentials can be used to estimate the driving force for photoinduced electron transfer from the polymers to PC₆₁BM. A summary of the electrochemical data is provided in Table 3-3 and representative cyclic voltammograms of **M-1** and **P1** are shown in Figure 3-12. The cyclic voltammograms of **M-2** and **P2** are shown in Figure

3-12. Figure 3-12 reveals that all of the materials exhibit a single, reversible reduction at negative potentials and two reversible oxidation waves at positive potentials. As outlined below, all of the waves can be attributed to oxidation/reduction of electrophores concentrated on the π -conjugated segments that contain the three heterocyclic rings. In particular, the reduction waves occur at *ca.* $E_{1/2} = -1.75$ V (-1.85 V for the EDOT series), which corresponds very closely to the reduction potentials previously reported for the “free oligomers” (*i.e.* Th-BTD-Th and EDOT-BTD-EDOT).²⁰⁵⁻²⁰⁶ The reduction potentials for the free oligomers Th-BTD-Th and EDOT-BTD-EDOT are *ca.* $E_{1/2} = -1.55$ V and -1.73 V, respectively, in V vs. Fc/Fc^+ . Note that the reduction of the BTD-Th materials occurs at a potential approximately 100 mV less negative compared to that for the BTD-EDOT materials. This difference reflects the influence of the EDOT donor moiety, which slightly raises the energy of the LUMO level in the BTD-EDOT system relative to its position in the BTD-Th system.

As shown in Figure 3-12, the platinum acetylide oligomers and polymers also exhibit two oxidation waves that occur at potentials moderately anodic relative to Fc/Fc^+ . The two waves are reversible for the oligomers, whereas they are much less well-defined for the polymers. Like the reductions, the oxidations arise from electrophores concentrated on the π -conjugated organic segments. This assignment is supported by the fact that the first oxidation potentials for the oligomers and polymers correspond closely with those of the corresponding free oligomers.²⁰⁵⁻²⁰⁶ Importantly, the potential for the first oxidation waves for the BTD-Th materials are shifted positive by approximately 300 mV relative to those for the BTD-EDOT materials. This trend reflects the stronger donor nature of the EDOT moieties, which leads to a substantial increase in the energy of the HOMO level in the BTD-EDOT materials and allows these compounds to be more easily oxidized.

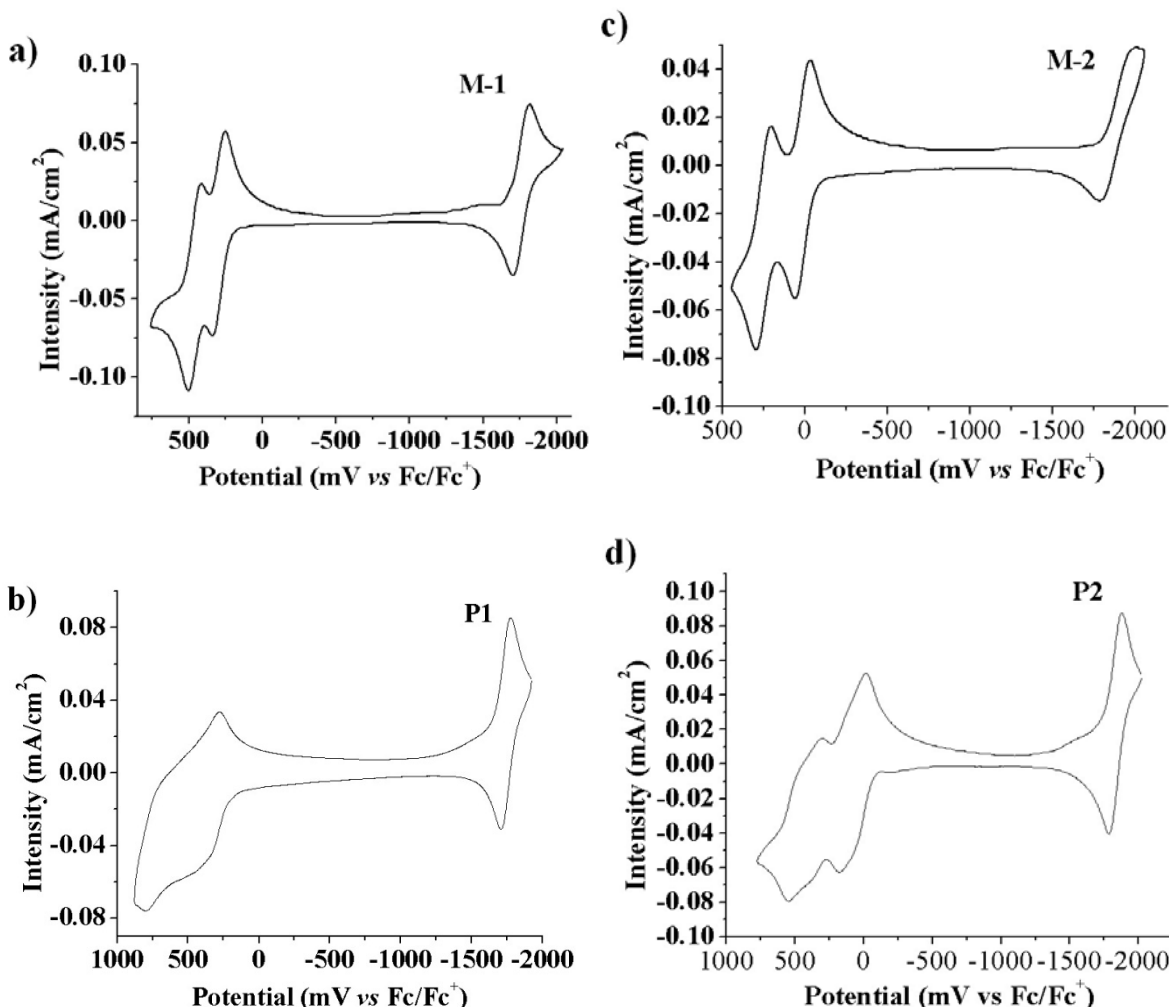


Figure 3-12. Cyclic voltammograms of a) M-1, b) P1, c) M2, and d) P2 in CH_2Cl_2 with 0.1 M TBAPF₆ as supporting electrolytes, scanned at 100 mV/s. Potentials are referenced to Fc/Fc⁺ as an internal standard.

The oxidation and reduction potentials of the oligomers and polymers were used to calculate the electrochemical HOMO-LUMO gap (E_g) of the materials and the results are listed in the last column of Table 3-3. As expected, the BTD-EDOT materials exhibit a smaller E_g (~1.8 eV) compared to the BTD-Th materials (~2 eV). This difference reflects the strong donor property of the EDOT moieties, which raises the HOMO levels more than the LUMO levels leading to a decrease in the band gap (relative to the BTD-Th materials). Note that there is only a small difference in E_g between the model compounds and the corresponding polymers. This

result indicates that the HOMO and LUMO are concentrated on a single chromophore segment (e.g., Th-BTD-Th or EDOT-BTD-EDOT) rather than being delocalized over several repeat units. These E_g values agree very closely with optical E_g values obtained by spectroscopic methods (*vide infra*). In addition to electrochemical characterization of these compounds, reduction potentials of PC₆₁BM were measured under the same conditions. The first and second reduction potentials were found to be -1.10 V and -1.48 V respectively. **P3** and its corresponding model complexes have a much lower lying LUMO, around -1.3 eV, due to the stronger electron-accepting ability of [1,2,5]thiadiazolo[3,4-g]quinoxaline. The low lying LUMO accordingly lowers its energy gap to 1.45 eV. Interestingly, all three model complexes have almost the same energy gap, even though their HOMO and LUMO levels are different.

Table 3-3. Electrochemical properties of model compounds and polymers

| Compound | Red ₁ | E _{1/2} /V Ox ₁ | Ox ₂ | Δ E _g /eV ^b |
|------------|------------------|--|--------------------|-----------------------------------|
| M-1 | -1.76 | +0.30 | +0.46 | 2.03 |
| P1 | -1.74 | +0.29 ^c | +0.73 ^c | 2.02 |
| M-2 | -1.89 | +0.01 | +0.25 | 1.89 |
| P2 | -1.85 | +0.01 ^c | +0.41 ^c | 1.84 |
| M-3 | -1.21 | +0.20 | +0.42 | 1.44 |
| M-4 | -1.28 | +0.16 | +0.40 | 1.44 |
| M-5 | -1.31 | +0.13 | +0.41 | 1.44 |
| P-3 | -1.27 | +0.13 | +0.41 | 1.40 |
| P-4 | -1.35 | +0.10 | +0.32 | 1.45 |

^a Measured in CH₂Cl₂ with 0.1 M TBAPF₆ as the supporting electrolyte using a 100 mV/s scan rate and referenced to Fc/Fc⁺ as an internal standard. ^b Electrochemical gap determined by taking the difference between the first oxidation potential and the reduction potential of the species. ^c E⁰ determined by DPV.

3.5 Solar Cells

3.5.1 Optical Properties and Hole Mobility of Polymer Films

Since the main focus of this project was on examining the performance of the organometallic polymers in bulk heterojunction solar cells, experiments were also carried out to

characterize the optical and charge carrier mobility properties of the polymers as spin-coated films. For these experiments, neat polymer films were spin-cast on borosilicate glass and polymer/PC₆₁BM blend films were cast onto PEDOT-PSS coated ITO substrates. First, experiments were carried out to determine the absorption coefficient of **P1** films as an example. In these experiments, a series of four films of different thickness were fabricated and the absorption and reflectance spectra of the films were measured. Subsequently, the thickness of the same set of films was determined by atomic force microscopy (AFM). A thin film optical analysis was carried out as described in the Supporting Information, and this analysis provided estimates for the wavelength dependent optical constants for the polymer, as well as the absorption coefficient spectrum. The absorption coefficient spectrum is corrected for reflectance and is consistent across the set of four films. The absorption spectrum of the **P1** film is very similar to that of the material in solution. In particular, two primary bands are observed with $\lambda_{\max} = 383$ and 588 nm. Note that these bands are red-shifted somewhat from their position in THF solution (378 and 563 nm). Analysis of absorption by the thin films provides absorption coefficient values of $\alpha = 1.4 \times 10^5$ and $1.1 \times 10^5 \text{ cm}^{-1}$ at 383 and 588 nm, respectively. The absorption coefficient at 588 nm corresponds to a value of $\kappa = 0.51$ for the imaginary component of the refractive index. A similar set of thickness dependent absorption experiments was carried out on a set of spin-coated films consisting of 4:1 (w:w) blends of PC₆₁BM and **P1**, and the results indicate that the absorption coefficient of the blend film is ~20% lower than that of the pure polymer, with a value of $\alpha = 2.2 \times 10^4 \text{ cm}^{-1}$ at 576 nm. Using the α value for the blend film we compute a value of $\epsilon = 0.10 \pm 0.02$ at 576 nm. This is slightly lower than the κ value for a 4:1 blend of PC₆₁BM and P1 reported by Wong and co-workers which was determined by spectroscopic ellipsometry ($\kappa \approx 0.14$).¹⁹⁴

In order to characterize the carrier mobility of films consisting of the organometallic polymers, hole mobilities were determined by space charge limited current (SCLC) measurements. In these measurements a device configuration consisting of glass/ITO/PEDOT-PSS/polymer/Au was used, where the polymer is a spin-coated film of one of the organometallic polymers. In these measurements the zero-field hole-mobility of **P1** and **P2** were determined to be $1.4 \pm 0.3 \times 10^{-7}$ and $1.1 \pm 0.2 \times 10^{-8} \text{ cm}^2\text{-V}^{-1}\text{-s}^{-1}$, respectively. Note that the hole mobility in both polymers is comparatively low compared with poly(3-hexylthiophene) which has a mobility of *ca.* $10^{-3} \text{ cm}^2\text{-V}^{-1}\text{-s}^{-1}$.²⁰⁷ Also of note is the fact that the mobility of **P1** is an order of magnitude higher than that of **P2**.¹³⁹ However, it is important to point out that the SCLC model is very sensitive to the thickness of the measured film. Given these extremely low mobilities, it is difficult to determine whether the results actually reflect the properties of the materials or if they are artificially low due to experimental errors.

3.5.2 Solar Cell Studies

The utility of **P1** and **P2** as light absorbing and electron donating materials with electron acceptor PC₆₁BM for photovoltaic cells was investigated. Devices were constructed on PEDOT/PSS coated indium tin oxide (ITO) glass substrates by spin coating blends from toluene or o-dichlorobenzene solutions. Each ITO substrate was masked and etched to allow an array of 4 active photovoltaic pixels each having an area of 0.25 cm^2 . An aluminum electrode was then deposited onto the active layer by thermal evaporation under vacuum. Though typically a thin inter-layer of LiF would also be evaporated, but this resulted in decreased performance. As noted in the results below, cell optimization required careful control of spin coating speed and sample handling. Each entry reported in Table 3-4 is the average of at least 3 different pixels. Note that the entire process of active layer spin-coating and electrode evaporation were carried out in the

inert atmosphere of a glove box, whereas the photovoltaic measurements were obtained with the devices in air and without electrode encapsulation.

As demonstrated by the I-V characteristics of optimized pixels upon AM1.5 irradiation in Figure 3-13, it is evident that **P1** has an enhanced PV performance relative to **P2**. Examination of the data shows that this difference is mainly due to the increased short circuit current (3.4 mA/cm^2 for **P2** relative to $\sim 7\text{ mA/cm}^2$ for **P1**). This is born out in the spectral efficiency results of Figure 3-14 where **P1** shows a peak efficiency of 36% at 570 nm while **P2** shows a broadened response between 500 – 650 nm with an efficiency of $\sim 15\%$. It is interesting that both of these polymers demonstrate photovoltaic activity to wavelengths longer than 700 nm, a desired consequence of using the donor-acceptor-donor triad for long wavelength absorption. The distinct long wavelength peaking of the absorption spectrum and IPCE response for **P1** relative to **P2** is likely due to film quality and scattering from the **P2/PC₆₁BM** film in which aggregation was indicated in the GPC studies.

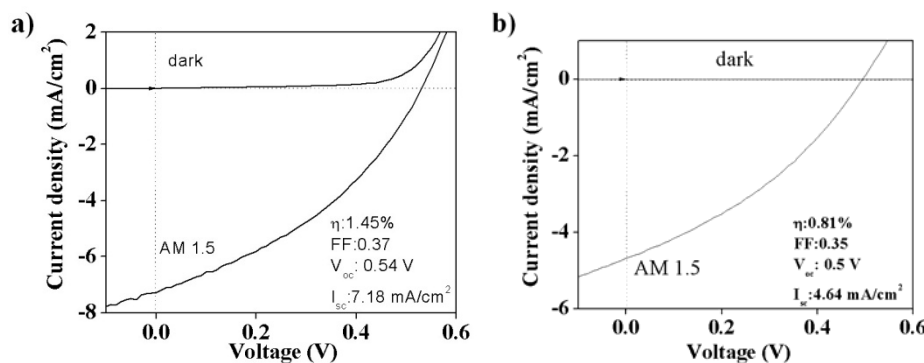


Figure 3-13. I-V characteristic curves of a) P1/PC₆₁BM and b) P2/PC₆₁BM photovoltaic cells under AM 1.5 simulated solar irradiation (100mW·cm⁻²)

A close analysis of the results of Table 3-4 for the **P1/PC₆₁BM** devices indicates how important processing conditions and film quality are with respect to the performance of the resulting photovoltaic devices. Films prepared from both ODCB and toluene could present similarly high AM 1.5 efficiencies of 1.3 to 1.4%. In general, we and others^{165,208-209} find there is

a “sweet spot” in the thickness of the photoactive materials in these devices. With films that are too thin, light absorption is reduced. More importantly in the cells under study here, a drop off in the I_{sc} is observed with an increase in thickness. This is attributed to the relatively low hole mobilities exhibited by these polymers (*vide supra*) making charge collection difficult. Unfortunately, in our studies we utilized a thin film profilometer for thickness measurements and found the absolute values to be somewhat inaccurate. (*Ex-situ* AFM thickness measurements suggest that the profilometer thickness values in Table 3-4 may be underestimated by a factor of ~2). As such, the relative thicknesses showing a doubling in the set of cells studied in Table 3-4 is the best way to compare the results. While the cells’ open circuit voltages are relatively invariant, the I_{sc} and fill factors are distinctly affected. Overall, this work demonstrates that the **P1/PC₆₁BM** system has a strong PV activity; however, importantly in our hands the response of these cells is not nearly as high as reported previously.¹⁹⁴

Table 3-4. I-V characteristics of P1/PC₆₁BM photovoltaic devices

| Solvents ^b | Thickness / nm ^c | Relative thickness ^d | V_{oc} / V | $I_{sc} / mA \cdot cm^{-2}$ | FF | $\eta / \%$ |
|-----------------------|-----------------------------|---------------------------------|--------------|-----------------------------|------|-------------|
| ODCB | 33 | 0.33 | 0.49 | 7.26 | 0.35 | 1.23 |
| | 45 | 0.45 | 0.54 | 7.17 | 0.36 | 1.39 |
| | 52 | 0.52 | 0.49 | 7.41 | 0.31 | 1.13 |
| | 62 | 0.62 | 0.43 | 5.73 | 0.32 | 0.75 |
| | 69 | 0.69 | 0.51 | 4.53 | 0.26 | 0.61 |
| | 99 | 1.00 | 0.46 | 5.10 | 0.29 | 0.67 |
| Toluene | 38 | 0.50 | 0.51 | 4.42 | 0.33 | 0.65 |
| | 50 | 0.66 | 0.59 | 6.49 | 0.34 | 1.28 |
| | 68 | 0.89 | 0.54 | 5.70 | 0.29 | 0.9 |
| | 76 | 1.00 | 0.40 | 4.01 | 0.31 | 0.51 |

a) Average values of 3 pixels. b) Used in spin-coating polymer/PC₆₁BM blends. c) Photoactive layer.
d) Film thickness ratio relative to thickest film in each set.

Examination of the PV cell results for the **P2/PC₆₁BM** system shows distinctly lower AM1.5 efficiencies ranging from 0.2 to 0.8%. These results are not nearly as consistent as the **P1/PC₆₁BM** cells and strongly points to the importance of film quality due to the aggregation

issues in this polymer. **P3** and **P4** have inferior performance to **P1** and **P2**. Considering the smaller energy offsets between LUMO levels of these polymers and PC₆₁BM, low charge separation efficiencies are expected.

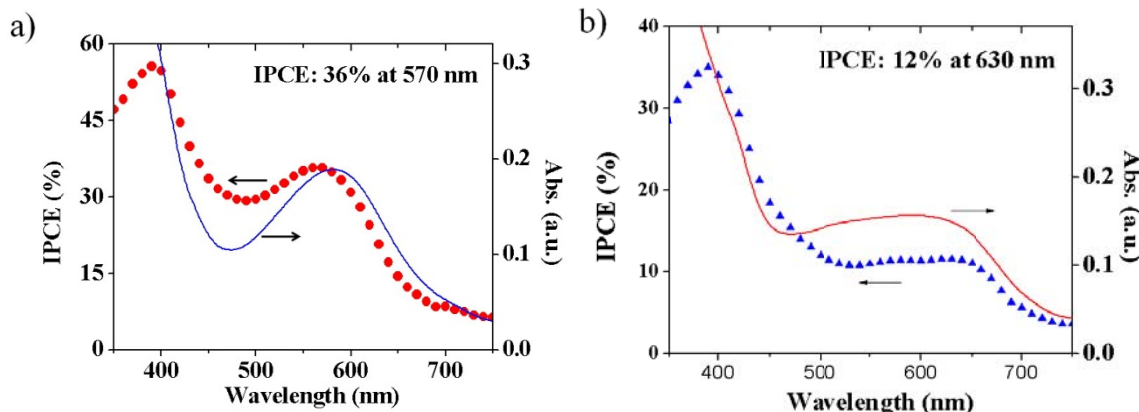


Figure 3-14. External quantum efficiencies and absorption spectra of a) P1/PC₆₁BM blend, and b) P2/PC₆₁BM.

Table 3-5. Summary of *I-V* characteristics of polymer/PC₆₁BM Solar Cells

| Compound | <i>V_{oc}</i> /V | <i>I_{sc}</i> /mA cm ⁻² | FF | h/% |
|-----------------|--------------------------|--|-----------|------------|
| p-PtTh | 0.64 | 0.99 | 0.43 | 0.27 |
| P1 | 0.54 | 7.17 | 0.36 | 1.39 |
| P2 | 0.50 | 4.56 | 0.35 | 0.78 |
| P3 | 0.29 | 0.6 | 0.27 | 0.06 |
| P4 | 0.63 | 1.9 | 0.31 | 0.40 |

* Illumination: AM 1.5, 100 mW cm⁻².

3.7 Mechanism and Energetics of Charge Separation in the Pt-polymer/PC₆₁BM Blends

As noted in the introduction, a key objective of this work is to probe the involvement of the triplet excited state in organometallic photovoltaic materials. However, in order for the triplet excited state to be involved the energetics for photoinduced electron transfer (PET) must be favorable. Thus, in this section we consider the energetics of photoinduced electron transfer from the platinum polymers to PC₆₁BM for both singlet and triplet excited states of the polymers.

The thermodynamic driving force for PET from the singlet or triplet state of a polymer to PC₆₁BM is given by the expression,

$$\Delta G = E_{CS} - E_{es} \quad (3-1)$$

where E_{CS} is the energy of the charge separated state and E_{es} is the energy of the singlet or triplet excited state (all states are referenced to the ground state of the polymer and PC₆₁BM).^{174,210-211}

The first term in this expression (E_{CS}) is given approximately by the difference in the oxidation potential of the donor (**P1** or **P2**) and the reduction potential of PC₆₁BM, i.e., E_{CS} ≈ E_{ox}(polymer) – E_{red}(PC₆₁BM).²¹¹ By using the E_{ox} values for the polymers determined by electrochemistry (Table 3-2) combined with E_{red}(PC₆₁BM) = -1.10 V, the estimated E_{CS} values are 1.39 eV (**P1**/PC₆₁BM) and 1.11 eV (**P2**/PC₆₁BM). For the singlet excited states of the polymers, the second term in Eq. 1 can be determined from the onset of the fluorescence emission band, and these values are 2.07 eV (**P1**) and 1.93 eV (**P2**). Since the lack of phosphorescence emission precluded direct measurement of the polymers' triplet energies, the triplet energy levels are estimated by assuming a singlet-triplet splitting of 0.8 eV,^{180,212-213} affording values of ~1.3 eV (**P1**) and ~1.1 eV (**P2**). Using the estimated values for E_{CS} and E_{es} in Eq. 1, we can now see that for both polymers the PET is exothermic from the singlet excited states, (-0.57 and -0.63 eV for **P1** and **P2**, respectively), whereas PET is weakly endothermic from the triplet states (+0.1 and +0.05 eV for **P1** and **P2**, respectively).

The energetics for the **P1**/PC₆₁BM system is summarized in the Jablonski diagram provided in Figure 3-15. This diagram makes it clear that the energy of the singlet state of the polymer is above that of the charge separate state, and therefore PET is quite exothermic and consequently is anticipated to be rapid. By contrast, since the energy of the triplet state is slightly below that of the charge separated state, PET from the triplet manifold is not expected to

occur to any appreciable extent. (The Jablonski diagram for the **P2**/PC₆₁BM blend is similar, and therefore is not shown.) The energetic considerations outlined here are in direct accord with the experimental observations. In particular, as outlined above, it was observed that in solution PC₆₁BM does not quench the transient absorption arising from the triplet state of either polymer. However, PC₆₁BM does efficiently quench the polymers' fluorescence, which indicates that PET from the singlet state is rapid. We conclude from this that in the active materials of the photovoltaic devices studied in this work, only the singlet state is active in giving rise to charge carriers. Although the triplet excited state of the polymer does not contribute to charge separation, it could influence the efficiency of charge separation indirectly by providing a pathway for direct charge recombination to the lower lying triplet state.²¹⁴⁻²¹⁵

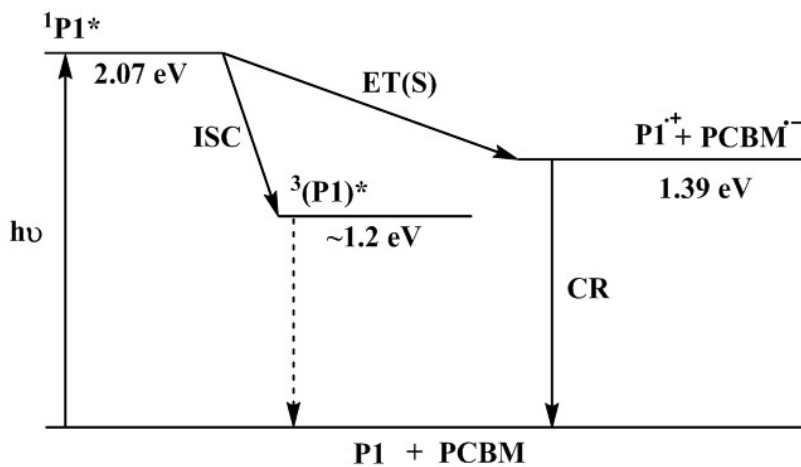


Figure 3-15. Energy level diagram for P1.

The performance of the photovoltaic devices based on **P1** or **P2** blended with PC₆₁BM are summarized in Table 3-5. Significant improvement in efficiency is observed for both devices in comparison to the efficiency of the p-PtTh/PC₆₁BM based device we reported previously.¹⁷³ The improvement in efficiency arises mainly due to a large increase (5~7 fold) in short circuit current density, which results from the considerably enhanced light absorption efficiency by the low-

bandgap **P1** and **P2** materials. This result clearly demonstrates that the strategy to improve the photovoltaic performance via red-shifting the absorption profile of the active polymer was successful.

The second objective of this work was to harness the triplet exciton to generate charge in photovoltaic devices that are based on relatively low bandgap polymers. However, on the basis of the thermodynamic analysis presented above and the solution triplet quenching data, it is evident that even though the triplet state is produced with moderate efficiency in both **P1** and **P2**, due to its low energy the triplet exciton is unable to undergo charge separation (PET with PC₆₁BM). This result points to a significant problem with the concept of harvesting the triplet exciton in photovoltaic devices. Specifically, for materials in which there is limited singlet-triplet mixing, the absorption spectrum is dominated by the spin-allowed transitions from the singlet ground state to the singlet excited state.²¹⁶ As a result, when considering charge separation from the triplet state, there is a significant loss of energy that occurs following photon absorption but before charge separation occurs. (The energy loss is analogous to the Stokes shift, but it includes losses due to both internal conversion within S₁ and intersystem crossing, S₁ → T₁. The amount of energy that is lost is approximately equivalent to the singlet-triplet splitting energy, which has shown to be a minimum of 0.7 eV in π-conjugated polymers.^{180,212-213} Thus, if the triplet state is to be active in charge generation, the material must have a sufficiently large bandgap to overcome the energy loss associated with the singlet-triplet splitting. Alternatively an acceptor with a less negative reduction potential (lower LUMO) than PCBM must be used as the acceptor. For a π-conjugated material with a HOMO level comparable to **P1**, the bandgap must be above *ca.* 2.1 eV to insure that the triplet exciton is sufficiently energetic to undergo charge separation. An alternative approach to solving this problem would be to use an organometallic

material in which there is a much greater degree of singlet-triplet mixing.²¹⁶ In this case the direct singlet ground state to triplet excited state transition would be sufficiently allowed so that it contributes to the low-energy absorption of the material.

3.6 Conclusion

Two types of platinum acetylide polymers featuring low bandgap donor-acceptor π -conjugated chromophores were synthesized and characterized by electrochemical and photophysical methods. The polymers were also used to construct organometallic photovoltaic devices when blended with PC₆₁BM as an acceptor and electron transporting material. The photovoltaic devices based on the low bandgap polymers display considerably improved performance compared to devices based on blends of a wide bandgap (blue absorbing) platinum acetylide polymer. The results suggest that charge separation in the photovoltaic materials occurs with high internal quantum efficiency, but incomplete light harvesting and low carrier mobility limit the overall photovoltaic performance.

The photophysical studies of the polymers reveal that although a triplet excited state is produced following light absorption, it is too low in energy to undergo photoinduced electron transfer with PC₆₁BM. Studies carried out in solution demonstrate that quenching of the singlet state of the polymers by PC₆₁BM is efficient, and this leads to the conclusion that the photovoltaic response of the solid materials arises due to charge separation from the singlet state of the polymer. The results point to the fact that, in order to harness triplet excitons for charge separation in low bandgap materials, it would be necessary to manipulate the energy levels of either the polymer or the acceptor. For example, decreasing the reduction potential of the acceptor by 0.1 – 0.2 eV would make charge separation with the triplet state of either **P1** or **P2**

energetically favorable.²¹⁷ Alternatively, lowering the oxidation potential of the platinum acetylide polymer without changing the bandgap could accomplish the same goal.

As noted in the introduction, while the project described in the present manuscript was underway, a manuscript was published reporting that photovoltaic devices containing **P1/PC₆₁BM** blends as the active layer exhibit a peak IPCE of 87% at 580 nm and an overall AM1.5 power conversion efficiency in excess of 4.9%.¹⁹⁴ While these results are significant and interesting, in the course of our work with the same active materials we have been unable to attain comparably high photovoltaic device efficiencies. Specifically, as can be seen in Tables 3-3, optimization of processing conditions and active layer thickness affords **P1/PC₆₁BM** based devices that exhibit peak IPCE of 36 % and overall AM1.5 power conversion efficiency of 1.39%.

Careful consideration of the available optical data suggests that the results reported herein for the **P1/PC₆₁BM** devices are in accord with expectation given the intrinsic limitations of active layer film thickness and light harvesting efficiency. In particular, consideration of the absorption coefficient for the **P1/PC₆₁BM** blend films ($\alpha = 1.2 \times 10^4 \text{ cm}^{-1}$ for the 1:4 P1/PC61BM blend) suggests that the active layer film thickness would need to be $> 200 \text{ nm}$ in order for a device to operate with an IPCE of $> 85\%$ at 580 nm.²¹⁸ Although the measurements of the film thicknesses for the active layers in the photovoltaic devices reported herein are believed to underestimate the film thickness, the external quantum yields and power conversion efficiencies that we have measured are consistent with devices that operate with a high internal quantum efficiency, but are limited in overall performance due to incomplete light absorption by the active material. More specifically, the results are consistent with the expected performance of devices with active layers in the range of 75 – 125 nm that have high internal quantum efficiency

but absorb only 30 - 40% of the incident light in the 550 – 600 nm region. While it may be coincidental, it is very interesting to note that the performance reported herein for the **P1**/PC₆₁BM devices is in very good agreement with the optical modeling results reported by Janssen and co-workers.¹⁹⁶⁻¹⁹⁷ Furthermore, in a very recent manuscript, Jen and co-workers report that an optimized device containing a 4:1 blend of **P1**/PC₆₁BM as the active layer exhibited an AM1.5 power conversion efficiency of 1.32% with a short circuit current of 4.2 mA·cm⁻².²¹⁹ These values are in good agreement with the findings reported herein, supporting the suggestion that the performance of the **P1**/PC₆₁BM devices is limited by incomplete light absorption by the active layer and by the low hole mobility which in turn limits the efficiency of cells with a thicker active layer.

3.7 Experimental Details

4,7-dibromobenzo[c][1,2,5]thiadiazole (3-1): benzo[c][1,2,5]thiadiazole (27 g, 198 mmol) was dissolved in 300 mL of HBr (47%). Then, a solution of Br₂ (30 ml, 592 mmol) dissolved in 300 mL of HBr (47%) was added dropwise. After complete addition of the Br₂ the solution was refluxed at 100-110 °C overnight. After the mixture was cooled down to room temperature, a saturated aqueous solution of Na₂S₂O₃ was added to completely consume the excess Br₂. The precipitates were collected by suction filtration and washed with water, acetone, and ether. The product was purified by recrystallization from THF to yield white crystals (52.4g, 90 %). ¹H NMR (300 MHz, CDCl₃, δ): 7.71 (s, 2H), ¹³C NMR (75 MHz, CDCl₃, δ): 152.81, 132.17, 113.64.

4,7-di(thiophen-2-yl)benzo[c][1,2,5]thiadiazole (3-2): 4, 7-dibromo-2, 1, 3-benzothiadiazole (**2**) (2.94 g, 10.0 mmol), tributyl(2-thienyl)stannane (8.20 g, 22 mmol) and PdCl₂(PPh₃)₂ (140 mg, 2 mol%) were added to Schlenk flask (100 ml) charged with DMF (50

ml). The mixture was, after three freeze-pump-thaw cycles, heated to 85 °C under argon overnight. After the mixture was cooled to room temperature, aqueous potassium fluoride was added. The solid was filtered and the filtrate was extracted with CH₂Cl₂ (3 x 50 mL). The combined organic phases were washed with brine, dried over MgSO₄, and solvent removed under reduced pressure. The residue was purified by column chromatography on silica gel eluting with CH₂Cl₂–hexane, 1 : 1. The product was obtained as an orange-red solid after removal of solvent (1.75 g, 59 %).

4,7-bis(5-bromothiophen-2-yl)benzo[c][1,2,5]thiadiazole (3-3): To a 100 mL flask charged with compound **3** (1.50 g, 5.0 mmol) in CHCl₃ (25 mL), N-iodosuccinimide (NIS, 1.92g, 10.8 mmol) was added under a stream of argon. A catalytic amount acetic acid (0.2 ml) was injected through the septum. The resulting mixture was stirred at room temperature overnight. The dark red precipitate formed was collected by suction filtration, washed with water, methanol, and chloroform. The product was isolated as dark, red crystals after recrystallization from chloroform (2.05 g, 89.6 %).

4,7-bis(5-((trimethylsilyl)ethynyl)thiophen-2-yl)benzo[c][1,2,5]thiadiazole (3-4): To a 100 mL Schlenk tube, piperidine-THF (v:v, 1:4, 50 ml) co-solvent was added and degassed for 30 min. by bubbling argon. Compound **4** (2.29g, 5 mmol), Pd(PPh₃)₂Cl₂ (70 mg, 0.05 mmol) and CuI (38 mg, 0.2 mmol) were added subsequently under argon. Trimethylsilylacetylene (1.23 g, 12.5 mmol) was injected through the septum and the reaction refluxed overnight. Upon cooling to room temperature the solvent was removed under reduced pressure and the residue was purified by flash chromatography on silica gel eluting with CH₂Cl₂ and hexane (1:9, silica gel), 2.26 g obtained (91.8 %). ¹H-NMR (300 MHz, CDCl₃): 7.96 (d, J = 4 Hz, 2H), 7.85 (s, 2H), 7.30 (d, J = 4 Hz, 2H), 0.275 (s, 18H); ¹³C-NMR (75 MHz, CDCl₃): 152.4, 140.4, 133.4, 127.1, 125.6,

124.7, 101.1, 97.6, 77.2, 0.15; HRMS (ESI) Calculated for $C_{24}H_{25}N_2S_3Si_2$ ($M + H^+$): m/z 493.0712. Found: m/z 493.0724.

4,7-bis(5-ethynylthiophen-2-yl)benzo[c][1,2,5]thiadiazole (3-5): Compound **5** (1.24g, 2.5 mmol) was dissolved into methanol and THF (volume?). KOH (560 mg., 10 mmol) aqueous solution was then added. The resulting mixture was stirred under room temperature and monitored by TLC. After compound **5** was consumed, the solvent was removed under vacuum. Deionized water (10 mL) was added followed by extraction with CH_2Cl_2 (3 x 10 mL). The combined organic phases were washed with brine and dried over $MgSO_4$. Removal of the solvent gave the desired product as a red solid (845 mg, 97 %). 1H -NMR (300 MHz, $CDCl_3$): 7.98 (d, $J = 4$ Hz, 2H), 7.87 (s, 2H), 7.36 (d, $J = 4$ Hz, 2H), 3.49 (s, 2H); ^{13}C -NMR (75 MHz, $CDCl_3$): 152.3, 140.6, 133.9, 127.1, 125.7, 125.6, 123.5, 83.1, 77.2; HRMS (ESI) Calculated for $C_{18}H_9N_2S_3$ ($M + H^+$): m/z 348.9922. Found: m/z 349.9944.

4,7-bis(2,3-dihydrothieno[3,4-b][1,4]dioxin-5-yl)benzo[c][1,2,5]thiadiazole: To a solution of compound **4** (1.47 g, 5 mmol) and compound **5** (4.27 g, 14 mmol) in DMF (50 mL), $PdCl_2$ (35 mg, 2 mol %), [tBu_3PH]BF₄ (116 mg, 4 mol %), CuI (10 mol %, 95 mg) and CsF (10 mmol, 1.50 g) were added. The resulting mixture was refluxed overnight under argon. After the mixture was cooled to room temperature, deionized water (400 mL) was added. The product was then extracted by CH_2Cl_2 (3 x 200 mL). The combined organic phases was subsequently passed through a pad of celite, washed with brine and dried over $MgSO_4$. The solvent was concentrated under reduced pressure to afford a dark red solid. The solid was collected by suction filtration and washed with hexane to give the title compound in high purity (1.54 g, 74 %). 1H -NMR (300 MHz, $CDCl_3$): 8.39 (s, 2H), 6.65 (s, 2H), 4.31-4.40 (m, 8H); HRMS (ESI) Calculated for $C_{18}H_{12}N_2O_4S_3Na$ ($M + Na^+$): m/z 438.9953. Found: m/z 438.9937.

4,7-bis(7-bromo-2,3-dihydrothieno[3,4-b][1,4]dioxin-5-yl)benzo[c][1,2,5]thiadiazole:

To a 100 mL flask charged with compound **6** (1.67 g, 4.0 mmol) in CHCl₃ (350 mL), N-iodosuccinimide (NIS, 1.80 g, 10 mmol) was added. A catalytic amount acetic acid (0.2 mL) was added. The resulting mixture was stirred under room temperature for 2 days. The precipitate formed was collected by suction filtration and washed with water, methanol, and chloroform. The desired product was obtained as a dark purple solid (2.10 g, 91 %). ¹H-NMR (300 MHz, C₂D₂Cl₄, 80 °C): 4.38-4.46 (m, 8H); HRMS (CI) Calculated for C₁₈H₁₀Br₂N₂O₄S₃ (M⁺): *m/z* 571.8164. Found: *m/z* 571.8218.

4,7-bis(7-((trimethylsilyl)ethynyl)-2,3-dihydrothieno[3,4-b][1,4]dioxin-5-yl)benzo[c][1,2,5]thiadiazole (3-6) To a 100 mL Schlenk tube, piperidine-THF (v : v = 1:5, 60 mL) was added and degassed for 30 min. Compound **7** (1148 mg, 2 mmol), Pd(PPh₃)₂Cl₂ (112 mg, 0.16 mmol, 4 mol %) and CuI (76 mg, 0.4 mmol, 10 mol %) were added subsequently under argon. Trimethylsilylacetylene (588 mg, 6 mmol) was injected through the septum. The resulting mixture was refluxed overnight. Upon cooling to room temperature the solvent was removed under reduced pressure and the residue was subjected to flash chromatography on silica eluting with CH₂Cl₂ and hexane (1:9). After removal of solvent, the desired product was obtained as purple solid (766 mg, 63%). ¹H-NMR (300 MHz, C₆D₆): 8.50 (s, 2H), 3.40-3.36 (m, 8H), 0.23 (s, 18H); ¹³C-NMR (75 MHz, C₆D₆): 152.4, 145.2, 139.9, 126.8, 124.1, 115.6, 103.9, 101.9, 96.7, 64.4, 64.0, 0.03. HRMS (ESI) Calculated for C₂₈H₂₉N₂O₄S₃Si₂Na (M + Na⁺): *m/z* 632.0720. Found: *m/z* 632.0742.

P1: Compound **1** (0.20 mmol, 69.6 mg), *trans*-Pt(PBu₃)₂Cl₂ (0.20 mmol, 134.1 mg) and CuI (1.0 mg) were added to a Schlenk flask. The reaction flask was evacuated and backfilled with argon three times followed by addition of piperidine-toluene (v:v = 1:1, 8 mL), which was

injected through the septum. The mixture was stirred at room temperature for 24 h and then passed through a bed of neutral alumina to remove catalysts. The solvent was removed under reduced pressure. The dark-purple solid (film) was redissolved into a minimum amount of CHCl₃ and the solution poured into cold methanol. The precipitate was collected and the precipitation repeated three times. A fibrous purple product (144 mg, 73%) was obtained after the final precipitation. Further purification was effected through Soxhlet extraction by methanol, hexane, and CHCl₃. ¹H-NMR (300 MHz, C₆D₆): 8.11 (d, J = 4 Hz, 2H), 7.40 (s, 2H), 7.27 (d, J = 4 Hz, 2H), 2.20-2.24 (m, 12H), 1.74-1.77 (m, 12H), 1.47-1.59 (m, 12H), 1.03 (t, J = 7.5 Hz, 18H); ³¹P-NMR (121 MHz, C₆D₆): 5.11 (J_{Pt-P} = 2336 Hz). GPC: M_n = 22, 000 g/mol, PDI = 1.9. FT-IR (KBr): 2955, 2871, 2884, 2084, 1481, 1440, 801 and 667 cm⁻¹.

M1: To a 100 mL Schlenk flask, compound **3** (0.1 mmol, 34.8 mg) and *trans*-ethynylphenylchlorobis(*tri-n*-butylphosphine)platinum(II) (0.2 mmol, 147.3 mg) were added. The reaction flask was evacuated and backfilled with argon three times followed by addition of degassed piperidine-toluene (v:v = 1:1, 10 mL), which was injected through a septum. The resulting mixture was stirred under mild reflux overnight. Upon cooling to room temperature, silica gel was added to the purple solution, and the solvent was evaporated. The product was purified by column chromatography using ethyl acetate/hexane (5/95) as the eluent. The desired product **M-1** was obtained in 87 % yield after drying (143.9 mg). ¹H-NMR (300 MHz, C₆D₆): 8.09 (d, J = 4 Hz, 2H), 7.63 (d, J = 8 Hz, 4H), 7.37 (s, 2H), 7.24 (d, J = 4 Hz, 2H), 7.17 (m, 4H), 7.01 (t, J = 7.5 Hz, 2H), 2.12-2.19 (m, 24H), 1.64-1.77 (m, 24H), 1.39-1.51 (m, 24H), 0.94 (t, J = 7.5 Hz, 18H); ¹³C-NMR (75 MHz, C₆D₆): 152.9, 136.7, 132.2, 131.1, 129.9, 128.5, 128.4, 125.7, 125.3, 124.8, 119.0 (t), 110.1, 108.2 (t), 102.5, 26.9 (m) 24.8 (m), 24.5, 14.0 (due to superimposition, one carbon is missing); ³¹P-NMR (121 MHz, C₆D₆): 4.93 (J_{Pt-P} = 2356 Hz).

HRMS (MALDI-TOF, terthiophene as matrix) calculated for C₈₂H₁₂₂N₂P₄S₃Pt₂: *m/z* 1744.7010.

Found: *m/z* 1744.7170.

P2: Compound **2** (0.2 mmol, 122 mg) and *trans*-Pt(PBu₃)₂Cl₂ (0.2 mmol, 134 mg) were added to a Schlenk flask with magnetic stir bar. After degassing, piperidine-toluene (v:v = 1:2, 15 mL) was injected through the septum at 0 °C followed by a solution of teterabutylammonium fluoride (TBAF) (0.5 mmol, 1 M in THF). The color of the resulting solution turned from red to blue and the mixture was stirred for 24 h at room temperature. After removing the solvent under reduced pressure, the blue solid (film) was dissolved into CHCl₃ and passed through a bed of alumina. The filtrate was concentrated and precipitated from methanol. A blue solid was obtained (177 mg, 83%). Further purification was effected through Soxhlet extraction by methanol, hexane, and CHCl₃. ¹H-NMR (300 MHz, C₆D₆): 8.68 (s, 2H), 3.57-3.52 (m, 8H), 2.34-2.30 (m, 12H), 1.81-1.78 (m, 12H), 1.64-1.54 (m, 12H), 1.00 (t, J = 7.2 Hz, 18H); ³¹P-NMR (121 MHz, C₆D₆): 4.20 (J = 2365 Hz). M_n = 33,000 g/mol, PDI = 16.

M-2: To a 100 mL Schlenk flask, compound **8** (30.5 mg, 0.05 mmol) and *trans*-ethynylphenylchlorobis(tri-*n*-butylphosphine)platinum(II) (0.1 mmol, 73.6 mg) and CuI (19 mg) were added. After degassing, piperidine-toluene (v:v = 1:1, 10 ml) was injected through the septum. Upon addition of TBAF (0.2 mL, 1 M in THF), the solution turned from red to purple-blue and the resulting mixture was stirred under ambient temperature overnight. The solvent was evaporated under reduced pressure and the product purified by column chromatography on silica using hexane:ethyl acetate (3:1) as the eluent. The desired product **M-2** was obtained in 74 % yield (69.5 mg). ¹H-NMR (300 MHz, C₆D₆): 8.67 (s, 2H), 7.63(d, J = 7.6 Hz, 4H), 7.19 (m, 4H), 7.17 (t, J = 7.0, 2H), 3.51-3.48 (m, 8H), 2.23-2.15 (m, 24H), 1.70-1.64 (m, 24H), 1.54-1.42 (m, 24H), 0.95 (t, J = 1 Hz, 36H); ¹³C-NMR (75 MHz, C₆D₆): 153.0, 141.4, 140.5, 131.2, 130.1,

126.1, 125.2, 124.0, 121.2 (t, J = 14.7 Hz), 111.5, 110.4, 109.1, 109.1, 108.9 (t, J = 14.7 Hz), 99.8 (t, J = 1.8 Hz), 64.6, 64.0, 26.9 (m) 24.7 (m), 24.5 (m), 14.1; ^{31}P -NMR (121 MHz, C_6D_6): 4.48 ($J_{\text{Pt-P}} = 2360$ Hz). HRMS (MALDI-TOF, terthiophene as matrix) calculated for $\text{C}_{86}\text{H}_{128}\text{N}_2\text{O}_4\text{P}_4\text{S}_3\text{Pt}_2$ (M^+): m/z 1863.7292; Found: m/z 1863.7432.

4,7-dibromo-5,6-dinitro-2,1,3-benzothiadiazole (3-7): Compound **1-1** (20 g, 68 mmol) was suspended in conc. sulfuric acid (100 mL) at 0°C. Then fuming nitric acid (100 mL) is added over 3h. The mixture is stirred for an additional 2 h at room temperature before poured into ice water. The precipitate is collected by suction filtration and washed with water. The solid was dissolved in THF (30 mL) and adsorbed on SiO_2 . Column chromatography with a toluene/hexane mixture (1:1) affords a yellowish solid (10.43 g, 39%). HRMS (ESI TOF) m/z calcd. for $\text{C}_6\text{Br}_2\text{N}_4\text{O}_4\text{S}$: 383.7987 (M^+) found 383.7942 (M^+).

5.6-Dinitro-4,7dithien-2yl-2,1,3-benzothiadiazole (3-8): To a solution of 4,7-dibromo-5,6-dinitro-2,1,3-benzothia-diazole (4.05 g, 10.54 mmol) and tibutyl(thien-2-yl)stannane (9.05 g, 24.26 mmol) in THF (40 ml), $\text{Pd}(\text{PPh}_3)_2\text{Cl}_2$ (300 mg, 4 mol %) was added. The mixture was refluxed for 4 h. After cooling to room temperature, a orange red solid appeared, which was collected by suction filtration, washed with hexane and CH_3CN . Column chromatography on silica eluting with CH_2Cl_2 and hexane (1:1) gave a orange red solid (3.14 g, 76 %). Mp: 256 °C – 259 °C; ^1H NMR (300 MHz, CDCl_3 , δ): 7.75 (d, 2H), 7.53 (d, 2H), 7.24 (dd, 2H); HRMS (DIPCI) m/z calcd. for $\text{C}_{14}\text{H}_6\text{N}_4\text{O}_4\text{S}_3$: 389.9551 (M^+) found 389.9426 (M^+); Anal. calcd. for $\text{C}_{14}\text{H}_6\text{N}_4\text{O}_4\text{S}_3$: C 43.07, H 1.55, N 14.35 found C 43.19, H 1.48, N 14.21.

5.6-Diamino-4,7dithien-2yl-2,1,3-benzothiadiazole (3-9): A mixture of 5.6-dinitro-4,7dithien-2yl-2,1,3-benzothiadiazole (3.3 g, 8.45 mmol) and iron dust (5.31 g, 97.1 mmol) in acetic acid is stirred at 45 °C for 5 h. The reaction was poured into 5 % NaOH (300 mL) and

extracted with CH₂Cl₂ (500 mL). The organic layer was dried over MgSO₄ and the residue was purified by column chromatography on silica eluting with CH₂Cl₂ to obtain a bright yellow solid (2.21 g, 79 %). Mp: 240 °C - 245 °C; ¹H NMR (300 MHz, CDCl₃, δ): 7.57 (d, 2H), 7.38 (d, 2H), 7.25 (dd, 2H); ¹³C NMR (75 MHz, CDCl₃, δ): 143.76, 132.32, 128.25, 121.56, 120.34, 120.21, 100.14; HRMS (DIPCI) *m/z* calcd. for C₁₄H₁₀N₄S₃: 301.0101 (M+H)⁺ found 301.0129 (M+H)⁺; Anal. calcd. for C₁₄H₁₀N₄S₃: C 50.88, H 3.05, N 16.95 found C 50.54, H 3.04, N 16.85.

6,7-dihexyl-4,9-di(thiophen-2-yl)-[1,2,5]thiadiazolo[3,4-g]quinoxaline (3-10): 5.6-diamino-4,7-dithien-2-yl-2,1,3-benzothiadiazole (2.08 g, 6.3 mmol) and tetradecane-7,8-dione (1.59 g, 6.9 mmol) in CHCl₃ (100 mL) was stirred at room temperature for 6 h. Upon removal of solvent under reduced pressure, the remaining residue was purified by column chromatography on silica eluting with toluene:hexane (1:1) to obtain a blue violet solid (2.65 g, 80 %). Mp: 114 °C - 115 °C; ¹H NMR (300 MHz, CDCl₃, δ): 8.97 (d, 2H), 7.64 (d, 2H), 7.30 (dd, 2H); ¹³C NMR (75 MHz, CDCl₃, δ): 157.31, 152.67, 151.43, 135.87, 135.1, 132.65, 130.57, 126.54, 35.42, 31.82, 29.31, 27.86, 22.61, 14.12; HRMS (DIPCI) *m/z* calcd. for C₂₈H₃₂N₄S₃: 521.1862 (M+H)⁺ found 521.1852 (M+H)⁺; Anal. calcd. for C₂₈H₃₂N₄S₃: C 64.58, H 6.19, N 10.76, found C 64.51, H 6.21, N 10.57.

4,9-bis(5-iodothiophen-2-yl)-6,7-dihexyl-[1,2,5]thiadiazolo[3,4-g]quinoxaline (3-11). To a 50 mL round flask charged with 6,7-dihexyl-4,9-di(thiophen-2-yl)-[1,2,5]thiadiazolo[3,4-g]quinoxaline (0.63 mmol, 330 mg) in DMF (20 mL), N-iodosuccinimide (1.28 mmol, 312 mg) was added. The resulting mixture was stirred at room temperature for 6 h. The resulting violet precipitate was collected by suction filtration and washed with copious amounts of water and methanol. The solid was then dried under vacuum to give desired product (428 mg, 87 %). Mp: 146 °C - 149 °C; ¹H NMR (300 MHz, CDCl₃): δ 8.64 (d, *J* = 4 Hz, 2H), 7.36 (d, *J* = 4 Hz, 2H),

2.94 (t, $J = 7.5$ Hz, 4H), 1.95-2.03 (m, 4H), 1.40-1.55 (m, 12H), 0.97 (t, $J = 7.5$ Hz, 6H). HRMS (ESI-TOF) Calculated for $C_{28}H_{30}I_2N_4S_3$ ($M + H^+$): m/z 772.9795. Found: m/z 772.9825. Anal. Calcd for $C_{12}H_{10}N_4O$: C, 43.53; H, 3.91; N, 7.27; Found: C, 42.87; H, 3.84; N, 7.25.

6,7-dihexyl-4,9-bis(5-((trimethylsilyl)ethynyl)thiophen-2-yl)-[1,2,5]thiadiazolo[3,4-g]quinoxaline (3-12). To a 25 ml Schlenk tube, iPr_2NH -THF (v : v, 1:5, 15 ml) was added and degassed for 30 min. Compound **2** (298 mg, 0.42 mmol), $Pd(PPh_3)_2Cl_2$ (4 mol %) and CuI (10 mol %) were added subsequently under argon. Trimethylsilylacetylene (96 g, 1 mmol) was injected through the septum. The resulting mixture was stirred overnight at room temperature. The mixture was then concentrated, passed through a short alumina column eluting with ???, and washed with methylene chloride. The product solution was concentrated to minimum volume and the product precipitated into methanol. The desired product, a blue solid, was collected by suction filtration and washed with methanol (230 mg, 84 %). 1H -NMR (300 MHz, C_6D_6 , 7.16 ppm): 8.69 (d, $J = 4$ Hz, 2H), 7.48 (d, $J = 4$ Hz, 2H), 2.83 (m, 4H), 1.93 (m, 4H), 1.40-1.48 (m, 12H), 0.95-1.00 (t, 6H), 0.32 (s, 18H); ^{13}C -NMR (75 MHz, C_6D_6 , 128.39 ppm): 157.4, 150.36, 137.24, 134.32, 132.94, 132.35, 128.03, 119.56, 101.64, 99.12, 35.83, 32.11, 29.72, 27.93, 22.94, 14.41, 0.25.1. HRMS (ESI) Calculated for $C_{38}H_{48}N_4S_3Si_2$ ($M + H^+$): m/z 713.2652. Found: m/z 713.2664. Anal. Calcd for $C_{38}H_{48}N_4S_3Si_2$: C, 64.00; H, 6.78; N, 7.86; Found: C, 63.80; H, 6.66; N, 7.64.

P3: Compound **3** (0.1 mmol, 71.32 mg), trans- $Pt(PBu_3)_2Cl_2$ (0.1 mmol, 67.06 mg) and CuI (0.2 mmol, 19 mg) were added to a Schlenk flask with magnetic stir bar. After evacuation and backfilling with argon three times, Et_3N - CH_2Cl_2 (degassed with argon) was injected through the septum at 0 °C (ice-water bath). TBAT (0.4 mmol, 216 mg) was then added. The mixture was stir for 24 h at room temperature. After removing solvent under reduced pressure, the remaining

green solid (film) was dissolved in CHCl₃ and passed through a short alumina column. The collected solution was concentrated and then precipitated into methanol. A green solid was obtained (77 mg, 66%). Further purification was affected by Soxhlet extraction with methanol, hexane, and CHCl₃. ¹H-NMR (300 MHz, C₆D₆, 7.16 ppm): 8.93 (d, 2H), 7.05 (d, 2H), 3.13-3.15 (m, 4H), 2.55-1.95 (m, 14H), 1.25-1.70 (m, 44H), 1.00-0.75 (m, 24H) ³¹P-NMR (121 MHz, C₆D₆): 4.77 (J = 2894 Hz). M_n = 27 Kda, PDI = 3.5.

CHAPTER 4

VINYLENE-LINKED DONOR-ACCEPTOR POLYMERS FOR PHOTOVOLTAIC APPLICATIONS

4.1 Introduction

As pointed out in Chapter 3, solution-processable π -conjugated polymers have gained considerable interests as active materials in organic optoelectronics, such as organic solar cells (OPVs), light-emitting diodes (OLED), thin-film transistors (OTFTs) and electrochromic devices.²²⁰⁻²²³ Of particular interest has been the study of various PPVs [poly(p-phenylene vinylenes)] and regioregular P3ATs [poly(3-alkyl-thiophenes)] derivatives, which exhibit remarkable optical and electronic properties. PTVs [poly(thienylene vinylene)s], another class of conjugated polymers with a similar structure repeat unit, have also drawn a great deal of attention. A variety of methods have been developed for making thienylene vinylene-based conjugated polymers, including Gilch reaction, acyclic diene metadissertation (ADMET), Witting/Witting-Horner reaction, Stille cross-coupling, Heck reaction, Kumada coupling , as well as TiCl₄/Zn-promoted coupling.²²⁴⁻²²⁶ Unfortunately, it should be emphasized that no versatile synthetic route has been available for making highly regioregular PTVs (with regioregularity higher than 95 %) so far. The highest regio-regularity was around 90 % claimed by McCullough through Stille coupling between 2,5-dibromo-3-dodecylthiophene with (E)-1,2-(bistributylstannylyl)ethylene),²²⁷ which was reported earlier to generate a region-random PTV.

It is now accepted that structural homogeneity of polymer chains plays a crucial role in device performance, particularly in OTFTs and OPVs. This has been well-examined in the case of poly(3-hexyl-thiophene) that regioregular P3HTs have much higher electrical conductivities, more improved charge carrier mobilities and optical responses than their regio-irregular counterparts. The bulk-heterojunction solar cell based on regioregular P3HTs has reached PCEs of 5 %, a milestone in the history of OPVs.¹²⁶ Considering structure resemblance with P3HTs,

P3HTVs with broader absorption are expected to show enhanced solar cell efficiency. In contrast, only less than 1 % efficiency has been obtained for PTVs-based solar cells.²²⁸ So it is very intriguing to design a synthetic route which can lead to PTVs with high structure regularity. It will be not only beneficial for PTVs-based solar cells, but also other PTVs-based organic optoelectronics.

Typical donor-acceptor conjugated polymers are made of electron-deficient nitrogen-containing aromatic heterocycles (2,1,3-benzothiadiazole, [1,2,5]thiadiazolo[3,4-g]quinoxaline, and benzo[1,2-c;3,4-c]bis[1,2,5]-thiadiazole, etc.) as effective acceptors and electron-rich derivatives (thiophene, alkxybenzene, carbazole and fluorene , etc.) as donors.²²⁹⁻²³¹ Vinylene-linked donor-acceptor (VDA) conjugated polymers are low bandgap polymers that have a vinylene linkage between the donor and acceptor groups. An advantage of incorporating these vinylene linkages is that they allow to planarization of the polymer backbone by eliminating torsional interactions between donor and acceptor rings, thus extending conjugation length, which could lead to a decreased bandgap. In addition, the introduction of these vinylene groups into the polymer backbones provides rotational flexibility which partially increases polymer solubility, allowing chromophore concentration to be increased (defined as the molecular weight ratio of conjugated backbone to solubilizing side chains).²³²

Currently, this class of polymers is still largely unexplored, in contrast to the extensive studies of fully heterocyclic donor-acceptor alternating conjugated polymers. This is perhaps, to a great extent, due to the synthetic challenges. The well-established Gilch and Witting-Horner routes to PPVs and PFVs as mentioned above, are not suitable for VDA conjugated polymers,²²⁴⁻²²⁶ since the above mentioned acceptors are usually prone to decompose under strong basic conditions. Stille coupling reaction of dibromoaryl compounds with commercially available (E)-

1,2-bis(tributylstanny)ethene is also used to prepare poly(arylenevinylenes)²³³. However, to install bis(stannylvinyl) functional groups on either a donor or an acceptor is not an easy task. Only a few bis(stannylvinyl)arylene compounds have been reported through hydrostannation.²³⁴ Very recently, a boron-protected haloalkenylboronic acid building block has been reported, which provides a possibility to install a vinylboronic acid functional group.²³⁵ This potential Suzuki polymerization route still has a drawback that vinylboronic acid derivatives are usually unstable.²³⁶ An alternative means to overcome the problem has been reported by preparing PPVs via making bromovinylarylene derivatives,²³⁷⁻²³⁹ However, this method has not been extendable to prepare VDA conjugated polymers. A notable approach in the literature to VDA conjugated polymers is to use Heck polymerization.²⁴⁰⁻²⁴² Unfortunately, the Heck reaction is notoriously known for producing structural α -vinyl cross-coupling defects,²⁴³⁻²⁴⁴ which even in small amount play a detrimental role in organic optoelectronic devices²⁴⁵.

In this chapter, we report our attempts to prepare defect-free PTVs and VDA conjugated polymers via a new strategy using a two-step consequent Heck and Hunsdiecker reaction. Poly(3-hexyl thienylenevinylene) (**P3HTV**) and the vinylene-linked benzothiadiazole-thiophene (**PTVBT**) polymer have been chosen to demonstrate the chemistry. For the purpose of structural elucidation, its model compound **bisTVBT** has also been prepared. Electrochemical studies were performed and photovoltaic cells were fabricated using **PTVBT**. Chemical structures of them are shown in Figure 4-1.

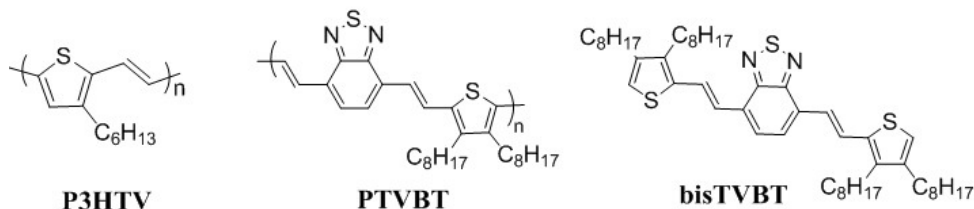


Figure 4-1. Chemical structures of P3HTV, PTVBT and bisTVBT

4.2 Synthesis of P3HTV and PTVBT

The attempted Synthesis of **P3HTV** is outlined in Figure 4-2. Starting from 3-hexylthiophene (**4-1**), 2-bromo-3-hexylthiophene (**4-2**) was obtained in good yields using NBS as a bromination source in DMF. Subsequently, palladium-catalyzed Heck reaction was carried out reacting **4-2** with acrylic acid, yielding (E)-3-(3-hexylthiophen-2-yl)acrylic acid (**4-3**) in 95%. The *trans*-configuration is confirmed by $^1\text{H-NMR}$, showing a large coupling constant of 16 Hz. Conversion of carboxylic acid group into vinyl bromide was successfully achieved using revised Hunsdiecker reaction, giving the (E)-2-(2-bromovinyl)-3-hexylthiophene (**4-4**) in 48%. The attempts to access the proposed monomer ((E)-2-(5-(2-bromovinyl)-4-hexylthiophen-2-yl)-4,4,5,5-tetramethyl-1,3,2-dioxaborolane), however, failed after many trials. The successful preparation of **4-4** has opened the door for the study of vinylene-linked donor-acceptor conjugated polymers.

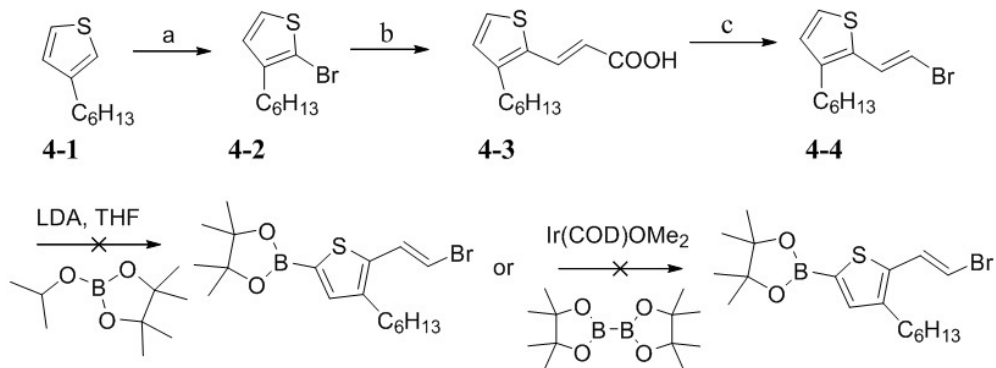


Figure 4-2. Synthesis of regioregular poly(3-hexylthienylenevinylenes) (P3HTV). a) NBS, DMF, 88%; b) acrylic acid, $\text{Pd}(\text{OAc})_2$, $\text{P}(\text{o-tol})_3$, $\text{Et}_3\text{N-CH}_3\text{CN-THF}$, 95%; b) NBS, LiOAc , $\text{CH}_3\text{CN-H}_2\text{O}$, 48%.

The Synthesis of **PTVBT** is shown in Figure 4-3. Kumada reaction of 3, 4-dibromothiophene with 1-bromooctane gave compound **4-6** in 88 % yield, which after Ir-catalyzed borylation afforded compound **4-7** in 81 % yield.²⁴⁶ Compound **4-7** is one the monomer that will be used in polymerization via Suzuki coupling. Heck coupling of 4, 7-

dibromobenzo[c][1,2,5]thiadiazole directly with acrylic acids afforded compound **4-8** in 65 % yield. Compound **4-8** was poorly soluble in most common solvents. Some exceptions are THF, DMF and DMSO. The poor solubility makes it difficult to purify through flash chromatography. Fortunately, its triethylamine salt was soluble in water. Hence the purification of compound **4-8** was readily achieved by forming the triethylamine salt, following by acidification with aqueous HCl. The catalytic Hunsdiecker reaction of compound **4-8** with NBS in the presence of lithium acetate as catalyst afforded compound **4-9** in 64 % yield as light yellow crystals, which appear to be green fluorescent. Low yield or no reaction was noticed when triethylamine or potassium acetate were used instead of lithium acetate. Therefore, it is possible that the small cationic ion size (Li^+) has pronounced effect on the transition state of decarboxylation. In addition, the choice of solvents also played a critical role in this reaction. It turned out that a mixture of acetonitrile and water gave the best results when their volume ratio was around 20 to 25 %, while it was usually around 3 % for other catalytic Hunsdiecker reactions in literature.²⁴⁷ Compound **4-9** was obtained in 71 % overall yield through two steps.

PTVBT was prepared by a Suzuki polycondensation between compound **4-7** and **4-9** in 87 % yield after Soxhlet extraction and precipitation.²⁴⁸ The polymer obtained from the chloroform fraction was soluble in THF, toluene and chlorinated solvents (> 10 mg/mL in chloroform). GPC analysis revealed that **PTVBT** had number-average molecular weights ranging 20,000 to 31,000 Da and polydispersity indices from 1.7 to 2.4 on the base of batch to batch. As a model compound, **bisTVBT** was prepared by a similar synthetic route by Suzuki coupling of compound **4-9** with 2-(3,4-dioctylthiophen-2-yl)-4,4,5,5-tetramethyl-1,3,2-dioxaborolane. In this reaction, a different catalytic system containing $\text{Pd}_2(\text{dba})_3$, [(Bu_3PH) BF_4^-], and CsF is used, showing the versatility of Suzuki coupling.

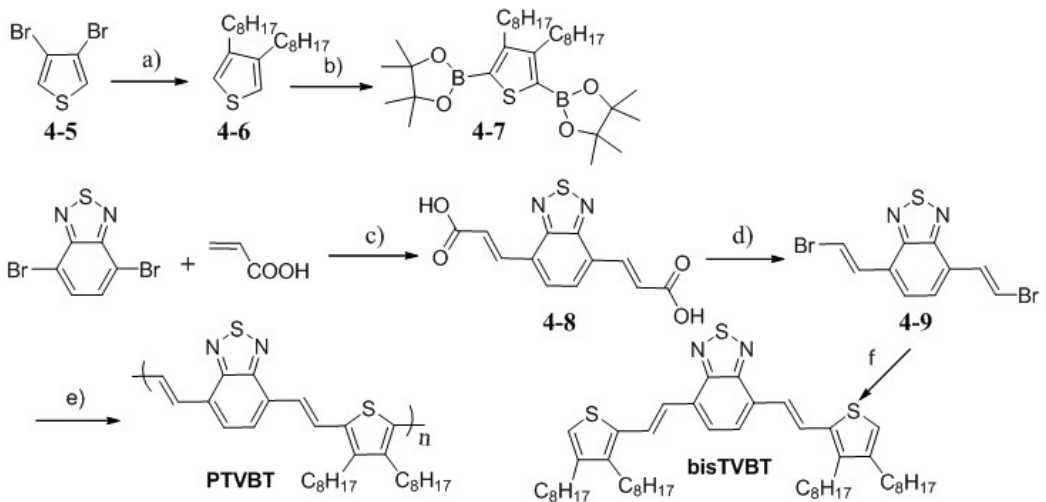


Figure 4-3. Synthesis of PTVBT and bisTVBT. a) 1) $\text{C}_8\text{H}_{17}\text{Br}$, Mg , Et_2O ; 2) $\text{Ni}(\text{dppf})\text{Cl}_2$, Et_2O , reflux, 88%; b) 4,4,4',4',5,5,5',5'-octamethyl-2,2'-bi(1,3,2-dioxaborolane) [$\text{Ir}(\text{OMe})\text{COD}$]₂-dtbpy Heptane, 50 °C, 81%; c) $\text{Pd}(\text{OAc})_2$, $\text{P}(\text{o-tol})_3$, Et_3N , CH_3CN - THF , reflux, 65%; d) NBS , LiOAc , CH_3CN - H_2O , rt, 60%; e) $\text{Pd}_2(\text{dba})_3$, $\text{P}(\text{o-tol})_3$, Et_4NOH , toluene-water, 60 °C, 87%; f) 2-(3,4-di-octylthiophen-2-yl)-4,4,5,5-tetramethyl-1,3,2-dioxaborolane, $\text{Pd}_2(\text{dba})_3$, [($^{\prime}\text{Bu}_3\text{PH}$) BF_4], CsF , THF-water, rt, 86%;

4.3 Structural Characterizations and Optical Studies

The structure of **PTVBT** was confirmed by $^1\text{H-NMR}$, $^{13}\text{C-NMR}$, IR and elemental analysis. The $^1\text{H-NMR}$ of **PTVBT** is here compared with that of **bisTVBT** to illustrate the polymer structure, as shown in Figure 4-4. Model complex **bisTVBT** shows a very clear splitting pattern. Two doublets are assigned to two *trans*-vinyl protons, which have a coupling constant of 16.2 Hz. Two singlets (7.50 and 6.84 ppm) are evident from the protons on the benzothiadiazole and thiophene rings, respectively. The $^1\text{H-NMR}$ of **PTVBT** appears broad at room temperature and even at 60 °C, a feature common to high molecular weight polymers. In addition, the existence of strong polymer aggregation in solution is also responsible for NMR broadening. When heated to 100 °C in deuterated tetrachloroethane, the $^1\text{H-NMR}$ of **PTVBT** clearly exhibits three broad, but distinguishable signals among 7.2 to 8.5 ppm, corresponding respectively to H_b , H_a and H_c in model complex. It is worth mentioning that no $^1\text{H-NMR}$ signals are found in the region of 5.0 – 6.0 ppm, where the $^1\text{H-NMR}$ signals of 1,1-diarylenevinylene

defects (α -vinyl coupling defects) usually appear in Heck polymerization²². The presence of the *trans*-vinylene functionality is also confirmed by the appearance of FT-IR bands at 955 and 947 cm^{-1} for **bisTVBT**, respectively, as shown in Figure 4-5. These bands are due to the out-of-plane C-H bending of *trans*-vinylene linkages^{22, 249}.

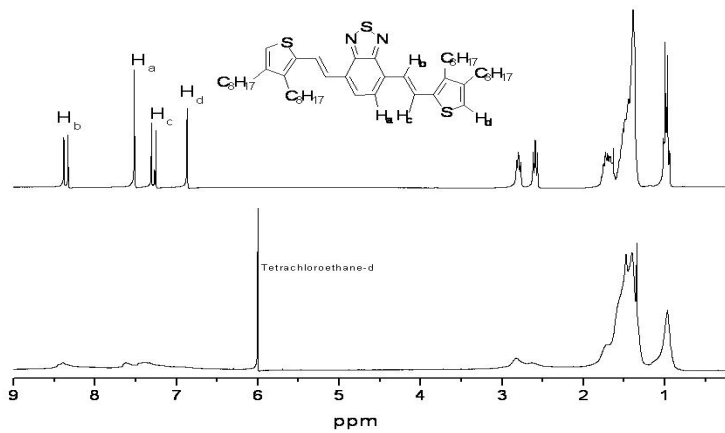


Figure 4-4. ^1H -NMR spectra of bisTVBT in deuterated chloroform (top) at room temperature and PTVBT in deuterated tetrachloroethane at 100 °C

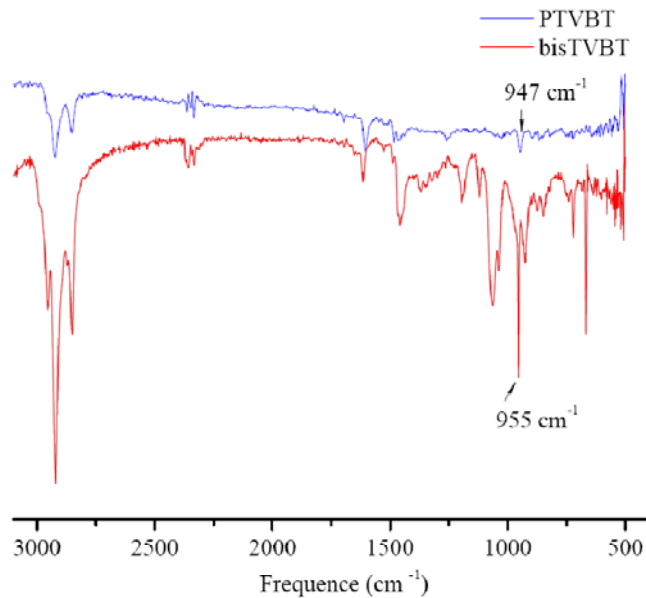


Figure 4-5. IR spectra of bisTVBT and PTVBT

Thermogravimetric analysis (TGA) was carried out to evaluate the thermal stability of **PTVBT**. A mass loss of 5 % is defined as the threshold for thermal decomposition. **PTVBT**

demonstrated good thermal stability with an onset of decomposition at 380 °C. Differential scanning calorimetry (DSC) was performed to characterize the thermal transitions of **PTVBT**. **PTVBT** exhibited a glass transition-like feature at 100 °C and a broad endothermic transition at 235 °C on the forward sweep of the first DSC heating cycle. No thermal transitions were observed after the first cycle in the range of -100 to 300 °C.

The absorption spectrum of **PTVBT** exhibits a significant change in comparison with that of **bisTVBT**. **BisTVBT** has a two-band spectrum with absorption maxima at 359 and 499 nm in THF, while **PTVBT** shows absorption maxima at 416 and 618 nm as shown in Figure 4-6. There is a ~119 nm red shift in the λ_{max} of the low energy peaks between **PTVBT** and **bisTVBT**. In contrast, due to the steric hindrance imparted by the octyl solubilizing groups, only a 60 nm red shift is observed for a directly-linked benzothiadiazole-thiophene alternating polymer and its model compound.²⁵⁰ More strikingly, **PTVBT** has a more red-shifted absorption maximum than its analogy polymer with a thienylene linkage (Poly(BTD-*at*-Th)), which has a λ_{max} at 602 nm in chloroform.²⁵¹ Clearly, the red shift in **PTVBT** indicates the polymer is highly conjugated through the planarization of the benzothiadiazole and thiophene units along the polymer backbone. The absorption maximum of PTVBT on ITO exhibits another 15 nm red shift compared to its absorption maximum in THF, due to enhanced π - π interactions in the solid state. In a fluorescence measurement, **bisTVBT** shows a well-resolved emission spectrum with a maximum at 610 nm. The photoluminescence efficiency of **bisTVBT** was relatively high at 51 % compared to that of Rhodamine B in THF. Surprisingly, no fluorescence emission was detected for **PTVBT** with excitation at 618 nm. Varying the concentration of the polymer solutions yielded no further success. This lack of fluorescence emission can be explained by two facts: the formation of polymer aggregates in solution as illustrated by temperature-dependent

¹H-NMR study and the low bandgap of **PTVBT**. The former weakens fluorescence emission through self-quenching and the latter leads to favorable non-radiative pathways for relaxation of excited states, governed by energy gap law.²⁵² The decay rate of excited electronic states in a conjugated polymer is calculated for a model of a large number of displaced harmonic oscillators. The rate depends exponentially on the energy difference (“gap”) between the initial and final electronic states.²⁵³ Considering dramatically lowering of energy gap from **bisTVBT** to **PTVBT** and a very small bandgap of 1.4 eV **PTVBT** exhibits, it is no surprise that **bisTVBT** is fluorescent and **PTVBT** presents no fluorescence.

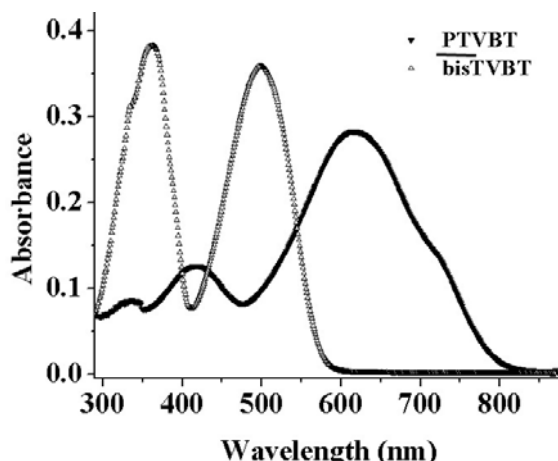


Figure 4-6. Absorption spectra of bisTVBT and PTVBT in THF

4.4 Electrochemical and Spectroelectrochemical Studies

Cyclic voltammetry (CV) and differential pulse voltammetry (DPV) were employed to estimate the HOMO and LUMO levels, and along with the band gap of **PTVBT**, as shown in Figure 4-7. Electrochemical measurements were performed in an argon-filled dry box in 0.1M TBAP/PC electrolyte solution for the polymer thin films, which were solution drop-cast on platinum button electrodes. All the potentials have been calibrated versus ferrocene/ferrocenium.

Compared to CV, DPV offers better sensitivity and reveals sharper oxidation and reduction potential onsets, which results in an enhanced accuracy when estimating electrochemical band

gaps. As illustrated in Figure 4-7a, there is a broad p-type doping process which occurs at potentials in the range of -0.2 to +0.8 V vs Fc/Fc⁺ with an oxidation onset at +0.27 V, which is more positive than the onset for the polymer oxidation determined via CV (Figure 4-7b). Based on the electrochemical results, **PTVBT** showed relatively good air stability. The HOMO energy value was estimated to be between -5.23 and -5.37 eV, based on the assumption that the Fc/Fc⁺ redox couple is -5.1 eV relative to vacuum²⁵⁴. After 100 potential switching cycles at 50 mV s⁻¹ between -0.2 and +0.9 V the polymer retained 85 % of its peak current. The reductive process was found to be less stable than the oxidative doping; the current of the reduction peak at -1.72 V decreased significantly after the third cathodic scan. The onset for reduction is around -1.43 V and about ~100 mV more anodic than the corresponding CV reduction onset, indicating a LUMO energy level between -3.55 and -3.61 eV. Hence, the electrochemically determined band gaps of **PTVBT** are 1.76 eV from DPV and 1.68 eV from CV, respectively.

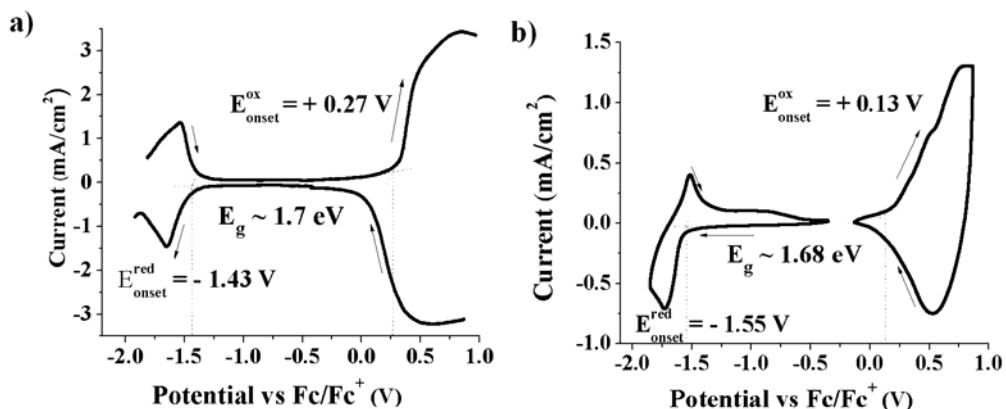


Figure 4-7. a) Differential pulse voltammetry of PTVBT on a platinum working electrode in 0.1M TBAP/PC solution with a step time of 0.02 s, a step size of 2 mV, and amplitude of 100 mV; b) Cyclic voltammetry of PTVBT on a platinum working electrode (0.02 cm^2) in 0.1M TBAP/PC solution at 50 mV s^{-1}

Spectroelectrochemical measurements can be used not only to determine the band structure of the polymer, but also to directly evaluate its electrochromic properties, which is important from an application standpoint. Figure 4-7 shows the oxidative spectroelectrochemistry for

PTVBT air-brush spray cast on ITO coated glass electrodes in deoxygenated (via argon purge) 0.1M TBAP/PC supporting electrolyte solution. The applied potential was increased in 50 mV intervals from +0.2 V to +0.85 V vs Fc/Fc⁺. For the neutral form of the polymer (+0.2 V, thick line in Figure 4-8) two absorption maxima at 416 and 633 nm were observed, which correspond to the $\pi - \pi^*$ transitions of the polymer and induce a deep blue color in the film. Upon oxidation these transitions vanished with the simultaneous formation of a broad peak outside the visible region at longer wavelengths, associated with low energy charge carriers (polarons and bipolarons). When the film is completely oxidized (+0.85 V), it is converted into a pale blue color due to the remnant absorption between 600-800 nm. The optical band gap (E_g) has been determined by the onset of the $\pi - \pi^*$ absorption for the neutral form of the polymer and relatively low around 1.52 eV. After performing oxidative spectroelectrochemical studies no significant degradation of the polymer was observed (7% loss of the anodic and cathodic peak currents of the cyclic voltammograms compared to those of the freshly prepared and switched polymer film). The optically estimated band gap was found to be smaller than electrochemically determined values, but remain within a good agreement within 0.02 eV.

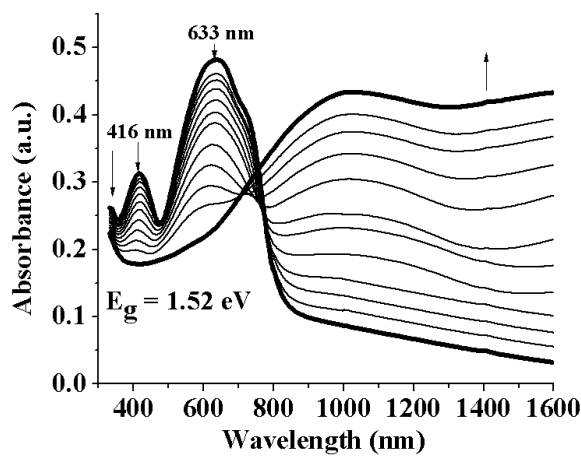


Figure 4-8. Spectroelectrochemistry of PTVBT spray cast on ITO/glass from 3 mg/mL solution of the polymer in toluene in 0.1M TBAP/PC between 0.2 and 0.85V in 50mV steps (vs Fc/Fc⁺). The thick line corresponds to the neutral state of the polymer at 0.2 V.

4.5 Organic Solar Cells

Polymer photovoltaic cells were fabricated with a layered structure of glass/ITO/PEDOT:PSS/PTVBT-PCBM blend/Al. Use of LiF did not have a noticeable effect on the device performance in our case. Characteristic *I-V* plots of several representative photovoltaic cells with different PTVBT to PCBM weight percentages are shown in Figure 4-9a. As is illustrated with the 10% polymer blend cell, fill factors ranged from 33 to 55% percent. Open circuit voltages in these cells ranged between 0.5 to 0.6 V. These values are typical for low bandgap polymers.²⁵⁵²⁵⁶ Simple metal-insulator-metal models suggest that open circuit voltages should depend only on the difference between the electrode work functions, however it is well known that the polymer HOMO level can influence the maximum open circuit voltage in polymer cells.¹³³ Given the low-lying HOMO level of PTVBT, it is possible that further work will result in improved open circuit voltages. To date, short circuit current densities are relatively low, at ~1 mA/cm². This is possibly due to blend film morphologies.

Variation of the blend film weight percentage of PTVBT to PCBM resulted in optimal performance with surprisingly low polymer percentages as is illustrated in Figure 4-9b. Power conversion efficiencies (PCE) mostly fell in the range of 0.2-0.3 %. At low polymer percentages the light absorbing capabilities of the cells could be a limiting factor. Increasing the blend film polymer percentage led to improvement in current densities and overall efficiencies as can be seen in the figures. Upon reaching 10-15 % polymer no further improvements in current densities were noted. At higher polymer concentrations we noted a gradual decrease in fill factor resulting in an overall drop in PCE. At just 35% polymer the cell performance dropped by a factor of ~3. This indicates that light absorption by the polymer was not the performance-limiting factor. The variation in current through the bias voltage sweep remained small, especially at low polymer percentages, indicating good transport properties. IPCE measurements

showed a broad absorption following the polymer spectrum, but low overall external quantum efficiencies, as shown in Figure 4-9c.

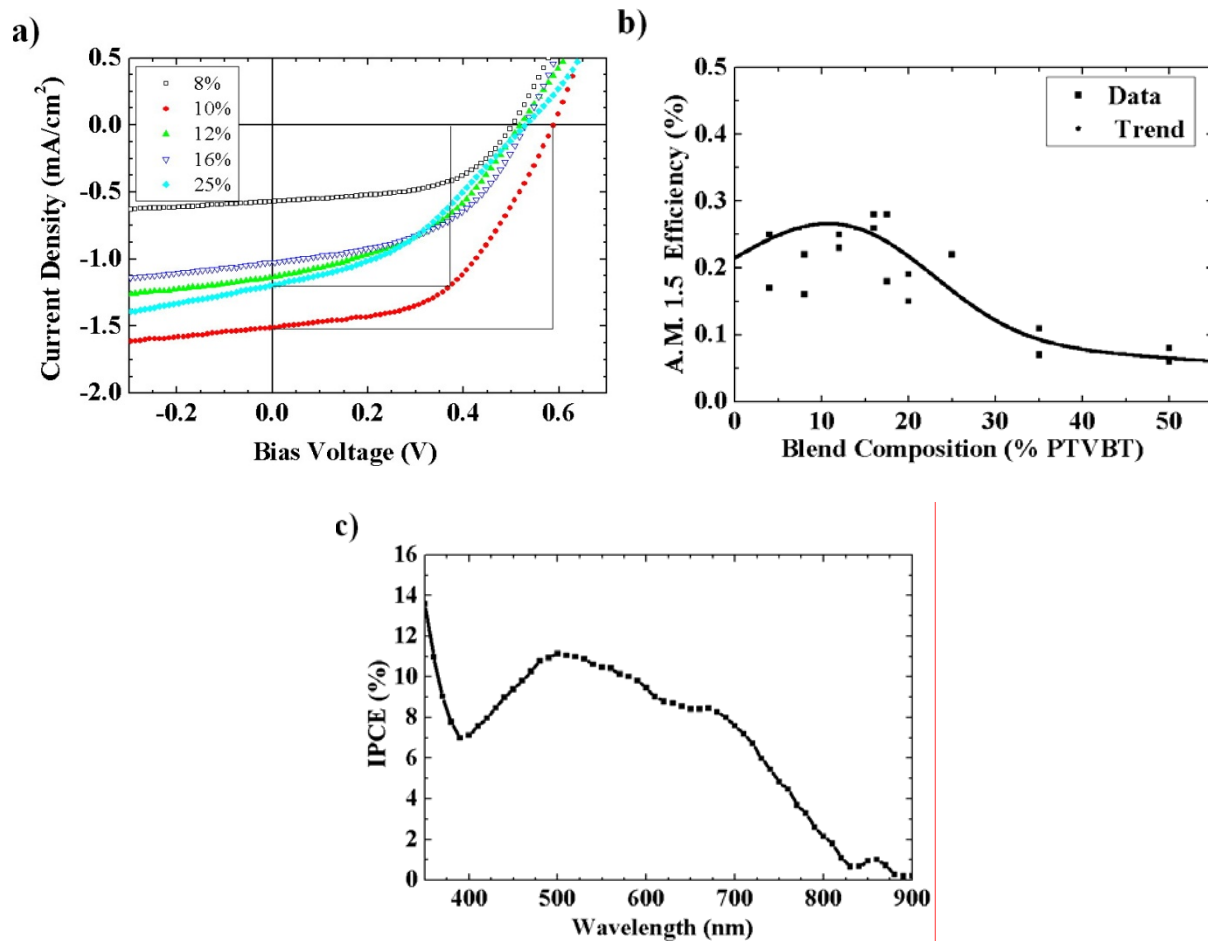


Figure 4-9. a) A.M. 1.5 J - V characteristics of devices with varied PTVBT/PC₆₁BM weight percentages; b) A.M. 1.5 Efficiencies measured from cells of differing PTVBT-PC₆₁BM weight percentages and also differing active layer thicknesses; c) IPCE of a representative device.

Blend film morphologies are possibly the dominant factor limiting photovoltaic performance. Tapping mode AFM measurements revealed a strong correlation between blend film surface morphologies and polymer percentage. A number of differing surface features resulted with small changes in polymer percentages, as shown in Figure 4-10. With a blend of just 4 % polymer and 96 % PCBM, the films were very low in RMS roughness. When the polymer percentage was increased to 8%, the result was the formation of small, round pits. At

12% polymer many of these pits became quite deep ~25nm. Further increases to the polymer percentage led to shallower pits which begin to coalesce. At 20%, the morphology appeared to be dominated by multiple small valleys. This effect was much more pronounced at 25% where the valleys deepen and lengthen. These vastly differing morphologies may indicate that the polymer was concentrating at the surface of the anode, an undesirable phase separation that may account for the low IPCE and PCE results.

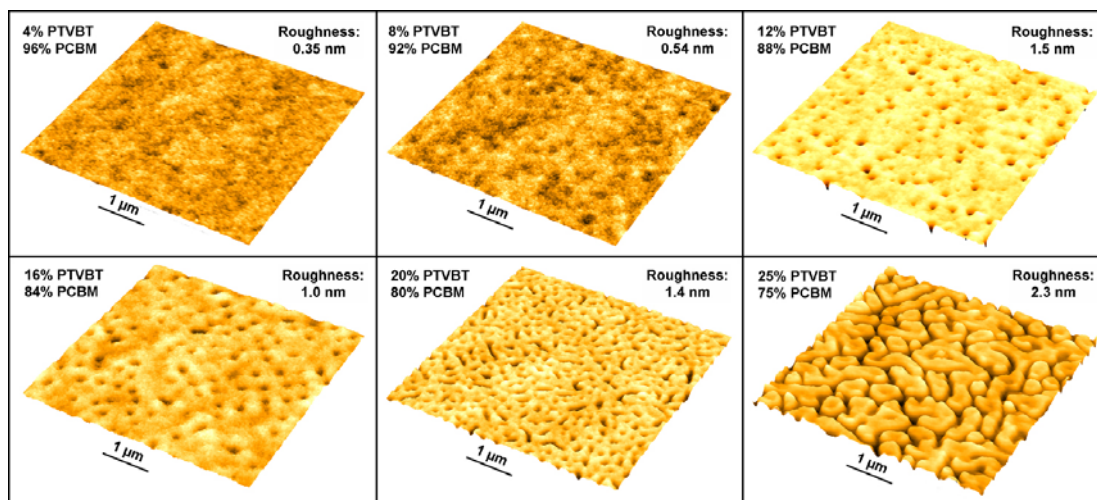


Figure 4-10. Tapping mode atomic force microscopy images of spin coated blend films from solutions of varying PTVBT:PCBM weight ratios. The z-scale factor is 20.

4.6 Conclusion

We have demonstrated a facile approach to synthesize vinylene-linked donor-acceptor (VDA) conjugated polymers with a method that can find broad applicability for preparing polymers for redox active and organic electronic applications. Structural α -coupling defect-free low bandgap **PTVBT** has been successfully obtained. UV-Vis absorption spectroscopy results show that introducing vinylene-linkage can erase steric hindrance imparted by solubilizing groups and planarize the polymer backbone. Spectroelectrochemistry reveals that **PTVBT** is an electroactive polymer that can be potentially used in electrochromic devices. The solar cells made of **PTVBT: PCBM** blends did not give satisfying performance, probably due to low

content of **PTVBT** used in the blend and the unfavorable phase separation observed. Future work will be directed towards using the vinylene chemistry we developed to prepare other Vinylene-linked donor-acceptor (VDA) conjugated polymers with less intense interchain interactions for OPVs and design VDA materials for Near-IR light-emitting diodes.

4.7 Experimental Details

2-bromo-3-hexylthiophene (4-2).²⁵⁷ To a 100 mL flask charged with 3-hexylthiophene (2.96 g, 17.6 mmol) in DMF (40 mL), N-bromosuccinimide (3.30 g, 18.5 mmol) was added at 0 °C. Catalytic amount acetic acid (0.2 mL) was added subsequently. The resulting mixture was warmed up to room temperature after 4h and stirred in the absence of light overnight. After the reaction was completed, the mixture was diluted with water and then extracted with diethyl ether. The organic phase was washed brine, dried over magnesium sulfate, and concentrated under vacuum to provide crude product. The crude product was purified by ball-to-ball distillation via a Kugelrohr apparatus to yield colorless oil (3.80 g, 88 %). ¹H NMR (CDCl₃, δ ppm) 7.18 (d, J = 5.1 Hz, 1H), 6.79 (d, J = 5.1 Hz, 1H), 2.58 (t, J = 7.5 Hz, 2H), 1.57-1.53 (m, 2H), 1.29-1.34 (m, 6H), 0.89 (t, J = 6.9, 3 H); ¹³C NMR (CDCl₃, δ ppm) 142.2, 128.4, 125.3, 190.0, 31.8, 29.9, 29.6, 29.1, 22.8, 14.3.

(E)-3-(3-hexylthiophen-2-yl)acrylic acid (4-3). To a 125 mL Schlenk flask charged with CH₃CN (35 mL), THF (15 mL) and Et₃N (5.6 mL, 40 mmol), 2-bromo-3-hexylthiophene 1 (3.4 g, 13.7 mmol) was added. The resulting solution was degassed through bubbling argon for 25 min and then heated up to 60 °C. Under argon flow, Pd(OAc)₂ (2 mol %, 61 mg) and tri-*o*-tolylphosphine (4 mol %, 167 mg) were added. Acrylic acid (1.44 g, 20 mmol) was then injected through a septum. The resulting mixture was stirred under vigorous reflux for 36 h (shiny palladium mirror was usually formed during the reaction). When it was still hot, the solution was

transferred to a 250 mL clean flask and the solvent was removed under vacuum to yield a brown viscous oil. The yellow precipitates were formed upon the addition of aqueous HCl (1 M, 100 mL) and were collected and washed with water. The obtained solids then dissolved into aqueous K₂CO₃ (1 M). The insoluble solids were removed by filtration. Acidification of the filtrate with aqueous HCl (1 M, 100 mL) gave yellow solids, which were collected and washed with water. The desired products were obtained by drying at 85 °C under vacuum for 2h in the yield of 95 %, 3.10 g. ¹H NMR (CDCl₃, δ ppm) 7.98 (dd, J₁ = 16 Hz, J₂ = 0.6 Hz 1H), 7.31 (d (broad), J = 5.1 Hz, 1H), 6.92 (d, J = 5.1 Hz, 1H), 6.21 (d, J₁ = 16 Hz, 1H), 2.74 (t, J = 7.5 Hz, 2H), 1.60-1.54 (m, 2H), 1.25-1.40 (m, 6H), 0.90 (t, J = 6.9, 3 H); ¹³C NMR (CDCl₃, δ ppm) 172.5, 147.8, 137.9, 133.4, 130.4, 128.1, 115.0, 31.8, 31.3, 29.2, 28.8, 22.7, 14.7. HRMS (ESI-TOF) calculated for C₁₃H₁₈O₂S (M+H)⁺: *m/z* 239.1100. Found: *m/z* 239.1089.

(E)-2-(2-bromovinyl)-3-hexylthiophene (4-4). To a flask charged with (E)-3-(3-hexylthiophen-2-yl)acrylic acid 2 (2.38 g, 10 mmol) in CH₃CN-H₂O (96 mL – 4 mL), lithium acetate dihydrate (0.1 eq, 1 mmol, 102 mg) was added and stirred for 15 min. N-Bromosuccinimide (1.82 g, 10.2 mmol) was then added portionwise. Bubbles were observed through bubbler, which disappeared after 30 min. The solution was stirred for another 4 h. The solution was diluted with water and brine and then extracted with diethyl ether. The organic phase was washed brine, dried over magnesium sulfate, and concentrated under vacuum to provide crude product. The crude product was purified by column chromatography on silica gel using hexane as eluent to give a pale yellow oil in the yield of 48 %, 1.32 g. ¹H NMR (CDCl₃, δ ppm) 7.22 (dd, J₁ = 13.8 Hz, J₂ = 0.6 Hz 1H), 7.10 (d (broad), J = 5.4 Hz, 1H), 6.83 (d, J = 5.4 Hz, 1H), 6.21 (d, J₁ = 13.8 Hz, 1H), 2.59 (t, J = 7.5 Hz, 2H), 1.56-1.51 (m, 2H), 1.25-1.35 (m, 6H), 0.90 (t, J = 6.9, 3 H); ¹³C NMR (CDCl₃, δ ppm) 141.3, 133.6, 129.7, 129.2, 123.8, 104.6,

31.9, 31.0, 29.2, 28.6, 22.8, 14.3. HRMS (ESI-TOF) calculated for C₁₂H₁₇BrS (M)⁺: *m/z*

273.0307. Found: *m/z* 273.0313.

(2E,2'E)-3,3'-(benzo[c][1,2,5]thiadiazole-4,7-diyl)diacrylic acid (4-8). To a 250 ml Schlenk flask charged with 4,7-dibromobenzo[c][1,2,5]thiadiazole (5.85 g, 20 mmol), Pd(OAc)₂ (2 mol %, 0.8 mmol, 178 mg) and tri(o-tolyl phosphine) (4 mol %, 1.6 mmol, 488 mg) under argon, the degassed mixture of CH₃CN (120 mL), THF (60 mL) and Et₃N (28 mL, 200 mol) was injected through a septum. The resulting mixture was heated to 60 °C. Acrylic acid (4.32 g, 60 mmol) was then injected slowly. The solids started to disappear and the solution turned orange. The solution was refluxed at 84 °C for 20 h. The reaction was monitored by TLC. A uniform palladium mirror was formed on the wall of the flask during the period of reaction. While the dark solution was still hot, it was transferred to a clean round-bottom flask (500 mL). The solvent was concentrated on rotavap. To the concentrated dark viscous mixture was added hexane and diethyl ether (1:1, 200 mL). The resulting precipitates were collected and washed with hexane and diethyl ether mixture. The dark red solids were then dissolved into water (1000 mL, with 7 mL Et₃N) and stirred for 1 h. The orange solution was filtered and the filtrate was acidified with 1M HCl (100 mL) to give orange yellow precipitates. The precipitates were collected, washed with water and dried under air overnight. The obtained crude products were dissolved into hot THF (~ 300 mL) and filtered. Hexane was then slowly added to the filtrate. The precipitates were filtered and dried under vacuum over 60 °C to afford yellow-orange powder (3.55 g, yield: 65 %).¹H-NMR (DMF) δ: 12.6 (bs, 2H), 8.16 (s, 2H), 8.13 (d, *J* = 15.9 Hz, 2H), 7.52 (d, *J* = 15.9 Hz, 2H), ¹³C-NMR (DMF) δ: 168.6, 154.3, 139.9, 132.3, 129.7, 125.8; HRMS (DIP-CI-MS) Calculated for C₁₂H₈O₄N₂S(M⁺): 276.0187 Found: *m/z* 276.0205

4,7-bis((E)-2-bromovinyl)benzo[c][1,2,5]thiadiazole (4-9). To a suspension of (2E,2'E)-3,3'-(benzo[c][1,2,5]thiadiazole-4,7-diyl)diacrylic acid (5 mmol, 1.38 g) in acetonitrile (50 mL) was added a solution of lithium acetate dihydrate (4 mmol, 408 mg) in water (15 mL). *N*-Bromosuccinimide (10.5 mmol, 1.87 g) was then added. Carbon dioxide gas was observed through bubbler immediately after the addition NBS. The resulting solution was stirred at room temperature for another 2 h after the evolution of gas ceased. Water (100 mL) was added. The yellow orange precipitates were collected, washed with water and dried under air. The crude product was then purified by silica gel column chromatography, eluting with CH₂Cl₂/Hexane (4:96) to yield light yellow solids (1.10 g, 64 %). ¹H-NMR (CDCl₃) δ: 8.01 (d, *J* = 13.8 Hz, 2H), 7.43 (d, *J* = 13.8 Hz, 2H), 7.37 (s, 2 H); ¹³C-NMR (CDCl₃) δ: 153.1, 133.6, 128.5, 114.5; HRMS (DIP-CI-MS) Calculated for C₁₀H₇N₂SBr₂(M⁺): 343.8624 Found: *m/z* 343.8618; Anal. Calcd for C₁₀H₇N₂SBr₂: C, 34.71; H, 1.75; N, 8.10. Found: C, 34.88; H, 1.59; N, 7.95.

2,2'-(3,4-dioctylthiophene-2,5-diyl)bis(4,4,5,5-tetramethyl-1,3,2-dioxaborolane) (4-7). To a 100 mL two-neck flask charged with 3,4-octylthiophene (10 mmol, 2.73 g), 4,4'-di-tert-butyl-2,2'-bipyridine (3.0 mol %, 81 mg) and bis(pinacolato)diboron (8 mmol, 2.03 g) were added subsequently under argon. Three cycles of argon-vacuum were then applied. Degassed heptane (50 ml) was injected. [Ir(OMe)(COD)]₂ (1.5 mol %, 98 mg) was added under argon and the mixture was stirred at 50 °C for 16 h. After cooling down to room temperature, the mixture was filtered and washed with hot hexane. The filtrate was concentrated to yield viscous oil. The crude product was purified by silica gel column chromatography, eluting with Ethyl acetate/Hexane (5:95) to give colorless oil (4.56 mg, 81 %). ¹H-NMR (CDCl₃) δ: 2.80 (t, *J* = 7.5 Hz, 2H), 1.56–1.20 (m, 48H), 0.90 (t, *J* = 6.3 Hz, 6H); ¹³C-NMR (CDCl₃) δ: 154.3, 83.6, 32.7, 32.2, 30.0, 29.7, 29.6, 28.7, 25.0, 22.9, 14.3; HRMS (APCI-TOF) Calculated for C₃₂H₅₈B₂O₄S (M + H⁺):

561.4326. Found: *m/z* 561.4383. Anal. Calcd for C₃₂H₅₈B₂O₄S: C, 68.57; H, 10.43; Found: C, 68.69; H, 10.67.

Model Complex: To a flask charged with 4,7-bis((E)-2-bromovinyl)benzo[c][1,2,5]thiadiazole (1 mmol, 346 mg), Pd₂(dba)₃ (2.5 mmol, 23 mg), [(*t*Bu)₃]BF₄ (7.5 mol %, 22 mg), CsF (6 mmol, 912 mg) under argon atmosphere, 4,4,5,5-tetramethyl-2-(octylthiophen-2-yl)-1,3,2-dioxaborolane (2.4 mmol) in THF (40 ml) was injected. The resulting mixture was stirred at room temperature for 10 h. Water (100 ml) was added and the organic phase was extracted with diethyl ether (2 x 20 mL). The combined organic phase was dried over MgSO₄. The solvent was removed and the crude product was purified by silica gel column chromatography, eluting with Dichloromethane/Hexane (15: 85) to yield red solids.

4,7-bis((E)-2-(3-octylthiophen-2-yl)vinyl)benzo[c][1,2,5]thiadiazole. (490 mg, 85%) ¹H-NMR (CDCl₃) δ: 8.35 (dd, J₁ = 15.9 Hz, J₂ = 0.6 Hz, 2H), 7.49 (s, 2H), 7.29 (d, J = 15.9 Hz, 2H), 7.17 (d, J = 5.4 Hz, 2H), 6.91 (d, J = 5.4 Hz, 2H), 2.81 (t, J = 7.5 Hz, 4H), 1.69–1.64 (m, 4H), 1.49–1.25 (m, 20H), 0.90 (t, J = 6.3 Hz, 6H); ¹³C-NMR (CDCl₃) δ: 153.9, 142.7, 137.2, 130.1, 129.2, 127.4, 125.4, 124.0, 123.8, 32.1., 31.2., 29.6, 29.5, 28.8, 22.9, 14.3; HRMS (APCI-TOF) Calculated for C₃₄H₄₄N₂S₃ (M + H⁺): 577.2739. Found: *m/z* 577.2731. C₃₄H₄₄N₂S₃ (M + H⁺): 577.2739. Found: *m/z* 577.2740. Anal. Calcd for C₃₄H₄₄N₂S₃: C, 70.78; H, 7.69; N, 4.86. Found: C, 70.79; H, 7.87; N, 4.34.

4,7-bis((E)-2-(4-octylthiophen-2-yl)vinyl)benzo[c][1,2,5]thiadiazole (465 mg, 81%) ¹H-NMR (CDCl₃) δ: 8.19 (d, J = 16.2 Hz, 2H), 7.54 (s, 2H), 7.34 (d, J = 16.2 Hz, 2H), 7.06 (s, 2H), 6.85 (s, 2H), 2.61 (t, J = 7.5 Hz, 4H), 1.65–1.61 (m, 4H), 1.40–1.20 (m, 20H), 0.90 (t, J = 6.3 Hz, 6H); ¹³C-NMR (CDCl₃) δ: 153.9, 144.3, 143.1, 129.0, 128.8, 127.4, 127.1, 124.0, 120.3, 32.1., 30.7., 30.6, 29.7, 29.54, 29.48, 22.9, 14.3; HRMS (APCI-TOF) Calculated for C₃₄H₄₄N₂S₃

(M + H⁺): 577.2739. Found: m/z 577.2740. Anal. Calcd for C₃₄H₄₄N₂S₃: C, 70.78; H, 7.69; N, 4.86. Found: C, 70.77; H, 7.58; N, 4.85..

4,7-bis((E)-2-(3,4-dioctylthiophen-2-yl)vinyl)benzo[c][1,2,5]thiadiazole (689 mg, 86%)
¹H-NMR (CDCl₃) δ: 8.38 (d, J = 16.2 Hz, 2H), 7.50 (s, 2H), 7.29 (d, J = 16.2 Hz, 2H), 6.84 (s, 2H), 2.75 (t, J = 6.6 Hz, 4H), 2.55 (t, J = 7.5 Hz, 4H), 1.70–1.20 (m, 48H), 0.90–0.98 (m, 12H);
¹³C-NMR (CDCl₃) δ: 154.0, 143.6, 142.0, 137.8, 129.3, 127.4, 126.2, 123.4, 119.4, 32.2., 32.1, 31.3, 30.0., 29.9, 29.8, 29.7, 29.6, 29.56, 29.5, 29.3, 27.3, 22.9, 14.3; HRMS (APCI-TOF)
Calculated for C₅₀H₇₆N₂S₃ (M + H⁺): 577.2739. Found: m/z 577.2740. Anal. Calcd for
C₅₀H₇₆N₂S₃: C, 74.94; H, 9.56; N, 3.50. Found: C, 75.08; H, 9.56; N, 3.50.

PBTVT: In a 25 mL flame dried Schlenk flask, 4,7-bis((E)-2-bromovinyl)benzo[c][1,2,5]thiadiazole (346.0 mg, 1 mmol), 2,2'-(3,4-dioctylthiophene-2,5-diyl)bis(4,4,5,5-tetramethyl-1,3,2-dioxaborolane) (560.5 mg, 1 mmol), Pd₂(dba)₃ (13.5 mg, 1.45 mmol %), and tri(o-tolyl)phosphine (18.0 mg, 6 mmol %) were dissolved in 12.0 mL of degassed toluene and degassed 20 % aqueous tetraethylammonium hydroxide (3.4 mL, 4.25 mmol). The reaction mixture was vigorously stirred at 60 °C for 24 h and then heated up to 95 °C for 6 h. The solution turned from orange to red, dark purple and finally blue after an hour. After cooling back to 60 °C, 4-iodotoluene (21.8 mg, 0.10 mmol) was added to the mixture. After 2 h, 4,4,5,5-tetramethyl-2-p-tolyl-1,3,2-dioxaborolane (21.8 mg, 0.10 mmol) was added and the reaction was stirred for another 6 h to complete the end-capping reaction. The polymer was purified by precipitation in methanol/water (10:1), filtered through 0.45 µm nylon filter and purified on a Soxhlet apparatus with methanol, hexanes, and chloroform. To the chloroform fraction was added palladium removal reagent (E)-N,N-diethyl-2-phenyldiazene carbothioamide (22 mg, 0.1 mmol). The resulting solution was stirred for 2 h. The solution was concentrated

under reduced pressure, precipitated in methanol (300 mL), filtered through 0.45 μ m nylon filter, washed with methanol and dried under vacuum at 60 °C overnight to afford PBTVT (432 mg, 87.4 %). 1 H-NMR (C₂D₂Cl₄, 100 °C) δ : 8.34 (broad, 2H), 7.62(bs, 2H), 7.39 (broad, 2 H), 2.4-2.9 (broad, 4H), 1.8-1.20 (m, 24), 0.97 (b, 6H); Anal. Calcd : C, 73.10; H, 8.21; N, 5.68; Found: C, 72.64; H, 8.07; N, 5.67; GPC M_n = 31,100, M_w = 73,400, and PDI = 2.36.

PF8VBT. In a 25 mL flame dried Schlenk flask, 4,7-bis((E)-2-bromovinyl)benzo[c][1,2,5]thiadiazole (346.0 mg, 1 mmol), 2,2'-(9,9-dioctyl-9H-fluorene-2,7-diyl)bis(4,4,5,5-tetramethyl-1,3,2-dioxaborolane) (642.57 mg, 1 mmol), Pd₂(dba)₃ (13.5 mg, 1.45 mmol %), and tri(o-tolyl)phosphine (18.0 mg, 6 mmol %) were dissolved in 12.0 mL of degassed toluene and degassed 20 % aqueous tetraethylammonium hydroxide (3.7 mL, 4.6 mmol). The reaction mixture was vigorously stirred 60 oC for 12 h and then heated up to 95 oC for 24 h. The polymer was purified by precipitation in methanol/water (9:1), filtered through 0.45 μ m nylon filter and purified on Soxhlet apparatus with methanol, hexanes, and chloroform. The chloroform fraction was concentrated under reduced pressure, precipitated in methanol (300 mL), filtered through 0.45 μ m nylon filter and dried under vacuum at 60 oC overnight to give metallic-texture solids (100.1 mg, 17.4 %). 1 H-NMR (CDCl₃) δ : 8.19 (d, J = 16.2 Hz, 2H), 7.90-7.6 (m, 10H), 2.16 (bs, 4H), 1.5-1.1 (m, 20H), 1.0–0.79 (m, 10H); 13 C-NMR (CDCl₃) δ : 154.0, 151.9, 141.0, 136.7, 134.0, 129.5, 126.7, 126.0, 123.9, 121.4, 120.0, 55.1, 40.1, 31.5, 29.9, 29.0, 28.9, 23.8, 22.3, 13.7; Anal. Calcd : C, 81.46; H, 8.12; N, 4.86; Found: C, 81.23; H, 8.21; N, 4.30; M_n = 12,900, M_w = 27,400, PDI = 2.1 and DP = 22.

PF10VBT. In a 25 mL flame dried Schlenk flask, 4,7-bis((E)-2-bromovinyl)benzo[c][1,2,5]thiadiazole (346.0 mg, 1 mmol), 2,2'-(9,9-dioctyl-9H-fluorene-2,7-diyl)bis(4,4,5,5-tetramethyl-1,3,2-dioxaborolane) (698.7 mg, 1 mmol), Pd₂(dba)₃ (13.5 mg, 1.45

mmol %), and tri(o-tolyl)phosphine (18.0 mg, 6 mmol %) were dissolved in 12.0 mL of degassed toluene and degassed 20 % aqueous tetraethylammonium hydroxide (3.7 mL, 4.6 mmol). The reaction mixture was vigorously stirred 60 °C for 48 h and then heated up to 95 °C for 4 h. The polymer was purified by precipitation in methanol/water (9:1), filtered through 0.45 µm nylon filter and purified on Soxhlet apparatus with methanol, hexanes, and chloroform. The chloroform fraction was concentrated under reduced pressure, precipitated in methanol (300 mL), filtered through 0.45 µm nylon filter and dried under vacuum at 60 °C overnight to give metallic-texture solids (354.0 mg, 56 %). ¹H-NMR (CDCl₃) δ: 8.19 (d, J = 16.2 Hz, 2H), 7.90-7.65 (m, 10H), 2.16 (bs, 4H), 1.5-1.1 (m, 28H), 1.0–0.79 (m, 10H); Anal. Calcd : C, 81.85; H, 8.66; N, 4.43; Found: C, 81.44; H, 8.63; N, 4.06; M_n = 19500, M_w = 50300, PDI = 2.6 and DP = 31.

CHAPTER 5
DIKETOPYRROLOPYRROLE-BASED SEMICONDUCTING MATERIALS FOR
PHOTOVOLTAIC APPLICATIONS

5.1 Introduction

In Chapters 3 and 4, we developed two different types of polymeric materials for photovoltaic applications. In this chapter, the focus is switched to molecular materials and thermally cleavable polymers to explore other possibilities for obtaining high performance materials for field-effect transistors and photovoltaic applications.

As discussed in Chapter 1, monomeric materials have some intrinsic advantages over polymeric materials, such as having well-defined molecular structures, ease of functionalization, and versatile methods of purification. However, PCEs of small molecule solar cells are, to date, not competitive with those of polymer based devices.^{76,78,83,142,146,258-260} This is due, in part, to homogeneous mixing of donor and acceptor components in as-spun thin films and/or large phase separation upon crystallization; it also results from the reduced crystallinity in thin films prepared via solution processing (e.g., spin-coating or spray coating) versus films prepared via thermal-vacuum deposition.²⁶¹ It is now widely accepted that charge mobility in organic semiconducting materials, as in inorganic semiconductors, is strongly linked to the degree of long range order (i.e., higher crystallinity correlates with larger charge mobility).²⁶² Low charge mobility leads to charge accumulation, and inefficient charge collection, and ultimately decreased fill factors and poor performance in a photovoltaic device.²⁶³ Another fundamental characteristic, exciton diffusion length, is also closely related to the extent of crystallinity. Forrest, *et al.* has correlated the four-fold increase in the exciton diffusion length of 3,4,9,10-perylenetetracarboxylic dianhydride (PTCDA) with the enhanced degree of crystalline order that accompanies vacuum deposition.²⁶¹ In general, small crystalline molecules exhibit higher intrinsic charge mobilities and exciton diffusion lengths compared to their polymeric

counterparts.²⁶⁴ Therefore, in principle, superior photovoltaic performance can be expected for small molecule solar cells provided that nanoscale phase segregation among donor and acceptor π -stacks occurs while retaining high-order crystallinity in solution-processed thin films. Toward this goal, materials that can undergo self-assembly and self-organization have emerged as attractive targets.²⁶⁵⁻²⁶⁷

Access to various supramolecular nanostructures via self-assembly of small organic molecules has been the focus of extensive research.²⁶⁸⁻²⁷² To date, much success has been achieved in this regard. Nanostructures, e.g. one-dimensional rods, tubes, fibrils and helical columns, two-dimensional rings and layered sheets, as well as three-dimensional vesicles, have been demonstrated to a large extent. In addition, a great deal of attention in this field has also been gradually shifting towards development of self-assembled materials for functional applications.²⁷³⁻²⁷⁸ In both cases, amphiphilic molecular design has been shown to be an effective strategy to achieve these goals.^{275,279} Along these lines, we discuss in this Chapter the Synthesis and characterization of the first cruciform-shaped amphiphilic diketopyrrolopyrrole-based (DPP) molecule with a rich self-assembly behavior in the bulk, in solution, and on a surface. We also demonstrate that the amphiphilicity endows the molecule with attractive properties (e.g., solution-processable, self-assembled long-range order, etc.) for organic field-effect transistors and solar cells.

One problem associated with the commercialization of polymer based solar cells is their instability during prolonged light exposure. In a typical MDMO-PPV/PCBM device, photodegradation of the polymer was observed under illumination both in the presence and absence of oxygen. The homolytic scission of the O-CH₂ bond creates radical species that attack double bonds in the polymer chains, and lead to the degradation and loss of conjugation.²⁸⁰ The

photoinstability of P3HT has also been examined by Gardette, et. al., and it is believed that the instability is caused by the hexyl side chains.²⁸¹

Thermally cleavable polymers draw attention because of their potentially better operational stability in OPVs, as a result of their lower density of solubilizing groups in the blend film after cleavage. In addition, this type of polymer is potentially useful for solution-processed multi-layer devices, realized by repeating the cycle of solution processing-thermal cleavage. Lastly, a bonus from thermal cleavage is the improvement in chromophore density in the thin-film, which is beneficial for device performance. At this stage, thermocleavable materials remain underdeveloped and less competitive when compared to P3HT and other state-of-the-art materials in OPVs. In this chapter, we discuss the Synthesis, characterization and use of diketopyrrolopyrrole-based (DPP) thermocleavable conjugated polymers on photovoltaic applications.

DPP-containing materials are vibrantly colored and highly fluorescent with exceptional photochemical, mechanical, and thermal stability, and are therefore widely used in industrial applications as high-performance pigments in plastics, paints, and inks.²⁸² Due to strong π - π interactions and extensive hydrogen-bonding forces, these DPP-based molecules can not be directly used as organic solution-processed materials in OPVs, rather functionalization of these parent molecules is desired, and is generally accomplished through N-alkylation.²⁸³⁻²⁸⁸ Nguyen, et. al demonstrated a series of DPP-based small molecules used as active materials in BHJ OPVs and achieved PCEs of ~2.2-4.4%.^{76,78,80,83} Janssen, et al. reported high performance OPVs above 5% based on DPP-based conjugated polymers.⁴¹ These results greatly promote the study of DPP-containing molecules and polymers as photovoltaic materials. Here, two types of unconventional DPP-based materials will be studied as follows.

5.2 Diketopyrrolopyrrole-based Amphiphilic Oligothiophene

The molecule designed in this section has a constrained geometrical configuration and is composed of a diketopyrrolopyrrole oligothiophene (**DPP-1**) conjugated rigid core, one pair of terminal lipophilic paraffinic chains and one pair of lateral hydrophilic triglyme chains, as shown in Figure 5-1. The extended conjugated component is designed to ensure strong π - π interactions and secure a columnar π -stacking arrangement.²⁸⁷⁻²⁸⁸ At the same time, the molecule is expected to broadly absorb in the visible region of the solar spectrum and have appropriate energy levels for charge transfer to the acceptor materials commonly used in molecular BHJ solar cells.^{76,78,80,83} The long paraffinic chains will confer some degree of solubility, but should induce crystallization below a certain temperature. Finally, orthogonal placement of the two flexible triglyme chains should enforce hydrophobic effects with the two long aliphatic chains, and provide the desired processing solubility for device fabrication.

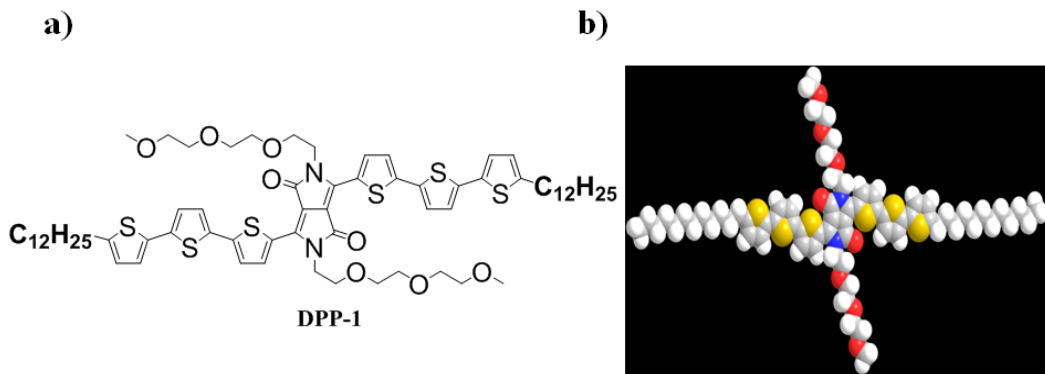


Figure 5-1. Chemical structure and model of DPP-1.

5.2.1 Synthesis of DPP-1

The Synthesis of DPP-1 is outlined in Figure 5-2. Compound **5-1** was first reported by Ciba in 1986.²⁸⁹ Briefly, thiophene-2-carbonitrile and potassium *tert*-butoxide were mixed in *tert*-amyl alcohol and then heated to 95 °C under a nitrogen atmosphere. As soon as this temperature was reached, a solution of di-*n*-methyl succinate in *tert*-amyl alcohol was added

using a dropping funnel. When the addition was completed, the reaction mixture was kept at 95 °C for 14 h, then cooled to 50 °C, carefully neutralized with glacial acetic acid, and boiled briefly at the reflux temperature. The resulting pigment suspension was diluted with water and filtered at room temperature. The filter cake was suspended in a large amount of water, and the dark pigment was isolated again by filtration, and then finally washed with methanol and water. After being dried at 100 °C, crude compound **5-1** was obtained. Due to the existence of strong hydrogen bonding and extensive pi-pi interactions, compound **5-1** is highly insoluble in common organic solvents and cannot be further purified by conventional methods. In this study, we use it as collected from filtration after drying.

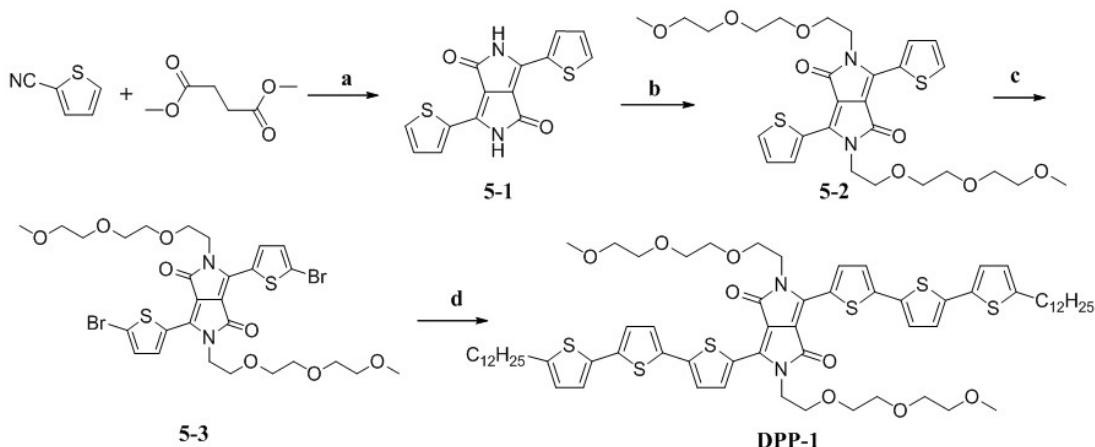


Figure 5-2. Synthesis of DPP-1. a) potassium *tert*-butoxide, *tert*-amyl alcohol, 95 °C, ~30%; b) 1-bromo-2-(2-(2-methoxyethoxy)ethoxy)ethane, potassium carbonate, DMF, 46%; c) NBS, chloroform, 61%; d) tributyl(5'-dodecyl-2,2'-bithiophen-5-yl)stannane, $\text{Pd}_2(\text{dba})_3$, $\text{P}(\text{o-tolyl})_3$, THF, 49%.

N-alkylation of compound **5-1** with 1-bromo-2-(2-(2-methoxyethoxy)ethoxy)ethane was carried out in the presence of potassium carbonate using DMF as solvent at 100 °C. Because of the impurities inherited from the prior reaction, purification of compound **5-2** was troublesome. Many repeated silica gel columns were performed in order to isolate compound **5-2**, a dark red viscous liquid which solidifies after a few days. Bromination of **5-2** with N-bromosuccimide in

chloroform gave compound **5-3** in a fair yield. Stille coupling between tributyl(5'-dodecyl-2,2'-bithiophen-5-yl)stannane and **5-3** yielded the desired product of **DPP-1**.

5.2.2 Structural Characterization, Optical and Electrochemical Studies

The structure of **DPP-1** has been confirmed by ¹H-, ¹³C-NMR, HRMS and elemental analysis. **DPP-1** has clear-cut NMR spectra for both proton and carbon, as shown in Figure 5-3, even though it contains 92 hydrogen atoms and 68 carbon atoms. In the aromatic region of ¹H-NMR, the protons on thiophene rings split into four separated peaks with integral ratios of 1:2:2:1 from 6.5 to 9.0 ppm. The downfield signal at 8.78 ppm can be assigned to the thienyl protons next to the DPP core; while the upfield doublet at 6.66 ppm is assigned to the protons on the thiophene rings attached the alkyl chains. The signals from protons on the triglyme chains are located around 3.3-4.4 ppm. A singlet at 3.32 ppm is assigned to the terminal methyl group of the triglyme chain. The ¹³C NMR of **DPP-1** also exhibits a similar trend, as evidenced in Figure 5-3. In the upfield region from 108 to 165 ppm, there are 13 carbon signals from the conjugated segment; it should be mentioned that there are totally 15 sp² carbons in this molecule. It is likely that the middle thiophene only gives two set of signals, provided that this thiophene can be considered nearly centrosymmetric and has very similar chemical surroundings for the 2,5 and 3,4 positions. The downfield signal at 161.4 ppm and the upfield signal at 108.5 ppm are readily assigned to the carbonyl carbon and the adjacent carbon. The signal at 146.4 ppm can be also tentatively assigned to the third carbon on the DPP core. It is difficult to make any further assignments of the peaks resulting from the remaining carbons within the thiophene rings. The signals from triglyme chains are easily distinguished from alkyl chains for their different environments.

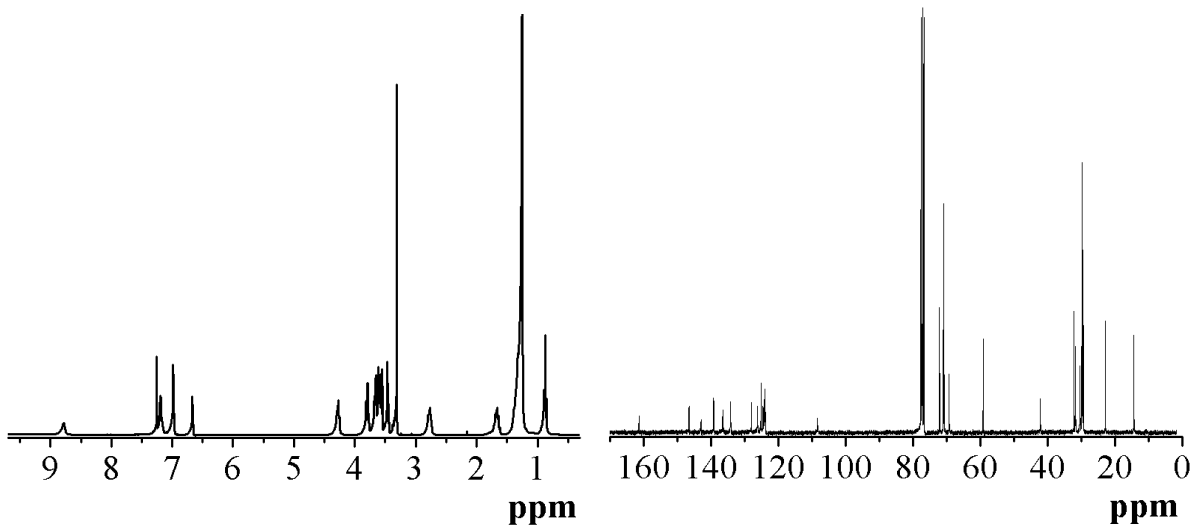


Figure 5-3. ^1H -, and ^{13}C -NMR of DPP-1 in CDCl_3

DPP-1 has good solubility ($> 10 \text{ mg/mL}$) in most common organic solvents, such as methylene chloride, chloroform, THF, toluene and dichlorobenzene. It is also fairly soluble in some polar solvents, including NMP and DMF. Figure 5-4a shows the absorption and emission spectra of **DPP-1** in toluene. It has a two-band absorption pattern, characterized by two peaks at ~ 390 and $\sim 640 \text{ nm}$. The high energy band can be attributed to terthiophene components, and the long wavelength band is associated with charge transfer between terthiophene and the DPP core. This observation is very similar with previously reported DPP based molecules.⁷⁸ In the solid state, the entire spectrum becomes broader, and a shoulder appears at longer wavelengths ($\sim 730 \text{ nm}$), indicating the strong molecular interactions.

DPP-1 in toluene emits with a λ_{\max} at $\sim 687 \text{ nm}$ and a broad shoulder at $\sim 732 \text{ nm}$; this shoulder is likely resulting from the formation of fluorescent excimers in solution. The fluorescence is completely quenched in thin-films, suggesting the formation of extensive pi stacks.²⁹⁰

Figure 5-4b shows the absorption spectra of **DPP-1** in four different solvents, THF, dimethoxyethane (DME), DCM and N-methylpyrrolidone (NMP), in the order of their relative

polarities 0.207, 0.231, 0.309, and 0.355, and photographs of the solutions are shown in Figure 5-4c. As seen from Figure 5-4b, the high energy bands, associated with the terthiophene units, have relatively even absorption intensities; while the low energy bands, attributed to charge transfer, are more influenced by the solvent polarity. In the case of this series of solvents, NMP is the most polar while DME is the least polar. The observation reflects this trend well in the low energy bands, in which the absorption intensities decrease with increasing of polarities.

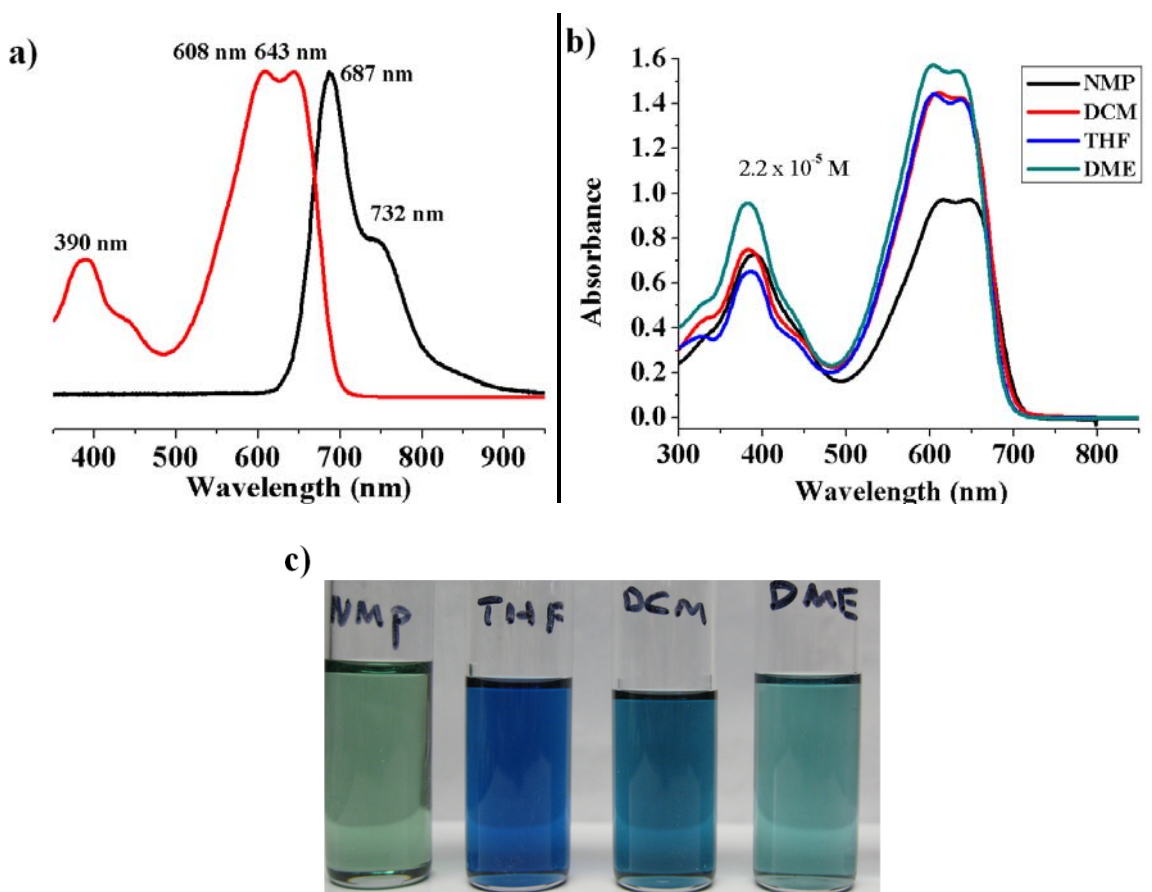


Figure 5-4. a) Absorption and emission of DPP-1 in toluene; b) absorption of DPP-1 (2.2×10^{-5} M) in NMP, DCM, THF and DME; c) the images of DPP-1) in NMP, DCM, THF and DME

Electrochemical studies were then performed to obtain information on energy levels and gaps for **DPP-1**. Cyclic voltammetry (CV) of **DPP-1** in CH_2Cl_2 using TBAPF₆ as an electrolyte shows four quasireversible consecutive redox processes with half-wave potentials around 0.65,

0.47, -1.30 and -1.79 V vs Ag/Ag⁺, respectively. The differential pulse voltammograms (DPV) for **DPP-1** also reveal two well-defined and highly reversible anodic and cathodic processes with a high degree of symmetry, and the half-wave potentials are very close to the potentials observed in CV, as shown in Figure 5-5. This gives LUMO and HOMO levels of **DPP-1**, -3.9 and -5.5 eV, respectively. The potential difference between oxidation and reduction of 1.77 V is in excellent agreement with the optical gap (1.77 eV) of the molecularly dissolved **DPP-1** in CH₂Cl₂, which has an onset of absorption near 700 nm. A significant shift of absorption onset to 825 nm was observed for the thin film, giving a calculated optical energy gap of 1.5 eV, slightly larger than its corresponding polymer. Since solid state electrochemical studies are hindered by the fair solubility of **DPP-1** in ACN and PC (two commonly used solvents for E-chem), direct comparison can not be provided between the energy gaps from the solid state optical measurement and from solid state electrochemical experiment. Nevertheless, all the electrochemical and optical results indicate that **DPP-1** is indeed a low energy gap molecule as proposed.

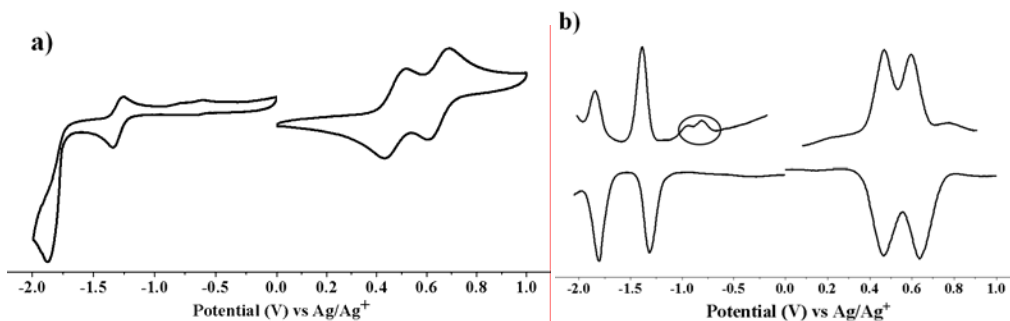


Figure 5-5. a) Cyclic voltammetry, and b) differential pulse voltammetry of **DPP-1** measured in a 0.1M solution of TBAPF₆/DCM (scan rate 25mV/s) vs Ag/Ag⁺ ($E_{\text{Fc/Fc}^+} = E_{\text{Ag/Ag}^+} + 0.16 \text{ V}$)

5.2.3 Thermal Analysis, Polarized Light Microscopy and X-ray Analysis

The identification of **DPP-1** mesophases was carried out by differential scanning calorimetry (DSC), polarized light microscopy and X-ray diffraction. DSC thermograms of

DPP-1 reveal reversible phase transition behavior as shown in Figure 5-6a. Upon heating (5 °C /min), **DPP-1** underwent a first endothermic transition at 68 °C (12.4 kJ/mol), followed by a second thermal transition at 98 °C (25.2 kJ/mol), and finally reached a clearing point at 184 °C (33.0 kJ/mol). On the cooling cycle, three corresponding exothermic transitions were observed at 181, 92 and 65 °C with enthalpies of 32.8, 22.2, and 17.7 kJ/mol, respectively. After the second scan, the subsequent scans reproducibly overlapped the prior scan. In order to gain insight into its phase transition behavior in the blend of **DPP-1/PC₆₁BM**, PC₆₁BM and the blend were subjected to thermal studies as well, as shown in Figure 5-6b and 5-6c. It is surprising to find that **DPP-1** still exhibits relatively well-defined thermal behaviors. The disappearances of the melting and recrystallization peaks for PC₆₁BM are anticipated, since **DPP-1** is still in its melting state above 248 °C in the blend. Lowering of the recrystallization temperature for **DPP-1** is also expected, considering PC₆₁BM as an impurity in the blend.

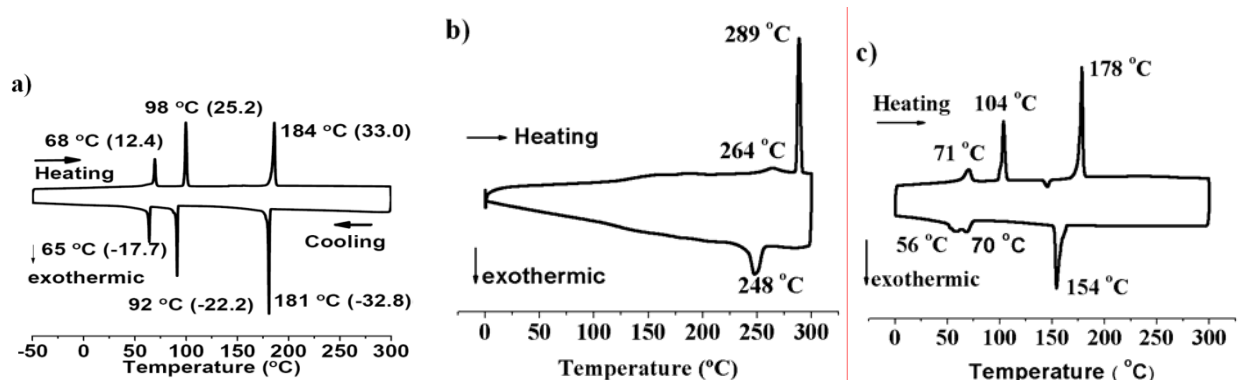


Figure 5-6. Differential scanning calorimetry thermograms. a) DPP-1, b) PC₆₁BM, and c) DPP-1 and PC₆₁BM mixture (1:1, wt %).

With the rich phase transition behaviors exhibited by **DPP-1** in the DSC study, we were encouraged to further investigate phase transitions using polarized optical microscopy (POM). Upon cooling the sample from the isotropic melt and shearing at 170 °C, a highly ordered, slightly birefringent palm-tree-leaf-like texture appeared under POM (Figure 5-7a). Its

appearance (i.e., domain size and color) and pseudo-uniaxial solid phase growth could be controlled by external forces (e.g. shearing).

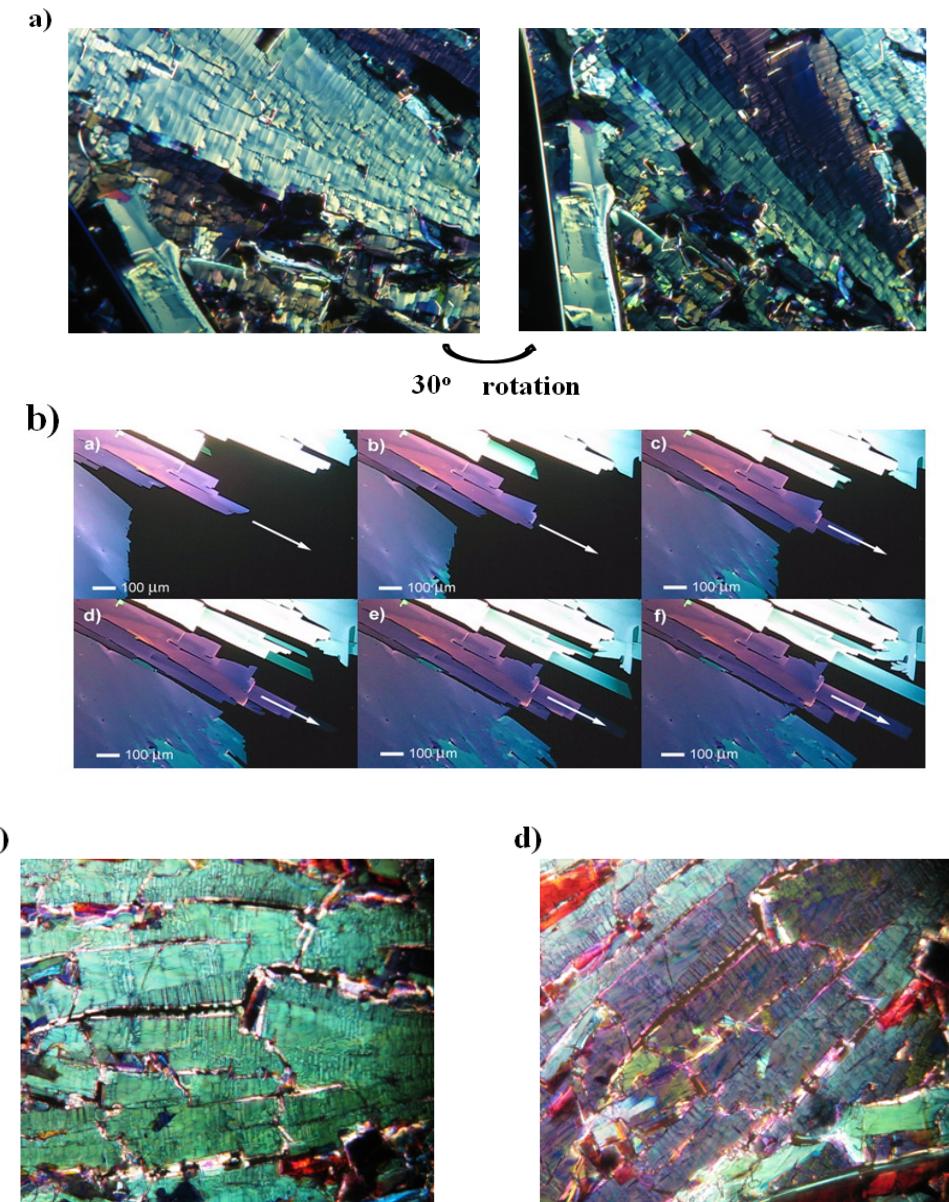


Figure 5-7. a) Polarized optical microscope (POM) images of DPP-1 under 170 °C at two different angles; b) Snapshots of the directed growth of a DPP-1 plastic phase as viewed by POM at 170 °C after shearing (pictures taken at 5 s intervals and the arrow indicates the shearing direction); c) POM images of DPP-1 under 80 °C, and d) RT

Figure 5-7b shows snapshots of directed solid phase growth that accompanied external shearing, where the images were taken every five seconds. Noticeably, while the fluidity of

DPP-1 was largely reduced after shearing, the material still appeared to be soft and waxy, suggesting that this mesophase is not liquid crystalline, but likely a columnar plastic phase.^{270,291} Another phase change, possibly from a less ordered to a more ordered columnar plastic crystal phase, was subsequently observed around 90 °C, in good agreement with the DSC results. This lower temperature phase transition may correspond to the crystallization of the two terminal alkyl chains. With the formation of another crystalline phase below 65 °C, possibly associated with solidification of the flexible triglyme chains, a mosaic-like appearance was observed by polarized light microscopy, as shown in Figure 5-7d.

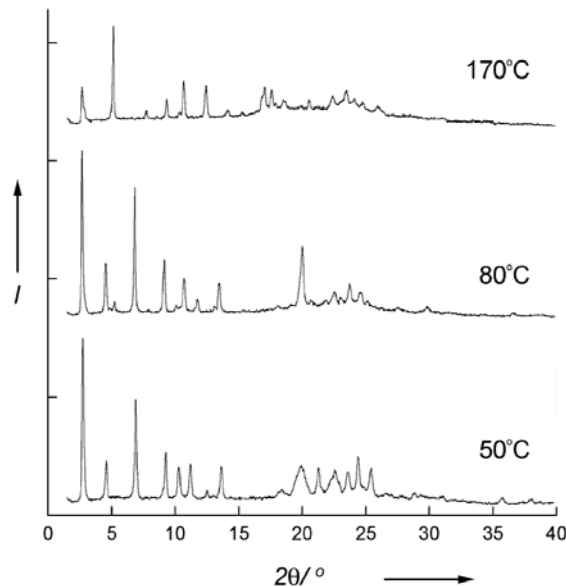


Figure 5-8. Diffraction patterns obtained from DPP-1 at 170, 80, and 50 °C.

Variable temperature X-ray diffraction was used to further confirm the formation of mesophases. Figure 5-8 shows the diffraction patterns of **DPP-1** obtained at 170, 80 and 50 °C (temperatures corresponding to the phases reported by DSC) upon cooling from the isotropic melt. Sharp Bragg reflections accompanied both high temperature mesophases (170 and 80 °C), consistent with long-range ordering and the assignment of plastic phases.²⁷⁶ That the substance is shearable at temperatures close to the clearing temperature and bears a rather soft and waxy

texture excludes the possibility that a true crystalline phase exists at 170 °C. By the same argument, **DPP-1** is likely not a plastic crystal below 65 °C given that the texture is not deformable. The nature of the mesophase around 80 °C remains unclear, since it is rather difficult to examine the texture. Unfortunately, due to the considerable orientational disorder, it is generally not very insightful to index the reflection peaks for plastic crystal phases obtained by one-dimensional X-ray diffraction.²⁹²⁻²⁹³

5.2.4 Morphology Studies

In order to “visualize” the formation of π -stacks (aggregates) in solution and on surfaces, we then examined aggregates and thin-films by atomic force microscopy (AFM). A solution investigation was performed as follows. A 2.2×10^{-4} M solution of **DPP-1** in tetrahydrofuran (THF), a good solvent for this molecule, was added dropwise to hexane, a poor solvent, while vigorously stirring. The solution turned from blue to purple after some time (a few minutes), suggesting the formation of **DPP-1** aggregates. Deposition of the suspension on mica and analysis by AFM revealed uniform nanoscale fiber-like assemblies as shown in Figure 5-9a. Similar aggregates were also formed in methylcyclohexane (MCH). These observations were also consistent with results obtained from UV-vis measurements. Briefly, UV-vis spectra of **DPP-1** in MCH were recorded every 45 seconds at 30 °C, after initial equilibration at 60 °C. Figure 5-9b clearly shows the growth of a broad absorption with $\lambda_{\text{max}} \sim 750$ nm accompanied by a solution color change from blue to purple, indicating the existence of strong excitonic interactions and the formation of π -stacks. The isobestic point at 680 nm further demonstrates a stoichiometric conversion from free molecules to crystals (aggregates). These solution studies demonstrate that **DPP-1** has a strong tendency to self-assemble into highly ordered nanostructures, most likely through synergistic solvophobic effects and π - π interactions.

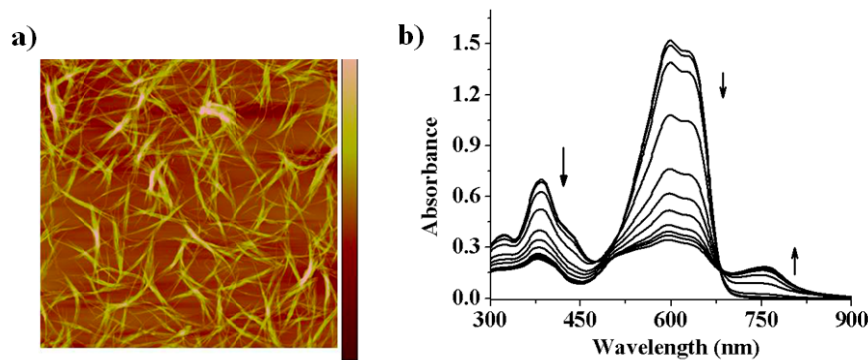


Figure 5-9. a) tapping mode AFM image ($20 \times 20 \mu\text{m}$, 250 nm in height) of DPP-1 as deposited from THF-hexane onto mica. b) UV-vis spectra of DPP-1 in methylcyclohexane ($2.2 \times 10^{-5} \text{ M}$, at 30°C) recorded at 45 s intervals;

To investigate the effect of self-organization of **DPP-1** at the interface between solution and substrate, a process relevant to the fabrication of organic electronic devices, **DPP-1** chlorobenzene solutions ($2.2 \times 10^{-4} \text{ M}$) were drop-cast onto the surface of freshly cleaved mica and studied by AFM. Tapping mode AFM images and line traces, as exhibited in Figure 5-10, showed a significant increase in ordering as the solvent evaporation time was increased from 3.5 to 8.5 minutes.

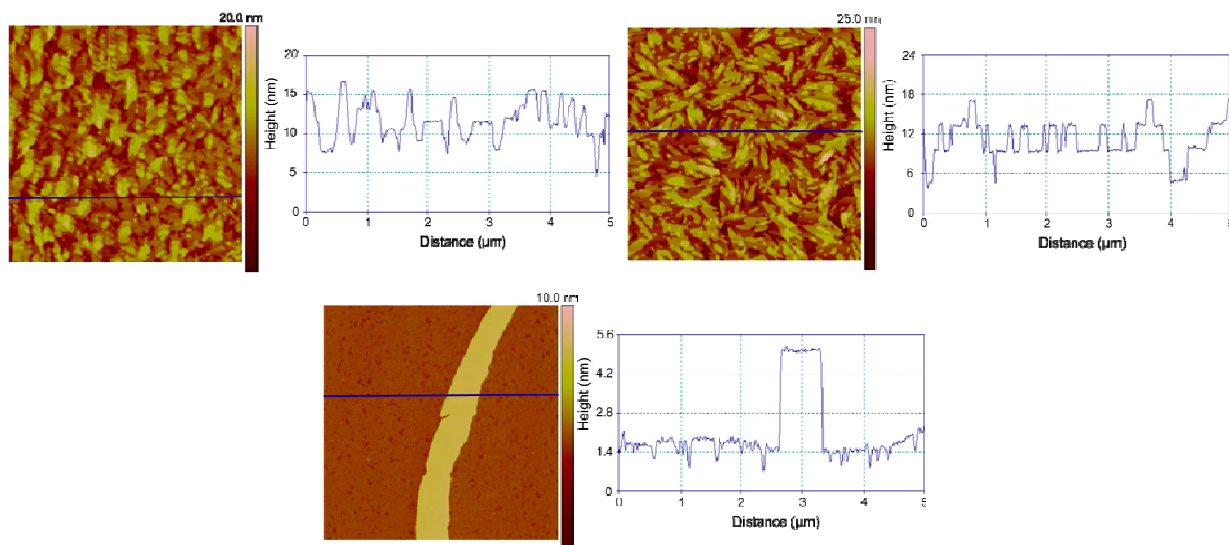


Figure 5-10. Tapping mode AFM images ($5 \times 5 \mu\text{m}$) with z-height line scan profiles of DPP-1 drop-cast from chlorobenzene ($2.2 \times 10^{-4} \text{ M}$) on mica. Solvent evaporation times are a) 3.5 min, b) 5 min and c) 8.5 min.

At 3.5 minutes, irregular aggregates formed based on the height fluctuation of the line trace across the surface. At 5 minutes, sharper features with even steps in height of 3.6–4.0 nm developed, a much more ordered arrangement. At an evaporation time of 8.5 minutes, the molecules had assembled into larger, belt-like domains with uniform step height of 3.6–4.0 nm. We propose that the step-height of 3.6–4.0 nm corresponds to **DPP-1** molecules that are packed with their long axes oriented perpendicular to the substrate.

5.2.5 Organic Field-Effect Transistors and Molecular Heterojunction Solar Cells

This section describes collaborative work on OFETs and OPVs with Professor Bernard Kippelen's group at Georgia Institute of Technology. Specifically, Dr. Shree Prakash Tiwari fabricated field-effect transistor devices, offered the data and helped in its interpretation. Dr. Hyeunseok Cheun and Jaewon Shim carried out solar cell studies and provided the data.

To determine whether the proclivity of **DPP-1** to form π -stacks via self-assembly has a pronounced impact on device performance, top contact field-effect devices with gold top source/drain electrodes and **DPP-1** as the organic semiconductor were spun-cast from chlorobenzene on O₂ plasma cleaned SiO₂. Figure 5-11 shows the output and transfer characteristics of a particular p-channel OFET ($W/L = 1000 \mu\text{m}/25 \mu\text{m}$) with **DPP-1** after annealing at 130 °C for 30 min. The operating voltage for these devices was –60 V. These OFETs exhibited average hole mobility values of $4 \times 10^{-3} \text{ cm}^2/\text{Vs}$, and current on/off ratios of 1×10^4 , with the average threshold voltage of 6.4 V (more details in Table 5-1). These results are comparable to some of the best molecular solution-processable OFET devices.^{139,294} More importantly, it suggests introducing flexible triglyme chains does not necessarily depreciate the device performance, while imparting the desired solubility for purification and processing.⁷⁸

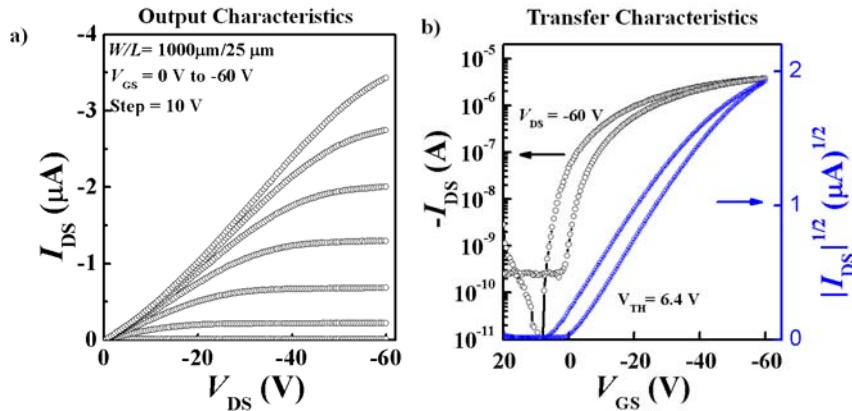


Figure 5-11. a) Output and b) transfer characteristics of a representative DPP-1 field-effect transistor device

Table 5-1. Summary of DPP-1 based OFET devices

| W/L | μ (cm^2/Vs) | V_{TH} (V) | $I_{on/off}$ |
|-----------------------------------|-----------------------------------|-----------------|-----------------|
| 1000 μ m/25 μ m (3 Dev.) | $4.1 (\pm 0.4) \times 10^{-3}$ | $6.3 (\pm 0.1)$ | 1×10^4 |
| 1000 μ m/50 μ m (4 Dev.) | $3.2 (\pm 0.8) \times 10^{-3}$ | $2.5 (\pm 1.3)$ | 8×10^3 |
| 1000 μ m/100 μ m (4 Dev.) | $3.0 (\pm 0.3) \times 10^{-3}$ | $1.5 (\pm 0.4)$ | 3×10^3 |

Solution-processed molecular bulk-heterojunction solar cells were subsequently fabricated using **DPP-1** as an electron donor material and PC₆₁BM as an electron acceptor material in a standard device configuration ITO/PEDOT:PSS/**DPP-1**:PC₆₁BM/Al. The current–voltage characteristics of a representative device before and after annealing are shown in Figure 5-12. Devices with an active layer thickness of ~ 100 nm yielded a short circuit current density (J_{sc}) of 1.56 ± 0.06 mA/cm², an open circuit voltage (V_{oc}) of 0.50 ± 0.01 V, a fill factor (FF) of 0.54 ± 0.01 , and a power conversion efficiency of $0.43 \pm 0.01\%$ under AM 1.5 G, 100 mW/cm² illumination (the values have been obtained and averaged from five devices). Upon annealing at 90 °C, the devices exhibited an enhanced J_{sc} of 2.41 ± 0.07 mA/cm², a V_{oc} of 0.55 ± 0.02 V, a FF of 0.55 ± 0.03 , and a power conversion efficiency of $0.68 \pm 0.02\%$. The external quantum efficiency increased upon annealing from 10% to above 15% in the 415–580 nm and 620–770

nm range. The PCEs of these minimally optimized devices are less than the state-of-the-art solution-processable molecular BHJ solar cells,⁸⁰ however, their fill factors before and after annealing are much higher than other solution-processed molecular solar cells reported in the literature,^{57,71,76-77,295} and are comparable to the best performing vacuum-deposited molecular heterojunction solar cells.¹⁵³ This observation indicates that there is a great deal of potential to improve the overall device efficiency, provided that a high *FF* is a prerequisite to achieving high performance from photovoltaic devices.

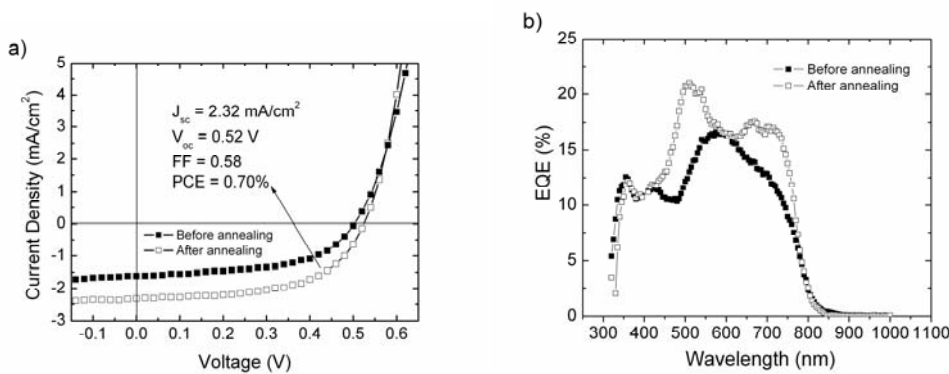


Figure 5-12. a) *J-V* characteristics and b) external quantum efficiencies of a representative DPP-1 : PC₆₁BM photovoltaic device before and after annealing at 90 °C

In summary, we have demonstrated the design, Synthesis, and characterization of the first cruciform-shaped amphiphilic π -conjugated low energy gap oligothiophene. We are hopeful that the same design principles used to achieve the desired self-assembly tendency with **DPP-1** can be extended to other polycyclic aromatic cores. We have measured hole mobilities through field-effect transistor devices and tested **DPP-1** blended with PC₆₁BM in molecular heterojunction solar cells. The high mobility indicates that self-assembly of the molecule indeed has a pronounced influence on device performance. Our preliminary results bode well for the use of this type of molecules (i.e. that is possess solution processability and long-range order via self-assembly) as active materials in field-effect transistors and photovoltaic devices.

5.3 Diketopyrrolopyrrole-based Hydrogen-bonded Amphiphilic Oligothiophenes

The self-assembly properties exhibited by **DPP-1** encouraged us to investigate other DPP-based oligothiophenes by applying a similar amphiphilic molecular design. In this section, we focus on a new set of amphiphilic oligothiophenes (**DPP-OH-n**, n=1, 2, 3 and 4), as shown in Figure 5-13. This set of molecules has structural features that are unique relative to **DPP-1**: first, the hydrophobic effect is much enhanced due to the existence of long paraffinic chains. Second, the hydrophilic chains are terminated with hydroxyl groups; strong hydrogen bonding forces are preinstalled in this manner. For comparison's purpose, **DPP-TEG** and **DPP-C12** have also been prepared. By making a comparison between **DPP-TEG** and **DPP-OH-n**, we anticipated getting insight into whether and how hydrogen bonding interactions play a role in self-assembly and their phase transition; the pair of **DPP-C12** and **DPP-OH-n** is expected to provide information on hydrophobic effects, which are obviously absent in **DPP-C12** and present in **DPP-OH-n**. Third, a set of **DPP-OH** molecules is proposed and prepared; in these materials, the strength of pi-pi interactions is varied via the number of thiophene rings.

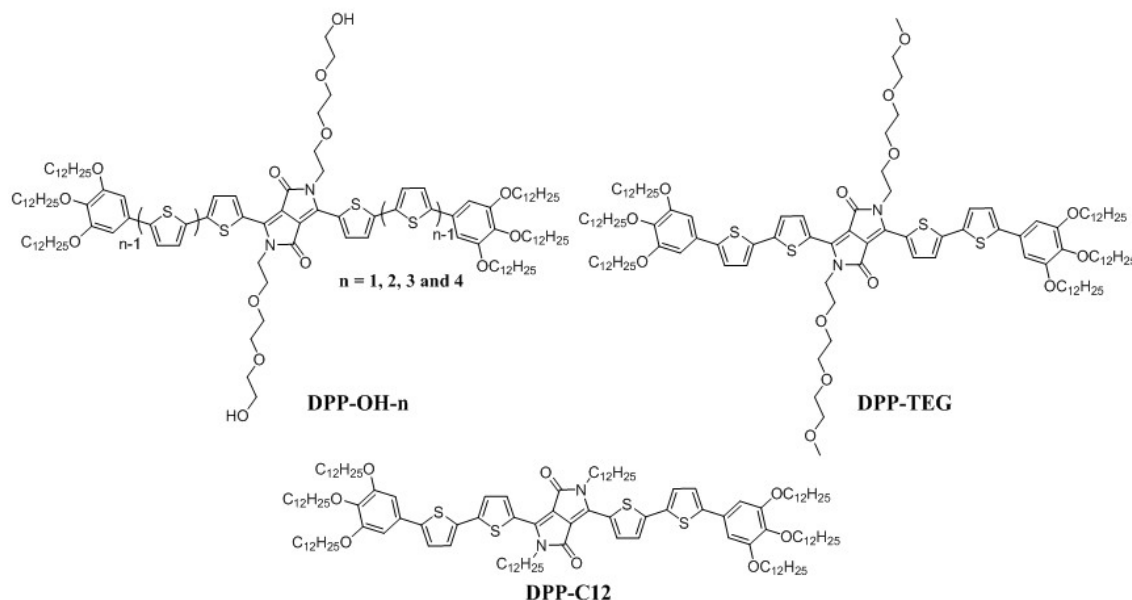


Figure 5-13. Molecular structures of DPP-OH-n and DPP-TEG.

5.3.1 Synthesis of DPP-OH-n ($n = 0, 1, 2$ and 3) and DPP-TEG

The Synthesis of the donor building blocks is illustrated in Figure 5-14. Compound **5-5** is a donor for **DPP-OH-1**, and also acts as an intermediate for other extended pi-conjugated donor building blocks. It is worth mentioning that **5-5***, an analog of compound **5-5**, has been previously prepared in a multi-step ($n > 5$) Synthesis, as shown in Figure 5-15.²⁹⁶ Using iridium-catalyzed borylation,²⁹⁷ we are able to shorten the sequence to two steps from the commercially available pyrogallol (benzene-1,2,3-triol). And the overall yield has increased to 86% from 26%. Upon reacting **5-5** with 2-bromothiophene, 5-bromo-2,2'-bithiophene, and 2-Bromo-5,2':5',2"-terthiophene via the palladium-catalyzed Suzuki reaction, followed by the iridium-catalyzed selective borylation on the 5 position of the terminal thiophene ring, donor building blocks **5-7**, **5-9** and **5-11** were successfully prepared in good yields. Due to the simplicity of the chemistry demonstrated here, these donor building blocks can be easily scaled up to tens of grams.

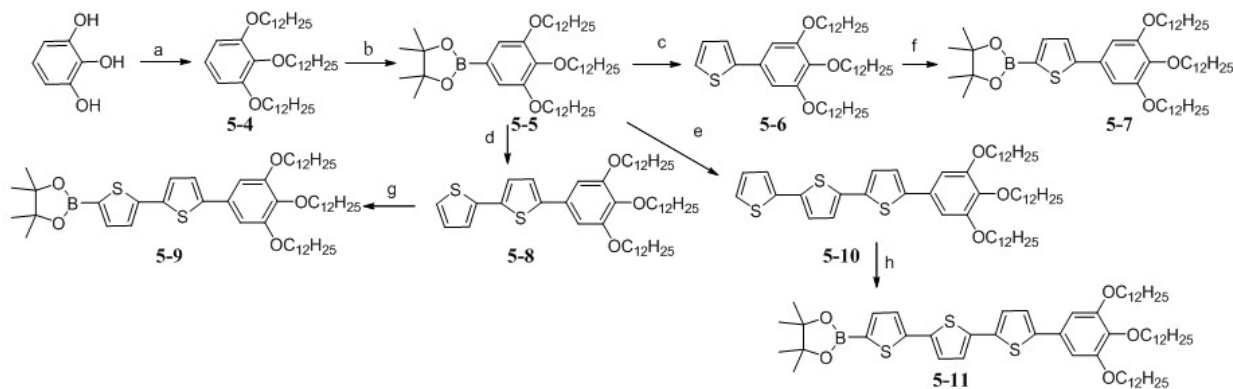


Figure 5-14. Synthesis of donor building blocks for DPP-OH-n. a) $\text{C}_{12}\text{H}_{25}\text{Br}$, K_2CO_3 , DMF, 60°C , 94%; b) 4,4,4',4',5,5,5',5'-octamethyl-2,2'-bi(1,3,2-dioxaborolane), $\text{Ir}[\text{OMe}(\text{COD})]_2$, heptane, 80°C , 91%; c) 2-bromothiophene, $\text{Pd}_2(\text{dba})_3$, $\text{P}(\text{o-tyl})_3$, aqueous Et_4NOH , toluene, 98%; d) 2-bromobithiophene, $\text{Pd}_2(\text{dba})_3$, $\text{P}(\text{o-tyl})_3$, aqueous Et_4NOH , toluene, 71%; e) 2-bromotertithiophene, $\text{Pd}_2(\text{dba})_3$, $\text{P}(\text{o-tyl})_3$, aqueous Et_4NOH , toluene, 72%; f) 4,4,4',4',5,5,5',5'-octamethyl-2,2'-bi(1,3,2-dioxaborolane), $\text{Ir}[\text{OMe}(\text{COD})]_2$, heptane, 80°C , 50%; g) 4,4,4',4',5,5,5',5'-octamethyl-2,2'-bi(1,3,2-dioxaborolane), $\text{Ir}[\text{OMe}(\text{COD})]_2$, heptane, 80°C , 50%; h) 4,4,4',4',5,5,5',5'-octamethyl-2,2'-bi(1,3,2-dioxaborolane), $\text{Ir}[\text{OMe}(\text{COD})]_2$, heptane, 80°C

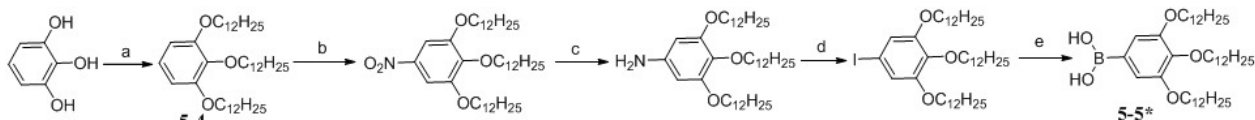


Figure 5-15. Synthesis of 3,4,5-tris(dodecyloxy)phenylboronic acid. a) K_2CO_3 , $\text{C}_{12}\text{H}_{25}\text{Br}$, DMF, 90°C , 24h, 85%; b) NaNO_2 , HNO_3 , H_2O , CH_2Cl_2 , rt, 3h, 90%; c) hydrazine, graphite, EtOH , 110°C , 24h, 88%; d) NaNO_2 , HCl , H_2O , 0°C and then KI , rt, 12h, 49%; e) $n\text{BuLi}$, THF , -78°C followed by $\text{B}(\text{OMe})_3$, -78°C and HCl , H_2O , 80%.

The Synthesis of the DPP core is shown in Figure 5-16. The Synthesis started with the protection of 2-(2-bromoethoxy)ethoxy with the *tert*-butyldimethylsilyl (TBDMS)group, yielding 12-bromo-2,2,3,3-tetramethyl-4,7,10-trioxa-3-siladodecane (**5-12**). N-alkylation of **5-1** with **5-12** was carried out in DMF using potassium carbonate as a base. It should be mentioned that direct N-alkylation of **5-1** with 2-(2-bromoethoxy)ethoxyethanol was also successful, however, subsequent purification turned out to be extremely difficult as a result of the limited solubility of the resulting product. By attaching TBDMS groups this problem is resolved. The relatively low yield of 42% is in part caused by the poor purity of the starting material **5-1**, as was mentioned earlier. We also attempted an alternative route to obtain **5-13** by replacing compound **5-12** with its tosylate analog, however the yield was even lower. Bromination of **5-13** was problematic in our hands and the reaction yields were extremely low; it was later discovered that the TBDMS groups were partially removed during this process.²⁹⁸ After optimizing the reaction conditions, we were able to obtain compound **5-14** in ~60% yield. The Synthesis of DPP cores for **DPP-TEG** and **DPP-C12** has been previously described in section 5.2.

With the donor building blocks and the DPP cores in hand, **DPP-OH-n**, **DPP-TEG** and **DPP-C12** were synthesized by Suzuki coupling, using $\text{Pd}_2(\text{dba})_3$ and $\text{P}(\text{o-tyl})_3$ as the catalyst and ligand respectively, aqueous Et_4NOH as the base, and toluene as the solvent. The yields ranged from 54% to 84%. The synthetic details can be found in the experimental section.

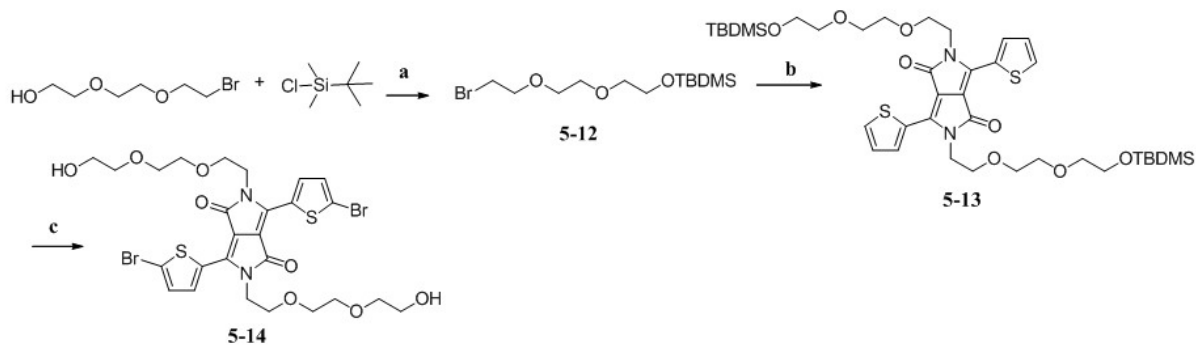


Figure 5-16. Synthesis of DPP core for DPP-OH-n. a) Et₃N, CH₂Cl₂, rt, 95%; b) **5-1**, K₂CO₃, DMF, 90°C, 24h, 42%; c) NBS, chloroform, then HCl, H₂O, rt, 60%.

5.3.2 Structural Characterization, Optical and Electrochemical Studies

The structures of the molecules under investigation have been supported by ¹H- and ¹³C-NMR, as well as HRMS. As an example, Figure 5-17 shows ¹H-NMR spectra of **DPP-C12**, **DPP-TEG** and **DPP-OH-2**. Their peak assignments are briefly discussed as follows.

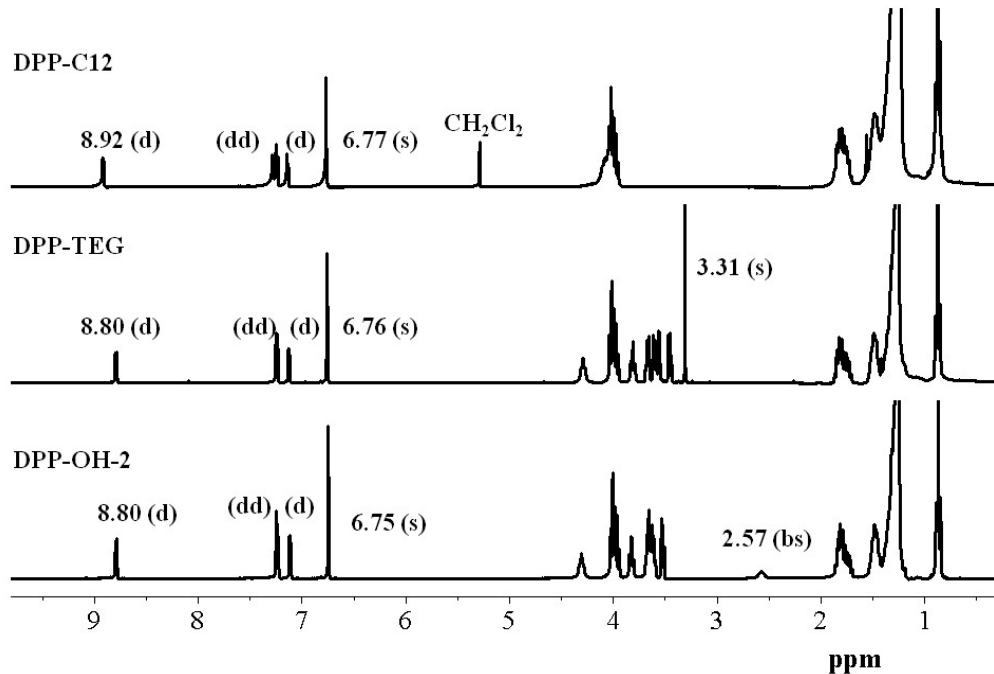


Figure 5-17. ¹H-NMR spectra of DPP-C12, DPP-TEG and DPP-OH-2

It is clear from Figure 5-17 that the chemical shift patterns in the aromatic region from 6.7 to 8.9 ppm are very similar for all three molecules, resulting from the same pi-conjugated

segment that all three have in common. Four protons on the two thiophene rings (one side) are split into four doublets. The most downfield doublet at ~8.8-8.9 ppm corresponds to the proton on the thiophene ring next to the DPP core; while the doublet at 7.1 ppm is assigned to the proton on the thiophene ring next to the benzene ring. Due to their similar chemical surroundings, the two inner protons (3 and 3' positions) on the thiophene rings are partially overlapped and appear as a doublet of doublets (dd) around 7.26 ppm, with the signal from deuterated chloroform (residue) also overlapping. The singlet that stands at ~6.76 ppm is undoubtedly assigned to the two symmetric protons on the benzene ring. The similarity in the aromatic region among the three NMR spectra suggests that these molecules are highly solvated and little or no influence is observed from pi-pi interactions.

In the aliphatic region from 3.31 to 4.31 ppm, **DPP-TEG** and **DPP-OH-2** also look very similar except that **DPP-TEG** has a sharp singlet located at 3.31 ppm from the terminal methyl group on the triglyme chains, and **DPP-OH-2** has a broad singlet located at 2.57 ppm from the terminal hydroxyl group. **DPP-C12** has a different appearance in this region; only one broad multiplet sitting around ~3.90-4.15 ppm is observed, corresponding to the methylene groups connected to the nitrogen atoms. All three molecules exhibit the same pattern in the region below 2 ppm. These peaks are from the protons on the aliphatic chains attached to the benzene rings.

Figure 5-18 shows the absorption spectra of the **DPP-OH-n** series along with photographs of their methylene chloride solutions. With increasing the numbers of thiophene rings, the absorption onsets move from 642, to 693, to 711 and finally to 721 nm for **DPP-OH-1**, **2**, **3** and **4**, respectively. From **DPP-OH-1** to **DPP-OH-2**, the difference in absorption onset is about 50 nm. The difference decreases to 18 nm from two to three thiophene rings. And it continually decreases to 10 nm when moving from **DPP-OH-3** to **DPP-OH-4**. The trend for high energy

bands (π to π^* transition), however, is not clear. **DPP-OH-1** and **DPP-OH-3** have very similar high energy bands with absorption maxima at \sim 401 nm. The intensity ratio of the high energy band to the charge transfer band for these two molecules is different. **DPP-OH-3** has a very strong absorption for the π to π^* transition; where **DPP-OH-1** has a relatively weak π to π^* transition. In the case of **DPP-OH-2** and **DPP-OH-4**, they have very similar intensity ratios of the two bands, but rather different absorption maxima at 371 and 421 nm, respectively, which may be caused by the odd/even effect,²⁹⁹⁻³⁰⁰ which refers to the electronic geometry difference between odd and even number of rings.

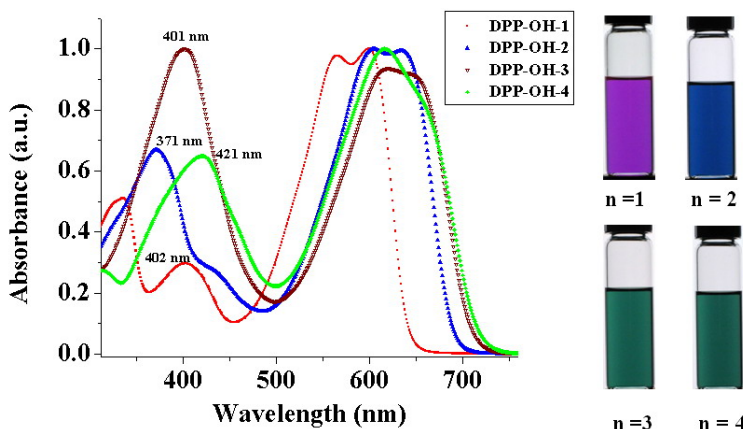


Figure 5-18. Absorption spectra of DPP-OH-n ($n = 1-4$) in CH_2Cl_2 and their optical images

Table 5-2 shows the electrochemical energy levels and gaps of **DPP-OH-n** ($n = 1-4$) obtained from DPV by drop casting of the samples on platinum electrodes. With increasing donor strength, the HOMO levels from **DPP-OH-1** to **DPP-OH-4** increase from -5.55 to -5.26 eV. Interestingly, the LUMO levels deepen as well from -3.77 to -3.69 eV, which suggests that the LUMO level is affected by the extension of conjugation length as well. The change of HOMO and LUMO levels consequently leads to a narrowing of energy gaps, which drops from 1.78 to 1.57 eV from **DPP-OH-1** to **DPP-OH-4**. It is noticed that the interval of energy gaps is consistent with that of the absorption onset aforementioned; an observation which is also evident

in the color of these molecules, from purple, to blue and eventually to green. These results indicate the conjugation length is almost saturated after attaching three thiophene rings to both sides of the molecule.

Table 5-2. Electrochemical energy levels and gaps of DPP-OH-n (n = 1-4) from DPV

| | DPP-OH-1 | DPP-OH-2 | DPP-OH-3 | DPP-OH-4 |
|--------------------------|----------|----------|----------|----------|
| HOMO (eV) | -5.55* | -5.38 | -5.29 | -5.26 |
| LUMO (eV) | -3.77 | -3.74 | -3.70 | -3.69 |
| E_g(eV) | 1.78 | 1.64 | 1.59 | 1.57 |

* This is obtained through solid stage optical energy gap and the LUMO level via solid state electrochemical measurements. E_g = LUMO-HOMO

5.3.3 Thermal Analysis

DSC studies have been carried out to investigate the influence of hydrophobic effects and hydrogen bonding on the self-assembly and phase transition behaviors of these molecules. Figure 5-19a shows the DSC thermogram of **DPP-12**. It has two well-defined thermal transitions. At ~33 °C, the broad peak corresponds to melting of the terminal dodecyl chains. This transition has also been observed in **DPP-TEG** and **DPP-OH-2**. **DPP-12** melts around 122 °C. In contrast, **DPP-TEG** melts around 91 °C; there is about a 30 °C decrease in melting temperatures between **DPP-12** and **DPP-TEG**. This can be ascribed to the flexible nature of triglyme chains in **DPP-TEG**. On the contrary, the melting (clearing) temperature increases to 141 °C for **DPP-OH-2**, in which triglyme chains are terminated with hydroxyl groups. This higher clearing temperature is associated with the strong hydrogen bonding forces that hold the individual molecules in the form of supramolecular nanostructures. The hydrogen bonded network of **DPP-OH-2** is indicated by the appearance of a cold recrystallization at 77 °C, a behavior of some high polymers.³⁰¹⁻³⁰²

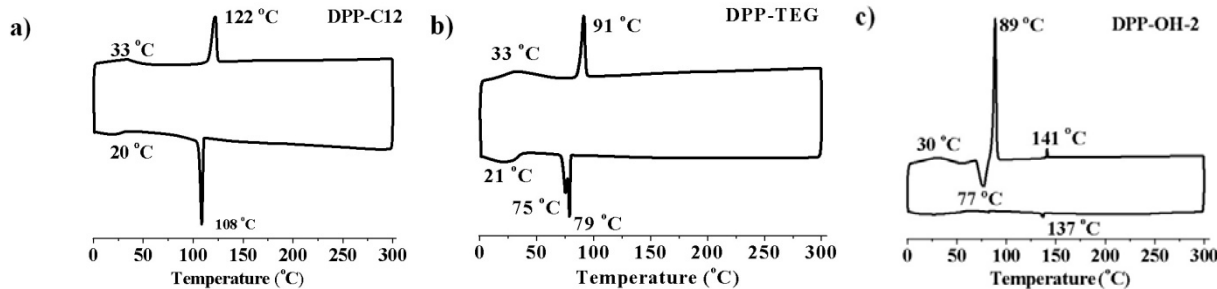


Figure 5-19. DSC thermograms of DPP-C12, DPP-TEG and DPP-OH-2.

It is clear that we can alter the phase transition behaviors to a large degree by altering the passive groups on the functional electroactive molecules. Phase transition behaviors are directly associated with the microstructures (or morphology) in a material. In other words, we can alter microstructures of a material via changing the passive groups. Therefore, this approach seems applicable to designing new electroactive materials for organic electronics, where material morphology plays a very important role.

Figure 5-20 illustrates the thermal transition behaviors of **DPP-OH-n** ($n = 1-4$). With the extension of the conjugated segments from one to four thiophene rings, the melting temperature increases from ~ 100 °C to ~ 237 °C. A ~ 40 , 45 and 50 °C increase in melting temperature is observed for each thiophene extension. This trend can be explained by the decreasing mass ratio of flexible chains to conjugated rigid core, however, it may also result from the stronger pi-pi interactions that occur on increasing the pi surface areas (from **DPP-OH-1** to **DPP-OH-4**). This could be easily verified by the pi-pi distance in an X-ray study; unfortunately, we do not have this data set on hand at this time.

We also studied these molecules by POM. Surprisingly, no obvious birefringence was observed for any of the molecules, while it was clearly shown in **DPP-1** (Note: the melting temperature is too high in the case of **DPP-OH-4**, and is out of the operation range of our instrument. It is thus not included in this discussion). These observations once again raise the

question of whether these amphiphilic cruciform shaped molecules are plastic crystals, as we proposed for **DPP-1** (Section 5.2.2). To answer this question, a series of advanced 2-D X-ray studies should be carried out, however, this has been delayed due to technical difficulties we have encountered; we will continue to work toward the realization of these phase assignments in the future.

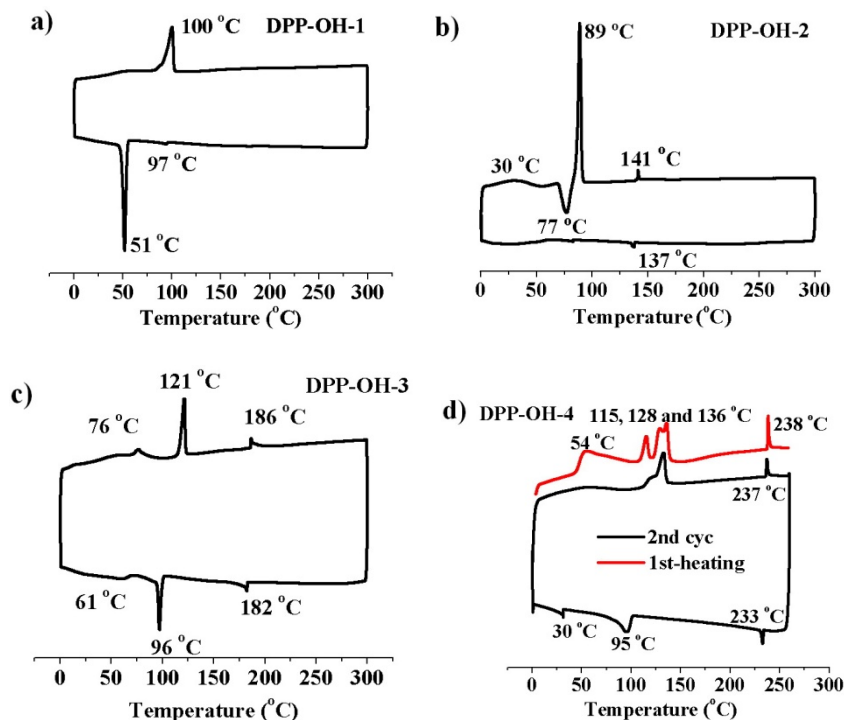


Figure 5-20. DSC thermograms of DPP-OH-n (n=1, 2, 3 and 4).

5.4 Thermally Cleavable DPP-Based Low Bandgap Polymer

As introduced at the beginning of this chapter, thermally cleavable conjugated polymers are of interest for a number of reasons. For instance, the loss of solubilizing groups will likely lead to an increase in glass transition temperature, which is closely related to the stable and rigid morphologies desired in blends, hence providing more reliable photovoltaic performance. In the course of studying DPP-based materials, we realized the convenience of functionalization of diketopyrrolopyrrole building block **5-1** with thermocleavable *tert*-butoxycarbonyl groups (^tBoc)

at the N,N' positions (^tBoc groups can be thermally removed around 180-200 °C³⁰³⁻³⁰⁴). In this section, we use the following polymer **PDPP-Boc** (Figure 5-21) as an example to investigate its performance as an active materials before and after cleavage in BHJ solar cells.

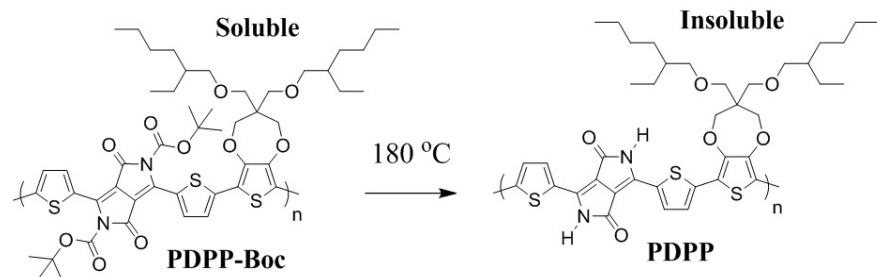


Figure 5-21. Thermal transition of PDPP-Boc

The Synthesis of **PDPP-Boc** is outlined in Figure 5-22. First, conversion of insoluble pigment **5-1** into soluble compound **5-15** was successfully achieved at room temperature by stirring **5-1** in THF with di-*tert*-butyl dicarbonate, using 4-dimethylaminopyridine (DMAP) as a catalyst. Compound **5-15** was subsequently brominated with NBS at the 2 and 5 positions on the thiophene rings to give compound **5-16**. Due to its proclivity to cleave the ^tBoc group, acetic acid should be avoided as a catalyst in the bromination step, as is often practiced in previous studies. With the DPP core **5-16** in hand, **PDPP-Boc** polymer was obtained by Stille coupling the DPP-core with 2,5-tributylstannyl-2-ethylhexyloxy-substituted-3,4-propylenedioxythiophene (ProDOT-Sn2) in toluene. The number-average molecular weight obtained was around 26.8 kDa, with a PDI of 2.2 by GPC measurement.

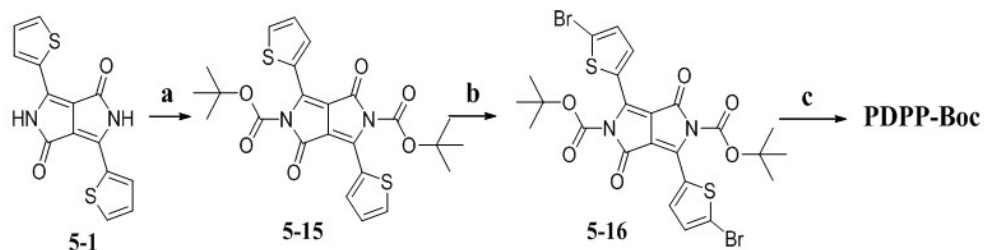


Figure 5-22. a) di-*tert*-butyl dicarbonate, DMAP, THF, rt, 60%; b) NBS, CHCl₃, rt, 77%; c) ProDOT-Sn2, Pd₂(dba)₃, P(o-tolyl)₃, toluene, 85 °C, 85%.

A thermal cleavage study of **PDPP-Boc** was carried out by TGA, as shown in Figure 5-23a. The onset of weight loss starts from \sim 155 °C and ends at 210 °C with a rate of 50 °C min⁻¹. The percent mass loss for this temperature window is about 23.1%, in good agreement with the theoretical value of 21.4%, thus confirming the successful cleavage of the ^tBoc groups.

Figure 5-23b shows the UV-vis absorption spectra of **PDPP-Boc** in chloroform solution and as thin films (before and after cleavage). In solution, **PDPP-Boc** has a single broad absorption starting from 450 and extending to 1039 nm, with an absorption maximum at \sim 783 nm and an absorption shoulder around \sim 887 nm. Upon spin-casting from chlorobenzene solution on a glass substrate, the absorption maximum has a red-shift to 809 nm, together with a bathochromic shift to 1068 nm for the onset. Surprisingly, the absorption maximum of the film has a hypsochromic shift back to 800 nm upon annealed at 180 °C for 20 min. Similarly, the absorption onset moves back to 1036 nm.

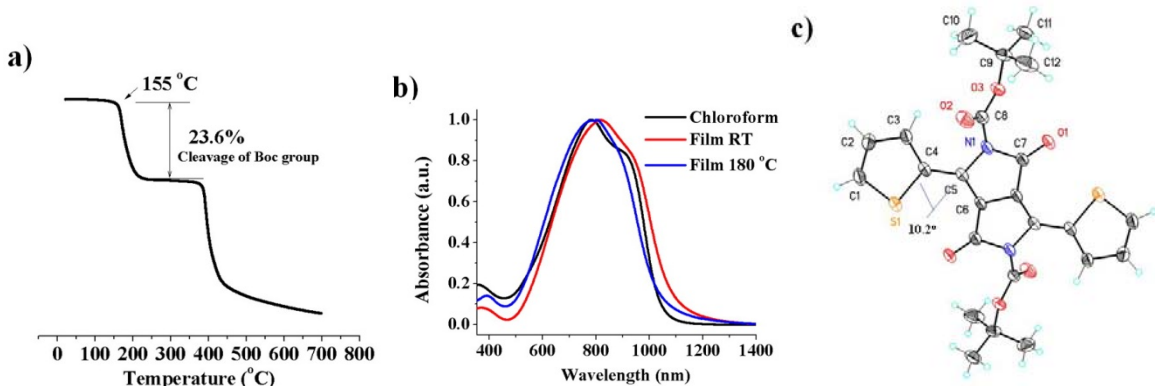


Figure 5-23. a) Weight loss of PDPP-Boc as a function of temperature; b) Absorption spectra of PDPP-Boc in solution, thin-film before and after cleavage; c) Crystal structure for compound 5-15.

These observations were not expected at first glance for a number of reasons. **PDPP-Boc** has a fairly planar backbone before the cleavage, as indicated by the crystal structure of **5-15** (Figure 5-23c). The ^tBoc sticks out and causes little distortion. Therefore, the contribution from planarization is expected to be minimal upon cleavage and will not likely lead to a significant

bathochromic shift. On the other hand, the expected formation of hydrogen bonding interactions may create a large bathochromic shift. Iqbal et al studied DPP-based latent pigment, as illustrated in Figure 5-24, where the bathochromic shift was found to be as large as 100 nm after cleavage of the ^tBoc group, accompanied with a color change from yellow to red.³⁰⁵ The planization of the molecule, and concurrent formation of hydrogen bonding, resulting from the cleavaging reaction, leads to enhanced J aggregates and causes the color change.

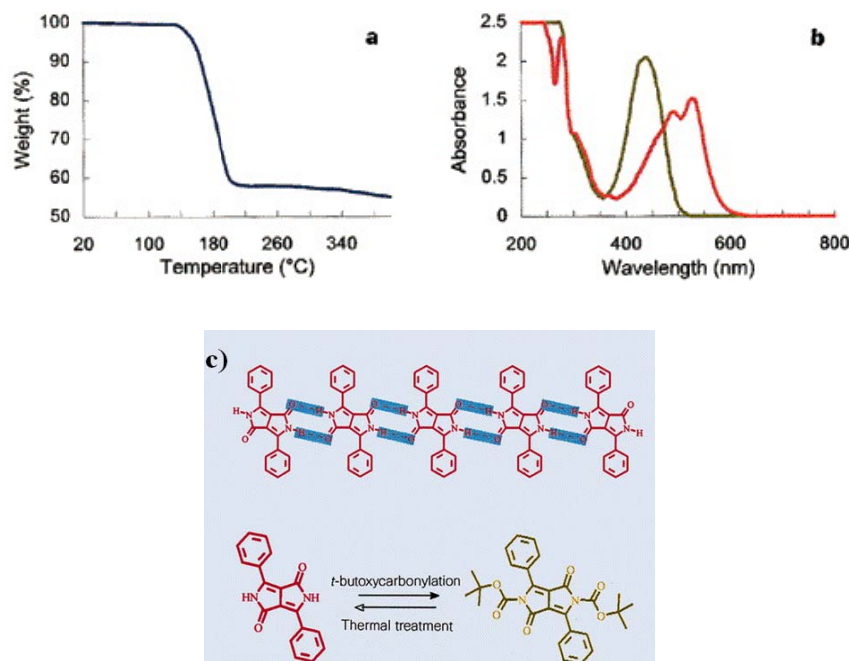


Figure 5-24. a) Weight loss of N, N' -bis-(*tert*-butoxycarbonyl)-DPP as a function of temperature (rate, 10 °C min-1; onset, 163.6 °C; midpoint, 177.7 °C; end point 191.8 °C; step height, 40.7%); b) Ultraviolet-visible absorption spectra of a 1.5- μ m-thick p - hydroxy-polystyrene film containing 40% N, N' -bis-(*tert*-butoxycarbonyl)-DPP, spin-coated (yellow) and after 2 min at 180 °C (red); c) Schematic illustration of the hydrogen-bonding network of DPP. (Adapted with permission from Ref 248.)

The hypsochromic shift in the **PDPP-Boc** polymer can then be *possibly* ascribed to a lack of hydrogen bonding and a weakening in acceptor strength. **PDPP-Boc** has 2-ethylhexyloxy-substituted-3,4-propylenedioxythiophene monomers incorporated along the backbone. The bulky solubilizing groups on the dioxythiophene likely block the formation of the desired hydrogen

bonding interaction, or at least lower it to some extent. In addition, the ^tBoc group is an electron-withdrawing substituent, which can possibly lower the LUMO level of the DPP core. After the cleavage of the ^tBoc, its contribution as an electron-withdrawing group disappears. The combination of the two factors may eventually account for the blue shift upon cleavage.

CV and DPV analyses of drop cast thin films of **PDPP-Boc** were also performed, as shown in Figure 5-25. Applying an anodic potential to **PDPP-Boc** shows a single oxidation at an $E_{1/2}$ of 0.59 V with an onset of oxidation at 0.26 V. Reduction of **PDPP-Boc** (Figure 5-25a) shows a first reduction at an $E_{1/2}$ of -1.23 V, with an onset for the first reduction at -1.08 V. This reduction is quasi-reversible with adequate charge compensation on the reverse scan. A second reduction is observed that is chemically irreversible. The electrochemical band gap is taken as the onset of oxidation minus the onset of reduction. Thus, **PDPP-Boc** has an electrochemical band gap of 1.34 eV estimated by CV. One of the advantages of DPV is the increased sensitivity allowing for a more accurate estimation of the onsets of oxidation and reduction. DPV was performed on **PDPP-Boc** (Figure 5-25b) and shows an onset for reduction at -1.02 V, and an onset for oxidation at 0.07 V, leading to an estimated band gap of 1.09 eV. In comparison, **PDPP-Boc** has an optical band gap of ~1.16 eV, in the middle of the electrochemical band gaps estimated from CV and DPV.

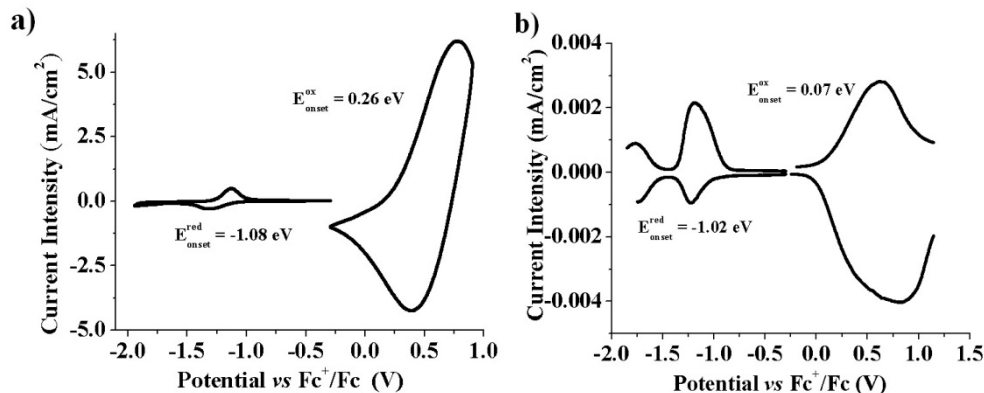


Figure 5-25. Cyclic voltammograms and differential pulse voltammograms of **PDPP-Boc**.

The HOMO levels estimated from CV and DPV are -5.36 and -5.17 eV, respectively. This relatively high HOMO level suggests that **PDPP-Boc** is prone to air oxidation. The LUMO levels estimated from CV and DPV are very close at \sim -3.9-4.0 eV. Thus the energy offset between **PDPP-Boc** and PCBM is merely 0.2 eV, which may cause inefficient electron transfer in the polymer/PCBM BHJ solar cells.

The solar cell study as follows was performed by *Dr Jegadesan Subbiah*. The photovoltaic properties of **PDPP-Boc** were studied in bulk heterojunction solar cells using (6,6)-phenyl-C₇₁-butyric acid methyl ester (PC₇₁BM) as the electron acceptor. All solar cell results were collected under atmospheric conditions, and under 100 mWcm⁻² simulated AM 1.5G illumination. The **PDPP-Boc**/PC₇₁BM blends were spin-cast from chlorobenzene on PEDOT-PSS coated ITO glass substrates. The photoactive layers were subjected to thermal annealing at either 75 °C or 180 °C before the top electrode was deposited. Figure 5-26 shows the current density-voltage characteristics of the PV devices with various polymer:PC₇₁BM compositions and the device performance is presented in Table 5-3.

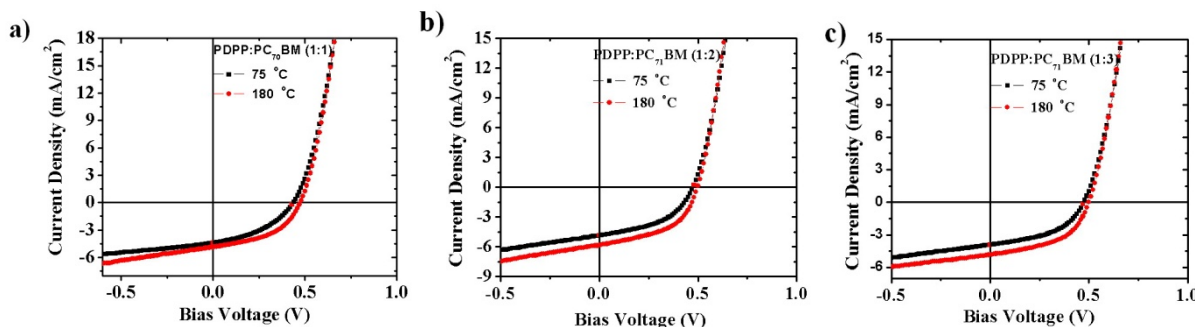


Figure 5-26. The J-V curve of a DPP polymer solar cell under AM 1.5 conditions with a blend ratio of a) 1:1, b) 1:2, and c) 1:3.

A polymer:PC₇₁BM ratio of 1:2 was found to be the optimum blend ratio, yielding a power conversion efficiency (PCE) of 1.44%, as shown in Table 5-3. Here, the device annealed at 75 °C exhibit a power conversion efficiency (PCE) of 1.08%, a short-circuit current density

(J_{sc}) of 4.86 mA/cm², an open-circuit voltage (V_{oc}) of 0.47 V and a fill factor (FF) of 0.48.

Annealing the device at 180 °C leads to the thermo-cleavage which improves the cell performance resulting in an increase in PCE, V_{oc} , J_{sc} and FF to 1.44%, 5.88 mA/cm², 0.49 V and 0.50, respectively. The enhancement in the device performance is perhaps due to the chemical change in the polymer film due to thermal treatment and associated changes in thickness and morphology of the film. Similar enhancement in the performance due to thermocleavage was observed for the solar cell fabricated with the blend ratios of 1:1 and 1:3. The possible chemical transition from thermal treatment is shown in Figure 5-1. As evident for the clearance, the photoactive layer became insoluble in organic solvent after annealing at 180 °C for 10 min. Here, the performance of the solar cell with a blend ratio of 1:1 exhibited lower performance with a PCE of 0.78% before annealing and 1.08 % after annealing; a PCE of 0.87% before annealing and 1.21% after annealing was obtained in the case of a polymer/PC₇₁BM ratio of 1:3.

Table 5-3. Photovoltaic performance of PDPP/PC₇₁BM solar cells with different blend ratio.

| PDPP-Boc:PCBM (wt%) | Annealing condition (°C) | J_{sc} (mA/cm ²) | V_{oc} (V) | FF (%) | PCE (%) |
|---------------------|--------------------------|--------------------------------|--------------|--------|---------|
| 1:1 | 75 | 4.40 | 0.43 | 41 | 0.78 |
| 1:1 | 180 | 4.79 | 0.47 | 48 | 1.07 |
| 1:2 | 75 | 4.86 | 0.47 | 48 | 1.08 |
| 1:2 | 180 | 5.88 | 0.49 | 50 | 1.44 |
| 1:3 | 75 | 3.93 | 0.47 | 47 | 0.87 |
| 1:3 | 180 | 4.83 | 0.49 | 51 | 1.21 |

The overall performance of **PDPP-Boc** remains moderate with a PCE of 1.44% at the optimum blend ratio, in spite of the enhancement in the PCE after thermocleavage. This can be in part explained by an inefficient charge transfer between the polymer and PC₇₁BM, due to the small energy offset between their LUMO levels (~0.2 eV). In addition, these results are also likely to correlate with the polymer's charge mobility. In this regard, charge mobilities of **PDPP-**

Boc and **PDPP** in pure films and in blends are measured by modeling of the *J-V* response of space-charge limited current diode devices. These results are exhibited in Table 5-4. The pure **PDPP-Boc** polymer film presents a SCLC hole mobility of $1 \times 10^{-5} \text{ cm}^2\text{V}^{-1}\text{s}^{-1}$; while its blend film yields a hole mobility of $8.5 \times 10^{-6} \text{ cm}^2\text{V}^{-1}\text{s}^{-1}$. Compared to the hole mobilities of $4 \times 10^{-2} \text{ cm}^2\text{V}^{-1}\text{s}^{-1}$ exhibited by a known DPP-based polymer in a field effect transistor device,⁴¹ our charge mobilities are considerably lower (Note: the direct comparison of mobilities from SCLC and OFET is usually not valid, considering the different device structures for diodes and transistors, but it gives us a rough idea of how big the difference is). The low hole mobility in the blend may be partially responsible for the moderate photovoltaic performance. Upon cleavage, the hole mobilities from **PDPP** are still relatively low around $6.2 \times 10^{-5} \text{ cm}^2\text{V}^{-1}\text{s}^{-1}$ for the pure film and the blend, but they are significantly higher than those of **PDPP-Boc**. This observation may explain the boost in PCE after cleavage of the ^tBoc group.

Table 5-4. Transport properties of PDPP-Boc and PDPP polymer and their blends with PC₇₁BM in a ratio of 1:2

| Active layer | PDPP-Boc | PDPP ^a | PDPP-Boc:PC ₇₁ BM | PDPP:PC ₇₁ BM ^a |
|--|--------------------|----------------------|------------------------------|---------------------------------------|
| Hole mobility [cm ² /Vs] | 1×10^{-5} | 6.2×10^{-5} | 8.5×10^{-6} | 6.2×10^{-5} |

a) annealing at 180 °C

PDPP gives a PCE of 1.44% in our preliminary study. Interestingly, this value still makes **PDPP** one of the best performing thermocleavable polymers for organic solar cells.^{303-304,306-309} This suggests that more effort shoud put forth to improve the photovoltaic performance of thermocleavable conjugated polymers. As we expect higher performance from this type of material is indeed feasible. In the case of DPP based conjugated polymers, more enhanced performance may be realized if we can improve the charge mobility, as well as enlarge the energy offset to provide for more efficient charge transfer. In addition, it may also be interesting

to develop a processing method for device fabrication that can highlight the solubility switching upon cleavage. In that sense, multi-layer devices with complementary absorbing polymers via solution processing may be an option to improve solar cell performance.

5.5 Conclusion

In this chapter, we have explored two classes of relatively undeveloped materials based on diketopyrrolopyrrole chemistry for field-effect transistor and solar cell applications. Using **DPP-1** as an example, we applied an amphiphilic molecular design to obtain a discrete oligomer with a well-defined molecular structure. With the amphiphilic nature and the special cruciform-shape, **DPP-1** exhibits a strong tendency to self-assemble into highly ordered nanostructures in solution, in the bulk, and on surfaces. Solution processed field-effect transistor devices yielded hole mobilities of up to $4 \times 10^{-4} \text{ cm}^2 \text{V}^{-1} \text{s}^{-1}$. PCEs of **DPP-1/PC₆₁BM** solar cell devices were only around 0.7%, but with high fill factors of ~0.58, great potential for further optimization exists. Encouraged by these findings, **DPP-OH-n** ($n = 1, 2, 3$ and 4), together with their control molecules **DPP-C12** and **DPP-TEG**, were prepared. DSC studies of these molecules suggests that phase transition behaviors can be largely altered by varying the passive solubilizing groups, which opens vast possibilities to control morphology in thin-film devices via the material design approach.

Thermocleavable polymers are of interest, motivated by their photochemical stability, improvement of the chromophore density in the device film, and significant advantages in terms of processing (solubility/insolubility switching). In this chapter, we introduced a DPP-based thermocleavable conjugated polymer (**PDPP-Boc**) and studied its utilization as an electron donor in bulk-heterojunction solar cells. A typical **PDPP-Boc/PC₇₁BM** bulk-heterojunction solar cell showed a PCE of 1.08%, V_{oc} of 0.47, J_{sc} of 4.68 mA/cm² and FF of 0.48. Upon cleavage of the solubilizing (protecting) groups, the **PDPP/PC₇₁BM** photovoltaic device exhibited a PCE of

1.44%, V_{oc} of 0.49, J_{sc} of 5.88 mA/cm² and FF of 0.50. A significant enhancement has been observed. This encouraging observation will draw more attention to the use of thermocleavable materials for solar cell applications, and further investigation is required to fully unveil their potential for photovoltaic applications.

5.6 Experimental Details

N,N'-bis-(10-(3,6,9-trioxadecyl)-3,6-di(5-thienyl)-1,4-diketo-pyrrolo[3,4-c]pyrrole (5-2). To a mixture of 3,6-Bis-(2-thienyl)-1,4-dioxopyrrolo[3,4-c]pyrrole (4.50 g, 15 mmol), tetrabutylammonium bromide (483 mg, 1.5 mmol) and potassium carbonate (10.35 g, 75 mmol) in DMF (120 mL) and 2-(2-methoxyethoxy)ethyl 4-methylbenzenesulfonate (18.1 g, 57 mmol) in DMF (30 mL) was added. The mixture was heated at 120 °C and stirred for 40 h. The DMF was removed under vacuum. To the concentrated solution, distilled water (150 mL) was added. The organic phases were extracted with CHCl₃ (5 x 50 mL), washed with brine and dried over MgSO₄. The viscous purple liquids obtained were purified by silica gel chromatography, eluting with CH₂Cl₂ / Acetone (9:1 to 8:2) to give red solids (4.1 g, 46%).

¹H-NMR (CDCl₃) δ: 8.69 (dd, J₁ = 1.2 Hz, J₂ = 3.9 Hz, 2H), 7.56 (dd, J₁ = 1.2 Hz, J₂ = 5.1 Hz, 2H), 7.17 (dd, J₁ = 3.9 Hz, J₂ = 5.1 Hz, 2H), 4.19 (t, J = 6.3 Hz, 4H), 3.71 (t, J = 6 Hz, 2H), 3.59-3.39 (m, 16H), 3.26 (s, 6H). ¹³C-NMR (CDCl₃) δ: 161.6, 140.5, 135.0, 131.1, 129.9, 128.6, 108.0, 72.1, 70.9, 70.7, 69.1, 59.2, 42.0. HRMS (ESI-TOF) Calculated for C₂₈H₃₆N₂O₈S₂ (M+H)⁺: 593.1986, found: m/z 593.1982. Anal. Calcd for C₂₈H₃₆N₂O₈S₂: C, 56.74; H, 6.12; N, 4.73. Found: C, 55.88; H, 6.12; N, 4.67.

N,N'-bis-(10-(3,6,9-trioxadecyl)-3,6-di(5-bromothienyl)-1,4-diketo-pyrrolo[3,4-c]pyrrole (5-3). To a solution of N,N'-bis-(10-(3,6,9-trioxadecyl)-3,6-di(5-thienyl)-1,4-diketo-pyrrolo[3,4-c]pyrrole (593 mg, 1 mmol) in CHCl₃ (50 mL), N-bromosuccimide (NBS) (374 mg, 2.1 mmol) was added in one portion. The solution was stirred for 48 h at room temperature in the dark

(covered by aluminum foil). After the reaction was complete (as indicated by TLC), distilled water was added. The organic phases were washed with brine and dried over MgSO₄. The dark purple solids obtained were purified by silica gel chromatography, eluting with CH₂Cl₂/ Acetone (9:1) to give violet-purple solids (4.56 g, 61%). ¹H-NMR (CDCl₃) δ: 8.46 (d, J = 4.5 Hz, 2H), 7.16 (d, J = 4.5 Hz, 2H), 4.12 (t, J = 6.0 Hz, 4H), 3.73 (t, J = 6.0 Hz, 4H), 3.61-3.43 (m, 16H), 3.10 (s, 6H). ¹³C-NMR (CDCl₃) δ: 161.3, 139.6, 135.0, 131.5, 131.3, 119.4, 108.1, 72.1, 70.9, 70.7, 69.1, 59.1, 42.4. HRMS (ESI-TOF) Calculated for C₂₈H₃₄Br₂N₂O₈S₂ (M+H)⁺: 751.0183, found: m/z 751.0161.

Anal. Calcd for C₂₈H₃₄Br₂N₂O₈S₂: C, 44.81; H, 4.57; N, 3.73. Found: C, 44.51; H, 5.53; N, 3.71.

N,N'-bis-(10-(3,6,9-trioxadecyl)-3,6-di(5''-dodecyl-terthienyl)-1,4-diketo-pyrrolo[3,4-c]pyrrole (DPP-1). To a Schlenk flask (125 mL) charged with a stirring bar were N,N'-bis-(10-(3,6,9-trioxadecyl)-3,6-di(5-bromothienyl)-1,4-diketo-pyrrolo[3,4-c]pyrrole (750 mg, 1 mmol), tributyl(5'-dodecyl-2,2'-bithiophen-5-yl)stannane (1.56 mg, 2.50 mmol), Pd₂(dba)₃ (20.8 mg) and P(o-tyl)₃ (24 mg) was added. Subsequently, it was purged with argon gas, followed by applying vacuum for 10 min; this process was repeated three times and the flask was refilled with argon. Degassed toluene (20 mL) was injected through a septum. The resulting mixture was heated up to 80 °C under argon and stirred for 20 h. The reaction mixture was poured into hexane and the precipitates were collected by vacuum filtration. The dark olive-green solids obtained were purified by silica gel chromatography, eluting with CHCl₃ / Acetone (from 96:4 to 92:8) to give purple solids (708 mg, 49%). ¹H-NMR (CDCl₃) δ: 8.78 (d, J = 4.2 Hz, 2H), 7.20 (d, J = 4.2 Hz, 2H), 7.18 (d, J = 3.9 Hz, 2H), 7.00 (d, J = 3.9 Hz, 2H), 6.99 (d, J = 3.6 Hz, 2H), 6.67 (d, J = 3.6 Hz, 2H), 4.27 (t, J = 6.0 Hz, 4H), 3.82 (t, J = 6.0 Hz, 4H), 3.67-3.44 (m, 16H), 3.31 (s, 6H), 2.80 (t, J = 7.5 Hz, 4H), 1.70 (quintet, 4H), 1.40-1.20 (m, 36H), 0.90 (t, J = 7.2 Hz, 6H). ¹³C-NMR

(CDCl₃) δ: 161.4, 146.6, 143.0, 139.2, 136.5, 134.2, 128.1, 126.2, 125.2, 124.6, 124.2, 124.0, 108.4, 72.1, 71.0, 70.8, 69.2, 59.2, 42.2, 32.1, 31.8, 30.4, 29.88, 29.85, 29.8, 29.59, 29.57, 29.3, 22.9, 14.3. HRMS (ESI-TOF) Calculated for C₆₈H₉₂N₂O₈S₆ (M+Na)⁺: 1279.5070, found: *m/z* 1279.5065. Anal. Calcd for C₆₈H₉₂N₂O₈S₆: C, 64.93; H, 7.37; N, 2.23. Found: C, 64.81; H, 7.35; N, 2.23.

1,2,3-tris(dodecyloxy)benzene (5-4).²⁹⁶ A mixture of pyragallol (6.35 g, 50 mmol, 1 equiv.), *n*-bromododecane (39.53 g, 38 mL, 159 mmol, 3.15 equiv.), anhydrous K₂CO₃ (41.75 g, 302 mmol, 6 equiv.), and DMF (100 ml) was heated at 65 °C for 18 h under nitrogen atmosphere. Then the reaction mixture was then poured into ice-water (1000 ml) and extracted with dichloromethane (3 × 100 ml). The combined organic solution was washed with water (3 × 100 ml), brine and dried over anhydrous MgSO₄. The solution was concentrated and precipitated into methanol (400 mL), yielding pale white solids. The crude product was further purified by silica gel chromatography, using CH₂Cl₂/Hexane (1:1) as eluents. The combined fractions were concentrated and poured into methanol (200 mL), yielding white precipitates (29.8 g, 94%). ¹H-NMR (CDCl₃) δ: 6.91 (t, J = 8.6 Hz, 1H), 6.55 (d, J = 8.6 Hz, 2H), 4.01-3.32 (m, 6H), 1.85-1.28 (m, 60H), 0.88 (t, J = 6.0 Hz, 9H); ¹³C-NMR (CDCl₃) δ: 153.6, 138.6, 123.2, 106.9, 73.4, 69.1, 32.1, 30.6, 30.0, 29.9, 29.86, 29.64, 29.61, 29.58, 26.4, 26.3, 22.9, 14.2.

4,4,5,5-tetramethyl-2-(3,4,5-tris(dodecyloxy)phenyl)-1,3,2-dioxaborolane (5-5). To a 100 mL two-neck flask containing a magnetic stir bar was added 1,2,3-tris(dodecyloxy)benzene (3.16 g, 5 mmol), bis(pinacolato)diboron (1.27 g, 5 mmol) and 4,4'-di-tert-butyl-2,2'-bipyridine (40.3 mg, 0.15 mmol). The flask was evacuated and back-filled with argon three times, after which degassed heptane (50 mL) was transferred to the mixture. [Ir(OMe)(COD)]₂ (0.075 mmol) was added under argon. The reaction was immediately immersed in an oil bath at 80 °C

and stirred for 24 hours at that temperature. The reaction was cooled to RT, the mixture was filtered through a pad of silica gel and washed with methylene chloride. The solution was concentrated and poured into methanol (100 mL), yielding white solids (3.48 g, 92%). $^1\text{H-NMR}$ (CDCl_3) δ : 6.99 (s, 2H), 4.05-3.94 (m, 6H), 1.92-1.68 (m, 6H), 1.52-1.25 (m, 66H), 0.87 (t, J = 6.0 Hz, 9H); $^{13}\text{C-NMR}$ (CDCl_3) δ : 153.1, 141.4, 113.0, 83.9, 73.6, 69.3, 32.2, 30.6, 30.0, 29.94, 29.90, 29.84, 29.72, 29.66, 29.62, 29.60, 26.4, 25.1, 22.9, 14.3; HRMS (APCI-TOF) Calculated for $\text{C}_{48}\text{H}_{89}\text{BO}_5$ ($\text{M} + \text{H}^+$): 757.6908 Found: m/z 757.6908.

2-(3,4,5-tris(dodecyloxy)phenyl)thiophene (5-6). In a flame-dried Schlenk flask (50 mL), 4,4,5,5-tetramethyl-2-(3,4,5-tris(dodecyloxy)phenyl)-1,3,2-dioxaborolane (5-5) (6.81 g, 9 mmol), 2-bromothiophene (4.40 g, 27 mmol), Tris(dibenzylideneacetone)dipalladium(0) (117 mg) and $\text{P}(\text{o-tyl})_3$ (138 mg) were added. The flask was evacuated and back-filled with argon three times, after which degassed toluene (15 mL) and tetraethylammonium hydroxide (6.2 mmol, 20 wt aqueous solution) was transferred to the mixture through a septum. The resulting solution was heated up to 90 °C under argon and stirred for 20 h. The solvent was concentrated and poured into cold methanol (200 mL). The precipitates were filtered and purified by silica gel chromatography, eluting with CH_2Cl_2 -hexane (1:2) to give a yellowish oil (the oil solidified over a few days. 6.30 g, 98%). $^1\text{H-NMR}$ (CDCl_3) δ : 7.24-7.20 (m, 2H), 7.06-7.03 (m, 1H), 6.84 (s, 2H) 4.07-4.03 (m, 6H), 1.92-1.80 (m, 6H), 1.62-1.30 (m, 54H), 0.97 (t, J = 6.0 Hz, 9H); $^{13}\text{C-NMR}$ (CDCl_3) δ : 153.5, 144.9, 138.4, 129.8, 127.8, 124.1, 122.7, 105.2, 73.5, 69.3, 32.1, 30.5, 29.9, 29.86, 29.84, 29.83, 29.63, 29.61, 29.57, 29.55, 26.34, 26.30, 22.8, 14.2; HRMS (APCI-TOF) Calculated for $\text{C}_{46}\text{H}_{80}\text{O}_3\text{S}$ ($\text{M} + \text{H}^+$): 713.5901 Found: m/z 713.5908.

4,4,5,5-tetramethyl-2-(5-(3,4,5-tris(dodecyloxy)phenyl)thiophen-2-yl)-1,3,2-dioxaborolane (5-7). To a 100 mL two-neck flask containing a magnetic stir bar was added 2-

(3,4,5-tris(dodecyloxy)phenyl)thiophene (5-6) (3.56 g, 5 mmol), bis(pinacolato)diboron (1.27 g, 5 mmol) and 4,4'-di-tert-butyl-2,2'-bipyridine (40 mg, 0.15 mmol). The flask was evacuated and back-filled with argon three times, after which degassed heptane (50 mL) was transferred to the mixture. $[\text{Ir}(\text{OMe})(\text{COD})]_2$ (0.075 mmol, 49 mg) was added under argon. The reaction was immediately immersed in an oil bath at 80 °C and stirred for 24 hours at that temperature. The reaction was cooled to RT, the mixture was filtered through a pad of silica gel and washed with methylene chloride. The solution was concentrated and poured into methanol (100 mL), yielding white solids (2.1 g, 50%). $^1\text{H-NMR}$ (CDCl_3) δ : 7.57 (d, $J = 3.6\text{Hz}$, 1H), 7.29 (d, $J = 3.6\text{Hz}$, 1H), 6.83 (s, 2H), 4.01-3.94 (m, 6H), 1.85-1.72 (m, 6H), 1.52-1.25 (m, 66H), 0.90 (t, $J = 6.6\text{ Hz}$, 9H); $^{13}\text{C-NMR}$ (CDCl_3) δ : 153.6, 138.6, 129.6, 124.3, 105.2, 84.3, 73.7, 69.4, 32.1, 30.6, 30.0, 29.92, 29.87, 29.62, 29.59, 26.35, 26.30, 25.0, 22.9, 14.3; HRMS (APCI-TOF) Calculated for $\text{C}_{52}\text{H}_{91}\text{BO}_5\text{S} (\text{M}^+)$: 839.6712 Found: m/z 838.6757.

5-(3,4,5-tris(dodecyloxy)phenyl)-2,2'-bithiophene (5-8). In a flame-dried Schlenk flask (50 mL), 4,4,5,5-tetramethyl-2-(3,4,5-tris(dodecyloxy)phenyl)-1,3,2-dioxaborolane (5-5) (2.27 g, 3 mmol), Tris(dibenzylideneacetone)dipalladium(0) (39 mg), $\text{P}(\text{o-tyl})_3$ (46 mg) and 5-bromo-2,2'-bithiophene (1.10 g, 4.5 mmol), were added. The flask was evacuated and back-filled with argon three times, after which degassed toluene (15 mL) and tetraethylammonium hydroxide (4.5mL, 20 wt aqueous solution) was transferred to the mixture through a septum. The resulting solution was heated up to 90 °C under argon and stirred for 20 h. The solvent was concentrated and poured into cold methanol (200 mL). The precipitates were filtered and purified by silica gel chromatography, eluting with hexane/toluene (3:1) to give a yellow solid (2.05 g, 86%). $^1\text{H-NMR}$ (CDCl_3) δ : 7.20-7.18 (m, 2H), 7.12 (s, 2H), 7.03-7.00 (m, 1H), 6.81 (s, 2H) 4.07-4.00(m, 6H), 1.92-1.78 (m, 6H), 1.62-1.30 (m, 54H), 0.95 (t, $J = 6.3\text{ Hz}$, 9H); $^{13}\text{C-NMR}$ (CDCl_3) δ : 153.6,

143.6, 138.4, 137.6, 136.3, 129.4, 127.9, 124.5, 124.2, 123.4, 123.35, 104.7, 73.6, 69.3, 32.1, 30.6, 29.96, 29.94, 29.92, 29.90, 29.86, 29.82, 29.63, 29.60, 29.58, 26.35, 26.31, 22.9, 14.3; HRMS (APCI-TOF) Calculated for C₅₀H₈₂O₃S₂(M⁺): 795.5778 Found: *m/z* 795.5750.

4,4,5,5-tetramethyl-2-(5'-(3,4,5-tris(dodecyloxy)phenyl)-2,2'-bithiophen-5-yl)-1,3,2-dioxaborolane (5-9). To a 100 mL two-neck flask containing a magnetic stir bar was added 5-(3,4,5-tris(dodecyloxy)phenyl)-2,2'-bithiophene (5-8) (1.20 g, 1.5 mmol), bis(pinacolato)diboron (230 mg, 0.9 mmol) and 4,4'-di-tert-butyl-2,2'-bipyridine (12 mg). The flask was evacuated and back-filled with argon three times, after which degassed heptane (50 mL) was transferred to the mixture. [Ir(OMe)(COD)]₂ (16 mg) was added under argon. The reaction was immediately immersed in an oil bath at 80 °C and stirred for 24 hours at that temperature. The reaction was cooled to RT, the mixture was filtered through a pad of silica gel and washed with methylene chloride. The solution was concentrated and poured into methanol (100 mL), yielding yellow solids (700 mg, 50%). ¹H-NMR (CDCl₃) δ: 7.55 (d, J = 3.6Hz, 1H), 7.25 (d, J = 3.6Hz, 1H), 7.19 (d, J = 3.9Hz, 1H), 7.13 (d, J = 3.9Hz, 1H), 6.78 (s, 2H), 4.05-3.96 (m, 6H), 1.86-1.73 (m, 6H), 1.52-1.25 (m, 66H), 0.90 (t, J = 6.6 Hz, 9H); ¹³C-NMR (CDCl₃) δ: 153.6, 144.4, 138.7, 138.2, 136.2, 129.4, 125.3, 124.8, 123.7, 104.9, 84.3, 73.8, 69.5, 32.1, 30.6, 30.0, 29.95, 29.92, 29.86, 29.83, 29.63, 29.61, 29.58, 26.34, 26.32, 24.9, 22.9, 14.3; HRMS (APCI-TOF) Calculated for C₅₆H₉₃BO₅S₂(M⁺): 920.6562 Found: *m/z* 920.6616.

2-(3,4,5-tris(dodecyloxy)phenyl)-5,2':5',2"-terthiophene (5-10). In a flame-dried Schlenk flask (50 mL), 4,4,5,5-tetramethyl-2-(3,4,5-tris(dodecyloxy)phenyl)-1,3,2-dioxaborolane (5-5) (2.27 g, 3 mmol), 2-Bromo-5,2':5',2"-terthiophene (981 g, 3 mmol), Tris(dibenzylideneacetone)dipalladium(0) (39 mg), and P(o-tyl)₃ (46 mg) were added. The flask was evacuated and back-filled with argon three times, after which degassed toluene (8 mL) and

tetraethylammonium hydroxide (4.5mL, 20 wt aqueous solution) was transferred to the mixture through a septum. The resulting solution was heated up to 80 °C under argon and stirred for 20 h. The solvent was concentrated and poured into cold methanol (200 mL). The precipitates were filtered and purified by silica gel chromatography, eluting with hexane/toluene (3:1) to give a yellow solid (1.90 g, 72%). ¹H-NMR (CDCl₃) δ: 7.20-7.17 (m, 3H), 7.16-7.08 (m, 3H), 7.02-6.99 (m, 1H), 6.79 (s, 2H) 4.07-3.98 (m, 6H), 1.92-1.78 (m, 6H), 1.62-1.30 (m, 54H), 0.95 (t, J = 6.3 Hz, 9H); ¹³C-NMR (CDCl₃) δ: 153.6, 143.7, 138.5, 137.3, 136.4, 136.2, 136.0, 129.4, 128.0, 124.5, 124.4, 124.1, 123.7, 123.5, 104.7, 73.7, 69.4, 32.1, 30.6, 29.97, 29.93, 29.91, 29.90, 29.88, 29.65, 29.61, 29.59, 26.36, 26.33, 22.9, 14.3; HRMS (APCI-TOF) Calculated for C₅₄H₈₄O₃S₃ (M⁺): 1002.6439 Found: *m/z* 1002.6464.

12-bromo-2,2,3,3-tetramethyl-4,7,10-trioxa-3-siladodecane (5-12). Triethylamine (13.7 mL, 98 mmol, 1.2 eq), (N,N-dimethylpyridin-4-amine) DMAP (8.2 mmol, 0.1 eq) and *tert*-butylchlorodimethylsilane (TBDMSCl) (13.56 g, 90 mmol, 1.1 eq) were dissolved in CH₂Cl₂ (100 mL). 2-(2-(2-hydroxyethoxy)ethoxy)ethyl 4-methylbenzenesulfonate (24.90 g, 82 mmol) was added dropwise over 10 min, then the mixture was stirred at rt for 6 h. The reaction was poured into H₂O and extracted with ethyl acetate. The viscous liquid was purified by silica gel column, yielding a colorless liquid (31.2 g, 91%). ¹H-NMR (CDCl₃) δ: 7.79 (d, J = 6.4 Hz, 2H), 7.33 (d, J = 6.4Hz, 2H), 4.15 (t, J = 4.8 Hz, 2H), 3.74 (t, J = 6.4 Hz, 2H), 3.74 (t, J = 4.8 Hz, 2H), 3. 56 (s, 4H), 3.51 (t, J = 6.4 Hz, 4H), 2.42 (s, 3H), 0.87 (s, 12H), 0.03 (s, 6H); ¹³C-NMR (CDCl₃) δ: 144.9, 133.2, 130.0, 128.2, 72.9, 71.0, 70.8, 69.4, 68.9, 62.9, 26.1, 25.8, 21.8, 18.5, - 5.09.

2,5-bis(2,2,3,3-tetramethyl-4,7,10-trioxa-3-siladodecan-12-yl)-3,6-di(thiophen-2-yl)pyrrolo[3,4-c]pyrrole-1,4(2H,5H)-dione (5-13). To a mixture of 3,6-Bis-(2-thienyl)-1,4-

dioxopyrrolo[3,4-c]pyrrole (3.0 g, 10 mmol), and potassium carbonate (8.3 g, 60 mmol) in DMF (120 mL), 12-bromo-2,2,3,3-tetramethyl-4,7,10-trioxa-3-siladodecane (10.87 g, 26 mmol) in DMF (60 mL) was added. The mixture was heated up to 120 °C and stirred for 24 h. The suspension was poured into water (1L). The organic phases were extracted by CHCl₃ (5 x 50 mL), washed by brine and dried over MgSO₄. Viscous dark red liquids obtained were purified by silica gel chromatography, eluting with CH₂Cl₂ / Acetone (97:3) to give purple-red solids (5.3 g, 61%). ¹H-NMR (CDCl₃) δ: 8.72 (dd, J₁ = 1.2 Hz, J₂ = 3.9 Hz, 2H), 7.56 (dd, J₁ = 1.2 Hz, J₂ = 5.1 Hz, 2H), 7.20 (dd, J₁ = 3.9 Hz, J₂ = 5.1 Hz, 2H), 4.22 (t, J = 6.3 Hz, 4H), 3.75 (t, J = 6 Hz, 4H), 3.66-3.65 (m, 4H), 3.57-3.53 (m, 8H), 3.45-3.42 (m, 4H), 0.82 (s, 18H). 0.01 (s, 12H); ¹³C-NMR (CDCl₃) δ: 161.6, 140.4, 134.8, 130.9, 129.7, 128.5, 107.9, 72.8, 70.8, 70.7, 69.0, 62.8, 41.9, 26.0, 18.4, -5.1. HRMS (ESI-TOF) Calculated for C₃₈H₆₀N₂O₈S₂Si₂ (M+H)⁺: 793.3402, found: *m/z* 793.3423.

3,6-bis(5-bromothiophen-2-yl)-2,5-bis(2-(2-(2-ydroxyethoxy)ethoxy)ethyl)pyrrolo[3,4-c]pyrrole-1,4(2H,5H)-dione (5-14). To a solution of 2,5-bis(2,2,3,3-tetramethyl-4,7,10-trioxa-3-siladodecan-12-yl)-3,6-di(thiophen-2-yl)pyrrolo[3,4-c]pyrrole-1,4(2H,5H)-dione (5-13) (3.0 g, 3.78 mmol) in CHCl₃ (40 mL), N-bromosuccimide (NBS) (1.62 g, 9.08mmol) was added in three portions over 1h. The solution was stirred 48 h under room temperature in the dark (covered by alumina foil). After the reaction was completed (indicated by TLC), HCl (4M, 30 mL) was added to cleave TBDMS protecting groups. The solution was vigorously stirred for another hour. The organic phases were then extracted with chloroform, washed by brine and dried over MgSO₄. Dark purple solids obtained were purified by silica gel chromatography, eluting with CH₂Cl₂/ Acetone (9:1) to give violet-purple solids (1.70 g, 63%) . Before Cleavage ¹H-NMR (CDCl₃) δ: 8.47 (d, J = 5.2 Hz, 2H), 7.17 (d, J = 5.2 Hz, 2H), 4.14 (t, J = 6.0 Hz, 4H), 3.77-3.68

(m, 8H), 3.60-3.57 (m, 8H), 3.49 (t, $J = 5.4$, 4H), 0.85 (s, 18H). 0.02 (s, 12H); ^{13}C -NMR (CDCl_3) δ : 161.4, 139.6, 135.0, 131.5, 131.3, 119.5, 108.1, 72.9, 71.0, 70.8, 69.1, 62.9, 42.4, 26.1, 18.5, -5.1. H HRMS (ESI-TOF) Calculated for $\text{C}_{38}\text{H}_{58}\text{Br}_2\text{N}_2\text{O}_8\text{S}_2\text{Si}_2$ ($\text{M}+\text{H}$) $^+$: 951.1596, found: m/z 951.1530. After cleavage ^1H -NMR (CDCl_3) δ : 8.45 (d, $J = 5.2$ Hz, 2H), 7.16 (d, $J = 5.2$ Hz, 2H), 4.15 (t, $J = 6.0$ Hz, 4H), 3.75-3.71 (m, 8H), 3.60-3.57 (m, 8H), 3.45 (t, $J = 5.4$, 4H); ^{13}C -NMR (CDCl_3) δ : 161.4, 139.6, 135.2, 131.7, 131.2, 119.6, 108.1, 72.7, 70.9, 70.6, 69.1, 61.8, 42.3.

The general method to prepare **DPP-OH-n**, **DPP-TEG** and **DPP-C12**. A Schlenk flask charged with **5-14** (0.2 mmol), $\text{Pd}_2(\text{dba})_3$ (2.5 mol %), $[(\text{C}_4\text{H}_9)_3\text{PH}]^+\text{BF}_4^-$ (5 mol %,), CuI (10 mol %), and were purged with argon atmosphere and vacuum for three cycles, and then filled with argon. Ar-B (2.1 eq, 5-7, 5-9 and 5-11, respectively) in degassed tetrahydrofuran (5 mL) was added through a septum, followed by an aqueous solution of CsF (6 eq, 1.2 mmol, 0.6 mL). The reaction mixture was heated up to 75 °C and stirred for 48 h. After cooling back to room temperature, the mixture was poured into methanol (100 mL) and stirred for 30 min. The precipitates were collected by vacuum filtration. The crude products were purified by silica gel chromatography, eluting with $\text{CH}_2\text{Cl}_2/\text{acetone}$ (95:5 to 90:10). The collected fractions were then concentrated and precipitated into methanol to yield the desired products.

DPP-1. ^1H -NMR (CDCl_3) δ : 8.80 (d, $J = 4.2$ Hz, 2H), 7.35 (d, $J = 4.2$ Hz, 2H), 6.83 (s, 4H), 4.35 (t, $J = 6$ Hz, 4H), 4.05-3.96 (m, 12H), 3.83 (t, $J = 6$ Hz, 4H), 3.67-3.55 (m, 12H), 3.50 (t, $J = 4.2$, 4H), 2.63 (bs, 2H), 1.87-1.70 (m, 12H), 1.57-1.25 (m, 108H), 0.87 (t, $J = 6.0$ Hz, 18H); ^{13}C -NMR (CDCl_3) δ : 161.7, 153.8, 150.8, 139.9, 139.7, 136.6, 128.4, 128.35, 124.5, 108.2, 105.5, 73.9, 72.8, 70.9, 70.6, 69.6, 69.3, 61.9, 32.1, 30.6, 29.98, 29.93, 29.88, 29.67, 29.61,

29.59, 26.35, 22.9, 14.3. HRMS (MALDI-TOF) Calculated for $C_{110}H_{184}N_2O_{14}S_2$ ($M+H$) $^+$:

1822.3223, found: m/z .

DPP-2. 1H -NMR ($CDCl_3$) δ : 8.80 (d, J = 4.5 Hz, 2H), 7.24 (dd, J_1 = 4.5 Hz, J_2 = 3.9 Hz, 2H), 7.12 (d, J = 3.9 Hz, 2H), 6.75 (s, 4H), 4.31 (t, J = 6 Hz, 4H), 4.20-3.94 (m, 12H), 3.83 (t, J = 6 Hz, 4H), 3.69-3.59 (m, 12H), 3.52 (t, J = 4.2, 4H), 2.57 (bs, 2H), 1.87-1.72 (m, 12H), 1.57-1.25 (m, 108H), 0.87 (t, J = 6.0Hz, 18H); ^{13}C -NMR ($CDCl_3$) δ : 161.5, 153.7, 150.8, 146.0, 143.3, 139.3, 138.7, 136.6, 134.8, 128.9, 127.9, 126.5, 124.6, 123.9, 108.4, 104.8, 73.8, 72.8, 71.0, 70.7, 69.5, 69.3, 61.95, 32.1, 30.5, 29.95, 29.91, 29.89, 29.86, 29.81, 29.65, 29.59, 29.56, 26.3, 22.9, 14.3. H HRMS (MALDI-TOF) Calculated for $C_{118}H_{188}N_2O_{14}S_4$ ($M+H$) $^+$: 1987.0203, found: m/z 1987.3120.

DPP-3. 1H -NMR ($CDCl_3$) δ : 8.80 (d, J = 4.2 Hz, 2H), 7.04 (d, J = 4.2 Hz, 2H), 6.95-6.88 (m, 8H), 6.65 (s, 4H), 4.24 (bs, 4H), 3.95-3.91 (m, 12H), 3.82 (m, 4H), 3.75-3.64 (m, 12H), 3.52 (t, J = 4.5, 4H), 3.09 (bs, 2H), 1.80-1.70 (m, 12H), 1.47-1.25 (m, 108H), 0.87 (t, J = 6.0Hz, 18H); ^{13}C -NMR ($CDCl_3$) δ : 161.2, 153.6, 144.3, 142.8, 138.6, 138.5, 136.9, 135.2, 134.4, 129.0, 127.8, 126.2, 125.1, 124.5, 124.2, 123.5, 108.2, 104.4, 73.8, 72.7, 70.9, 70.6, 69.4, 61.9, 32.2, 30.6, 30.0, 30.0, 29.94, 29.76, 29.71, 29.6, 26.4, 22.9, 14.3. H HRMS (MALDI-TOF) Calculated for $C_{126}H_{192}N_2O_{14}S_6$ ($M+H$) $^+$: 2151.2803 found: m/z 2151.2789.

DPP-TEG. 1H -NMR ($CDCl_3$) δ : 8.80 (d, J = 4.2 Hz, 2H), 7.26 (dd, J_1 = 4.5 Hz, J_2 = 3.9 Hz, 2H), 7.13 (d, J = 3.9 Hz, 2H), 6.76 (s, 4H), 4.30 (t, J = 6 Hz, 4H), 4.04-3.97 (m, 12H), 3.83 (t, J = 6 Hz, 4H), 3.69-3.55 (m, 12H), 3.45 (m, 4H), 3.31 (s, 6H), 1.87-1.72 (m, 12H), 1.57-1.25 (m, 108H), 0.88 (t, J = 6.0Hz, 18H); ^{13}C -NMR ($CDCl_3$) δ : 161.5, 153.7, 145.9, 143.2, 139.3, 138.8, 136.4, 134.9, 128.9, 128.1, 126.4, 124.5, 123.9, 108.4, 104.7, 73.8, 72.1, 71.0, 70.8, 69.5,

69.3, 59.2, 32.1, 30.6, 30.0, 29.92, 29.91, 29.87, 29.66, 29.60, 29.58, 36.3, 22.9, 14.3. HRMS (MALDI-TOF) Calculated for $C_{120}H_{192}N_2O_{14}S_4$ ($M+H$)⁺: 2015.3300, found: *m/z* 2015.3366.

DPP-C12. 1H -NMR ($CDCl_3$) δ : 8.92 (d, J = 4.2 Hz, 2H), 7.29 (d, J = 4.2 Hz, 2H), 7.25-7.23 (m, 4H), 7.15 (d, J = 3.6 Hz, 2H), 6.77 (s, 4H), 4.15-3.95 (m, 20H), 1.90-1.70 (m, 16H), 1.57-1.21 (m, 140H), 0.88 (m, 24H); ^{13}C -NMR ($CDCl_3$) δ : 161.4, 153.7, 145.9, 143.1, 139.0, 138.9, 136.8, 135.0, 129.0, 128.1, 126.2, 124.8, 123.9, 108.4, 104.9, 73.8, 69.5, 32.1, 31.8, 30.6, 30.2, 29.99, 29.94, 29.89, 29.77, 29.67, 29.62, 29.60, 29.47, 27.1, 26.4, 22.9, 14.3. HRMS (MALDI-TOF) Calculated for $C_{130}H_{212}N_2O_8S_4$ ($M+H$)⁺: 2059.5232, found: *m/z* 2059.5215.

N,N'-bis-(t-butoxycarbonyl)-3,6-di(2-thienyl)-1,4-diketo-pyrrolo[3,4-c]pyrrole (5-15).

This compound was prepared by following the literature procedure.⁸³ Briefly described as follows: To a solution of 3,6-Bis-(2-thienyl)-1,4-dioxopyrrolo[3,4-c]pyrrole (**1**) (3.0 g, 10 mmol) and DMAP (1.22 g, 10 mmol) in anhydrous THF (100 mL) was added a solution of di-tert-butyl dicarbonate (5 g, 22.9 mmol) in THF (20 mL) dropwise over 1 h. The mixture was stirred for 16 h and poured into water. The organic phase was extracted with chloroform, washed with brine and dried over $MgSO_4$. The solvent was concentrated under reduced pressure. Petroleum ether (100 mL) was added. The resulting solid was filtered, washed with petroleum ether and purified by silica gel column chromatography, eluting with $CHCl_3$ to give shiny red solids (3.0 g, 60 %).

1H -NMR ($CDCl_3$) δ : 8.22 (dd, J_1 = 3.9 Hz, J_2 = 1.2 Hz, 2H), 7.63 (dd, J_1 = 4.8 Hz, J_2 = 1.2 Hz, 2H), 7.19 (dd, J_1 = 4.8 Hz, J_2 = 3.9 Hz, 2H), 1.58 (s, 18H); ^{13}C -NMR ($CDCl_3$) δ : 159.2, 149.0, 138.1, 134.1, 132.0, 129.8, 128.2, 110.4, 86.1, 27.8; HRMS (APCI-TOF) Calculated for $C_{24}H_{24}N_2O_6S_2$ ($M + Na^+$): 523.0968 Found: *m/z* 523.0985.

N,N'-bis-(t-butoxycarbonyl)-3,6-di(5-bromothienyl)-1,4-diketo-pyrrolo[3,4-c]pyrrole (5-15).

This compound was prepared by following the literature procedure.⁸³ Briefly described as

follows: Compound **2** (1 g, 2 mmol) was dissolved in chloroform (30 mL) and cooled down to 0 °C. NBS (748 mg, 4.2 mmol) was added portionwise over 2h. The reaction was monitored by TLC. After the reaction was complete, the mixture was poured into a methanol/water mixture (200 mL - 50 mL). The resulting solid was filtered, washed with methanol and purified by silica gel column chromatography, eluting with CHCl₃ to yield purple solids (1.0 g, 77 %). ¹H-NMR (CDCl₃) δ: 8.08 (d, J = 4.2 Hz, 2H), 7.15 (d, J = 4.2 Hz, 2H), 1.61 (s, 18H); ¹³C-NMR (CDCl₃) δ: 158.2, 149.1, 137.0, 134.7, 131.4, 131.3, 121.0, 110.7, 86.5, 28.0; HRMS (APCI-TOF) Calculated for C₂₄H₂₂Br₂N₂O₆S₂(M + Na⁺): 680.9159 Found: *m/z* 680.9187.

PDPP-Boc. To a flame-dried Schlenk flask (50 mL), compound **3** (658.38 mg, 1 mmol), Tris(dibenzylideneacetone)dipalladium(0) (36 mg) and P(o-tyl)₃ (24 mg) were added. The flask was evacuated and back-filled with argon three times, after which degassed (3,3-bis((2-ethylhexyl)oxy)methyl)-3,4-dihydro-2H-thieno[3,4-b][1,4]dioxepine-6,8-diyl)bis(trimethylstannane) (766.29 mg, 1 mmol) in toluene (30 mL) was transferred to the flask through a septum. The resulting solution was heated up to 85 °C under argon and stirred for 36 h, after which the crude polymer was precipitated in methanol. The precipitate was collected in a Soxhlet thimble and was extracted with methanol, hexanes, and chloroform. The chloroform fraction was reduced in volume, precipitated in methanol, and filtered over a 4.5 μm PTFE filter. The polymer was collected and dried under vacuum in a vial at 60 °C overnight, resulting in 799 mg (85%) of dark blue solids. ¹H-NMR: 8.52 (b, 4H), 4.40-4.0 (b, 4H), 3.82-3.18 (b, 8H), 2.31-0.75 (b, 48H). GPC (THF): M_n = 26,800 g/mol, PDI = 2.2.

CHAPTER 6

ISOINDIGO-BASED SEMICONDUCTING MATERIALS FOR PHOTOVOLTAIC APPLICATIONS

6.1 Introduction

The field of organic solar cells is largely driven and fostered by continuously emerging new materials since the discovery of bulk-heterojunction (BHJ) for photovoltaic devices. As this dissertation was being prepared, several new small molecules and polymers have been have been added to the growing list of active materials in BHJ solar cells with PCEs above ~4%,^{61,310-312} which are not listed in Figure 1-18. In other words, these high performance photovoltaic materials were released one after the other over the course of three months. Thus, it is fair to state that design and Synthesis of new materials plays a central role in pushing the frontiers of organic solar cells.

In the previous several chapters, focus was placed on using known donor and acceptor moieties to build oligomers and polymers with desired optical and electrochemical properties. In particular, benzothiadiazole as an electron-accepting building block is frequently used in the previous studies (Chapters 3 and 4) and in literature.^{309,312-313} In this chapter, we focus on a new electron-deficient building block, namely isoindigo. Isoindigo is a naturally occurring pigment. Indigo is its more famous structural isomer. Since its importance in dyes, pigments, as well as intermediates in drug development, a number of approaches have been developed to prepare isoindigo derivatives.³¹⁴ Among them, the most widely used method is the acid-catalyzed condensation of isatin and oxindole derivatives.³¹⁵⁻³¹⁶ Another commonly used approach is to utilize a single electron transfer reaction by reacting isatin derivatives with hexaethylphosphinetriamine.³¹⁶

Surprisingly, the use of isoindigo as an electron acceptor has not been explored within the context of functional electroactive materials. Based on using isoindigo as a new electron-

deficient acceptor, we first initiate the study of isoindigo-based electroactive pi-conjugated materials. We have prepared a wide range of isoindigo-based small molecules, donor-acceptor type conjugated polymers, as well as a new class of n-type conjugated polymers containing only electron-deficient repeat units. Through our efforts the scope of isoindigo based electroactive materials has been expanded to a great extent.

6.2 Isoindigo-based Oligothiophenes

Portions of the material in this section have been previously reported.³¹⁷ Encouraged by recent reports on diketopyrrolopyrrole oligothiophenes as donor materials in molecular BHJ solar cells, where PCEs of 2.2 - 4.4 % have been demonstrated,^{41,60,76,78,83,285,295} we here investigate isoindigo-based oligothiophenes as electron donors in the same type of photovoltaic device. As shown in Figure 6-1, donor-acceptor-donor (DAD, **I-1**) and acceptor-donor-acceptor (ADA, **I-2**) isoindigo-based oligothiophenes are the two targeted molecules in this section. Their performance as donor materials in molecular BHJ solar cells will be discussed as well.

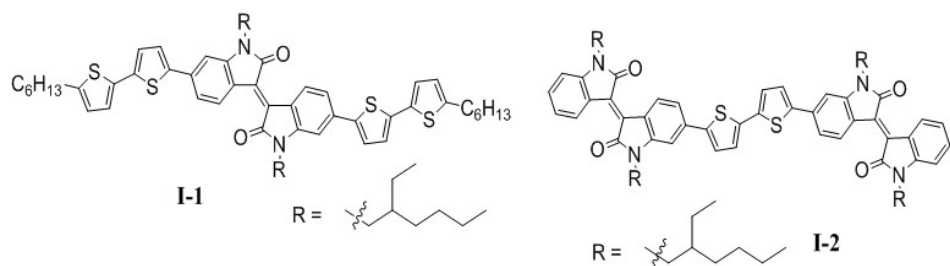


Figure 6-1. Chemical structures of I-1, and I-2.

6.2.1 Synthesis of Isoindigo-Based Oligothiophenes

The Synthesis of isoindigo building blocks is outlined in Figure 6-2. As mentioned earlier, there are two approaches that can lead to isoindigo derivatives. For its simplicity and mild reaction conditions, the acid-catalyzed condensation approach was chosen to prepare the isoindigo cores. Briefly, the work starts with the acid-catalyzed adol condensation and dehydration of commercially available 6-bromoisoasatin and 6-bromooxindole in acetic acid under

nitrogen atmosphere, yielding 6,6'-dibromoisoindigo **6-1** in a quantitative yield. It should be noted that a catalytic amount of concentrated hydrogen chloride is required for the reaction to proceed smoothly and to completion. Due to the existence of strong π - π interactions as well as hydrogen bonding interactions, compound **6-1** is only slightly soluble in common organic solvents. Subsequently shown is the *N*-alkylation of **6-1** using various alkyl bromides and efficient formation of soluble 6,6'-dibromoisoindigo derivatives **6-2**, **3**, **4** and **5** in good to excellent yields (> 65%). As alkylation precludes any hydrogen bonding, the alkylated isoindigo derivatives become readily soluble in common organic solvents and can thus be purified by column chromatography. In the case of **6-3** and **6-4**, where linear alkyl chains are used as solubilizing groups, the compounds are highly crystalline and can thus be purified by recrystallization.

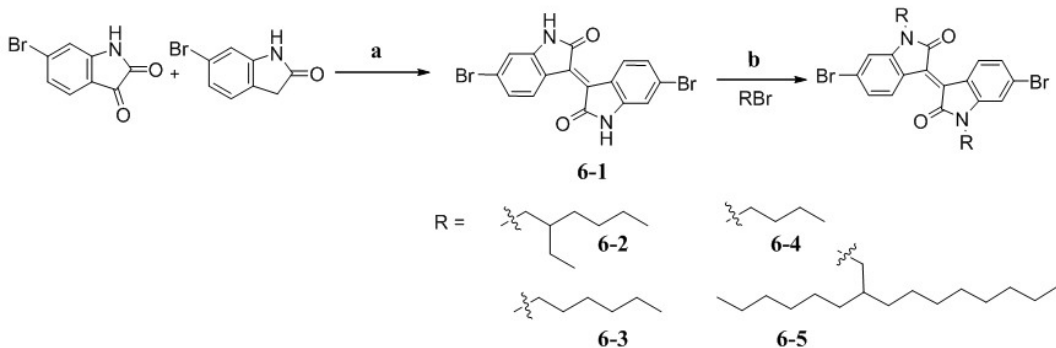


Figure 6-2. Synthetic scheme of isoindigo building blocks. a) con HCl (*cat.*), acetic acid, reflux, > 95%; b) RBr, K₂CO₃, DMF, 100 °C.

The same route is utilized to prepare alkylated 6-bromoisoindigo **6-7**, a precursor for the ADA oligothiophene, as illustrated in Figure 6-3. Interestingly, 6,6'-dibromoisoindigo **6-2** and isoindigo **6-8** were also observed, in addition to the desired product **6-7**, upon reaction of 6-bromoisoindigo and oxindole followed by alkylation. Fortunately, the mixture can be easily separated by silica gel chromatography. The molar ratio of **6-2**, **6-7**, and **6-8** is approximately 1:2:1 after purification. The unexpected formation of **6-8** and **6-2** in this sequence is likely due to

the acid- (the first step) or base- (the second step) promoted retro-adol/adol reaction that scrambled the product distribution under the experimental conditions employed. In order to test this hypodissertation, an equimolar mixture of **6-8** and **6-2** was stirred in the aforementioned reaction conditions. The experiments revealed that crossover was indeed observed in the second reaction, and compound **6-7** was produced in DMF with K_2CO_3 at 100 °C; while no crossover was observed in the acidic condition. It was further found that use of anhydrous DMF and freshly dried base can minimize the scrambling.

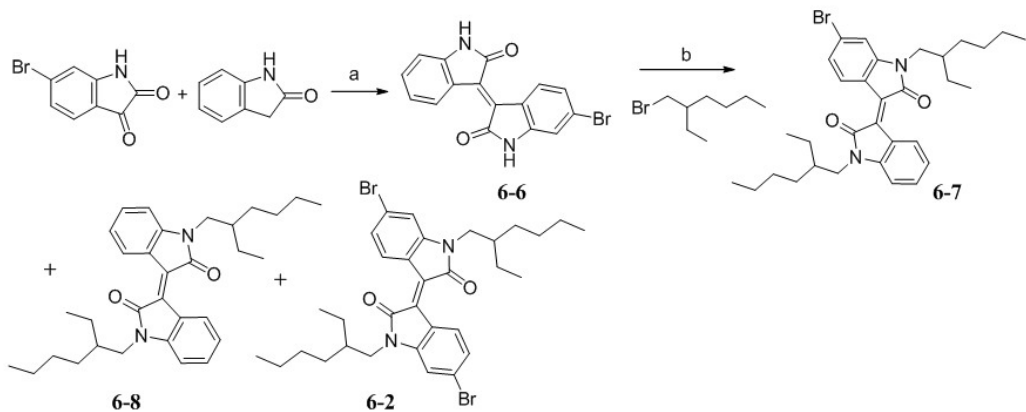


Figure 6-3. Synthetic scheme of mono-functionalized isoindigo building block. a) *conc.* HCl (*cat.*), acetic acid, reflux, > 95%; b) RBr, K_2CO_3 , DMF, 100 °C.

With **6-2** and **6-8** in hand, **I-1**, and **I-2** were successfully obtained by incorporating electron rich bithiophene units via Suzuki coupling, as shown in Figure 6-4.

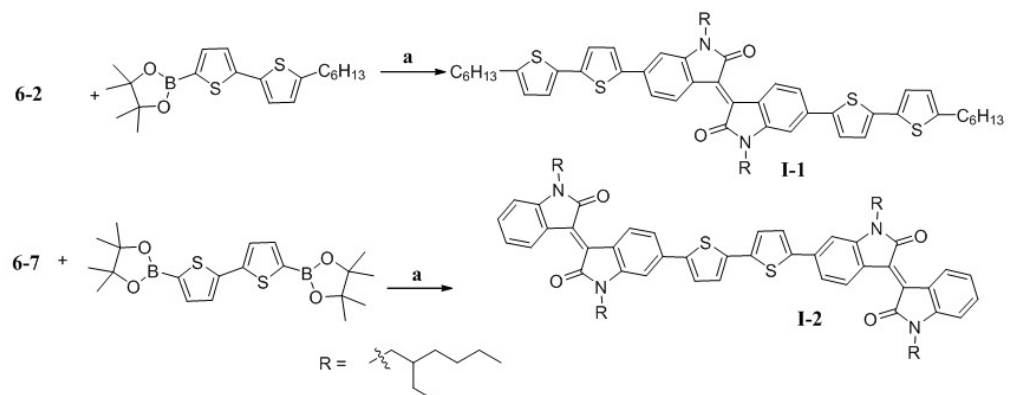


Figure 6-4. Synthesis of **I-1**, and **I-2**. a) $Pd_2(dbu)_3$, $P(o\text{-}tolyl)_3$, Et_4NOH , toluene, 85 °C, 83% and 57% for **I-1**, and **I-2**, respectively.

6.2.2 Structural Characterization, Optical and Electrochemical Studies

UV-vis absorption spectra of the oligomers, both in THF solution and as films on indium-tin oxide coated glass were measured and are shown in Figure 6-5. Compound **I-1** and **I-2** broadly absorb at wavelengths up to 688 and 655 nm in solution with molar absorptivities of 19 500, and $47\ 300\ L\ M^{-1}\ cm^{-1}$ at 579 and 560 nm, respectively, and are, thus, strongly absorbing through most of the visible spectrum as desired for solar cell applications. Markedly different from other donor-acceptor systems, there exists only a very shallow absorption valley between two absorption bands for both molecules, which makes them appear virtually black in solution. The spectra broaden and extend to 744 and 703 nm in the solid state with a peak emerging at 660 and 636 nm for **I-1** and **I-2**, indicating strong π - π interactions in their crystalline forms. Upon annealing at 100 °C for 20 min, a slight decrease in absorption intensity was observed for both oligothiophenes. From the absorption onsets in the solid state, the optical energy gaps are estimated to be 1.67 eV for the DAD molecule and 1.76 eV for the ADA molecule. Both **I-1** and **I-2** are fluorescent, emitting with maxima at 780 and 749 nm in chloroform, respectively.

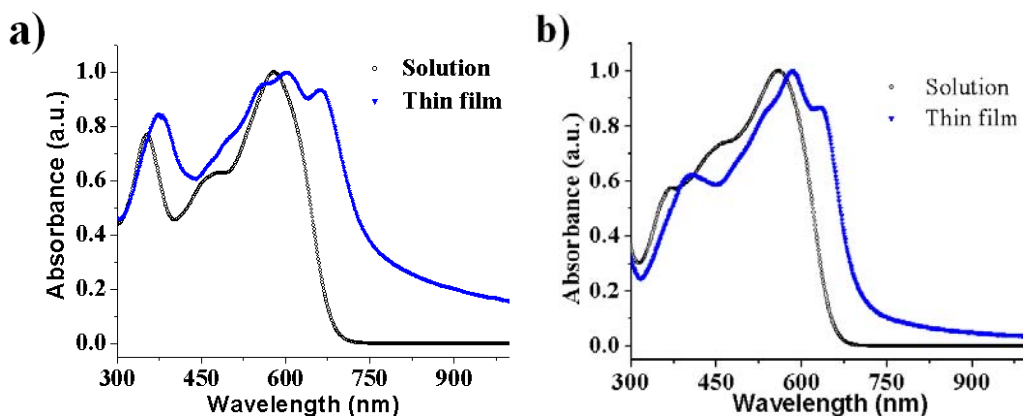


Figure 6-5. UV-vis spectra of I-1 and I-2 in solution and in thin-film

The redox behavior of the oligomers, shown in Figure 6-6, was investigated by cyclic voltammetry (CV) in dichloromethane (DCM) using tetrabutylammonium hexafluorophosphate

(TBAPF₆, 0.1M) as the supporting electrolyte. Both oligothiophenes present two consecutive quasi-reversible reduction peaks with E_{1/2}^{red} of -1.31 and -1.71 V for **I-1**, and of -1.35 and -1.74 V for **I-2**. Two oxidation waves appear in the CV of **I-1** with E_{1/2}^{ox} of 0.47 and 0.58 V; while only one oxidation wave was observed for **I-2** with E_{1/2}^{ox} of 0.52 V. This is in accordance with the more electron rich (easier to oxidize) DAD molecule than the ADA molecule. The LUMO and HOMO energies of **I-1** and **I-2**, estimated by CV, are -3.9 and -5.5 eV, and -3.8 and -5.5 eV, respectively.

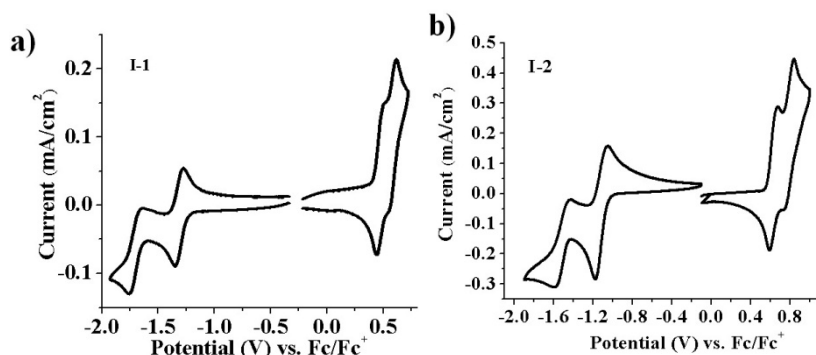


Figure 6-6. Cyclic voltammetry of **I-1** (left) and **I-2** (right) measured in a 0.1 M solution of TBAPF₆/DCM (scan rate 25 mV/s) vs Fc/Fc⁺.

In order to gain more insight into the energy levels in solid state, differential pulse voltammetry (DPV) was performed on drop-cast films of **I-1** and **I-2** on Pt button electrodes. From the onset of oxidation by DPV, the HOMO level of -5.6 eV is estimated for both **I-1** and **I-2**. Unfortunately, the first reduction wave was not observed for both molecules. Therefore, the LUMO levels were calculated using the values obtained from the solid state optical band gap, giving -3.9 and -3.8 eV for **I-1** and **I-2**. The solid state results are very close to the ones in solution. The appropriate energy levels and gap, together with the high absorption coefficients, suggest the new isoindigo-based oligothiophenes should be effective electron donors in BHJ solar cells. The energy levels of **I-1** and **I-2** are very similar with those of **DPP-1**, for which HOMO and LUMO levels are -5.5 and -3.9 eV, respectively. This observation suggests isoindigo

and diketopyrrolopyrrole as electron-accepting building blocks are very close regarding their ability to stabilize added electrons given that the LUMO levels are usually affected and governed by acceptors in donor-acceptor type materials.

Table 6-1. Solid state optical and electrochemical properties and calculated energy levels.

| | E_g^a (eV) | $E_{onset,ox}^b$ (V) | HOMO (eV) | LUMO (eV) |
|------------|--------------|----------------------|-----------|-----------|
| I-1 | 1.67 | 0.56 ^b | -5.6 | -3.9 |
| I-2 | 1.76 | 0.55 ^b | -5.6 | -3.8 |

^afrom thin film on ITO, after annealing. ^b from DPV of drop cast film on Pt button electrode, in 0.1 M solution of TBAPF₆/PC.

6.2.3 Molecular Bulk-Heterojunction Solar Cells

Molecular BHJ solar cells were fabricated by spin-coating **I-1/I-2:PC₆₁BM** blends from chlorobenzene onto a clean ITO/PEDOT:PSS bottom electrode on a glass substrate.

Optimization experiments exploring different blend ratios, annealing temperatures, and solution concentrations resulted in the highest power conversion efficiencies (PCEs) for **I-1/I-2:PC₆₁BM** blend ratios of 50:50 (**I-1**) and 60:40 (**I-2**), an annealing temperature of 100 °C, and a total solution concentration of 18 mg/mL.

The BHJ cells made from **I-1** performed significantly better than devices made from **I-2**. The *J-V* characteristics for annealed devices are shown in Figure 6-7. After annealing at 100°C, solar cells made from **I-1** showed a PCE of up to 1.76%, with a V_{oc} of 0.74 V, J_{sc} of 6.3 mA/cm², and fill factor of 0.38. Annealed photovoltaic devices (100 °C) of **I-2** had PCEs of up to 0.55%, with a V_{oc} of 0.66 V, J_{sc} of 2.4 mA/cm², and fill factor of 0.36. Pre-annealed devices were less efficient with PCEs of 0.72 and 0.11% for **I-1** and **I-2** respectively, as shown in Table 6-8. It is noted that the fill factors here are about ~0.38, typical for solution-processed small molecule solar cells,⁷¹ which is in sharp contrast with the high fill factors obtained for **DPP-1**. This observation indirectly proves that amphiphilic molecular design is indeed accountable for the

high fill factors in **DPP-1**. Future studies will work towards applying amphiphilic molecular design to isoindigo based oligothiophenes in order to achieve higher performance photovoltaic devices.

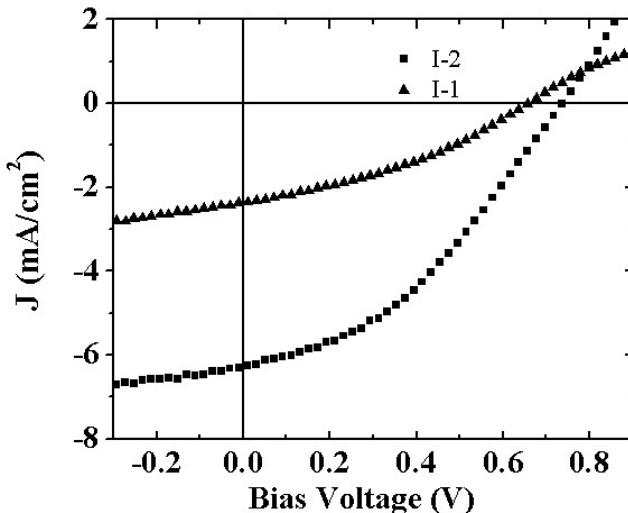


Figure 6-7. J-V characteristics of I-1/I-2:PC₆₁BM solar cells under 100 mW/cm² white light illumination annealed at 100 °C for 20 min.

Table 6-2. Performance of I-1/I-2:PC₆₁BM solar cells before and after annealing

| Donor | V _{oc} /V | J _{sc} /(mA/cm ²) | FF | η/(%) |
|------------------------|--------------------|--|------|-------|
| I-1 | 0.64 | 4.6 | 0.25 | 0.72 |
| I-1^a | 0.74 | 6.3 | 0.38 | 1.76 |
| I-2 | 0.62 | 0.9 | 0.21 | 0.11 |
| I-2^a | 0.66 | 2.4 | 0.36 | 0.55 |

a) Annealed at 100 °C for 30 min.

Considering the similar optical and electronic properties of **I-1** and **I-2**, it is interesting to look into their film morphologies in the device, which may explain their different photovoltaic performances. As with many examples found in the organic photovoltaic literature, device performance is highly dependent on thin-film morphologies in both small molecule and polymer based solar cells.^{81,318} For this purpose, AFM was used to examine the thin film morphologies of the optimized devices based on **I-1** and **I-2**. The AFM height images of the blend films before

and after annealing are presented in Figure 6-8. Before annealing, both films look very smooth. The desired phase separation is not observed, which in part explains the low device performance for both **I-1** and **I-2**. Upon annealing, however, the surface of both films become rougher and phase separation appears with more ordered crystalline domains found in the case of **I-1**/PC₆₁BM blend film. Apparently, the morphology changes lead to the enhancement in performance of both **I-1** and **I-2** based devices. However, it is difficult to draw a conclusion on which morphology is preferred between the crystalline domains (Figure 6-9b) or the amorphous domains (Figure 6-9d), since several fold increases in PCEs have been found in both cases.

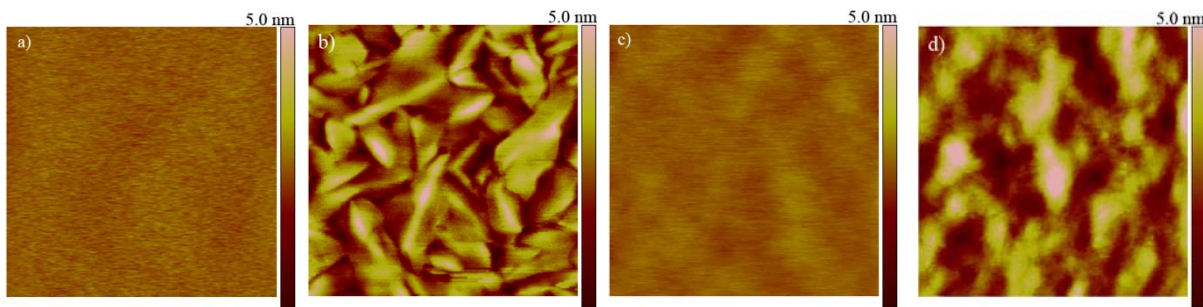


Figure 6-8. AFM height images of I-1:PCBM (50:50) spin-coated from chlorobenzene a) as cast, and b) annealed at 100 °C for 20 min; I-2:PCBM (60:40) spin-coated from chlorobenzene c) as cast, and d) annealed at 100 °C for 20 min. All images are 1 x 1 μm with 5 nm height scales. RMS surface roughness values of the AFM images are 0.15 nm, 0.98 nm, 0.14 nm, and 0.95 nm from left to right.

We note that polydimethylsiloxane (PDMS) has been found in the syringe we used for material processing and discovered to have a profound effect on device morphology. Since this so called “macromolecular effect” is beyond of the scope of this dissertation, it is not discussed here although more details will be revealed in later studies.

In summary, we have introduced isoindigo as an acceptor into the field of electroactive materials, presented the Synthesis and characterization of isoindigo-based oligothiophenes, and fabricated molecular BHJ solar cells using these oligothiophenes as electron donors for the first time. These devices exhibit some of the best power conversion efficiencies for solution

processed small molecules. We are currently working to fine tune the optical and electronic properties of isoindigo-based donor-acceptor materials through molecular design, to better understand the effect of chemical structure and film morphology on photovoltaic response, which will be discussed in more details in the next section.

6.3 Molecular Engineering in Isoindigo-based Oligomers

In the previous section, we reported two isoindigo-based oligothiophenes and their utilization as electron donor materials in molecular BHJ solar cells. In order to gain more insight into the structure-property relationships of isoindigo-based materials in solid-state electronic devices (OFETs and OPVs), we take a molecular engineering approach to access a set of oligomers that highly resemble each other structurally. While the proposed structures share the same isoindigo acceptor core, the difference only lies in the donor portion where 1-methylbenzopyrrole, benzofuran and benzothiophene are used as electron donors to give **IsoI-N**, **IsoI-O** and **IsoI-S**, respectively, as shown in Figure 6-9. This set of oligomers is expected to provide an excellent platform to look into how rational design and careful structural modification can be utilized to tune material properties.

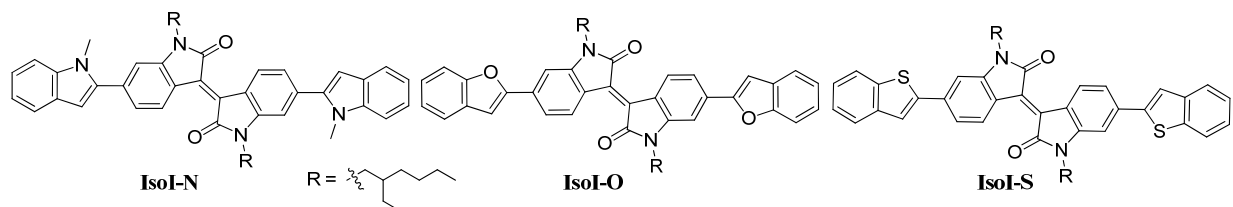


Figure 6-9. Chemical structures of IsoI-N, IsoI-O and IsoI-S.

6.3.1 Synthesis of Isoindigo-Based Oligomers

The Synthesis of **IsoI-N**, **IsoI-O** and **IsoI-S** was carried out via Suzuki coupling between **6-2** and commercially available boronic ester or boronic acid functionalized donor components, namely 1-methyl-2-(4,4,5,5-tetramethyl-1,3,2-dioxaborolan-2-yl)-1H-indole, benzofuran-2-

ylboronic acid and benzo[b]thiophen-2-ylboronic acid, yielding **IsoI-N**, **IsoI-O** and **IsoI-S** in excellent yields (84 –92%), as shown in Figure 6-10. It is worth mentioning that the purification process for these compounds is rather simple and can be achieved by a precipitation method (see the synthetic details).

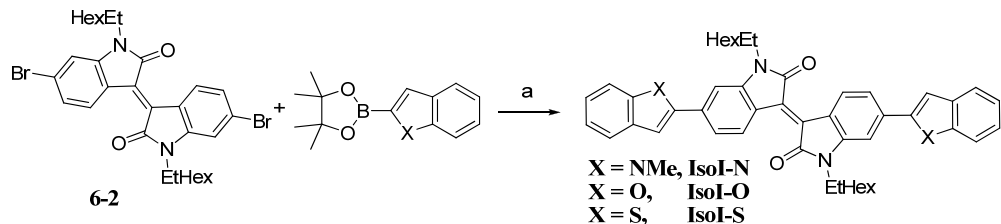


Figure 6-10. Synthesis of IsoI-N, IsoI-O and IsoI-S. a) $\text{Pd}_2(\text{dba})_3$, $\text{P}(\text{o-tyl})_3$, Et_4NOH , toluene, 85 °C, 88%, 92%, and 84% for IsoI-N, IsoI-O and IsoI-S, respectively.

6.3.2 Structural Characterization, Optical and Electrochemical Studies

The structures of **IsoI-N**, **IsoI-O** and **IsoI-S** have been confirmed by ^1H - and ^{13}C -NMR, HRMS, and elemental analysis. A brief analysis is given as follows to reflect the influence of structural differences on chemical shifts in ^1H -NMR. Figure 6-11a shows the full ^1H -NMR spectra of **IsoI-N**, **IsoI-O** and **IsoI-S**. The chemical shifts for the protons on the ethylhexyl chains are very similar in all three oligomers while the signal from the N-methyl group is located at ~3.84 ppm in the ^1H -NMR spectrum of **IsoI-N**. The peaks in the aromatic region present different splitting patterns and chemical shifts for **IsoI-N**, **IsoI-O**, and **IsoI-S**, and these regions are shown in Figure 6-11b, c and d, respectively. For example, a close look at Figure 6-10b leads to assignment of the doublet (it looks like a singlet because of the small coupling constant) at 6.71 ppm to H_a with a very small coupling constant ~0.6 Hz, a consequence of long range W (zigzag) coupling with H_c ; while H_b is shifted downfield to 9.29 ppm because of the *ortho*-bonded electron withdrawing group and possible hydrogen bonding interactions with the carbonyl group. The signal from H_d also is a doublet with a small coupling constant of 1.5 Hz, resulting from the interaction with H_c as well. The further assignments of H_e , H_f , H_g and H_h are

not very reliable based on 1-D ^1H -NMR in the case of **IsoI-N**, even though we can tentatively assign peaks at 7.69 and 7.41 ppm to H_e and H_f .

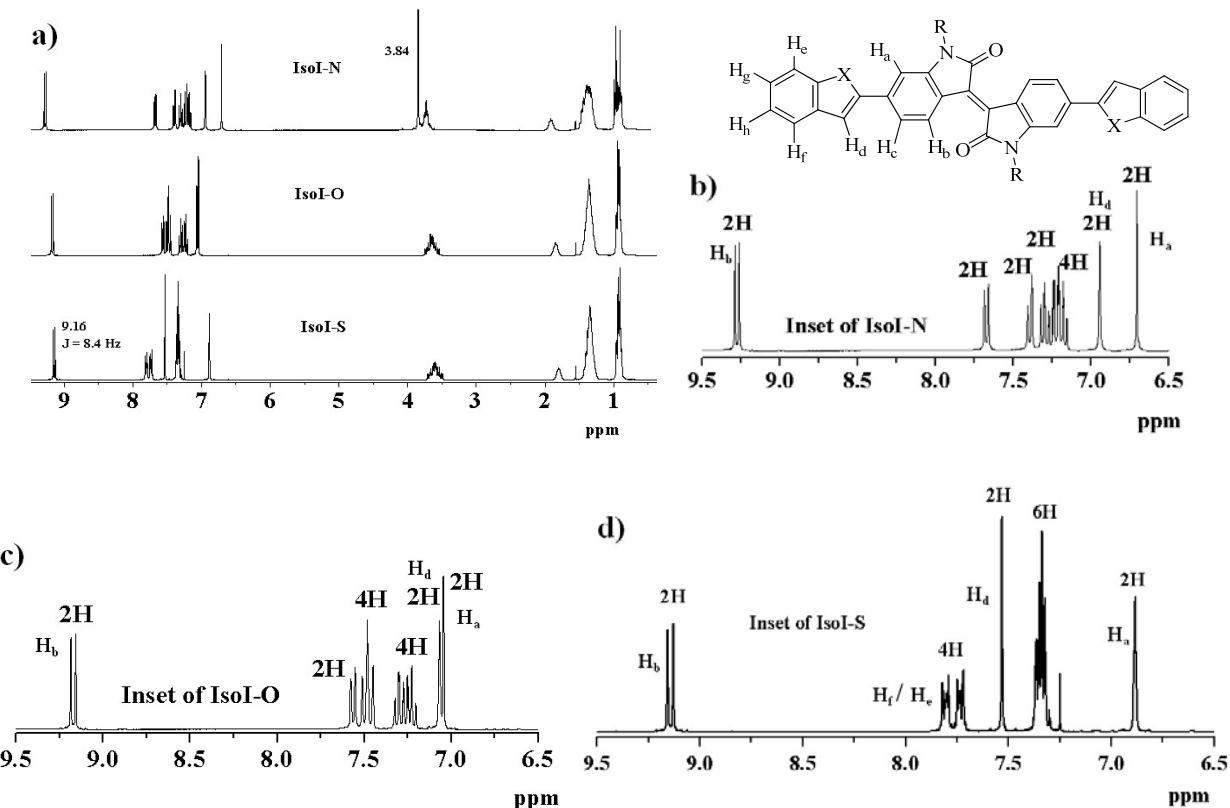


Figure 6-11. $^1\text{H-NMR}$ spectra of IsoI-N, IsoI-O and IsoI-S including a) the full spectra and the aromatic regions of b) IsoI-N, c) IsoI-O, and IsoI-S.

A similar analysis can be extended to **IsoI-O** and **IsoI-S**. It is found that H_a has shifted downfield to 7.05 ppm in **IsoI-O** and to 6.89 ppm in **IsoI-S** relative to the 6.71 ppm in **IsoI-N**. This observation is consistent with the decreasing electron-donating ability on moving from 1-methylbenzopyrrole to benzofuran and benzothiophene. It is also interesting to look at H_d which has shifted to 7.07 ppm in **IsoI-O** and 7.53 ppm in **IsoI-S** from 6.95 ppm in **IsoI-N**. This trend follows exactly the same chemical shift change in the parent compounds 1-methyl-benzopyrrole, benzofuran and benzothiophene, where H_d is in a region of greater aromatic character. It is particularly evident when a comparison is made between **IsoI-O** and **IsoI-S**, in which H_e, H_f, H_g and H_h have a vastly different chemical shift split patterns. In the case of **IsoI-S**, the peaks are

much more downshifted and have larger coupling constants due to its higher aromatic character of benzothiophene. The chemical shifts from H_e and H_f are much closer to those from H_g and H_h in **IsoI-O**. Through the simple NMR analysis, we do find that electronic properties displayed in the format of chemical shits here are affected by the delicate structural modifications.

The solution and solid-state UV-vis spectra of **IsoI-N**, **IsoI-O** and **IsoI-S** are exhibited in Figure 6-12. In solution, the spectra look alike with minor difference. **IsoI-N** absorbs past 669 nm with three absorption maxima at ~ 555, 457, and 299 nm in chloroform. A molar absorptivity of 20,400 M⁻¹ cm⁻¹ at 555 nm is obtained. Similarly, **IsoI-O** absorbs with an onset at ~675 nm and three absorption maxima at ~ 563, 461, and 318 nm. Its molar absorptivity is about 27,300 M⁻¹ cm⁻¹ at 563 nm; while **IsoI-S** absorbs past 662 nm with three absorption maxima at ~ 552, 452, and 319 nm. The molar absorptivity of 26,300 M⁻¹ cm⁻¹ at 552 nm is found for **IsoI-S**. As mentioned earlier, benzofuran is a stronger electron donor than benzothiophene. Our observation in solution absorbance for **IsoI-O** and **IsoI-S** is consistent with their electron donating ability that is the origin for a longer wavelength absorption in **IsoI-O**. Interestingly, **IsoI-N** does not strictly agree with this argument and its absorption onset and maxima fall in the middle of **IsoI-O** and **IsoI-S**, even though benzopyrrole is expected to be the strongest electron donor among the three. This is likely due to a slight distortion between the donor and acceptor caused by the methyl group on the nitrogen atom that weakens the donor-acceptor interaction and hence gives **IsoI-N** a slight hypsochromic shift in absorption.

An astonishing contrast for **IsoI-N**, **IsoI-O** and **IsoI-S** is observed in their solid-state absorption spectra, as shown in Figure 6-12b. Most significantly, the absorption of **IsoI-S** broadens and extends to 719 nm and a nearly 57 nm red shift is observed relative to solution absorbance. In addition, two new absorption maxima appear at 666 and 617 nm. In contrast,

there is ONLY a 6 nm red shift observed for **IsoI-N**. **IsoI-O** somehow behaves normally like the previously studied molecules **I-1** and a 23 nm red shift is found. It is also noticed that **IsoI-O** and **IsoI-S** have a relatively strong vibronic peaks across the spectra, indicating a strong coupling between electronic and vibrational states. An elegant analysis can be found elsewhere.³¹⁹ Considering the similarity in their solution absorbance, the difference in solid-state absorption can be only explained by their different crystallinity and solid state ordering. More specifically, it is logical to speculate that the crystallinity in **IsoI-S** is much higher than in **IsoI-N** and **IsoI-O**. In other words, the aggregation and interchain interactions are much more severe in **IsoI-S** thin films, which are supported by the much higher melting point for **IsoI-S**, as will be discussed later. To verify this speculation, however, single crystal X-ray diffraction experiments should be performed.

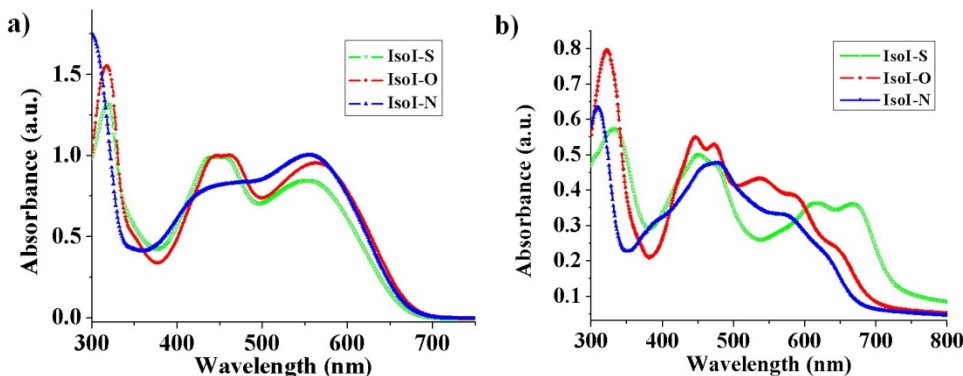


Figure 6-12. UV-vis spectra of IsoI-N, IsoI-O and IsoI-S a) in chlorobenzene, and b) in thin-film.

The absorption spectra of **IsoI-N**, **IsoI-O** and **IsoI-S** present similar optical responses upon thermal annealing, as shown in Figure 6-13. In the case of **IsoI-N**, a slight decrease in absorption intensity for the high-energy band is observed after annealing. This has also been observed in the DPP-based molecule in Nguyen's study.⁸⁰ Changes in optical response in **IsoI-O** are relatively minor upon annealing. It first has a slight drop in absorption intensity from room temperature to 100 °C followed by a significant increase in optical intensity from 100 °C to 150 °C. At this

point, this phenomenon is not fully understood. Likely, there is energy barrier to overcome before the molecules can be oriented in an orientation for favorable crystal packing. An interesting observation is found in **IsoI-S** where the optical change is almost absent upon annealing up to 150 °C. We speculate that the lack of thermally-induced optical change is resulted from high crystallinity for **IsoI-S** upon spin-casting.

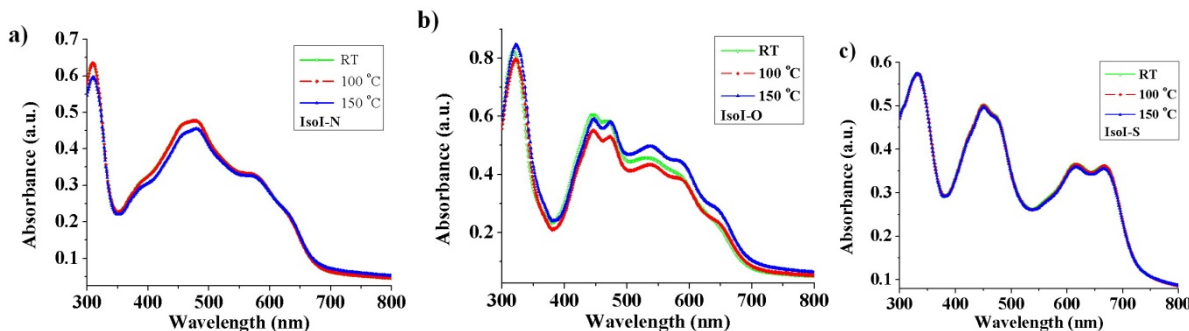


Figure 6-13. UV-vis spectra of as cast and thermally annealed a) IsoI-N, b) IsoI-O and c) IsoI-S.

Cyclic voltammetry (CV) and differential pulse voltammetry (DPV) were used to investigate the redox properties of **IsoI-N**, **IsoI-O** and **IsoI-S** with the goal of determining how oxidation and reduction potentials, together with HOMO and LUMO energy levels, vary from **IsoI-N**, to **IsoI-O** and to **IsoI-S**. The results are summarized in Table 6-3. The experimental setup consists of a platinum button electrode, a platinum counter-electrode, a Ag/Ag⁺ reference electrode and a electrochemical cell with a three-hole cap. The experiments were performed in 0.1 M TBAPF₆/DCM under inert atmosphere in an argon-filled dry box. All estimated potentials were subsequently calibrated versus Fc/Fc⁺.

CV and DPV analysis of **IsoI-N**, **IsoI-O** and **IsoI-S** were performed, as illustrated in Figure 6-14. **IsoI-N** shows an onset of reduction at -1.04 V with E_{1/2} of -1.13 and -1.56 V from cyclic voltammetry; while **IsoI-O** exhibits a reduction onset at -1.0 V with E_{1/2} of -1.08 and -1.48 V, and **IsoI-S** presents an onset of reduction at -1.0 V as well, with E_{1/2} of -1.10 and -1.49 V. These values from CV are consistent with the trends in the results obtained from DPV. All three

oligomers have stable and reversible scans for both reduction processes as observed in CV and DPV. Similar reduction onsets, together with $E_{1/2}$, suggest the LUMO levels are localized on the isoindigo core and are not strongly dependent on the donors used in these oligomers.

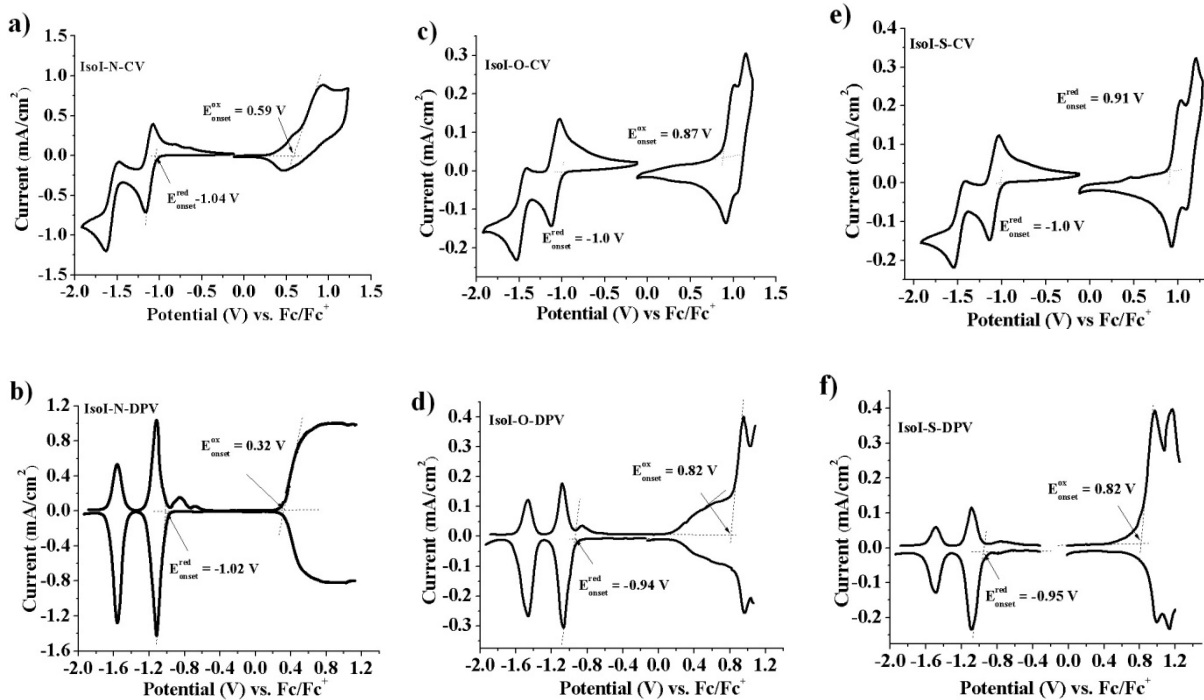


Figure 6-14. Cyclic voltammograms (scan rate = 50 mV/s) and differential pulse voltammetry (step size of 2 mV and step time of 0.1 seconds) of IsoI-N, IsoI-O and IsoI-S in 0.1 M TBAPF₆-CH₂Cl₂ electrolyte solution. a) CV of IsoI-N; b) DPV of IsoI-N; c) CV of IsoI-O; d) DPV of IsoI-O; e) CV of IsoI-S; f) DPV of IsoI-S.

To determine the exact oxidation onset from CV is difficult for **IsoI-N**, since the CV of **IsoI-N** appeared highly irreversible upon applying an anodic potential and the current intensity increased per scan. It was later discovered that this oligomer actually underwent electropolymerization, as shown in Figure 6-15a. The electropolymerized poly(**IsoI-N**) has a much broader and red-shifted absorption on ITO, as displayed in Figure 6-15b. Nevertheless, an oxidation onset was estimated to be 0.59 V with an $E_{1/2}$ of 0.71 from the first CV scan. The oxidation onset of 0.32 V from the DPV was tentatively assigned. The CV of **IsoI-O** yielded an oxidation onset of 0.87 V with $E_{1/2}$ of 1.03 and 1.04 V. In comparison, the onset of oxidation for

IsoI-S moves 0.91 V, slightly higher than **IsoI-O**, so does the $E_{1/2}$. Although **IsoI-O** had reversible CV scans, a shoulder appeared in DPV upon oxidation and on neutralization. The mechanism is not understood at this point. In contrast, **IsoI-S** has a prototypical DPV scan, yielding an oxidation onset of 0.82 V. Through the analysis of CV and DPV, it is clear that the oxidation process is largely determined by the donors. On changing the donor from benzothiophene to benzofuran to benzopyrrole, the oligomers became easier to oxidize.

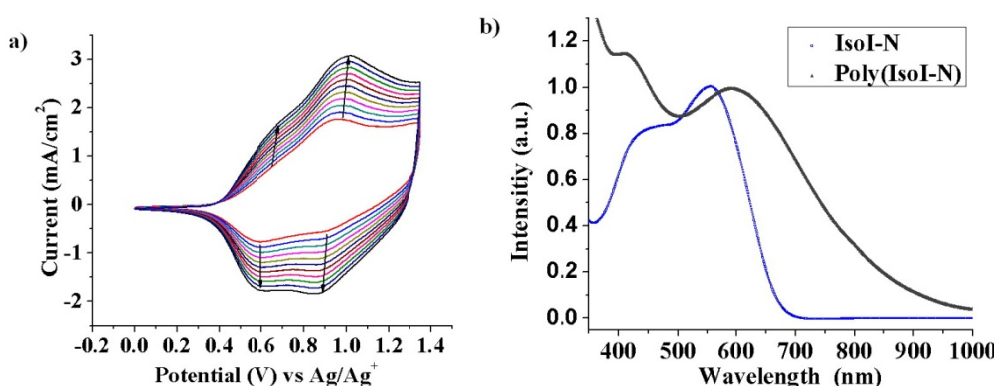


Figure 6-15. a) Repetitive scan electropolymerization of 5 mM IsoI-N on ITO in 0.1 M TBAPF₆/DCM ; b) UV-Vis spectra of IsoI-N in CH₂Cl₂ and electropolymerized Poly(IsoI-N) on ITO

Table 6-3. Electrochemically determined HOMO and LUMO energy levels of IsoI-N, IsoI-O and IsoI-S (by CV and by DPV).

| | CV | | DPV | | CV | | DPV | |
|---------------|-----------|-----------|-----------|-----------|------------|-----------|------------|-----------|
| | E(ex) (V) | HOMO (eV) | E(ex) (V) | HOMO (eV) | E(red) (V) | LUMO (eV) | E(red) (V) | LUMO (eV) |
| IsoI-N | 0.59 | -5.69 | 0.32 | -5.42 | -1.04 | -4.06 | -1.02 | 4.08 |
| IsoI-O | 0.87 | -5.97 | 0.82 | -5.92 | -1.00 | -4.10 | -0.94 | -4.16 |
| IsoI-S | 0.91 | -6.01 | 0.82 | -5.92 | -1.00 | -4.10 | -0.95 | -4.15 |

Note: oxidation (E_{ox}) and reduction (E_{red}) potentials are reported vs. Fc/Fc⁺, and energy level derived from the electrochemical data considering that Fc/Fc⁺ is 5.1 eV relative to vacuum.

In addition, it is also interesting to note that the energy levels of **IsoI-O** and **IsoI-S** are very close from both CV and DPV analyses. The energy gaps from CV (DPV) are 1.87 (1.86) and

1.91 (1.87) eV for **IsoI-O** and **IsoI-S**, respectively. These values are in good agreement with their optical energy gaps, which are 1.83 and 1.87 eV obtained from the onset of absorption in CH_2Cl_2 solution. However, there is a large difference between the electrochemical gaps (1.63 and 1.34 eV from CV and DPV) and the optical gap (1.84 eV). The large discrepancy between these gaps is not completely unexpected, as the values measured from CV and DPV may reflect more character of poly(**IsoI-N**) than that of the oligomer **IsoI-N**. To support this assertion, it is noted that the optical bandgap of poly(**IsoI-N**) is about 1.39 eV obtained from electropolymerized films on ITO.

6.3.3 Thermal Analysis

Thermogravimetric analysis was carried out for all three oligomers in order to provide necessary information for differential scanning calorimetry (DSC) studies. As illustrated in Figure 6-16, all these molecules are thermally stable up to more than 300 °C under nitrogen atmosphere. Interestingly, **IsoI-O** and **IsoI-S** have almost identical decomposition temperatures.

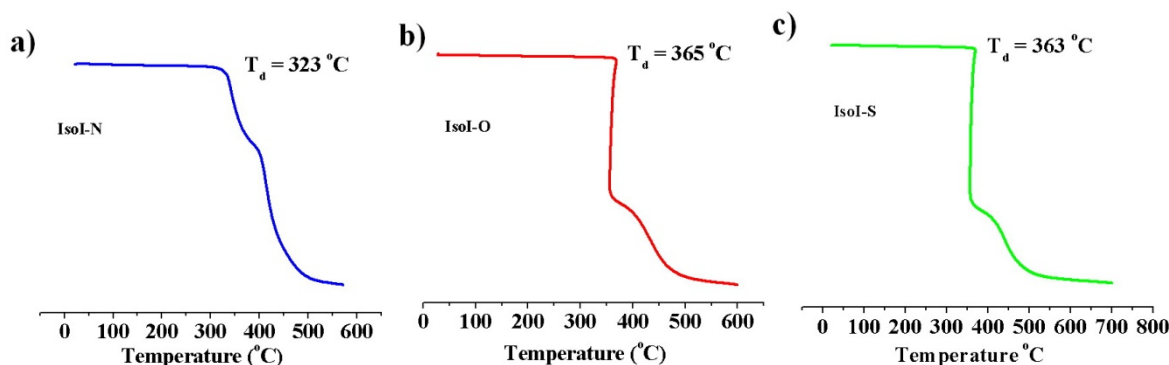


Figure 6-16. Thermogravimetric analysis of a) IsoI-N, b) IsoI-O and c) IsoI-S.

DSC analysis of **IsoI-N**, **IsoI-O** and **IsoI-S** was performed in order to provide phase transition information. Figure 6-17 shows the DSC thermograms. Other than **IsoI-O**, in which a normal crystalline-isotropic thermal transition is present with a melting temperature at ~225 °C, **IsoI-N** and **IsoI-S** both exhibit some unexpected thermal behaviors to a certain degree. Upon

heating at $10\text{ }^{\circ}\text{C min}^{-1}$, **IsoI-N** underwent a very broad endothermic transition around $\sim 192\text{ }^{\circ}\text{C}$ (starting at $185\text{ }^{\circ}\text{C}$) with an enthalpy change of 38.7 kJ mol^{-1} . Surprisingly, the recrystallization process failed to appear upon cooling. More strikingly, the endothermic transition also disappeared in the second heating scan. As confirmed by the TGA analysis, **IsoI-N** is thermally stable up to $300\text{ }^{\circ}\text{C}$. It is unlikely that **IsoI-N** experienced the decomposition event during the course of DSC experiment. We suspect that a thermally-induced Diel-Alder reaction occurs. The behavior of **IsoI-S** came unexpectedly as a consequence of its polycrystalline-like thermal behavior as shown in Figure 6-17c. In retrospect, this actually explains why black powder is obtained for **IsoI-S**. This also supports the solid state absorption where two new absorption maxima and an extended red-shift are observed. All these observations can be explained by the existence of two or multi-form crystalline mesophases, which have different crystal orientations and thus lead to their preferred absorbance in solid state.

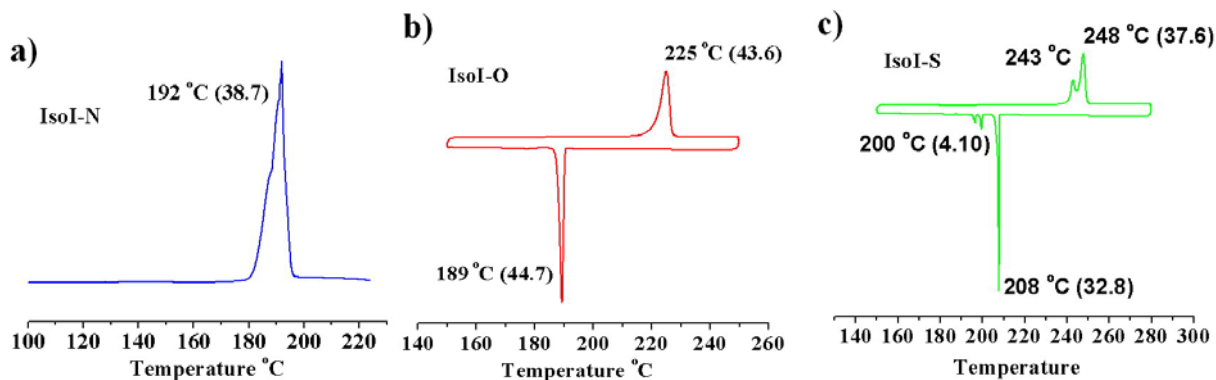


Figure 6-17. DSC thermograms of a) IsoI-N, b) IsoI-O and c) IsoI-S (kJ mol^{-1} , unit in parendissertation after transition temperature)

6.3.4 Field-Effect Transistors and Molecular Bulk-Heterojunction Solar Cells

The results of this OFET part are contributed by Dr. Shree Prakash Tiwari at Georgia Tech. Bottom-gate top-contact OFETs were fabricated on heavily doped n-type silicon substrate (which also serves the gate electrode) with 200 nm thick thermally grown SiO_2 as the gate dielectric, in top a contact configuration. Ti/Au (10 nm/100 nm) metallization on the backside of

the substrate was done to enhance the gate electrical contact. Firstly, the substrates were cleaned by O₂ plasma for three minutes, to insure the proper film formation by changing the surface property of SiO₂ towards hydrophilic. The capacitance of the SiO₂ layer was ~16.2 nF/cm². A thin layer of organic semiconductor was formed on the substrates by spin coating with a solution 10 mg/mL in chlorobenzene, or 15 mg/mL in chloroform. Then, Au (approximately 75 nm-thick film) was deposited through a shadow mask to act as top source/drain electrode. The device fabrication was done under inert (N₂) atmosphere. The samples were transferred in a vacuum tight vessel without being exposed to atmosphere into a N₂-filled glovebox (O₂, H₂O ~ 0.1 ppm) for electrical testing. An annealing step is done at 130°C for 30 minutes before device characterization.

Table 6-4 summarizes the FET response for all **IsoI-N**, **IsoI-O** and **IsoI-S** devices processed from either chloroform or chlorobenzene and annealed at 130 °C. Representative transfer/output plots for **IsoI-S** OFET devices processed from chloroform solution are shown in Figure 6-18. The negative gate and source-drain voltages demonstrate that **IsoI-S** is a p-channel material. This is consistent with previous reports on **DPP-1** and the aforementioned HOMO energy values, which are accessible for hole injection from Au contacts (5.1 eV). From the output plot of **IsoI-S** OFET device, hole mobility up to $\sim 4.1 \times 10^{-4} \text{ cm}^2 \text{ V}^{-1} \text{ s}^{-1}$ and I_{on}/I_{off} of 10³ is obtained under inert atmosphere. In sharp contrast, the mobility values of **IsoI-N** and **IsoI-O** are one order magnitude lower around $\sim 3.8 \times 10^{-5} \text{ cm}^2 \text{ V}^{-1} \text{ s}^{-1}$. The big difference between **IsoI-O** and **IsoI-S** is not anticipated, as they are both crystalline materials, and present very close electrochemically and optically determined energy levels. We speculate that the difference may arise with their different crystal packing and π-π interactions. A close look into the thin-film morphologies would be beneficial for understanding the difference, for instance, through AFM,

TEM and GISAXS (*Grazing-Incidence Small-Angle X-ray Scattering*) studies. In addition, we are also working to obtain single crystal structures of these molecules. A present effort is right now to replace the branched ethylhexyl alky chains with linear short linear alky chains in order to obtain single crystals.

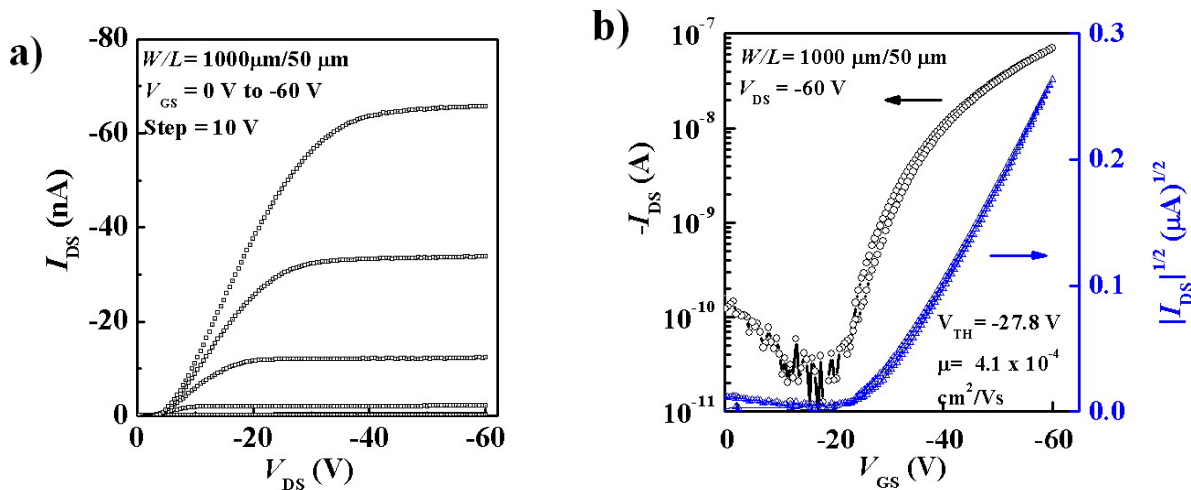


Figure 6-18. a) Output and b) transfer characteristics of a representative IsoI-S field-effect transistor device processed from chloroform solution.

Table 6-4. Bottom-Gate Top-Contact OFET Characteristics of IsoI-N, IsoI-O, and IsoI-S.

| Materials | IsoI-N ^a | IsoI-N ^b | IsoI-O ^a | IsoI-O ^b | IsoI-S ^a | IsoI-S ^b |
|--------------------------------------|---------------------|---------------------|---------------------|---------------------|---------------------|---------------------|
| μ (cm 2 /Vs) $\times 10^{-4}$ | 0.49 (\pm 0.04) | 0.38 (\pm 0.05) | n/a | 0.48 (\pm 0.13) | 1.8 (\pm 0.2) | 4.1 (\pm 0.1) |
| $I_{on/off}$ | 1×10^2 | 1×10^2 | n/a | 5×10^1 | 2×10^2 | 1×10^3 |

^a10 mg/ml in chlorobenzene; ^b15 mg/ml in chloroform

The preliminary solar cell results are kindly provided by Kenneth Graham at UF.

Molecular BHJ solar cells were fabricated by spin-coating **IsoI-N/IsoI-O/IsoI-S:PC₆₁BM** blends from chloroform onto a clean ITO/PEDOT:PSS bottom electrode on a glass substrate. A blend ratio of 60:40 was used for all three sets. The devices are annealed at a temperature of 100 °C for 20 min. Performance of **IsoI-N/IsoI-O/IsoI-S:PC₆₁BM** solar cells is summarized in Table 6-5.

The BHJ cells made from **IsoI-O** and **IsoI-S** performed significantly better than devices made from **IsoI-N**. The *J-V* characteristics for annealed devices are shown in Figure 6-19. The pair of **IsoI-N**/PC₆₁BM barely showed any photovoltaic response. Solar cells made from **IsoI-O** showed a PCE of up to 0.46%, with a V_{oc} of 0.71 V, J_{sc} of 2.0 mA/cm², and a fill factor of 0.33. Annealed photovoltaic devices of **IsoI-S** had PCEs of up to 0.36%, with a V_{oc} of 0.54 V, J_{sc} of 2.0 mA/cm², and a fill factor of 0.34. We speculate that the low performance of these oligomers is largely caused by inefficient charge transfer between the donors and PC₆₁BM, resulting from the extremely low LUMO levels (~4.1 eV) inherent to the oligomers. A possible way to increase solar cell efficiency is to introduce acceptors with even lower LUMO levels, such as PC₈₄BM (its electron affinity is about 0.35 eV higher than PC₆₁BM),³²⁰ which will provide sufficient energy offset (~0.4 eV) between the oligomers and PC₈₄BM and thus leads to the sufficient driving force for charge separation. Typically, it will cause small open circuit voltages (V_{oc}) with the deepening acceptor LUMO level, since V_{oc} is approximately determined by the offset between the LUMO level of the acceptor and the HOMO level of the donor. In this case, we would not have the concern, considering the low HOMO levels (~5.8-6.0 eV) for **IsoI-N**, **IsoI-O** and **IsoI-S**. A decent V_{oc} is still feasible. Based on Janssen' theory,¹²³ V_{oc} of 0.8-1.0 V is attainable. In addition, we once again noted that the fill factors here are about ~0.35, which is in sharp contrast with the high fill factors (~0.58) obtained for **DPP-1**. As we pointed out in the earlier section, future studies will work towards applying amphiphilic molecular design to isoindigo based oligothiophenes in order for achieving higher performance photovoltaic devices.

In this section, molecular engineering of isoindigo-based oligomers provides us an opportunity to closely examine the structure-property relationship in molecular organic semiconducting materials. From the optical, electrochemical and thermal analysis of **IsoI-N**,

IsoI-O and **IsoI-S**, we indeed observe big differences, which are induced by the small structural modifications. OFET and OPV studies support the same argument. Even though **IsoI-N**, **IsoI-O** and **IsoI-S** can not be considered as high performance organic electronic materials, this study is still fruitful. It conveys a very important message that designing materials for organic electronics is a very delicate process and small alternations can lead to big changes.

Table 6-5. Performance of IsoI-N/IsoI-O/IsoI-S:PC₆₁BM solar cells.

| Material | V _{oc} (V) | J _{sc} (mA/cm ²) | FF | % PCE |
|---------------------------------|---------------------|---------------------------------------|------|--------|
| IsoI-N:PC₆₁BM | 0.53 | 0.069 | 0.27 | 0.0099 |
| IsoI-O:PC₆₁BM | 0.71 | 2.0 | 0.33 | 0.46 |
| IsoI-S:PC₆₁BM | 0.54 | 2.0 | 0.34 | 0.36 |

In the weight ratio of 6:4 for all three sets and processed from CHCl₃ and annealed at 100 °C for 20 minutes prior to top electrode deposition.

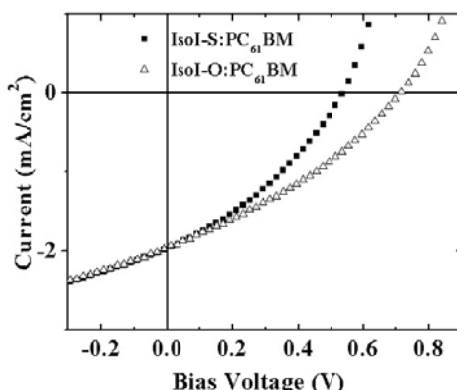


Figure 6-19. J-V characteristics of IsoI-O/IsoI-S:PC₆₁BM solar cells

6.4 Isoindigo-Based Polymers with Di-block Solubilizing Groups

In the previous several sections we discussed the structure-property relationships in isoindigo-based discrete oligomers. In this section, we investigate the structure-property relationship in isoindigo-based polymers. In order for solution processing to be possible from organic solvents, conjugated polymers typically contain linear or branched alkyl chains as solubilizing groups.^{2,145,321} Here, we introduce the concept of block (or biphasic) solubilizing groups to conjugated polymers. Block solubilizing groups, as the name implies, contain two or more immiscible segments along a hydrocarbon chain. We expect the driving force for phase

separation among solubilizing groups will enhance the interchain π - π interactions. This hypodissertation originates from the surfancant effect and rich phase separation behavior in block copolymers (e.g. PEO-*b*-PS-*b*-PMMA),³²²⁻³²⁴ where high ordering (both orientational and positional ordering) can be achieved via the process of self-assembly.

To test this hypodissertation, a set of three isoindigo-based donor-acceptor type conjugated polymers have been conceived and prepared. Their chemical structures are shown in Figure 6-20. All three polymers are composed of alternating isoindigo acceptor and thiophene donor units in the π -conjugated backbone. The difference among these polymers lies in their solubilizing groups. Specifically, **PIsoI_{AM}-1** has a biphasic solubilizing group where the hydrophobic end is attached to the nitrogen atom on the isoindigo unit; while **PIsoI_{AM}-2** has the hydrophilic end attached to the nitrogen atom. **PIsoI_{AM}-3** only contains a branched alkyl chain (hexyldecyl chain), serving as a control polymer for comparison.

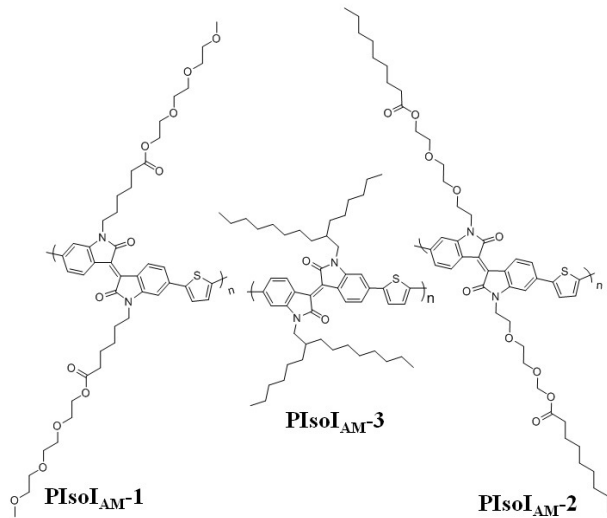


Figure 6-20. Polymer structures of PIsoI_{AM}-1, PIsoI_{AM}-2 and PIsoI_{AM}-3.

6.4.1 Synthesis of Isoindigo-Based Polymers with Biphasic Solubilizing Groups

The synthetic scheme is outlined in Figure 6-21. N-alkylation of isoindigo **6-1** with 7-(bromomethyl)hexadecane, 2-(2-(2-methoxyethoxy)ethoxy)ethyl 6-bromohexanoate, and 2-(2-

(2-(tosyloxy)ethoxy)ethyl nonanoate gave **6-5**, **6-9** and **6-10** in 70%, 35% and 49% yields, respectively. The yields for **6-9** and **6-10** are significantly lower than their derivatives with alkyl chains, likely due to side reactions caused by the presence of water as we described earlier. With **6-5**, **6-9** and **6-10** in hand, **PIsoI_{AM}-1**, **PIsoI_{AM}-2** and **PIsoI_{AM}-3** can be easily obtained by Stille coupling polymerization between their corresponding isoindigo monomer and 2,5-bis(trimethylstannyl)thiophene.

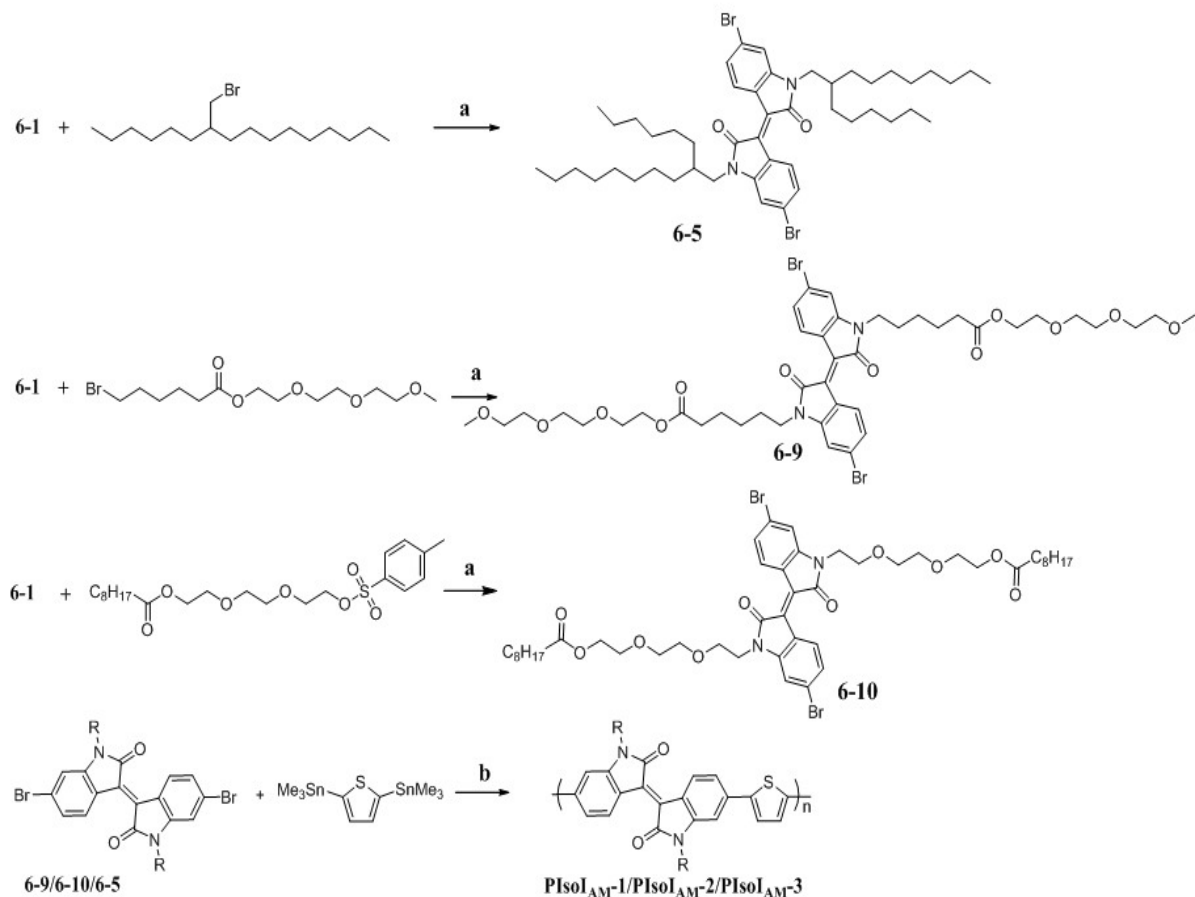


Figure 6-21. Synthesis of IsoI_{AM} building blocks and PIsoI_{AM}. a) K₂CO₃, DMF, 100 °C; b) Pd₂(dba)₃, P(o-tyl)₃, toluene, 85 °C.

6.4.2 Structural Characterization, Optical and Electrochemical Studies

The structures of these polymers were characterized by solution ¹H and ¹³C-NMR, and elemental analysis. Solution ¹H NMR gives very broad peaks in the aromatic region for these

polymers. Even in the aliphatic region the NMR spectrum is quite broad, and are thus not insightful for the structural elucidation. Elemental analysis of C, H, and N is consistent with the polymer structures. The experimental data are consistent with theoretical calculations. The errors for C, H and N are within 0.4% for all three polymers.

The GPC results are exhibited in Figure 6-22. **PIsoI_{AM}-1** and **PIsoI_{AM}-2** in THF likely contain a certain degree of aggregation as suggested by their GPC traces. High temperature GPC may give more insight. Therefore, it is difficult to estimate their molecular weights with high accuracy. It is believed that **PIsoI_{AM}-1** and **PIsoI_{AM}-2** have number average molecular weights higher than 25 kDa. **PIsoI_{AM}-3** shows a well-defined GPC trace, indicating the absence of severe aggregation. The number-average molecular weight estimated for **PIsoI_{AM}-3** is about 20.8 kDa and a PDI of 1.6.

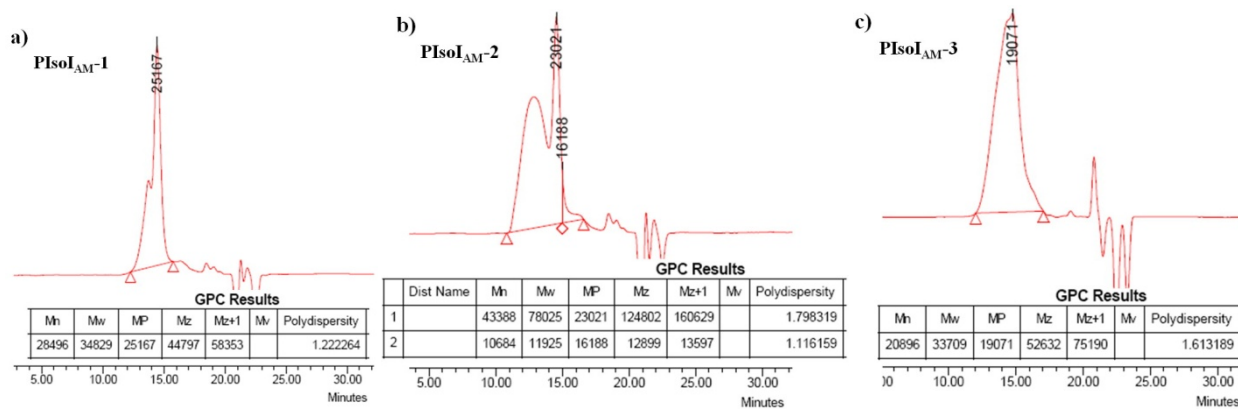


Figure 6-22. GPC traces of PIsoI_{AM}-1, PIsoI_{AM}-2 and PIsoI_{AM}-3

As stated in our hypodissertation, polymers with block solubilizing groups would have stronger π - π interactions both in solution and in solid state. A convenient solid-state UV-Vis measurement can be carried out to verify this argument, since strong and extensive π - π interactions will typically lead to a red shift in absorbance. Figure 6-23 shows UV-vis spectra of **PIsoI_{AM}-1**, **PIsoI_{AM}-2** and **PIsoI_{AM}-3** in thin film cast from chlorobenzene solutions. The

absorption onsets for **PIsoI_{AM}-1**, **PIsoI_{AM}-2** and **PIsoI_{AM}-3** are 785, 790 and 759 nm, respectively. A 30 nm red shift is indeed observed between **PIsoI_{AM}-2** and **PIsoI_{AM}-3**. This observation supports our aforementioned argument. Interestingly, a 5 nm red-shift is also noticed between **PIsoI_{AM}-1** and **PIsoI_{AM}-2**. This small change can be explained by two possibilities. First, the flexible oligoether chain is trapped between two incompatible segments, thus leading to higher degree of ordering in **PIsoI_{AM}-2**. On the opposite, the extremely flexible oligoether group has higher degree of freedom as a terminal chain in **PIsoI_{AM}-1**. The likelihood for the crystallization of terminal oligoether is low under ambient conditions. That is to say the first possibility is resulted from a higher degree of ordering in **PIsoI_{AM}-2** than in **PIsoI_{AM}-1**. The second possibility is due to a slightly lower LUMO level for **PIsoI_{AM}-2** because of the inductive effect from electronegative atom oxygen via the ethylene bridge connected to the nitrogen atom on isoindigo core.

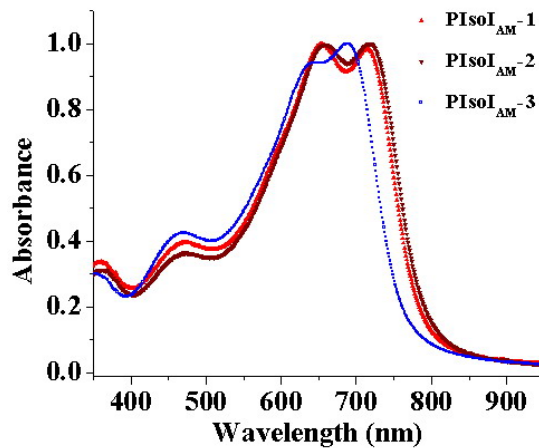


Figure 6-23. UV-vis spectra of **PIsoI_{AM}-1**, **PIsoI_{AM}-2** and **PIsoI_{AM}-3** in thin film.

Temperature-dependent UV-Vis measurements were carried out in order to provide additional information for their differences in absorbance, as shown in Figure 6-24. Upon heating from 5 to 95 °C in dichlorobenzene, a blue shift is observed for all three polymers and the absorption maxima at the longer wavelength of 709 and 711 nm for **PIsoI_{AM}-1** and **PIsoI_{AM}-2**

almost vanish. However, a noticeable absorption shoulder remains in both cases of **PIsoI_{AM}-1** and **PIsoI_{AM}-2**, indicating the polymers are still not full solvated even at 95 °C. We also notice that **PIsoI_{AM}-1** and **PIsoI_{AM}-2** are almost superimposed each other at 95°C, which suggests the local microstructures are responsible for the 5 nm difference in solid state absorption. We are also surprised to find out that **PIsoI_{AM}-2** is still much broader than **PIsoI_{AM}-3**. This was not anticipated. We had thought hoped that the gap would become smaller when the polymers are solvated, since they have the same conjugated backbone.

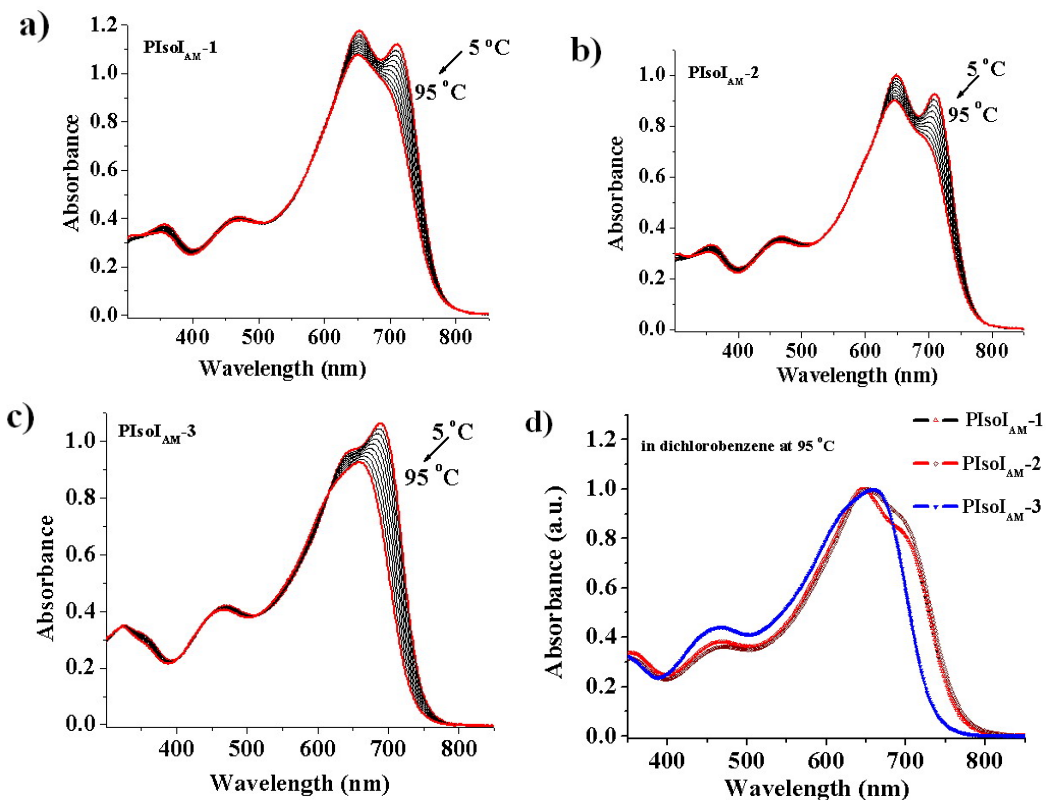


Figure 6-24. Temperature-dependent UV-Vis spectra of a) PIsoI_{AM}-1; b) PIsoI_{AM}-2; c) PIsoI_{AM}-3; and d) PIsoI_{AM}-1, PIsoI_{AM}-2 and PIsoI_{AM}-3 in dichlorobenzene at 95 °C.

Cyclic voltammetry analysis was carried out to obtain redox properties of **PIsoI_{AM}-1**, **PIsoI_{AM}-2** and **PIsoI_{AM}-3** by drop cast on platinum electrodes, as shown in Figure 6-25. From CV, the reduction onsets for **PIsoI_{AM}-1**, **PIsoI_{AM}-2** and **PIsoI_{AM}-3** are -1.15, -1.14 and -1.26 V, respectively; while the oxidation onsets are 0.32, 0.20 and 0.59 V, respectively. The

electrochemical bandgaps are 1.47, 1.34 and 1.85 eV accordingly. Figure 6-26 shows the DPV of **PIsoI_{AM}-1**, **PIsoI_{AM}-2** and **PIsoI_{AM}-3**. From DPV, the reduction onsets are -1.14, -1.08 and -1.07 V while the onsets of oxidation are 0.30, 0.20 and 0.65 V, respectively. The electrochemical bandgaps obtained from DPV are 1.44, 1.28 and 1.72 eV, respectively.

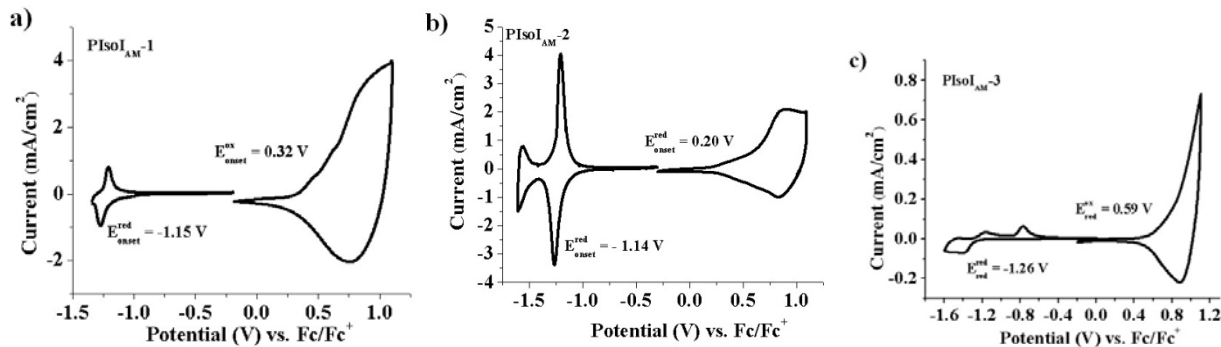


Figure 6-25. Cyclic voltammetry of a) PIsoI_{AM}-1; b) PIsoI_{AM}-2; c) PIsoI_{AM}-3 measured in a 0.1M solution of TBAPF₆/ACN vs Fc/Fc⁺.

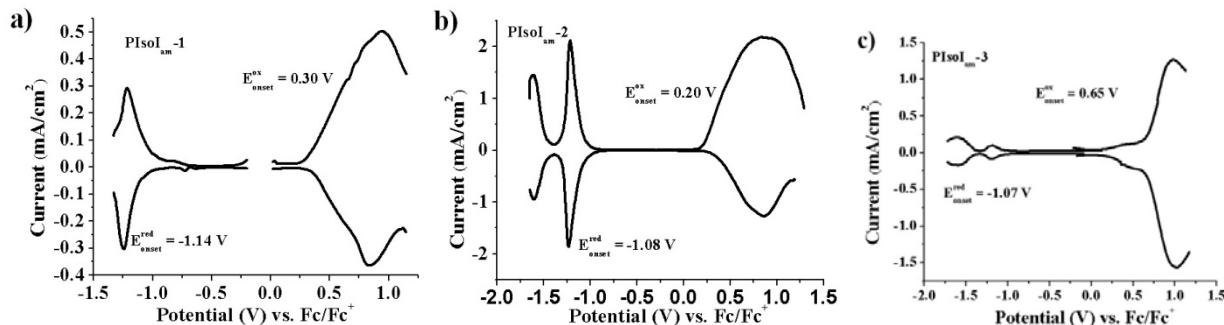


Figure 6-26. Differential pulse voltammetry of a) PIsoI_{AM}-1; b) PIsoI_{AM}-2; c) PIsoI_{AM}-3 measured in a 0.1M solution of TBAPF₆/ACN vs Fc/Fc⁺.

The data obtained from CV and DPV are consistent in the case of **PIsoI_{AM}-1** and **PIsoI_{AM}-2**. There is a relatively large discrepancy between the reduction onsets obtained from CV and DPV in the case of **PIsoI_{AM}-3**. This is likely due to the sensitivity issue in CV, where the first reduction peak, clearly seen by DPV, is not observed. This explanation is supported by the presence of two oxidation peaks in the neutralization process. The redox properties obtained from DPV are believed to be more reliable when making a comparison between three polymers.

It is surprising to see that the onsets of oxidation are affected to such a great extent by introducing different passive solubilizing groups. Because all three polymers share the same donor they are expected to exhibit very similar oxidation onsets, given that the oxidation onsets are usually governed by the donor used. It is also interesting that the three polymers have similar reduction onsets, which are much less affected by variation in the solubilizing group. These results, taken together, suggest the HOMO is more delocalized and thus more easily affected by the local environment; the LUMO is more localized and thus is not easily perturbed by the local morphology.

2D-WAXS study is contributed by Dr. Wojtek Pisula at MPI and Yuying Wei at UF. In order to explore the local microstructures of **PIsoI_{AM}-1**, **PIsoI_{AM}-2** and **PIsoI_{AM}-3**, 2D-WAXS was performed, as shown in Figure 6-27. The samples were prepared by fiber extrusion, a method that induces macroscopic orientation, and the fibers mounted vertically towards the 2D detector. All the polymers assemble into lamellar structures. In the case of **PIsoI_{AM}-1**, **PIsoI_{AM}-2**, two characteristic spacings are identified. The equatorial small-angle reflections (b) give chain-to-chain distances of 2.35 nm for **PIsoI_{AM}-1** and 2.47 nm for **PIsoI_{AM}-2**. A π -stacking distance of 0.36 nm is obtained for both **PIsoI_{AM}-1** and **PIsoI_{AM}-2** by measuring the wide-angle reflections (a). The observed π -stacking distances of 0.36 nm are some of the closest intermolecular interactions reported to date for a solution-processed conjugated polymer.³²⁵ In contrast, **PIsoI_{AM}-3** demonstrates a chain-to-chain distance of 1.9 nm, due to the shorter chain length of the solubilizing group, and a π -stacking distance of 0.40 nm. Additionally, one meridional reflection pair (c) is observed with a distance of ~1.36 nm, which is attributed to interactions between units along the backbone. To our surprise, the overall crystallinity seems higher for **PIsoI_{AM}-3**, supported by the sharper reflections of “b” and “c”, even though **PIsoI_{AM}-3**

1 and **PIsoI_{AM}-2** have much shorter π -stacking distances and stronger chain-chain interactions. Thus, charge mobility will be greatly affected by the orientations of the polymer lamella by adopting a path parallel or normal to the substrate.³²¹

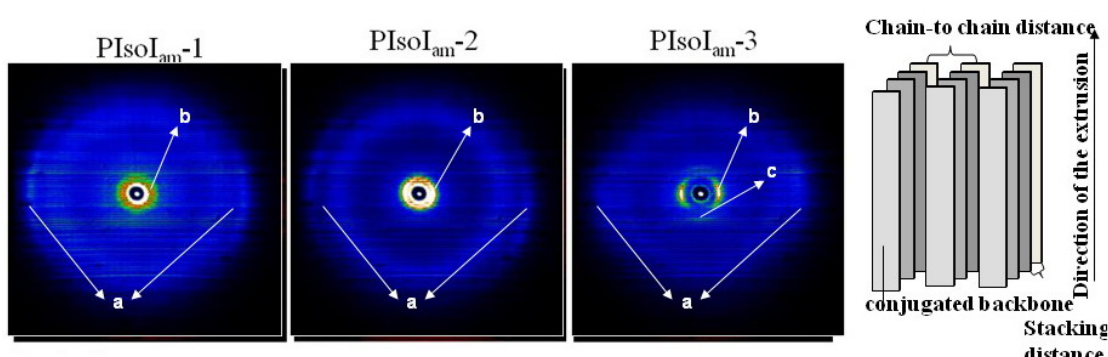


Figure 6-27. 2D wide-angle X-ray scattering of PIsoI_{AM}-1, PIsoI_{AM}-2 and PIsoI_{AM}-3.

6.4.3 Current-Voltage Measurements

From the 2D-WAXS study, we demonstrate that the π -stacking distances can indeed be enforced by introducing biphasic block solubilizing groups. A π -stacking distance as low as 0.36 nm can be obtained. The question is now whether the small pi-stacking distance can be transferred to high charge mobility in photovoltaic devices. Here we use the space-charge-limited-current (SCLC) model to determine hole mobility from simple current density-voltage (*J-V curve*) measurements using the Mott-Gurney equation, which was described in Chapter 2.

The architecture of the hole-only devices studied is ITO/PEDOT:PSS/Polymer/Au. The structures of the electron-only devices were Glass/Al/PEDOT-PSS/Polymer/Al. The films for both types of devices were annealed at 150 °C for 30 min. Figure 6-28a shows the experimental dark current densities in the hole-only devices of **PIsoI_{AM}-1**, **PIsoI_{AM}-2** and **PIsoI_{AM}-3**; while Figure 6-28b exhibits the experimental dark current densities in the electron-only devices of these polymers. The applied voltage V is corrected for the built-in voltage V_{bi} that results from the difference in the work function of the electrodes.

As illustrated in Figure 6-28, current densities at given electric field inside the device increase from **PIsoI_{AM}-3**, to **PIsoI_{AM}-2**, to **PIsoI_{AM}-1** in both hole-only and electron-only devices. Table 6-6 summarizes the zero-field hole mobility in **PIsoI_{AM}-1**, **PIsoI_{AM}-2** and **PIsoI_{AM}-3**, derived from fitting J-V data to the trap-free single-carrier SCLC model. **PIsoI_{AM}-1** shows hole mobilities of $9.5 \times 10^{-4} \text{ cm}^2 \text{V}^{-1} \text{s}^{-1}$ and electron mobilities of $9.1 \times 10^{-5} \text{ cm}^2 \text{V}^{-1} \text{s}^{-1}$. Hole mobilities of $8 \times 10^{-4} \text{ cm}^2 \text{V}^{-1} \text{s}^{-1}$ and electron mobilities of $6 \times 10^{-5} \text{ cm}^2 \text{V}^{-1} \text{s}^{-1}$ are obtained for **PIsoI_{AM}-2**, which are slightly lower than those of **PIsoI_{AM}-1**. **PIsoI_{AM}-3** exhibits hole mobilities of $7.2 \times 10^{-4} \text{ cm}^2 \text{V}^{-1} \text{s}^{-1}$ and electron mobilities of $2 \times 10^{-5} \text{ cm}^2 \text{V}^{-1} \text{s}^{-1}$. Hole mobilities observed from **PIsoI_{AM}-3** are about one order of magnitude lower than its counterpart polymers with biphasic solubilizing groups. Its electron mobilities are also significantly lower than **PIsoI_{AM}-1**.

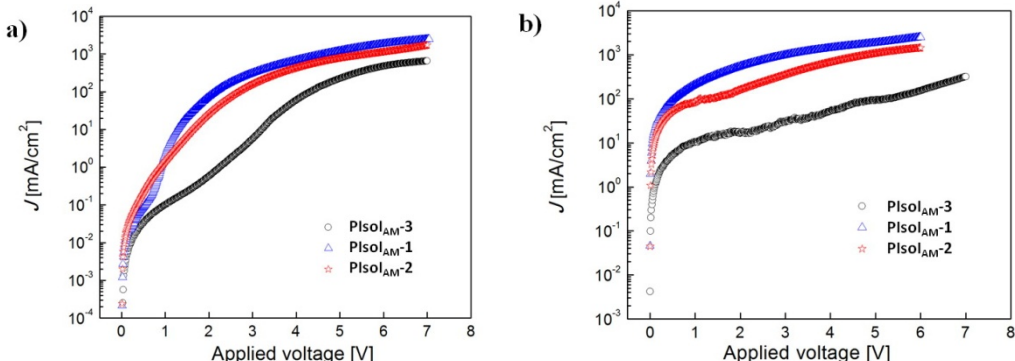


Figure 6-28. a) Experimental dark current densities for hole-only devices of PIsoI_{AM}-1, PIsoI_{AM}-2 and PIsoI_{AM}-3 as a function of the effective electric field; b) Experimental dark current densities for electron-only devices of PIsoI_{AM}-1, PIsoI_{AM}-2 and PIsoI_{AM}-3 as a function of the effective electric field.

Table 6-6. Zero-field hole mobility in PIsoI_{AM}-1, PIsoI_{AM}-2 and PIsoI_{AM}-3, derived from fitting J-V data to the trap-free single-carrier SCLC model.

| Polymer | PTIsoI _{AM} -1 | PTIsoI _{AM} -2 | PTIsoI _{AM} -3 |
|---|-------------------------|-------------------------|-------------------------|
| hole mobility [cm^2/Vs] | 9.5×10^{-4} | 8×10^{-4} | 7.2×10^{-5} |
| electron mobility [cm^2/Vs] | 9.1×10^{-5} | 6×10^{-5} | 2×10^{-5} |

These observations are consistent with our hypodissertation the charge mobility can be enhanced by introducing biphasic solubilizing groups. The enhanced charge mobilities of

PIsoI_{AM}-1 and **PIsoI_{AM}-2** are resulted from the short π -stacking distances of 0.36 nm, in comparison with the larger π -stacking distance of 0.40 nm that **PIsoI_{AM}-3** exhibits. Additionally, chain-to-chain distance also plays a role, even though less significant, in influencing charge mobility. This is evident through the comparison of **PIsoI_{AM}-1** and **PIsoI_{AM}-2**. They have the same π -stacking distances, but different chain-to-chain distances. **PIsoI_{AM}-1** has a smaller chain-to-chain distance and thus has a larger charge mobility than **PIsoI_{AM}-2**. Given the results obtained, we envision extending the biphasic solubilizing group concept to other systems.

6.5 N-type Isoindigo-Based Conjugated Polymers

The research in the field of organic solar cells has been largely directed to the development of suitable p-type materials.^{83,259-260,284} Many high performance p-type polymers are becoming available after more than a decade of effort.² In contrast, processable and stable n-type polymers remain limited.^{39,326-327} Few studies have been reported concerning all-polymer solar cells,^{89-90,106} mainly due to the limited availability of high electron affinity (EA) n-type polymers. Consequently, polymer-based photovoltaic devices have accordingly focused heavily on acceptor molecules such as methanofullerene phenyl-C₆₁-butyric-acid-methyl-ester (PCBM), which has an electron affinity of -4.2-4.3 eV, and its derivatives.^{125,154,320,328-329} Access to solution processable high electron affinity π -conjugated polymers remains a challenge, and one of the most successful strategies has been the construction of conjugated polymers based upon N-heterocyclic electron-deficient aromatics (e.g. perylene diimide or naphthalene bisimide).^{89,150-151,330} However, development of imide-based nitrogen-containing polyheterocycles with high electron affinities is greatly hindered by their poor reactivity. Extremely harsh conditions (for example refluxing under strongly oxidizing conditions) are used to prepare brominated and

nitrated monomer precursors.¹⁵¹ In most of cases, they are incorporated into a polymer chain via Stille coupling with electron rich monomers (e.g. thiophene and bithiophene).^{89,150-151,330-331} Soluble n-type conjugated polymers, other than imide-based nitrogen-containing polyheterocycles, are also reported and a few examples include indenofluorene-based and bisindenofluorene-based polymers.^{43,332} Unfortunately, Synthesis of these polymers typically involves multiple synthetic steps ($n > 7-10$) from readily available starting materials. The applicability of these monomer building blocks to obtain target polymers is thus adversely affected the lengthy syntheses involved.

Because isoindigo-based donor-acceptor type materials have a fairly low electron affinity of ~ 3.9 eV³¹⁷ we were encouraged to explore n-type isoindigo-based conjugated polymers. We report herein the syntheses and electron-accepting properties of two isoindigo-based n-type conjugated polymers composed of solely electron-deficient repeat units. The proposed polymers are shown in Figure 6-29.

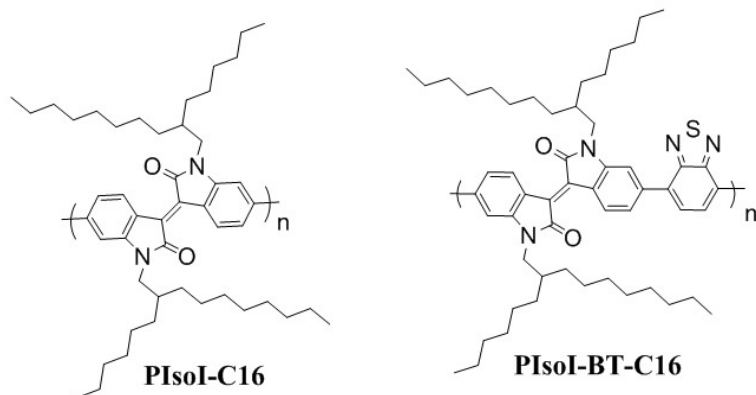


Figure 6-29. Polymer structures of PIsol-C16 and PIsol-BT-C16.

The Synthesis of **PIsol-C16** and **PIsol-BT-C16** is shown in Figure 6-30. The key compound **6-11** was successfully prepared by palladium-catalyzed Miyaura Borylation reaction of previously synthesized **6-5**.³³³ Purification of **6-11** is very convenient. No chromatography is

required in this process as the compound can be precipitated from a good solvent (e.g. CHCl₃) into a poor solvent (e.g. methanol). Compound **6-11** is isolated as a shiny, dark-red powder. This process can be repeated two or three time to obtain high purity **6-11**. In our hands, a 5.0 g (product) scale experiment was successfully performed. ¹H-NMR spectrum is shown (Figure 6-30) to demonstrate the purity of the material obtained by this simple purification.

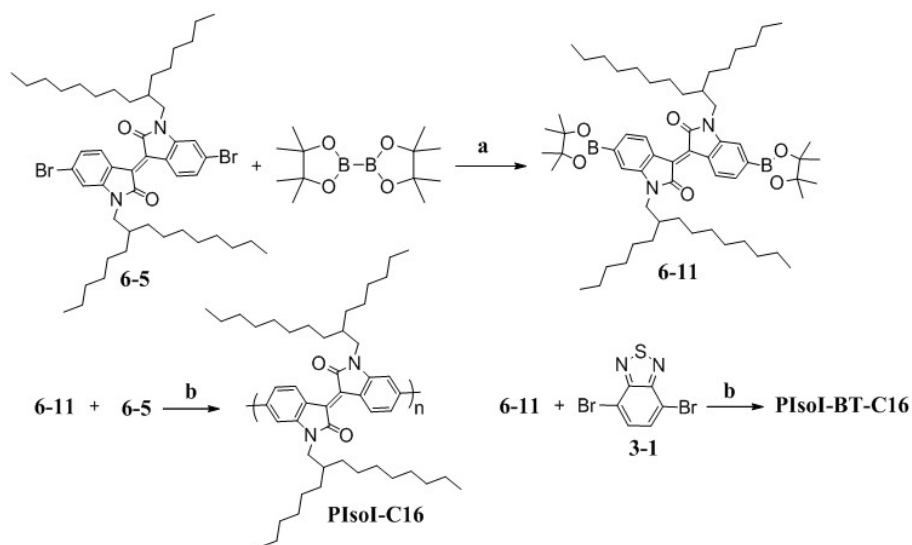


Figure 6-30. Synthesis of PIsol-C16 and PIsol-BT-C16. a) Pd(dppf)Cl₂, KOAc, 1,4-dioxane, 80 °C, 75%; b) Pd₂(dba)₃, P(o-tolyl)₃ Et₄NOH, toluene, 85 °C, 95% and 93% for PIsol-C16 and PIsol-BT-C16, respectively.

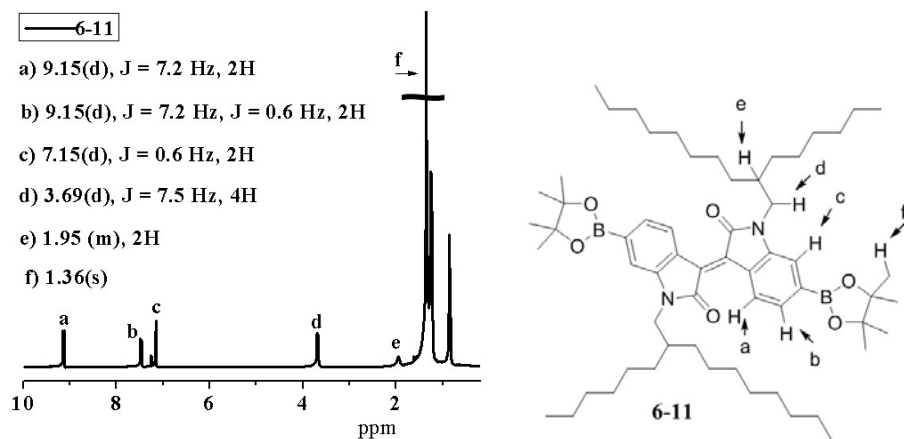


Figure 6-31. ¹H-NMR spectrum of compound **6-11**.

With the key monomer **6-11** in hand, we chose to begin exploring the chemistry of these electron deficient monomers by inclusion into two polymers **PIsoI-C16** and **PIsoI-BT-C16**. Suzuki polymerization of **6-11** with **6-5** and 4,7-dibromobenzo[c][1,2,5]thiadiazole (**3-1**) under our standard conditions ($\text{Pd}_2(\text{dba})_3$, $\text{P}(\text{o-tolyl})_3$ Et_4NOH , toluene, 85°C) gave **PIsoI-C16** and **PIsoI-BT-C16** in excellent yields with a number-average molecular weights of 28.7 kDa (PDI, 2.4) for **PIsoI-C16** and 16.3 kDa (PDI, 3.5) for **PIsoI-BT-C16**.

The most intriguing properties, as expected, are their electron affinity levels and ionization potentials, which determine the applicability of these polymers as a possible alternative to PCBM derivatives. Table 6-6 and Figure 6-32 summarize the energy levels and gaps of **PIsoI-C16** and **PIsoI-BT-C16** measured by differential pulse voltammetry. Polymer thin films were drop-cast from toluene solutions onto platinum button electrodes and characterized in an electrochemical cell comprising a platinum counter-electrode and an Ag/Ag^+ reference electrode. All the measurements were carried out in an argon-filled dry box. All estimated potentials were subsequently calibrated versus Fc/Fc^+ . The polymer films were repeatedly cycled prior to characterization, until a stable and reproducible redox response was finally obtained.

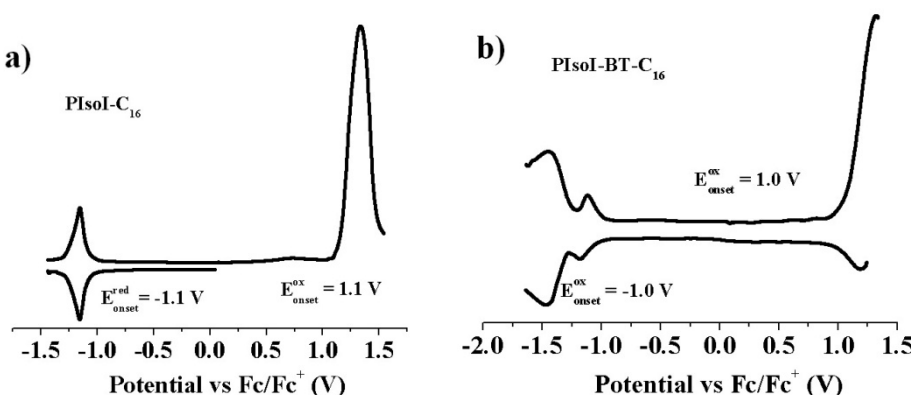


Figure 6-32. Differential pulse voltammetry of PIsoI-C16 and PIsoI-BT-C16. Electrochemical reduction and oxidation of the films on a platinum button was carried out in 0.1 M TBAP_6/ACN supporting electrolyte using Ag/Ag^+ reference electrode (calibrated against Fc/Fc^+) and a platinum flag as the counter electrode.

As shown in Figure 6-32 and Table 6-6, **PIsoI-C16** shows a low oxidation onset of 1.1 V and a reduction onset of -1.1 V (versus Fc/Fc⁺). These results suggest **PIsoI-C16** is difficult to oxidize, but easy to reduce. This implies that **PIsoI-C16** has more n-character than p-character. The HOMO and LUMO levels calculated from the redox onsets are -6.2 eV and -4.0 eV (versus vacuum), associated with a bandgap of 2.2 eV. These values are very close to the HOMO and LUMO levels of PC₆₁BM and PC₇₁BM, suggesting **PIsoI-C16** could find potential use as an excellent alternative to these commonly used acceptors in polymer-based solar cells. Similarly, **PIsoI-BT-C16** has a HOMO level of -6.1 eV and LUMO level of -4.1 eV. There is about 0.1 eV energy offset for both the HOMO and LUMO levels between **PIsoI-C16** and **PIsoI-BT-C16**. By inclusion of electron-deficient units other than benzothiadiazole it should be possible to fine-tune the energy levels of resulting polymers. In that sense, a polymer can be customized with the desired energy levels for n-type channel applications, which is absent or difficult to achieve in PCBM derivatives.

Table 6-7. Electrochemically determined energy levels and gaps of PIsoI-C16 and PIsoI-BT-C16 by DPV.

| | E_{ox}^{onset} (V) | HOMO (eV) | E_{red}^{onset} (V) | LUMO (eV) | E_g |
|--------------------------------------|---|------------------|--|------------------|----------------------|
| PC₆₁BM^a | 1.10 | -6.2 | -0.80 | -4.3 | 1.9 |
| PC₇₁BM^a | 0.91 | -6.0 | -0.81 | -4.3 | 1.7 |
| PIsoI-C₁₆ | 1.1 | -6.2 | -1.1 | -4.0 | 2.2 |
| PIsoI-BT-C₁₆ | 1.0 | -6.1 | -1.0 | -4.1 | 2.0 |

Note: oxidation ($E_{\text{ox}}^{\text{onset}}$) and reduction ($E_{\text{red}}^{\text{onset}}$) potentials are reported vs Fc/Fc⁺. HOMO and LUMO energy levels are derived from the electrochemical (DPV) data considering that the Fc/Fc⁺ is 5.1 eV relative to vacuum. a) adapted from Pierre Beaujuge, dissertation, University of Florid, 2009.

In summary, we demonstrated a facile approach to access isoindigo-based polymers composed of only electron-deficient units via environmental friendly chemistry (Suzuki coupling versus Stille coupling). This set of two polymers presents LUMO energy levels as deep as -4.1

eV, while still retaining a deep HOMO level. It is conceivable that the scope of this chemistry can be greatly expanded by using other readily available electron-deficient moieties and other isoindigo-based polymers can be readily prepared. We envision these polymers will be of interest in the utilization of n-type FETs and all-polymer solar cells.

6.5 Conclusion

This chapter devotes four sections to isoindigo-based materials. In Section 1, isoindigo was introduced as electron-accepting in electroactive material. DAD and ADA molecules based on this acceptor were prepared and used as active materials in bulk-heterojunction solar cells where power conversion efficiency as high as 1.85% was achieved. With the establishment of isoindigo-chemistry, molecular engineering was applied in the second section to design a set of four structurally similar isoindigo-based discrete oligomers. The structure-property relationships of these molecules were discussed in depth, connecting the significance of material design with achieving high performance photovoltaic materials. In the Section 3, three isoindigo-based polymers were synthesized in order to test a hypodissertation that charge mobility in conjugated polymers can be enhanced via enforcement of π - π interactions by means of introducing biphasic solubilizing groups. Various methods of characterization were employed to verify enhancement of π - π interactions in conjugated polymers with biphasic solubilizing groups, including solid-state UV-vis absorption, temperature-dependent solution UV-vis absorption, 2D-WAXS and solid-state NMR studies. The results from SCLC modeling of J-V characteristics of single-carrier diodes are consistent with the hypodissertation presented. Both electron and hole mobility have been significantly enhanced in polymers with biphasic groups, in comparison to the polymer with regular branched alkyl chains. The last section, Section 4, is devoted to a critical challenge in the field of conjugated polymer, access to stable and solution processable n-type

polymers. We conceived a facile approach to isoindigo-based electron deficient π -conjugated polymers in which the LUMO level is as deep as -4.1 eV while retaining a deep HOMO level as well. These polymers can be considered as an alternative to commonly used acceptors such as PCBM derivatives currently employed in polymer-based solar cell devices. These electron deficient polymers may also find utility in n-type FET devices or complimentary integrated circuits. Because of the simple chemistry involved, we envision that the Synthesis of these polymers can be easily moved to large scales for practical applications.

6.6 Experimental Details

6,6'-dibromoisoindigo (6-1). To a suspension of 6-bromooxindole (500 mg, 2.36 mmol) and 6-bromoisoatin (533 mg, 2.36 mmol) in AcOH (15 mL), conc. HC1 solution (0.1 ml) was added and heated under reflux for 24. The mixture was allowed to cool and filtered. The solid material was washed with water, EtOH and AcOEt. After drying under vacuum, it yielded brown 6,6'-dibromoisoindigo (951 mg, 95%). $^1\text{H-NMR}$ (((CD₃)₂NCOD), DMF at 80 °C) δ : 10.7 (bs, 2H), 9.14 (d, J = 8.7 Hz, 2H), 7.22-7.15 (m, 4H). $^{13}\text{C-NMR}$ (CDCl₃) δ : 170.3, 147.2, 134.0, 132.3, 127.0, 125.3, 122.6, 113.9.

6,6'-dibromo-N,N'-(2-ethylhexyl)-isoindigo (6-2). To a suspension of 6,6'-dibromoisoindigo (420 mg g, 1 mmol) and potassium carbonate (829 mg, 5 mmol) in dimethylformaldehyde (DMF) (20 mL), 1-bromo-2-ethylhexane (425 g, 2.2 mmol) was injected through a septum under nitrogen. The mixture was stirred for 15 h at 100 °C and then poured into water (200 mL). The organic phase was extracted by CH₂Cl₂, washed with brine and dried over MgSO₄. After removal of the solvent under reduced pressure, the deep-red solids were purified by silica chromatography, eluting with (CH₂Cl₂: Hexane = 1:1) to give 6,6'-dibromo-N,N'-(2-ethylhexyl)-isoindigo (548 mg, 85 %) $^1\text{H-NMR}$ (CDCl₃) δ : 9.00 (d, J = 8.7 Hz, 2H), 7.13 (dd, J₁

$J_1 = 8.7$ Hz, $J_2 = 1.5$ Hz, 2H), 6.81 (d, $J = 1.5$ Hz, 2H), 3.60-3.48 (m, 4H), 1.90-1.72 (m, 2H), 1.43-1.20 (m, 16H), 0.95-0.82 (m, 12H). ^{13}C -NMR (CDCl_3) δ : 168.1, 146.2, 132.6, 131.2, 126.8, 125.2, 120.5, 111.6, 44.5, 37.6, 30.7, 28.7, 24.1, 23.2, 14.2, 10.8. HRMS (ESI-TOF) Calculated for $\text{C}_{32}\text{H}_{40}\text{Br}_2\text{N}_2\text{O}_2$ ($\text{M}+\text{H}$) $^+$: 645.1512, found: m/z 645.1510. Anal. Calcd for $\text{C}_{32}\text{H}_{40}\text{Br}_2\text{N}_2\text{O}_2$: C, 59.64; H, 6.26; N, 4.35; Found: C, 59.79; H, 6.30; N, 4.26.

6,6'-(*N,N'*-heptyl)-dibromoisoindigo (6-3). To a suspension of 6,6'-dibromoisoindigo (1.39 g 3.31 mmol) and potassium carbonate (2.74 g, 19.85 mmol) in DMF (15 mL), 1-bromo-heptane (1.78 g, 9.93 mmol) was injected through a septum under nitrogen. The mixture was stirred for 15 h at 100 °C and then poured into water (200 mL). The organic phase was extracted by CH_2Cl_2 , washed with brine and dried over MgSO_4 . After removal of the solvent under reduced pressure, the pink-red solids were purified by silica chromatography, eluting with (CH_2Cl_2 : Hexane = 1:1) to give 6,6'-dibromo-*N,N'*-(2-heptyl)-isoindigo (1.74 g, 85 %) ^1H -NMR (CDCl_3) δ : 9.07 (d, $J = 9$ Hz, 2H), 7.17 (dd, $J_1 = 9$ Hz, $J_2 = 1.8$ Hz, 2H), 6.91 (d, $J = 1.8$ Hz, 2H), 3.71 (t, $J = 7.2$ Hz, 4H), 1.75-1.60 (m, 4H), 1.40-1.20 (m, 16H), 0.87 (t, $J = 6.6$ Hz, 6H); ^{13}C -NMR (CDCl_3) δ : 167.9, 146.0, 132.9, 131.4, 127.0, 125.3, 120.6, 111.5, 40.5, 31.9, 29.2, 27.6, 27.2, 22.8, 14.3. HRMS (ESI-TOF) Calculated for $\text{C}_{30}\text{H}_{36}\text{Br}_2\text{N}_2\text{O}_2$ ($\text{M}+\text{H}$) $^+$: 617.1198, found: m/z 617.1201; Anal. Calcd for $\text{C}_{30}\text{H}_{36}\text{Br}_2\text{N}_2\text{O}_2$: C, 58.45; H, 5.89; N, 4.54; Found: 58.56; H, 5.78; N, 4.61.

6,6'-(*N,N'*-propyl)-dibromoisoindigo (6-4). ^1H -NMR (CDCl_3) δ : 9.08 (d, $J = 8.7$ Hz, 2H), 7.15 (dd, $J_1 = 8.7$ Hz, $J_2 = 1.5$ Hz, 2H), 6.89 (d, $J = 1.5$ Hz, 2H), 3.70 (t, $J = 5.2$ Hz, 4H), 1.76 (sex, $J = 5.2$ Hz, 4H), 1.01 (t, $J = 5.2$ Hz, 6H); ^{13}C -NMR (CDCl_3) δ : 168.0, 146.2, 132.8, 131.6, 127.0, 125.3, 120.8, 111.5, 42.1, 21.0, 11.6.

6,6'-(N,N'-2-hexyldecyl)-dibromoisoindigo (6-5). To a suspension of 6,6'-dibromoisoindigo (4.20 g, 10.0 mmol) and potassium carbonate (8.29 g, 60 mmol) in DMF (45 mL), 2-hexyl-bromodecane (9.16 g, 30 mmol) was injected through a septum under nitrogen. The mixture was stirred for 15 h at 100 °C and then poured into water (200 mL). The organic phase was extracted by CH₂Cl₂, washed with brine and dried over MgSO₄. After removal of the solvent under reduced pressure, the dark red liquids were purified by silica chromatography, eluting with (CH₂Cl₂: Hexane = 1:2) to give 6,6'-dibromo-N,N'-(2-hexyldecyl)-isoindigo (6.1 g, 70 %). ¹H-NMR (CDCl₃) δ: 9.04 (d, J = 9 Hz, 2H), 7.14 (dd, J₁ = 9Hz, J₂ = 1.8 Hz, 2H), 6.83 (d, J = 1.8 Hz, 2H), 3.56 (d, J = 7.5 Hz, 4H), 1.83 (bs, 2H), 1.40-1.24 (m, 48H), 0.88-0.84 (m, 12H); ¹³C-NMR (CDCl₃) δ: 168.2, 146.3, 132.6, 131.3, 126.9, 125.2, 120.6, 112.7, 44.9, 36.3, 32.1, 32.0, 31.7, 30.2, 29.87, 29.77, 29.5, 26.6, 22.89, 22.87, 14.34, 14.31.

6-bromoisoindigo (6-6): To a suspension of oxindole (1.47g, 11.06 mmol) and 6-bromoisoindole (2.50 g, 11.06 mmol) in AcOH (40 mL), conc. HCl solution (0.2 ml) was added and heated under reflux for 24. The mixture was allowed to cool and filtered. The solid material was washed with water, EtOH and AcOEt. After drying under vacuum, it yielded deep red 6-bromoisoindigo (3.53 g, 94%). ¹H-NMR ((CD₃)₂NCOD), DMF at 80 °C) δ: 10.7 (bs, 1H), 10.6(bs, 1H), 9.20-9.13 (m, 2H), 7.42-6.95 (m, 5H). ¹³C-NMR (CDCl₃) δ: 170.5, 170.3, 147.0, 146.0, 135.4, 134.0, 133.3, 132.2, 130.9, 126.6, 125.1, 123.5, 122.7, 122.4, 113.7, 110.8.

6,-bromo-N,N'-(2-ethylhexyl)-isoindigo (6-7): To a suspension of 6-bromoisoindigo (1.0 g, 2.93 mmol) and fresh-dried potassium carbonate (2.43 g, 17.59 mmol) in anhydrous DMF (20 mL), 1-bromo-2-ethylhexane (1.70 g, 8.79 mmol) was injected through a septum under nitrogen. The mixture was stirred for 15 h at 100 °C and then poured into water (500 mL). The organic phase was extracted by CH₂Cl₂, washed with brine and dried over MgSO₄. After removal of the

solvent under reduced pressure, the deep-red solids were purified by silica chromatography, eluting with (CH_2Cl_2 : Hexane = 2:3) to give compound **7** ($R_f = 0.45$), **8** ($R_f = 0.35$), and **4** ($R_f = 0.53$), of, 740 mg (44.7 %), 362 mg (25.4 %) and 368 mg (19.5 %), respectively.

Compound 6-7: $^1\text{H-NMR}$ (CDCl_3) δ : 9.12 (dd, $J_1 = 7.8$ Hz, $J_2 = 1.2$ Hz, 1H), 9.04 (d, $J = 8.4$ Hz, 1H), 7.34 (dt, $J_1 = 7.8$ Hz, $J_2 = 1.2$ Hz, 1H), 7.13 (dd, $J_1 = 8.4$ Hz, $J_2 = 1.8$ Hz, 1H), 7.03 (dt, $J_1 = 7.8$ Hz, $J_2 = 0.6$ Hz, 1H), 6.83 (d, $J = 1.8$ Hz, 1H), 6.73 (dd, $J_1 = 7.8$ Hz, $J_2 = 0.6$ Hz, 1H), 3.65-3.45 (m, 4H), 1.95-1.85 (m, 2H), 1.43-1.20 (m, 16H), 0.98-0.82 (m, 12H). $^{13}\text{C-NMR}$ (CDCl_3) δ : 168.3, 168.2, 146.2, 145.3, 134.0, 132.7, 132.2, 131.1, 130.1, 126.4, 125.1, 122.4, 121.7, 120.6, 111.5, 108.3, 44.45, 44.34, 37.70, 37.58, 30.86, 30.74, 28.89, 28.75, 24.22, 24.15, 23.22, 14.22, 10.86, 10.80. HRMS (ESI-TOF) Calculated for $\text{C}_{32}\text{H}_{41}\text{BrN}_2\text{O}_2$ ($\text{M}+\text{H}$) $^+$: 567.2409, found: m/z 567.2416. Anal. Calcd for $\text{C}_{32}\text{H}_{41}\text{BrN}_2\text{O}_2$: C, 67.95; H, 7.31; N, 4.95; Found: C, 67.86, H, 7.27, N, 4.91.

Compound 6-8: $^1\text{H-NMR}$ (CDCl_3) δ : 9.17 (dd, $J_1 = 7.8$ Hz, $J_2 = 1.2$ Hz, 2H), 7.35 (dt, $J_1 = 7.8$ Hz, $J_2 = 1.2$ Hz, 2H), 7.05 (dt, $J_1 = 7.8$ Hz, $J_2 = 0.6$ Hz, 2H), 6.76 (dd, $J_1 = 7.8$ Hz, $J_2 = 0.6$ Hz, 2H), 3.75-3.58 (m, 4H), 1.92-1.78 (m, 2H), 1.45-1.20 (m, 16H), 0.98-0.80 (m, 12H). $^{13}\text{C-NMR}$ (CDCl_3) δ : 168.4, 145.3, 133.7, 132.4, 130.0, 122.3, 121.9, 108.3, 44.4, 37.7, 30.9, 28.9, 24.2, 23.2, 14.2, 10.9. HRMS (ESI-TOF) Calculated for $\text{C}_{32}\text{H}_{42}\text{N}_2\text{O}_2$ ($\text{M}+\text{H}$) $^+$: 487.3319, found: m/z 487.3351.

I-1: In a flame-dried Schlenk flask (50 mL), 6,6'-dibromoisoindigo (446 mg, 0.69 mmol), 2-(5'-hexyl-2,2'-bithiophen-5-yl)-4,4,5,5-tetramethyl-1,3,2-dioxaborolane (625 mg, 1.66 mmol, 2.4 eq), Tris(dibenzylideneacetone)dipalladium(0) (15 mg) and $\text{P}(\text{o-tyl})_3$ (10 mg) were added. The flask was evacuated and back-filled with argon three times, after which degassed toluene (15 mL) and tetraethylammonium hydroxide (4.2 mmol, 1M) was transferred to the mixture through

a septum. The resulting solution was heated up to 85 °C under argon and stirred for 20 h. The solvent was removed under reduced pressure. The dark red solids were purified by silica gel chromatography, eluting with CH₂Cl₂-hexane (1:1) to give brown solids (562 mg, 83 %). ¹H-NMR (CDCl₃) δ: 9.01 (d, J = 8.7, 2H), 7.25-7.18 (m, 4H), 7.05 (d, J = 3.6 Hz, 2H), 7.02 (d, J = 3.6 Hz, 2H), 6.78 (s, 2H), 6.70 (d, J = 3.3 Hz), 3.68-3.41 (m, 4H), 2.80 (t, J = 4.2 Hz, 4H), 1.82-1.65 (m, 6H), 1.44-1.20 (m, 28H), 0.98-0.81 (m, 18H). ¹³C-NMR (CDCl₃) δ: 168.7, 146.3, 145.6, 142.1, 138.9, 137.4, 134.7, 131.6, 130.3, 125.1, 125.07, 124.1, 123.9, 121.1, 118.8, 104.5, 44.2, 38.0, 31.79, 31.75, 31.1, 30.4, 29.2, 29.0, 24.5, 23.3, 22.8, 14.4, 14.3, 11.0. HRMS (ESI-TOF) Calculated for C₆₀H₇₄N₂O₂S₄ (M+H)⁺: 983.4706 Found: m/z 983.4741. Anal. Calcd for C₆₀H₇₄N₂O₂S₄: C, 73.27; H, 7.58; N, 2.85. Found: C, 73.39; H, 7.57; N, 2.80.

I-2: In a flame-dried Schlenk flask (50 mL), 6,6'-(N,N'-heptyl)-dibromoisoindigo (616 mg, 1 mmol), 2-(5'-hexyl-2,2'-bithiophen-5-yl)-4,4,5,5-tetramethyl-1,3,2-dioxaborolane (904 mg, 2.4 mmol, 2.4 eq), Tris(dibenzylideneacetone)dipalladium(0) (15 mg) and P(o-tyl)₃ (10 mg) were added. The flask was evacuated and back-filled with argon three times, after which degassed toluene (20 mL) and tetraethylammonium hydroxide (3 mmol, 1M) was transferred to the mixture through a septum. The resulting solution was heated up to 85 °C under argon and stirred for 20 h. The solvent was removed under reduced pressure. The dark red solids were purified by silica gel chromatography, eluting with CH₂Cl₂-hexane (1:1) to give metallic crystalline solids (795 mg, 83 %). ¹H-NMR (CDCl₃) δ: 9.11 (d, J = 8.4, 2H), 7.24 (d, J = 3.6 Hz, 2H), 7.19 (dd, J₁ = 8.4 Hz, J₂ = 1.8 Hz, 2H), 7.03 (d, J = 3.6 Hz, 2H), 7.00 (d, J = 3.6 Hz, 2H), 6.79 (d, J = 1.8 Hz, 2H), 6.68 (d, J = 3.6 Hz, 2H), 3.74 (t, J = 4.2 Hz, 4H), 2.78 (t, J = 7.8 Hz, 4H), 1.75-1.63 (m, 8H), 1.44-1.24 (m, 28H), 0.95-0.82 (m, 12H). ¹³C-NMR (CDCl₃) δ: 168.4, 146.2, 145.3, 142.1, 138.9, 137.5, 134.7, 131.7, 130.6, 125.2, 125.1, 124.1, 123.9, 121.1, 118.9, 104.3, 40.2, 32.0, ,

31.8, 30.5, 29.2, 29.0, 27.8, 27.3, 22.9, 22.8, 14.3. HRMS (ESI-TOF) Calculated for

$C_{58}H_{70}N_2O_2S_4$ ($M+H$)⁺: 955.4393 Found: m/z 955.4382. Anal. Calcd for $C_{58}H_{70}N_2O_2S_4$: C, 72.91; H, 7.38; N, 2.93. Found: C, 72.93; H, 7.51; N, 3.06.

I-3: In a flame-dried Schlenk flask (50 mL), 6-bromoisoindigo (1 g, 1.77 mmol), 5,5'-5,5'-bis(4,4,5,5-tetramethyl-1,3,2-dioxaborolan-2-yl)-2,2'-bithiophene (308 mg, 0.736 mmol), Tris(dibenzylideneacetone)dipalladium (16 mg) and P(o-tyl)₃ (12 mg) were added. The flask was evacuated and back-filled with argon three times, after which degassed toluene (15 mL) and tetraethylammonium hydroxide (4.5 mmol, 1M) was transferred to the mixture through a septum. The resulting solution was heated up to 85 °C under argon and stirred for 20 h. The solvent was removed under reduced pressure. The dark red solids were purified by silica gel chromatography, eluting with CH₂Cl₂-hexane (1:1) to give brown solids (476 mg, 57 %). ¹H-NMR (CDCl₃) δ: 9.22 (t, J = 9.0 Hz, 4H), 7.34-7.29 (m, 6H), 7.28 (d, J = 8.4 Hz, 2H), 7.20 (d, J = 3.9 Hz, 2H), 7.02 (t, J = 7.5 Hz, 2H), 6.94 (d, J = 1.2 Hz, 2H), 6.75 (d, J = 8.4 Hz, 2H), 3.80-3.55 (m, 8H), 1.98-1.83 (m, 4H), 1.55-1.25 (m, 32H), 1.05-0.90 (m, 24 H). ¹³C-NMR (CDCl₃) δ: 168.9, 168.7, 146.2, 145.5, 143.7, 138.0, 137.6, 133.0, 132.8, 132.3, 130.8, 130.1, 125.3, 122.31, 122.28, 121.6, 119.3, 108.3, 104.9, 44.66, 44.60, 38.22, 38.05, 31.33, 31.23, 29.25, 29.10, 24.75, 24.57, 23.33, 23.30, 14.27, 14.17, 11.08, 10.98. HRMS (ESI-TOF) Calculated for $C_{72}H_{86}N_4O_4S_2$ ($M+H$)⁺: 1135.6163, found: m/z 1135.6167; Anal. Calcd for $C_{72}H_{86}N_4O_4S_2$: C, 76.15; H, 7.63; N,

6-13 Temperature-dependent UV-vis spect

IsoI-N: In a flame-dried Schlenk flask (50 mL), 6,6'-(N, N'-ethylhexyl-)dibromoisoindigo (644 mg, 1 mmol), 1-methyl-2-(4,4,5,5-tetramethyl-1,3,2-dioxaborolan-2-yl)-1H-indole (669 mg, 2.5 mmol, 2.5 eq), Pd₂(dba)₃-CHCl₃ (18 mg) and P(o-tyl)₃ (10 mg) were added. The flask was evacuated and back-filled with argon three times, after which degassed toluene (30 mL) and

tetraethylammonium hydroxide (3 mmol, 1M) was transferred to the mixture through a septum. The resulting solution was heated up to 85 °C under argon and stirred for 16 h. The solvent was removed under reduced pressure. The dark red solids were purified by silica gel chromatography, eluting with CH₂Cl₂-hexane (1:1) to give metallic crystalline solids (656 mg, 88 %). ¹H-NMR (CDCl₃) δ: 9.29 (d, J = 8.1, 2H), 7.69 (d, J = 8.1 Hz, 2H), 7.40-7.15(m, 8H), 6..95 (d, J=1.5 Hz, 2H), 6.71 (d, J=0.6 Hz, 2H), 3.85 (s, 6H), 3.80-3.62 (m, 4H), 1.95-1.85 (m, 2H), 1.50-1.30 (m, 16H), 0.99-0.85 (m, 12 H). ¹³C-NMR (CDCl₃) δ: 168.8, 145.7, 141.4, 139.3, 136.7, 132.9, 130.0, 128.1, 122.9, 122.7, 121.3, 121.0, 120.5, 110.0, 108.8, 103.1, 44.6, 38.0, 31.9, 31.1, 29.1, 24.4, 23.3, 14.3, 11.0. HRMS (ESI-TOF) Calculated for C₅₀H₅₆N₄O₂ (M+H)⁺: 745.4447 Found: *m/z* 745.4476. Anal. Calcd for C₅₀H₅₆N₄O₂: C, 80.61; H, 7.58; N, 7.52. Found: C, 80.56; H, 7.63; N, 7.52.

IsoI-O: In a flame-dried Schlenk flask (50 mL), 6,6'-(N, N'-ethylhexyl-)dibromoisoindigo (616 mg, 1 mmol), benzo[b]thiophen-2-ylboronic acid (445 mg, 2.5 mmol, 2.5 eq), Pd₂(dba)₃-CHCl₃ (18 mg) and P(o-tyl)₃ (10 mg) were added. The flask was evacuated and back-filled with argon three times, after which degassed toluene (30 mL) and tetraethylammonium hydroxide (3 mmol, 1M) was transferred to the mixture through a septum. The resulting solution was heated up to 85 °C under argon and stirred for 16 h. The solvent was removed under reduced pressure. The dark red solids were purified by silica gel chromatography, eluting with CH₂Cl₂-hexane (1:1) to give metallic crystalline solids (688 mg, 92 %). ¹H-NMR (CDCl₃) δ: 9.11 (d, J = 8.4, 2H), 7.82-7.72 (m, 4H), 7.53 (s, 2H), 7.38-7.30 (m, 6H), 6.89(t, J=1.5 Hz, 2H), 3.72-3.45 (m, 4H), 1.83-1.77(m, 2H), 1.42-1.24 (m, 16H), 0.97-0.83 (m, 12H) ¹³C-NMR (CDCl₃) δ: 168.6, 145.7, 143.9, 140.7, 139.9, 137.7, 132.3, 130.5, 125.2, 125.0, 124.2, 122.5, 121.9, 120.8, 120.0, 105.6, 44.2, 38.0, 31.1, 29.2, 24.5, 23.3, 14.4, 11.1. HRMS (ESI-TOF) Calculated for

$C_{48}H_{50}N_2O_2S_2$ ($M+H$)⁺: 751.3386 Found: m/z 751.3382. Anal. Calcd for $C_{48}H_{50}N_2O_2S_2$: C, 76.76; H, 6.71; N, 3.73. Found: C, 76.53; H, 6.65; N, 3.74.

IsoI-S: In a flame-dried Schlenk flask (50 mL), 6,6'-(N, N'-ethylhexyl)-dibromoisoindigo (616 mg, 1 mmol), benzofuran-2-ylboronic acid (405 mg, 2.5 mmol, 2.5 eq), $Pd_2(dbu)_3$ - $CHCl_3$ (18 mg) and $P(o-tyl)_3$ (10 mg) were added. The flask was evacuated and back-filled with argon three times, after which degassed toluene (30 mL) and tetraethylammonium hydroxide (3 mmol, 1M) was transferred to the mixture through a septum. The resulting solution was heated up to 85 °C under argon and stirred for 16 h. The solvent was removed under reduced pressure. The dark red solids were purified by silica gel chromatography, eluting with CH_2Cl_2 -hexane (1:1) to give metallic crystalline solids (795 mg, 84 %). 1H -NMR ($CDCl_3$) δ : 9.19 (d, J = 8.4, 2H), 7.58-7.45 (m, 6H), 7.32-7.20 (m, 4H), 7.07-7.04(m, 4H), 3.76-3.52 (m, 4H), 1.88-1.78(m, 2H), 1.42-1.23 (m, 16H), 0.99-0.87 (m, 12H). ^{13}C -NMR ($CDCl_3$) δ : 168.6, 155.5, 155.3, 145.7, 133.6, 132.4, 130.3, 129.3, 125.3, 123.5, 122.1, 121.4, 118.7, 111.5, 104.1, 103.6, 44.3, 37.9, 31.0, 29.1, 24.5, 23.3, 14.4, 11.0. HRMS (ESI-TOF) Calculated for $C_{48}H_{50}N_2O_4$ ($M+H$)⁺: 719.3843 Found: m/z 719.3851. Anal. Calcd for $C_{48}H_{50}N_2O_4$: C, 80.19; H, 7.01; N, 3.90. Found: C, 79.97; H, 7.05; N, 3.91.

2-(2-(tosyloxy)ethoxy)ethoxyethyl nonanoate: To a round-bottom flask (250 mL), 2-(2-(2-hydroxyethoxy)ethoxy)ethyl 4-methylbenzenesulfonate (14.13 g, 46.41 mmol) and triethylamine (5.64 g, 7.76 mL, 55.69 mmol) in anhydrous dichloromethane (92 mL) were cooled in ice-water bath. nonanoyl chloride (8.61g, 48.73 mmol) in dichloromethane (8 mL) was added dropwise over 15 min. The mixture was stirred for 1 h and then warmed up to room temperature. After the alcohol was completely consumed, the mixture was poured into water. The organic phase was washed with brine and dried over magnesium sulfate. The solvent was

removed under reduced pressure. The viscous orange oil was purified by silica gel chromatography, eluting with ethyl acetate and hexane (1:1) to yield pale yellow oil (17.1 g, 83 %). $^1\text{H-NMR}$ (CDCl_3) δ : 7.76 (dd, $J_1 = 7.8$ Hz, $J_2 = 1.5$ Hz, 2H), 7.30 (dd, $J_1 = 7.8$ Hz, $J_2 = 1.5$ Hz, 2H), 4.19-4.06 (m, 4H), 3.70-3.55 (m, 4H), 3.53 (bs, 4H), 2.39 (s, 3H), 2.29 (t, $J = 7.5$ Hz, 2H), 1.61-1.49 (m, 2H), 1.28-1.16 (m, 10H), 0.82 (t, $J = 6$ Hz, 2H) $^{13}\text{C-NMR}$ (CDCl_3) δ : 173.8, 145.0, 133.0, 129.9, 128.0, 70.8, 70.5, 69.3, 69.29, 68.8, 63.3, 34.2, 31.9, 29.3, 29.2, 25.0, 22.7, 21.7, 14.2. HRMS (ESI-TOF) Calculated for $\text{C}_{22}\text{H}_{36}\text{O}_7\text{S}$ ($\text{M}+\text{H}$) $^+$: 444.2182 Found: m/z 843.3167; Anal. Calcd for $\text{C}_{22}\text{H}_{36}\text{O}_7\text{S}$: C, 59.43; H, 8.16; Found: C, 59.78; H, 8.25.

2-(2-(2-methoxyethoxy)ethoxy)ethyl 6-bromohexanoate. To a round-bottom flask (250 mL), 2-(2-(2-methoxyethoxy)ethoxy)ethanol (8.08 g, 49.18 mmol) and triethylamine (5.69 g, 7.83 mL, 56.21 mmol) in anhydrous dichloromethane (92 mL) were cooled in ice-water bath. 6-bromohexanoyl chloride (10g, 46.84 mmol) in dichloromethane (8 mL) was added dropwise over 15 min. The mixture was stirred for 1 h and then warmed up to room temperature. After 6-bromohexanoyl chloride was completely consumed, the mixture was poured into water. The organic phase was washed with brine and dried over magnesium sulfate. The solvent was removed under reduced pressure. The viscous orange oil was purified by silica gel chromatography, eluting with ethyl acetate and hexane (1:1) to yield colorless oil (13.5 g, 85 %). $^1\text{H-NMR}$ (CDCl_3) δ : 4.25-4.15 (m, 2H), 3.70-3.60 (m, 7H), 3.54-3.50 (m, 2H), 3.40-3.34 (m, 4H), 2.32 (t, $J = 7.2$ Hz, 2H), 1.85 (quin, $J = 4.2$ Hz, 2H), 1.64 (quin, $J = 7.5$ Hz, 2H), m 1.49-1.40 (m, 2H); $^{13}\text{C-NMR}$ (CDCl_3) δ : 173.6, 72.1, 70.78, 70.75, 70.73, 69.3, 63.6, 59.2, 34.1, 33.6, 32.5, 27.8, 24.2. HRMS (ESI-TOF) Calculated for $\text{C}_{13}\text{H}_{25}\text{BrO}_5$ ($\text{M}+\text{H}$) $^+$: 341.0958 Found: m/z 341.0964; Anal. Calcd for $\text{C}_{13}\text{H}_{25}\text{BrO}_5$: C, 45.76; H, 7.38; Found: C, 46.03; H, 7.46.

Compound 6-9. To a 6,6'-dibromoisoindigo mixture (841 mg, 2 mmol) and potassium carbonate (1.66 g, 12 mmol) in DMF (10 mL), 2-(2-(2-methoxyethoxy)ethoxy)ethyl 6-bromohexanoate (1.5 g, 4.4 mmol) was injected through a septum under nitrogen. The mixture was stirred for 15 h at 100 °C and then poured into water (100 mL). The organic phase was extracted by CH₂Cl₂, washed with brine and dried over MgSO₄. After removal of the solvent under reduced pressure, the deep-red solids were purified by silica chromatography, eluting with pure ethyl acetate to give the desired compound (665 mg, 35 %). ¹H-NMR (CDCl₃) δ: 8.91 (d, J = 8.4 Hz, 2H), 7.03 (dd, J₁ = 8.4 Hz, J₂ = 1.8 Hz, 2H), 6.76 (d, J = 1.8 Hz, 2H), 4.14 (t, J = 4.8 Hz, 4H), 3.62-3.51(m, 20H), 3.50-3.42 (m, 4H), 3.28 (s, 6H), 2.25 (t, J = 7.2 Hz, 4H), 1.63-1.53 (m, 8H), 1.37-1.25 (m, 4H); ¹³C-NMR (CDCl₃) δ: 173.2, 167.4, 145.5, 132.3, 131.1, 126.7, 125.0, 120.2, 111.0, 71.8, 70.52, 70.47, 69.1, 63.4, 58.9, 39.9, 33.8, 27.0, 26.4, 24.4. HRMS (MALDI-TOF) Calculated for C₄₂H₅₆Br₂N₂O₁₂ (M+H)⁺: 941.2258 Found: *m/z* 941.2220.

Compound 6-10. To a 6,6'-dibromoisoindigo mixture (2.10 g, 5mmol) and potassium carbonate (4.15 g, 30 mmol) in DMF (20 mL), 2-(2-(2-(tosyloxy)ethoxy)ethoxy)ethyl nonanoate (6.67 g, 15 mmol) was injected through a septum under nitrogen. The mixture was stirred for 15 h at 100 °C and then poured into water (200 mL). The organic phase was extracted by CH₂Cl₂, washed with brine and dried over MgSO₄. After removal of the solvent under reduced pressure, the deep-red solids were purified by silica chromatography, eluting with CH₂Cl₂/acetone (97:3) to give the desired compound (2.39 g, 49 %). ¹H-NMR (CDCl₃) δ: 8.93 (d, J = 9.3 Hz, 2H), 7.03-7.00 (m, 4H), 4.10 (t, J = 4.8 Hz, 4H), 3.83 (t, J = 5.4 Hz, 4H), 3.66 (t, J = 4.8 Hz, 4H), 3.57 (t, J = 4.8 Hz, 4H), 3.52 (s, 8H), 2.24 (t, J = 7.5 Hz, 4H), 1.60-1.48 (m, 4H), 1.28-1.15(m, 20), 0.80 (t, J = 7.2 Hz, 6H); ¹³C-NMR (CDCl₃) δ: 173.67, 167.7, 146.1, 132.2, 130.9, 12637, 125.0, 120.2,

112.3, 70.9, 70.6, 69.4, 68.96, 63.3, 40.5, 34.2, 31.8, 29.24, 29.13, 24.9, 22.7, 14.1. HRMS (MALDI-TOF) Calculated for $C_{46}H_{64}Br_2N_2O_{10}$ ($M+Na$)⁺: 987.2806 Found: *m/z* 987.2811.

The general method to prepare **PIsoIAM-1**, **PIsoIAM-2** and **PIsoIAM-3**. A Schlenk flask charged with compound 6-5/6-9/6-10 (1 mmol), Pd₂dba₃ (18 mg), P(*o*-Tolyl)₃ (15 mg), and 2,5-bis(trimethyltin)thiophene (1 mmol) was purged three times with successive vacuum and argon filling cycles. Degassed anhydrous toluene (15 mL) was injected through a septum. The polymerization reaction was heated to 95°C, and the mixture was stirred for 36 h under argon atmosphere. The mixture was cooled to room temperature and poured slowly in methanol (300 mL). The precipitates were collected through a 0.45 µm PTFE filter. The crude polymer was purified with Soxhlet extraction with methanol, hexane to remove low molecular species and catalyst residues. Finally the polymer was extracted with chloroform. The polymer solution was concentrated and slowly poured in methanol (300 mL). The precipitates were collected via vacuum filtration through a 0.45 µm PTFE filter and dried, yielding a dark purple polymer.

PIsoIAM-1. ¹H-NMR (CDCl₃) δ: 9.19-8.61 (m, 2H), 7.45-5.98 (m, 6H), 4.56-3.20 (m, 34H), 2.82-1.21 (m, 16H). Anal. Calcd for **PIsoIAM-1**: C, 63.06; H, 6.70; N, 3.25. Found: C, 64.00; H, 6.80; N, 3.25. GPC: M_w = 35 kDa, PDI = 1.2.

PIsoIAM-2. ¹H-NMR (CDCl₃) δ: 9.10-8.67 (m, 2H), 7.42-6.25 (m, 6H), 4.45-3.28 (m, 24H), 2.45-1.08 (m, 28H), 0.98-0.70 (m, 6H). Anal. Calcd for **PIsoIAM-2**: C, 67.04; H, 7.33; N, 3.08. Found: C, 67.42; H, 7.43; N, 3.20. GPC: M_w = 78 kDa, PDI = 1.8.

PIsoIAM-3. GPC: M_w = 34 kDa, PDI = 1.6.

Compound 6-11. 6,6'-(N,N'-2-hexyldecyl)-dibromoisoindigo (6-5) (4.35 g, 5.0 mmol), pinacol ester of diboron (3.05 g, 12 mmol), [PdCl₂(dppf)] (220 mg), and potassium acetate (2.95 g, 30 mmol) were mixed at room temperature under an argon atmosphere. Anhydrous 1,4-

dioxane (2 mL) was injected with a syringe through a septum. The solution was heated at 80 °C for 30 h and then cooled to room temperature. The reaction mixture was filtered by passing through a short pad of silica gel, and washed by a mixture of methylene chloride and hexane (1:1). The collected filtration was concentrated and precipitated into cold methanol (100 mL). The precipitates were filtered and dried to give dark red products (3.6 g, 75%). ¹H-NMR (CDCl₃) δ: 9.15 (d, J = 7.2 Hz, 2H), 7.48 (d, J₁ = 8.1 Hz, J₂ = 0.6 Hz, 2H), 7.15 (d, J = 0.6 Hz, 2H), 3.69 (d, J = 7.5 Hz, 2H), 1.95 (bs, 2H), 1.59-1.19 (m, 72H), 0.85 (t, J = 6.6 Hz, 6H); ¹³C-NMR (CDCl₃) δ: 168.3, 144.7, 134.5, 129.0, 128.9, 124.4, 113.7, 84.2, 44.6, 36.3, 32.1, 32.0, 31.8, 31.2, 29.8, 29.78, 29.5, 26.6, 25.1, 22.9, 22.8, 14.32, 14.30. HRMS (MALDI-TOF) Calculated for C₆₀H₉₆B₂N₂O₆ (M+Na)⁺: 963.7548 Found: m/z 963.7583. Anal. Calcd for C₆₀H₉₆B₂N₂O₆: C, 74.83; H, 10.05; N, 2.91. Found: C, 74.91; H, 10.7(5); N, 2.80.

P_{Iso}I-C16. In a flame-dried Schlenk flask (50 mL), **6-5** (434.45 mg, 0.5 mmol) and **6-11** (481.52 mg, 0.5 mmol), Pd₂(dba)₃-CHCl₃ (18 mg) and P(o-tyl)₃ (12 mg) were added. The flask was evacuated and back-filled with argon three times, after which degassed toluene (15 mL) and tetraethylammonium hydroxide (3 mmol, 1M) was transferred to the mixture through a septum. The resulting solution was heated up to 85 °C under argon and stirred for 36 h. The mixture was cooled to room temperature and poured slowly in methanol (300 mL). The precipitates were collected through a 0.45 μm PTFE filter. The crude polymer was purified with Soxhlet extraction with methanol, hexane to remove low molecular species and catalyst residues. Finally the polymer was extracted with chloroform. The polymer solution was concentrated and slowly poured in methanol (300 mL). The precipitates were collected via vacuum filtration through a 0.45 μm PTFE filter and dried, yielding dark brown solids (673 mg, 95%). ¹H-NMR (CDCl₃) δ:

8.98-8.70 (M, 2H), 7.40-6.80 (m, 4H), 3.60-3.25 (m, 4H), 2.20-0.60 (m, 62H). GPC: $M_w = 70.2$ kDa, PDI = 2.4.

PIsoI-C16-BT. $^1\text{H-NMR}$ (CDCl_3) δ : 9.42-8.95 (m, 2H), 7.78-5.98 (m, 8H), 3.60-3.20 (m, 4H), 2.20-0.45 (m, 62H). GPC: $M_w = 56.9$ kDa, PDI = 3.5.

CHAPTER 7 PERSPECTIVES AND OUTLOOK

The development of solution-processable organic semiconducting materials for photovoltaic applications has been the focus throughout this dissertation. Interest in organic solar cells mainly lies in several facts. First, they can be printed via solution-processing. This makes high-speed manufacturing process possible in the fabrication of the third generation organic solar cells, a distinction between organic and silicon-based solar cells. Fast processing makes organic solar cells more suitable and attractive as renewable energy sources to meet our energy consumption pace. Second, they can be assembled under the ambient conditions, and thus consume very little energy in the process. On the contrary, the fabrication of silicon-based solar cells involves massive energy consumption. In comparison, the manufacturing of organic solar cells has a lower environmental impact, an important argument when it comes to developing renewable energy sources. Third, solution processed organic materials are compatible with many flexible and light-weight substrates. This makes them easily integrated into a variety of products including camping tents, clothing articles, and commercial boards among others. They are seen rich with the opportunity to create their own niche markets. For instance, soldiers in battle fields are constantly on the move and in need of power for their equipment. They would greatly benefit from a solar cell coated tent or clothing that could produce electricity that would be used to recharge phones, GPS devices, and other electronics.

Bearing these features, organic solar cells present a huge potential market. This has drawn enormous research efforts from both ends of the spectrum- academia and industry. With certified power conversion efficiencies of 7.7 % (certified by the Fraunhofer Institute for Solar Energy Systems ISE in Freiburg) over an active area of 1.1 cm² achieved by the Dresden-based Heliatek GmbH and 7.9% (certified by the U.S. Department of Energy's National Renewable Energy

Laboratory) over 0.1 cm² reported by Solarmer Energy, the future of organic solar cells seems unprecedently promising for practical utilization.

On the other side, the competition to be first becomes increasingly fierce in the development of organic solar cells. This inevitably brings some undesired influences in our academic practices, even though a significant increase in photovoltaic efficiencies has been realized during this course. When Alan Heeger, Alan MacDiarmid, Hideki Shirakawa and their colleagues reported doped polyacetylene having extraordinarily high conductive properties, as a matter of fact, they had not foreseen organic solar cells (or any other electronic devices) and just wanted to understand the basic physics of how electrons were set free in the materials. But they, together with other people, opened the door of organic electronics with a simple mind of understanding things behind. Therefore, we need to reassure ourselves that our primary role as a scientific researcher is to explore the unknowns and understand the fundamental aspects.

The field of organic solar cells is indeed full of exciting and important problems which need investigation. Here are a few topics that may worth of our attention: 1) Systematically tuning optical density (absorption coefficient) of π -conjugated materials. It is well-understood that there is a trade-off between exciton diffusion length and optical absorption length in organic solar cells. An enhancement in optical density will release the tension of this trade-off to certain degree and also increase the possibility of free charge carriers reaching electrodes. An interesting question from a theoretical point of view arises as well. What are the upper limits for the absorption coefficient in π -conjugated materials? What kind of chemical structures will bring high optical densities? 2) Tentatively establishing the relationship between energy levels and charge carrier mobilities in π -conjugated materials remains a challenge. Charge mobilities are related to the chemical structures (inter/intra-chain interactions) and material morphologies. In

fact, are charge mobilities affected by a material's HOMO/LUMO energy since different energy levels correspond to different charge stabilization capabilities? As a chemist, how could we design a system to probe this relationship? 3) Constructing 2D or 3D conjugated materials. In 1-D rod-like organic materials, anisotropic charge transport is dominant, and therefore device performance is strongly dependent on orientation (morphology) of the material. Introducing (pseudo) 2D or 3D- π -conjugated materials will conceivably alleviate the anisotropy nature and enhance charge transport in these materials. Up to date, there are few efforts that have been directed towards in this regard. 4) Precisely positioning donor and acceptor components at nanoscales. In the natural systems, charge transfer and energy transfer are highly efficient, presumably because of the accurate locations of the components with respect to each other. How could we learn from Nature and build such a precisely positioned system? That is a challenge we need to face in order to make highly efficient solar cells.

There are certainly more exciting and important problems to be asked, answered, and tackled. If we can target these fundamental issues, other than making materials by trial-and-error, we will not only succeed in making high performance photovoltaic materials, but place us on a sound scientific base for unlimited possibilities.

To investigate the structure-property relationships and explore high performance photovoltaic materials have been our focus throughout this dissertation. Chapter 3 addressed whether triplet excitons can be generated and harvested in the blends of low bandgap platinum-acetylide polymers and PCBM. Our results revealed that triplet excited excitons cannot be harvested when triplet excited states are below charge separation states. Although platinum-acetylide polymers in our hands did not provided the expected photovoltaic properties, this study could become interesting and important if this system (platinum-acetylide polymers/PCBM) can

be used to probe where charge transfer states and/or charge separation states are located relative to the LUMO level of PCBM. It is well-known that charge separation states are closely related to the origin of open circuit voltage in the bulk-heterojunction solar cells. Currently, there are no readily available approaches to directly measure these states. If we are able to make a wide range of variable bandgap platinum acetylide polymers with similar HOMO levels and progressively changed LUMO levels, we should be able to indirectly estimate charge separation states relative to their singlet and triplet excited states. In other words, we can engineer the LUMO levels of the polymers through a donor-acceptor fashion where selected electron-deficient acceptors are used, and then determine whether triplet excitons can be generated and harvested. Owing to the existence of a rich library of electron-deficient acceptors, a precise control of LUMO levels of the resulting platinum-acetylide polymers can be expected. Therefore, estimation of these excited states can be made with a great accuracy.

Chapter 4 focused on the development of a general approach to prepare vinylene-containing donor-acceptor type low bandgap conjugated polymers. The performance of these vinylene-linked donor-acceptor conjugated polymers in BHJ solar cells were largely limited by their low charge mobilities. However, the scope of this approach can be extended. For instance, we can apply this method to make light-emitting polymers, since our approach can provide structurally defect-free vinylene-containing polymers. It is well understood that structural defects often act as charge traps and recombination centers in light-emitting devices. Using this approach to make near-IR light-emitting polymers is undoubtedly worthy of our immediate investigation. In addition, this approach can be certainly applied to make other alternating polymers (e.g. polyene containing conjugated polymers), even though our study up to date has only dealt with donor-acceptor type conjugated polymers.

DPP-based conjugated materials are generally high performance photovoltaic materials. Chapter 5 reported two types of unconventional DPP-based π -conjugated materials, namely amphiphilic DPP-based oligothiophenes and thermocleavable DPP-based polymers. Amphiphilic molecular design fulfilled our expectation to obtain self-assembled highly ordered nanostructures. Both field-effect transistors and solar cell devices based on amphiphilic DPP-based oligothiophenes exhibited highly remarkable properties. With continuously fine tuning the chemical structures of these molecules (e.g. adjusting the lengths of hydrophobic and hydrophilic chains, and changing the rigid cores), enhanced properties can be conceivably obtained. We should further investigate these structurally well-defined DPP-based discrete oligomers. From the aspect of device fabrication, we should develop suitable processing protocols for these unconventional materials. For instance, mixed solvents with different polarities can be used to control the materials morphologies.

The photovoltaic performance of thermocleavable polymer PDPP-Boc's was remarkable with power conversion efficiencies up to 1.5%, in spite of its poorly matched HOMO energy levels relative to PCBM. Considering the potential benefits of their use in solution-processed bilayer and tandem devices, as well as their remarkable thermal and morphological stabilities, thermocleavable DPP-based polymers with properly tuned energy levels and gaps are certainly of great interest as active materials in achieving high performance solar cells. For example, the alternating dithienosilole (DTS) and DPP-Boc polymer can be a good starting point.

In chapter 6, isoindigo was first introduced as an electron-acceptor moiety in π -conjugated materials. With the emphasis on the understanding of structure-property relationships, we have synthesized and studied a wide range of small molecules and polymers, such as IsoI-O/N/S and PIsoI_{AM}-1/2/3. In the study of IsoI-O/N/S, we showed that little changes in chemical structures

can lead to huge differences in material properties, and the study of PIsoI_{AM}-1/2/3 exhibited the power of the molecular design in controlling material properties.

Power conversion efficiencies up to ~2% demonstrated the remarkable applicability of isoindigo-based small molecules in bulk heterojunction solar cells. Of importance and urgency in the future study is, however, to develop purely n-type isoindigo-based conjugated polymers. With an established facile synthetic route for borylated isoindigo building blocks, a variety of homo- or alternating polymers composed of electron-deficient repeat units can be readily prepared via Suzuki polymerization under mild conditions opening up many possibilities. These polymers can play an important role in a number of electronic devices, such as all-polymer solar cells and ambipolar and n-type field-effect transistors. In combination with p-dopable conjugated polymers, these n-dopable isoindigo-based polymers can be possibly used in the realization of complementary multi-colored electrochromic devices.

Clearly, designing materials for organic photovoltaics (electronics) involves delicate balances and a comprehensive understanding of all of the processes. With a firm understanding of π -conjugated materials and device operation mechanisms at fundamental levels, we anticipate the era of organic electronics is coming in the foreseeable future.

LIST OF REFERENCES

- (1) Grimsdale, A. C.; Leok Chan, K.; Martin, R. E.; Jokisz, P. G.; Holmes, A. B. *Chem. Rev.* **2009**, *109*, 897.
- (2) Cheng, Y.-J.; Yang, S.-H.; Hsu, C.-S. *Chem. Rev.* **2009**, *109*, 5868.
- (3) Murphy, A. R.; Fréchet, J. M. J. *Chem. Rev.* **2007**, *107*, 1066.
- (4) Samuel, I. D. W.; Turnbull, G. A. *Chem. Rev.* **2007**, *107*, 1272.
- (5) Beaujuge, P. M.; Reynolds, J. R. *Chem. Rev.* **2010**, *110*, 268.
- (6) Gelinck, G. H.; Huitema, H. E. A.; van Veenendaal, E.; Cantatore, E.; Schrijnemakers, L.; van der Putten, J. B. P. H.; Geuns, T. C. T.; Beenhakkers, M.; Giesbers, J. B.; Huisman, B.-H.; Meijer, E. J.; Benito, E. M.; Touwslager, F. J.; Marsman, A. W.; van Rens, B. J. E.; de Leeuw, D. M. *Nat. Mater.* **2004**, *3*, 106.
- (7) Kelley, T. W.; Baude, P. F.; Gerlach, C.; Ender, D. E.; Muyres, D.; Haase, M. A.; Vogel, D. E.; Theiss, S. D. *Chem. Mater.* **2004**, *16*, 4413.
- (8) Hines, D. R.; Ballarotto, V. W.; Williams, E. D.; Shao, Y.; Solin, S. A. *J. Appl. Phys.* **2007**, *101*, 024503.
- (9) Eder, F.; Klauk, H.; Halik, M.; Zschieschang, U.; Schmid, G.; Dehm, C. *Appl. Phys. Lett.* **2004**, *84*, 2673.
- (10) Blanchet, G. B.; Loo, Y.-L.; Rogers, J. A.; Gao, F.; Fincher, C. R. *Appl. Phys. Lett.* **2003**, *82*, 463.
- (11) Chiang, C. K.; Fincher, C. R.; Park, Y. W.; Heeger, A. J.; Shirakawa, H.; Louis, E. J.; Gau, S. C.; MacDiarmid, A. G. *Phys. Rev. Lett.* **1977**, *39*, 1098.
- (12) Chien, J. C. W.; Karasz, F. E.; Shimamura, K. *Macromolecules* **1982**, *15*, 1012.
- (13) Roth, S.; Filzmoser, M. *Adv. Mater.* **1990**, *2*, 356.
- (14) Brédas, J.-L.; Cornil, J.; Heeger, A. J. *Adv. Mater.* **1996**, *8*, 447.
- (15) Walzer, K.; Maennig, B.; Pfeiffer, M.; Leo, K. *Chem. Rev.* **2007**, *107*, 1233.
- (16) Maennig, B.; Pfeiffer, M.; Nollau, A.; Zhou, X.; Leo, K.; Simon, P. *Phys. Rev. B* **2001**, *64*, 195208.
- (17) Novikov, S. V.; Dunlap, D. H.; Kenkre, V. M.; Parris, P. E.; Vannikov, A. V. *Phys. Rev. Lett.* **1998**, *81*, 4472.
- (18) Tessler, N.; Preezant, Y.; Rappaport, N.; Roichman, Y. *Adv. Mater.* **2009**, *21*, 2741.

- (19) Bredas, J. L.; Street, G. B. *Acc. Chem. Res.* **1985**, *18*, 309.
- (20) Reeves, B. D.; Unur, E.; Ananthakrishnan, N.; Reynolds, J. R. *Macromolecules* **2007**, *40*, 5344.
- (21) Takahashi, A.; Fukutome, H. *Solid State Commun.* **1987**, *62*, 279.
- (22) Roth, S. In *Field Theoretical Tools for Polymer and Particle Physics*; Springer Berlin 1998; Vol. 508, p 240.
- (23) Su, W. P.; Schrieffer, J. R.; Heeger, A. J. *Phys. Rev. Lett.* **1979**, *42*, 1698.
- (24) Gershenson, M. E.; Podzorov, V.; Morpurgo, A. F. *Rev. Mod. Phys.* **2006**, *78*, 973.
- (25) Druger, S. D.; Ratner, M. A.; Nitzan, A. *Mol. Cryst. Liq. Cryst.* **1990**, *190*, 171
- (26) Brédas, J.-L.; Norton, J. E.; Cornil, J.; Coropceanu, V. *Acc. Chem. Res.* **2009**, *42*, 1691.
- (27) Cornil, J.; Beljonne, D.; Calbert, J.-P.; Brédas, J.-L. *Adv. Mater.* **2001**, *13*, 1053.
- (28) Tiwari, S.; Greenham, N. *Opt. Quant. Electronics.* **2009**, *41*, 69.
- (29) Yang, X.; Wang, L.; Wang, C.; Long, W.; Shuai, Z. *Chem. Mater.* **2008**, *20*, 3205.
- (30) Coehoorn, R.; Pasveer, W. F.; Bobbert, P. A.; Michels, M. A. J. *Phys. Rev. B* **2005**, *72*, 155206.
- (31) Podzorov, V.; Menard, E.; Borissov, A.; Kiryukhin, V.; Rogers, J. A.; Gershenson, M. E. *Phys. Rev. Lett.* **2004**, *93*, 086602.
- (32) Novikov, S. V.; Vannikov, A. V. *J. Phys. Chem. C* **2009**, *113*, 2532.
- (33) Schmeichel, R.; Seggern, H. v. *physica status solidi (a)* **2004**, *201*, 1215.
- (34) Sheraw, C. D.; Jackson, T. N.; Eaton, D. L.; Anthony, J. E. *Adv. Mater.* **2003**, *15*, 2009.
- (35) Katz, H. E.; Laquindanum, J. G.; Lovinger, A. J. *Chem. Mater.* **1998**, *10*, 633.
- (36) Heeney, M.; Bailey, C.; Genevicius, K.; Shkunov, M.; Sparrowe, D.; Tierney, S.; McCulloch, I. *J. Am. Chem. Soc.* **2005**, *127*, 1078.
- (37) Yamamoto, T.; Kokubo, H.; Kobashi, M.; Sakai, Y. *Chem. Mater.* **2004**, *16*, 4616.
- (38) Coppo, P.; Cupertino, D. C.; Yeates, S. G.; Turner, M. L. *Macromolecules* **2003**, *36*, 2705.
- (39) Letizia, J. A.; Salata, M. R.; Tribout, C. M.; Facchetti, A.; Ratner, M. A.; Marks, T. J. *J. Am. Chem. Soc.* **2008**, *130*, 9679.

- (40) Zhan, X.; Tan, Z. a.; Domercq, B.; An, Z.; Zhang, X.; Barlow, S.; Li, Y.; Zhu, D.; Kippelen, B.; Marder, S. R. *J. Am. Chem. Soc.* **2007**, *129*, 7246.
- (41) Bijleveld, J. C.; Zoombelt, A. P.; Mathijssen, S. G. J.; Wienk, M. M.; Turbiez, M.; de Leeuw, D. M.; Janssen, R. A. J. *J. Am. Chem. Soc.* **2009**, *131*, 16616.
- (42) Kim, F. S.; Guo, X.; Watson, M. D.; Jenekhe, S. A. *Adv. Mater.* **2010**, *22*, 478.
- (43) Usta, H.; Risko, C.; Wang, Z.; Huang, H.; Deliomeroglu, M. K.; Zhukhovitskiy, A.; Facchetti, A.; Marks, T. J. *J. Am. Chem. Soc.* **2009**, *131*, 5586.
- (44) Steckler, T. T.; Zhang, X.; Hwang, J.; Honeyager, R.; Ohira, S.; Zhang, X.-H.; Grant, A.; Ellinger, S.; Odom, S. A.; Sweat, D.; Tanner, D. B.; Rinzler, A. G.; Barlow, S.; Brédas, J.-L.; Kippelen, B.; Marder, S. R.; Reynolds, J. R. *J. Am. Chem. Soc.* **2009**, *131*, 2824.
- (45) Schidleja, M.; Melzer, C.; Seggern, H. v. *Adv. Mater.* **2009**, *21*, 1172.
- (46) Bürgi, L.; Turbiez, M.; Pfeiffer, R.; Bienewald, F.; Kirner, H.-J.; Winnewisser, C. *Adv. Mater.* **2008**, *20*, 2217.
- (47) Zaumseil, J.; Sirringhaus, H. *Chem. Rev.* **2007**, *107*, 1296.
- (48) Cornil, J.; Brédas, J.-L.; Zaumseil, J.; Sirringhaus, H. *Adv. Mater.* **2007**, *19*, 1791.
- (49) Sirringhaus, H.; Wilson, R. J.; Friend, R. H.; Inbasekaran, M.; Wu, W.; Woo, E. P.; Grell, M.; Bradley, D. D. C. *Appl. Phys. Lett.* **2000**, *77*, 406.
- (50) Coropceanu, V.; Cornil, J.; da Silva Filho, D. A.; Olivier, Y.; Silbey, R.; Brédas, J.-L. *Chem. Rev.* **2007**, *107*, 926.
- (51) Soci, C.; Hwang, I.-W.; Moses, D.; Zhu, Z.; Waller, D.; Gaudiana, R.; Brabec, C. J.; Heeger, A. J. *Adv. Funct. Mater.* **2007**, *17*, 632.
- (52) Roncali, J. *Chem. Rev.* **1997**, *97*, 173.
- (53) Balaban, A. T.; Oniciu, D. C.; Katritzky, A. R. *Chem. Rev.* **2004**, *104*, 2777.
- (54) Brocks, G.; Tol, A. J. *Phys. Chem.* **1996**, *100*, 1838.
- (55) Wudl, F.; Kobayashi, M.; Heeger, A. J. *J. Org. Chem.* **1984**, *49*, 3382.
- (56) Bundgaard, E.; Krebs, F. C. *Macromolecules* **2006**, *39*, 2823.
- (57) Bagnis, D.; Beverina, L.; Huang, H.; Silvestri, F.; Yao, Y.; Yan, H.; Pagani, G. A.; Marks, T. J.; Facchetti, A. *J. Am. Chem. Soc.* **2010**, *132*, 4074.
- (58) Blouin, N.; Michaud, A.; Gendron, D.; Wakim, S.; Blair, E.; Neagu-Plesu, R.; Belletête, M.; Durocher, G.; Tao, Y.; Leclerc, M. *J. Am. Chem. Soc.* **2007**, *130*, 732.

- (59) Hou, J.; Chen, H.-Y.; Zhang, S.; Li, G.; Yang, Y. *J. Am. Chem. Soc.* **2008**, *130*, 16144.
- (60) Zou, Y.; Gendron, D.; Neagu-Plesu, R.; Leclerc, M. *Macromolecules* **2009**, *42*, 6361.
- (61) Zou, Y.; Najari, A.; Berrouard, P.; Beaupré, S.; Réda Aïch, B.; Tao, Y.; Leclerc, M. *J. Am. Chem. Soc.* **2010**, *132*, 5330.
- (62) Santamouris, M.; Argiriou, A.; Vallindras, M. *Sol. Energy* **1994**, *52*, 371.
- (63) Green, M. A. *Physica. E* **2002**, *14*, 65.
- (64) King, R. R.; Law, D. C.; Edmondson, K. M.; Fetzer, C. M.; Kinsey, G. S.; Yoon, H.; Sherif, R. A.; Karam, N. H. *Appl. Phys. Lett.* **2007**, *90*, 183516.
- (65) Wu, J.; Walukiewicz, W.; Yu, K. M.; Shan, W.; Ager Iii, J. W.; Haller, E. E.; Lu, H.; Schaff, W. J.; Metzger, W. K.; Kurtz, S. *J. Appl. Phys.* **2003**, *94*, 6477.
- (66) Takamoto, T.; Ikeda, E.; Kurita, H.; Ohmori, M. *Appl. Phys. Lett.* **1997**, *70*, 381.
- (67) Tang, C. W. *Appl. Phys. Lett.* **1986**, *48*, 183.
- (68) Peumans, P.; Forrest, S. R. *Appl. Phys. Lett.* **2001**, *79*, 126.
- (69) Jenekhe, S. A.; Yi, S. *Appl. Phys. Lett.* **2000**, *77*, 2635.
- (70) Stevens, D. M.; Qin, Y.; Hillmyer, M. A.; Frisbie, C. D. *J. Phys. Chem. C* **2009**, *113*, 11408.
- (71) Lloyd, M. T.; Mayer, A. C.; Subramanian, S.; Mourey, D. A.; Herman, D. J.; Bapat, A. V.; Anthony, J. E.; Malliaras, G. G. *J. Am. Chem. Soc.* **2007**, *129*, 9144.
- (72) Matsuo, Y.; Sato, Y.; Niinomi, T.; Soga, I.; Tanaka, H.; Nakamura, E. *J. Am. Chem. Soc.* **2009**, *131*, 16048.
- (73) Mikroyannidis, J. A.; Sharma, S. S.; Vijay, Y. K.; Sharma, G. D. *ACS Appl. Mater. Interfaces* **2009**, *2*, 270.
- (74) Roncali, J.; Frère, P.; Blanchard, P.; de Bettignies, R.; Turbiez, M.; Roquet, S.; Leriche, P.; Nicolas, Y. *Thin Solid Films* **2006**, *511-512*, 567.
- (75) Silvestri, F.; Irwin, M. D.; Beverina, L.; Facchetti, A.; Pagani, G. A.; Marks, T. J. *J. Am. Chem. Soc.* **2008**, *130*, 17640.
- (76) Tamayo, A. B.; Tantiwiwat, M.; Walker, B.; Nguyen, T.-Q. *J. Phys. Chem. C* **2008**, *112*, 15543.
- (77) Tamayo, A. B.; Walker, B.; Nguyen, T.-Q. *J. Phys. Chem. C* **2008**, *112*, 11545.

- (78) Tantiwiwat, M.; Tamayo, A.; Luu, N.; Dang, X.-D.; Nguyen, T.-Q. *J. Phys. Chem. C* **2008**, *112*, 17402.
- (79) Velusamy, M.; Huang, J.-H.; Hsu, Y.-C.; Chou, H.-H.; Ho, K.-C.; Wu, P.-L.; Chang, W.-H.; Lin, J. T.; Chu, C.-W. *Org. Lett.* **2009**, *11*, 4898.
- (80) Walker, B.; Tamayo, A. B.; Dang, X.-D.; Zalar, P.; Seo, J. H.; Garcia, A.; Tantiwiwat, M.; Nguyen, T.-Q. *Adv. Funct. Mater.* **2009**, *19*, 3063.
- (81) Winzenberg, K. N.; Kemppinen, P.; Fanchini, G.; Bown, M.; Collis, G. E.; Forsyth, C. M.; Hegedus, K.; Singh, T. B.; Watkins, S. E. *Chem. Mater.* **2009**, *21*, 5701.
- (82) Zhang, J.; Yang, Y.; He, C.; He, Y.; Zhao, G.; Li, Y. *Macromolecules* **2009**, *42*, 7619.
- (83) Tamayo, A. B.; Walker, B.; Nguyen, T.-Q. *J. Phys. Chem. C* **2008**, *112*, 11545.
- (84) Woo, C. H.; Holcombe, T. W.; Unruh, D. A.; Sellinger, A.; Fréchet, J. M. J. *Chem. Mater.* **2010**, *22*, 1673.
- (85) Alam, M. M.; Jenekhe, S. A. *Chem. Mater.* **2004**, *16*, 4647.
- (86) Brabec, C. J.; Cravino, A.; Meissner, D.; Sariciftci, N. S.; Fromherz, T.; Rispens, M. T.; Sanchez, L.; Hummelen, J. C. *Adv. Mater. Funct.* **2001**, *11*, 374.
- (87) Christopher, R. M.; Agnese, A.; Jana, Z.; Richard, W.; Mary, J. M.; Jeremy, H. B.; Jonathan, J. M. H.; Neil, C. G.; Richard, H. F. *Appl. Phys. Lett.* **2007**, *90*, 193506.
- (88) Granstrom, M.; Petritsch, K.; Arias, A. C.; Lux, A.; Andersson, M. R.; Friend, R. H. *Nature* **1998**, *395*, 257.
- (89) Guo, X.; Watson, M. D. *Org. Lett.* **2008**, *10*, 5333.
- (90) Holcombe, T. W.; Woo, C. H.; Kavulak, D. F. J.; Thompson, B. C.; Frechet, J. M. J. *J. Am. Chem. Soc.* **2009**, *131*, 14160.
- (91) Kietzke, T.; Egbe, D. A. M.; Horhold, H.-H.; Neher, D. *Macromolecules* **2006**, *39*, 4018.
- (92) Kietzke, T.; Horhold, H.-H.; Neher, D. *Chem. Mater.* **2005**, *17*, 6532.
- (93) Kietzke, T.; Shin, R. Y. C.; Egbe, D. A. M.; Chen, Z.-K.; Sellinger, A. *Macromolecules* **2007**, *40*, 4424.
- (94) Kim, G. J.; Wichard, J. D. B.; Yuri, Z.; Arkady, Y.; Mats, A.; Tonu, P.; Villy, S.; *Appl. Phys. Lett.* **2004**, *121*, 12613.
- (95) Kim, J.-S.; Ho, P. K. H.; Murphy, C. E.; Friend, R. H. *Macromolecules* **2004**, *37*, 2861.
- (96) Kim, Y.; Cook, S.; Choulis, S. A.; Nelson, J.; Durrant, J. R.; Bradley, D. D. C. *Chem. Mater.* **2004**, *16*, 4812.

- (97) Marc, M. K.; Jorgen, S.; Kornel, T. H.; Herman, F. M. S.; Sjoerd, C. V.; Jan, M. K.; Xiaoniu, Y.; Joachim, L. *Appl. Phys. Lett.* **2006**, *88*, 083504.
- (98) Marsh, R. A.; McNeill, C. R.; Abrusci, A.; Campbell, A. R.; Friend, R. H. *Nano Lett.* **2008**, *8*, 1393.
- (99) Martijn, M. W.; Kroon, J., M. ; Verhees, W. J. H.; Joop, K.; Hummelen, J. C.; van Hal, P., A. ; Janssen, R. A. J. *Angew. Chem. Int. Ed.* **2003**, *42*, 3371.
- (100) McNeill, C. R.; Abrusci, A.; Zaumseil, J.; Wilson, R.; McKiernan, M. J.; Burroughes, J. H.; Halls, J. J. M.; Greenham, N. C.; Friend, R. H. *Appl. Phys. Lett.* **2007**, *90*, 193506.
- (101) McNeill, C. R.; Greenham, N. C. *Adv. Mater.* **2009**, *21*, 3840.
- (102) McNeill, C. R.; Halls, J. J. M.; Wilson, R.; Whiting, G. L.; Berkebile, S.; Ramsey, M. G.; Friend, R. H.; Greenham, N. C. *Adv. Funct. Mater.* **2008**, *18*, 2309.
- (103) McNeill, C. R.; Westenhoff, S.; Groves, C.; Friend, R. H.; Greenham, N. C. *J. Phys. Chem. C* **2007**, *111*, 19153.
- (104) Sang, G.; Zhou, E.; Huang, Y.; Zou, Y.; Zhao, G.; Li, Y. *J. Phys. Chem. C* **2009**, *113*, 5879.
- (105) Sang, G.; Zou, Y.; Huang, Y.; Zhao, G.; Yang, Y.; Li, Y. *Appl. Phys. Lett.* **2009**, *94*, 193302.
- (106) Tan, Z. a.; Zhou, E.; Zhan, X.; Wang, X.; Li, Y.; Barlow, S.; Marder, S. R. *Appl. Phys. Lett.* **2008**, *93*, 073309.
- (107) Zhou, Y.; Pei, J.; Dong, Q.; Sun, X.; Liu, Y.; Tian, W. *J. Phys. Chem. C* **2009**, *113*, 7882.
- (108) Alivisatos, A. P. *Science* **1996**, *271*, 933.
- (109) Bai, Y.; Cao, Y.; Zhang, J.; Wang, M.; Li, R.; Wang, P.; Zakeeruddin, S. M.; Gratzel, M. *Nat. Mater.* **2008**, *7*, 626.
- (110) Black, C. T.; Murray, C. B.; Sandstrom, R. L.; Sun, S. *Science* **2000**, *290*, 1131.
- (111) Dayal, S.; Kopidakis, N.; Olson, D. C.; Ginley, D. S.; Rumbles, G. *Nano Lett.* **2009**, *10*, 239.
- (112) Greenham, N. C.; Peng, X.; Alivisatos, A. P. *Phys. Rev. B* **1996**, *54*, 17628.
- (113) Landi, B. J.; Castro, S. L.; Ruf, H. J.; Evans, C. M.; Bailey, S. G.; Raffaelle, R. P. *Sol. Energy Mater. Sol. Cells* **2005**, *87*, 733.
- (114) Lin, Y.-Y.; Chu, T.-H.; Li, S.-S.; Chuang, C.-H.; Chang, C.-H.; Su, W.-F.; Chang, C.-P.; Chu, M.-W.; Chen, C.-W. *J. Am. Chem. Soc.* **2009**, *131*, 3644.

- (115) Oosterhout, S. D.; Wienk, M. M.; van Bavel, S. S.; Thiedmann, R.; Jan Anton Koster, L.; Gilot, J.; Loos, J.; Schmidt, V.; Janssen, R. A. J. *Nat. Mater.* **2009**, *8*, 818.
- (116) O'Regan, B.; Gratzel, M. *Nature* **1991**, *353*, 737.
- (117) Sun, B.; Snaith, H. J.; Dhoot, A. S.; Westenhoff, S.; Greenham, N. C. *J. Appl. Phys.* **2005**, *97*, 014914.
- (118) Wang, P.; Zakeeruddin, S. M.; Moser, J. E.; Nazeeruddin, M. K.; Sekiguchi, T.; Gratzel, M. *Nat. Mater.* **2003**, *2*, 402.
- (119) Weintraub, B.; Wei, Y.; Wang, Zhong L. *Angew. Chem. Int. Ed.* **2009**, *48*, 8981.
- (120) Zhou, Y.; Riehle, F. S.; Yuan, Y.; Schleiermacher, H.-F.; Niggemann, M.; Urban, G. A.; Kruger, M. *Appl. Phys. Lett.* **2010**, *96*, 013304.
- (121) Zotti, G.; Vercelli, B.; Berlin, A.; Pasini, M.; Nelson, T. L.; McCullough, R. D.; Virgili, T. *Chem. Mater.* **2010**, *22*, 1521.
- (122) Peumans, P.; Yakimov, A.; Forrest, S. R. *J. Appl. Phys.* **2003**, *93*, 3693.
- (123) Veldman, D.; Meskers, S. C. J.; Janssen, R. A. J. *Adv. Funct. Mater.* **2009**, *19*, 1939.
- (124) Sariciftci, N. S.; Smilowitz, L.; Heeger, A. J.; Wudl, F. *Science* **1992**, *258*, 1474.
- (125) Yu, G.; Gao, J.; Hummelen, J. C.; Wudl, F.; Heeger, A. J. *Science* **1995**, *270*, 1789.
- (126) Kim, J. Y.; Kim, S. H.; Lee, H.-H.; Lee, K.; Ma, W.; Gong, X.; Heeger, A. J. *Adv. Mater.* **2006**, *18*, 572.
- (127) Nguyen, L. H.; Hoppe, H.; Erb, T.; Günes, S.; Gobsch, G.; Sariciftci, N. S. *Adv. Funct. Mater.* **2007**, *17*, 1071.
- (128) Moulé, A. J.; Meerholz, K. *Adv. Mater.* **2008**, *20*, 240.
- (129) Li, G.; Shrotriya, V.; Huang, J.; Yao, Y.; Moriarty, T.; Emery, K.; Yang, Y. *Nat. Mater.* **2005**, *4*, 864.
- (130) Ma, W.; Yang, C.; Gong, X.; Lee, K.; Heeger, A. J. *Adv. Funct. Mater.* **2005**, *15*, 1617.
- (131) Yao, Y.; Hou, J.; Xu, Z.; Li, G.; Yang, Y. *Adv. Funct. Mater.* **2008**, *18*, 1783.
- (132) Peet, J.; Kim, J. Y.; Coates, N. E.; Ma, W. L.; Moses, D.; Heeger, A. J.; Bazan, G. C. *Nat. Mater.* **2007**, *6*, 497.
- (133) Scharber, M. C.; Mühlbacher, D.; Koppe, M.; Denk, P.; Waldauf, C.; Heeger, A. J.; Brabec, C. J. *Adv. Mater.* **2006**, *18*, 789.
- (134) Thompson, B. C.; Kim, Y.-G.; Reynolds, J. R. *Macromolecules* **2005**, *38*, 5359.

- (135) Mühlbacher, D.; Scharber, M.; Morana, M.; Zhu, Z.; Waller, D.; Gaudiana, R.; Brabec, C. *Adv. Mater.* **2006**, *18*, 2884.
- (136) Lee, J. K.; Ma, W. L.; Brabec, C. J.; Yuen, J.; Moon, J. S.; Kim, J. Y.; Lee, K.; Bazan, G. C.; Heeger, A. J. *J. Am. Chem. Soc.* **2008**, *130*, 3619.
- (137) Hoven, C. V.; Dang, X.-D.; Coffin, R. C.; Peet, J.; Nguyen, T.-Q.; Bazan, G. C. *Adv. Mater.* **2010**, *22*, E63.
- (138) Wang, E.; Wang, L.; Lan, L.; Luo, C.; Zhuang, W.; Peng, J.; Cao, Y. *Appl. Phys. Lett.* **2008**, *92*, 033307.
- (139) Baek, N. S.; Hau, S. K.; Yip, H.-L.; Acton, O.; Chen, K.-S.; Jen, A. K. Y. *Chem. Mater.* **2008**, *20*, 5734.
- (140) Wong, W.-Y.; Wang, X.-Z.; He, Z.; Djurisic, A. B.; Yip, C.-T.; Cheung, K.-Y.; Wang, H.; Mak, C. S. K.; Chan, W.-K. *Nat. Mater.* **2007**, *6*, 521.
- (141) Gilot, J.; Wienk, M. M.; Janssen, R. A. J. *Nat. Mater.* **2007**, *6*, 704.
- (142) Huo, L.; Hou, J.; Zhang, S.; Chen, H.-Y.; Yang, Y. *Angew. Chem. Int. Ed.* **2010**, *49*, 1500.
- (143) Chen, C.-P.; Chan, S.-H.; Chao, T.-C.; Ting, C.; Ko, B.-T. *J. Am. Chem. Soc.* **2008**, *130*, 12828.
- (144) Chen, H.-Y.; Hou, J.; Zhang, S.; Liang, Y.; Yang, G.; Yang, Y.; Yu, L.; Wu, Y.; Li, G. *Nat Photon* **2009**, *3*, 649.
- (145) Liang, Y.; Wu, Y.; Feng, D.; Tsai, S.-T.; Son, H.-J.; Li, G.; Yu, L. *J. Am. Chem. Soc.* **2008**, *131*, 56.
- (146) Liang, Y.; Xu, Z.; Xia, J.; Tsai, S.-T.; Wu, Y.; Li, G.; Ray, C.; Yu, L. *Adv. Mater.* **2010**, 9999.
- (147) Halls, J. J. M.; Walsh, C. A.; Greenham, N. C.; Marseglia, E. A.; Friend, R. H.; Moratti, S. C.; Holmes, A. B. *Nature* **1995**, *376*, 498.
- (148) Pincus, P. *J. Chem. Phys.* **1981**, *75*, 1996.
- (149) Walheim, S.; Boltau, M.; Mlynek, J.; Krausch, G.; Steiner, U. *Macromolecules* **1997**, *30*, 4995.
- (150) Yan, H.; Chen, Z.; Zheng, Y.; Newman, C.; Quinn, J. R.; Dotz, F.; Kastler, M.; Facchetti, A. *Nature* **2009**, *457*, 679.
- (151) Chen, Z.; Zheng, Y.; Yan, H.; Facchetti, A. *J. Am. Chem. Soc.* **2008**, *131*, 8.

- (152) Sun, X.; Zhou, Y.; Wu, W.; Liu, Y.; Tian, W.; Yu, G.; Qiu, W.; Chen, S.; Zhu, D. *The J. Phys. Chem. B* **2006**, *110*, 7702.
- (153) Xue, J.; Uchida, S.; Rand, B. P.; Forrest, S. R. *Appl. Phys. Lett.* **2004**, *85*, 5757.
- (154) Kim, J. Y.; Lee, K.; Coates, N. E.; Moses, D.; Nguyen, T.-Q.; Dante, M.; Heeger, A. J. *Science* **2007**, *317*, 222.
- (155) Sista, S.; Park, M.-H.; Hong, Z.; Wu, Y.; Hou, J.; Kwan, W. L.; Li, G.; Yang, Y. *Adv. Mater.* **2010**, *22*, 380.
- (156) Dennler, G.; Scharber, M. C.; Ameri, T.; Denk, P.; Forberich, K.; Waldauf, C.; Brabec, C. J. *Adv. Mater.* **2008**, *20*, 579.
- (157) Thompson, B. C.; Kim, Y. G.; McCarley, T. D.; Reynolds, J. R. *J. Am. Chem. Soc.* **2006**, *128*, 12714.
- (158) Farley, R. T. Ph. D. Dissertation, University of Florida, 2008.
- (159) Brabec, C. J.; Sariciftci, N. S.; Hummelen, J. C. *Adv. Funct. Mater.* **2001**, *11*, 15.
- (160) Brabec, C. J. *Sol. Energy Mater. Sol. Cells* **2004**, *83*, 273.
- (161) Scharber, M. C.; Wuhlbacher, D.; Koppe, M.; Denk, P.; Waldauf, C.; Heeger, A. J.; Brabec, C. L. *Adv. Mater.* **2006**, *18*, 789.
- (162) Sariciftci, N. S.; Smilowitz, L.; Heeger, A. J.; Wudl, F. *Science* **1992**, *258*, 1474.
- (163) Brabec, C. J.; Zerza, G.; Cerullo, G.; De Silvestri, S.; Luzzati, S.; Hummelen, J. C.; Sariciftci, S. *Chem. Phys. Lett.* **2001**, *340*, 232.
- (164) Reyes-Reyes, M.; Kim, K.; Carroll, D. L. *Appl. Phys. Lett.* **2005**, *87*, 083506.
- (165) Li, G.; Shrotriya, V.; Huang, J. S.; Yao, Y.; Moriarty, T.; Emery, K.; Yang, Y. *Nat. Mater.* **2005**, *4*, 864.
- (166) Kim, Y.; Cook, S.; Tuladhar, S. M.; Choulis, S. A.; Nelson, J.; Durrant, J. R.; Bradley, D. D. C.; Giles, M.; McCulloch, I.; Ha, C. S.; Ree, M. *Nat. Mater.* **2006**, *5*, 197.
- (167) Kim, J. Y.; Kim, S. H.; Lee, H. H.; Lee, K.; Ma, W. L.; Gong, X.; Heeger, A. J. *Adv. Mater.* **2006**, *18*, 572.
- (168) Kim, K.; Liu, J.; Namboothiry, M. A. G.; Carroll, D. L. *Appl. Phys. Lett.* **2007**, *90*, 163511.
- (169) Kim, J. Y.; Lee, K.; Coates, N. E.; Moses, D.; Nguyen, T. Q.; Dante, M.; Heeger, A. J. *Science* **2007**, *317*, 222.
- (170) Green, M. A.; Emery, K.; Hishikawa, Y.; Warta, W. *Prog. Photovoltaics* **2008**, *16*, 61.

- (171) Huo, L.; Hou, J.; Zhang, S.; Chen, H.-Y.; Yang, Y. *Angew. Chem. Int. Ed.* **2010**, *49*, 1500.
- (172) Padinger, F.; Rittberger, R. S.; Sariciftci, N. S. *Adv. Funct. Mater.* **2003**, *13*, 85.
- (173) Guo, F. Q.; Kim, Y. G.; Reynolds, J. R.; Schanze, K. S. *Chem. Commun.* **2006**, 1887.
- (174) Guo, F.; Ogawa, K.; Kim, Y.-G.; Danilov, E. O.; Castellano, F. N.; Reynolds, J. R.; Schanze, K. S. *Phys. Chem. Chem. Phys.* **2007**, *9*, 2724.
- (175) Shao, Y.; Yang, Y. *Adv. Mater.* **2005**, *17*, 2841.
- (176) Giebink, N. C.; Sun, Y.; Forrest, S. R. *Org. Electron.* **2006**, *7*, 375.
- (177) Holten, D.; Gouterman, M.; Parson, W. W.; Windsor, M. W.; Rockley, M. G. *Photochem. Photobiol.* **1976**, *23*, 415.
- (178) Goodenough, J. B. *Phys. Rev.* **1968**, *171*, 466.
- (179) Beljonne, D.; Wittmann, H. F.; Kohler, A.; Graham, S.; Younus, M.; Lewis, J.; Raithby, P. R.; Khan, M. S.; Friend, R. H.; Bredas, J. L. *J. Chem. Phys.* **1996**, *105*, 3868.
- (180) Wilson, J. S.; Chawdhury, N.; Al-Mandhary, M. R. A.; Younus, M.; Khan, M. S.; Raithby, P. R.; Kohler, A.; Friend, R. H. *J. Am. Chem. Soc.* **2001**, *123*, 9412.
- (181) Kohler, A.; Wilson, J. S.; Friend, R. H.; Al-Suti, M. K.; Khan, M. S.; Gerhard, A.; Bassler, H. *J. Chem. Phys.* **2002**, *116*, 9457.
- (182) Silverman, E. E.; Cardolaccia, T.; Zhao, X. M.; Kim, K. Y.; Haskins-Glusac, K.; Schanze, K. S. *Coord. Chem. Rev.* **2005**, *249*, 1491.
- (183) Glusac, K.; Kose, M. E.; Jiang, H.; Schanze, K. S. *J. Phys. Chem. B* **2007**, *111*, 929.
- (184) Wong, W. Y. *Dalton Trans.* **2007**, 4495.
- (185) Kohler, A.; Wittmann, H. F.; Friend, R. H.; Khan, M. S.; Lewis, J. *Synth. Met.* **1996**, *77*, 147.
- (186) Zhang, Q. T.; Tour, J. M. *J. Am. Chem. Soc.* **1998**, *120*, 5355.
- (187) van Mullekom, H. A. M.; Vekemans, J. A. J. M.; Meijer, E. W. *Chem.-Eur. J.* **1998**, *4*, 1235.
- (188) Dhanabalan, A.; van Duren, J. K. J.; van Hal, P. A.; van Dongen, J. L. J.; Janssen, R. A. J. *Adv. Funct. Mater.* **2001**, *11*, 255.
- (189) Thomas, C. A.; Zong, K. W.; Abboud, K. A.; Steel, P. J.; Reynolds, J. R. *J. Am. Chem. Soc.* **2004**, *126*, 16440.

- (190) Winder, C.; Sariciftci, N. S. *J. Mater. Chem.* **2004**, *14*, 1077.
- (191) Steckler, T. T.; Abboud, K. A.; Craps, M.; Rinzler, A. G.; Reynolds, J. R. *Chem. Commun.* **2007**, 4904.
- (192) Blouin, N.; Michaud, A.; Leclerc, M. *Adv. Mater.* **2007**, *19*, 2295.
- (193) Blouin, N.; Michaud, A.; Gendron, D.; Wakim, S.; Blair, E.; Neagu-Plesu, R.; Belletete, M.; Durocher, G.; Tao, Y.; Leclerc, M. *J. Am. Chem. Soc.* **2008**, *130*, 732.
- (194) Wong, W.-Y.; Wang, X.-Z.; He, Z.; Djurisic, A. B.; Yip, C.-T.; Cheung, K.-Y.; Wang, H.; Mak, C. S. K.; Chan, W.-K. *Nat. Mater.* **2007**, *6*, 521.
- (195) Wong, W. Y.; Wang, X. Z.; He, Z.; Chan, K. K.; Djurisic, A. B.; Cheung, K. Y.; Yip, C. T.; Ng, A. M. C.; Xi, Y. Y.; Mak, C. S. K.; Chan, W. K. *J. Am. Chem. Soc.* **2007**, *129*, 14372.
- (196) Wong, W. Y.; Wang, X. Z.; He, Z.; Djurisic, A. B.; Yip, C. T.; Cheung, K. Y.; Wang, H.; Mak, C. S. K.; Chan, W. K. *Nat. Mater.* **2007**, *6*, 704.
- (197) Gilot, J.; Wienk, M. M.; Janssen, R. A. J. *Nat. Mater.* **2007**, *6*, 704.
- (198) Wu, P.-T.; Bull, T.; Kim, F. S.; Luscombe, C. K.; Jenekhe, S. A. *Macromolecules* **2009**, *42*, 671.
- (199) Wyatt, M. F.; Stein, B. K.; Brenton, A. G. *Anal. Chem.* **2006**, *78*, 199.
- (200) Frapper, G.; Kertesz, M. *Inorg. Chem.* **1993**, *32*, 732.
- (201) Parker, C. A.; Rees, W. T. *Analyst* **1960**, *85*, 587.
- (202) Rogers, J. E.; Cooper, T. M.; Fleitz, P. A.; Glass, D. J.; McLean, D. G. *J. Phys. Chem. A* **2002**, *106*, 10108.
- (203) Datta, K.; Banerjee, M.; Seal, B. K.; Mukherjee, A. K. *J. Chem. Soc. Perkin Trans. 2* **2000**, 531.
- (204) Bhattacharya, S.; Nayak, S. K.; Chattopadhyay, S.; Banerjee, M.; Mukherjee, A. K. *J. Phys. Chem. A* **2001**, *105*, 9865.
- (205) Karikomi, M.; Kitamura, C.; Tanaka, S.; Yamashita, Y. *J. Am. Chem. Soc.* **1995**, *117*, 6791.
- (206) Blanchard, P.; Raimundo, J. M.; Roncali, J. *Synth. Met.* **2001**, *119*, 527.
- (207) Bao, Z.; Dodabalapur, A.; Lovinger, A. J. *Appl. Phys. Lett.* **1996**, *69*, 4108.
- (208) Coakley, K. M.; McGehee, M. D. *Chem. Mater.* **2004**, *16*, 4533.

- (209) Valaski, R.; Canestraro, C. D.; Micaroni, L.; Mello, R. M. Q.; Roman, L. S. *Sol. Energy Mater. Sol. Cells* **2007**, *91*, 684.
- (210) Oevering, H.; Paddonrow, M. N.; Heppener, M.; Oliver, A. M.; Cotsaris, E.; Verhoeven, J. W.; Hush, N. S. *J. Am. Chem. Soc.* **1987**, *109*, 3258.
- (211) Chen, P. Y.; Meyer, T. J. *Chem. Rev.* **1998**, *98*, 1439.
- (212) Chawdhury, N.; Kohler, A.; Friend, R. H.; Wong, W. Y.; Lewis, J.; Younus, M.; Raithby, P. R.; Corcoran, T. C.; Al-Mandhary, M. R. A.; Khan, M. S. *J. Chem. Phys.* **1999**, *110*, 4963.
- (213) Wilson, J. S.; Kohler, A.; Friend, R. H.; Al-Suti, M. K.; Al-Mandhary, M. R. A.; Khan, M. S.; Raithby, P. R. *J. Chem. Phys.* **2000**, *113*, 7627.
- (214) Ohkita, H.; Cook, S.; Astuti, Y.; Duffy, W.; Heeney, M.; Tierney, S.; McCulloch, I.; Bradley, D. D. C.; Durrant, J. R. *Chem. Commun.* **2006**, 3939.
- (215) Ford, T. A.; Avilov, I.; Beljonne, D.; Greenham, N. C. *Phys. Rev. B* **2005**, *71*, 125212.
- (216) Yersin, H. *Top. Curr. Chem.* **2004**, *241*, 1.
- (217) Kooistra, F. B.; Knol, J.; Kastenberg, F.; Popescu, L. M.; Verhees, W. J. H.; Kroon, J. M.; Hummelen, J. C. *Org. Lett.* **2007**, *9*, 551.
- (218) Hoppe, H.; Arnold, N.; Sariciftci, N. S.; Meissner, D. *Sol. Energy Mater. Sol. Cells* **2003**, *80*, 105.
- (219) Baek, N. S.; Hau, S. K.; Yip, H.-L.; Acton, O.; Chen, K.-S.; Jen, A. K. Y. *Chem. Mater.* **2008**, *20*, 5734.
- (220) Bundgaard, E.; Krebs, F. C. *Sol. Energy Mater. Sol. Cells* **2007**, *91*, 954.
- (221) Kulkarni, A. P.; Zhu, Y.; Jenekhe, S. A. *Macromolecules* **2008**, *41*, 339.
- (222) Gunbas, G. E.; Durmus, A.; Toppore, L. *Adv. Mater.* **2008**, *20*, 691.
- (223) Beaujuge, P. M.; Ellinger, S.; Reynolds, J. R. *Adv. Mater.* **2008**, *20*, 2772.
- (224) Becker, H.; Spreitzer, H.; Ibrom, K.; Kreuder, W. *Macromolecules* **1999**, *32*, 4925.
- (225) Jin, S. H.; Park, H. J.; Kim, J. Y.; Lee, K.; Lee, S. P.; Moon, D. K.; Lee, H. J.; Gal, Y. S. *Macromolecules* **2002**, *35*, 7532.
- (226) Scherf, U. In *Carbon Rich Compounds II, Macrocyclic Oligoacetylenes and Other Linearly Conjugated Systems* 1999, p163.
- (227) Loewe, R. S.; McCullough, R. D. *Chem. Mater.* **2000**, *12*, 3214.

- (228) Kim, J. Y.; Qin, Y.; Stevens, D. M.; Ugurlu, O.; Kalihari, V.; Hillmyer, M. A.; Frisbie, C. D. *J. Phys. Chem. C* **2009**, *113*, 10790.
- (229) Kitamura, C.; Tanaka, S.; Yamashita, Y. *Chem. Mater.* **1996**, *8*, 570.
- (230) van Mullekom, H. A. M.; Vekemans, J. A. J. M.; Meijer, E. W. *Chem. Eur. J.* **1998**, *4*, 1235.
- (231) Zhu, Y.; Champion, R. D.; Jenekhe, S. A. *Macromolecules* **2006**, *39*, 8712.
- (232) Feng, X.; Liu, M.; Pisula, W.; Takase, M.; Li, J.; Müllen, K. *Adv. Mater.* **2008**, *20*, 2684.
- (233) Hou, J.; Tan, Z.; He, Y.; Yang, C.; Li, Y. *Macromolecules* **2006**, *39*, 4657.
- (234) Jung, I.; Lee, T.; Kang, S. O.; Ko, J. *Synthesis* **2005**, 986.
- (235) Lee, S. J.; Gray, K. C.; Paek, J. S.; Burke, M. D. *J. Am. Chem. Soc.* **2008**, *130*, 466.
- (236) Roush, W. R.; Brown, B. B. *J. Am. Chem. Soc.* **1993**, *115*, 2268.
- (237) Katayama, H.; Nagao, M.; Nishimura, T.; Matsui, Y.; Umeda, K.; Akamatsu, K.; Tsuruoka, T.; Nawafune, H.; Ozawa, F. *J. Am. Chem. Soc.* **2005**, *127*, 4350.
- (238) Katayama, H.; Nagao, M.; Nishimura, T.; Matsui, Y.; Fukuse, Y.; Wakioka, M.; Ozawa, F. *Macromolecules* **2006**, *39*, 2039.
- (239) Koch, F.; Heitz, W. *Macromol. Chem. and Phys.* **1997**, *198*, 1531.
- (240) Thompson, B. C.; Madrigal, L. G.; Pinto, M. R.; Kang, T.-S.; Schanze, K. S.; Reynolds, J. R. *J. Polym. Sci. Part A: Polym. Chem.* **2005**, *43*, 1417.
- (241) Fu, D.; Xu, B.; Swager, T. M. *Tetrahedron* **1997**, *53*, 15487.
- (242) Du, J.; Fang, Q.; Chen, X.; Ren, S.; Cao, A.; Xu, B. *Polymer* **2005**, *46*, 11927.
- (243) Grisorio, R.; Mastrorilli, P.; Nobile, C. F.; Romanazzi, G.; Suranna, G. P.; Gigli, G.; Piliego, C.; Ciccarella, G.; Cosma, P.; Acierno, D.; Amendola, E. *Macromolecules* **2007**, *40*, 4865.
- (244) Beletskaya, I. P.; Cheprakov, A. V. *Chem. Rev.* **2000**, *100*, 3009.
- (245) Johansson, D. M.; Wang, X.; Johansson, T.; Inganas, O.; Yu, G.; Srdanov, G.; Andersson, M. R. *Macromolecules* **2002**, *35*, 4997.
- (246) Ishiyama, T.; Takagi, J.; Hartwig, J. F.; Miyaura, N. *Angew. Chem. Int. Ed.* **2002**, *41*, 3056.
- (247) Jaya Prakash, D.; Sujit, R. *J. Org. Chem.* **2002**, *67*, 7861.

- (248) Perzon, E.; Zhang, F.; Andersson, M.; Mammo, W.; Inganäs, O.; Andersson, M. R. *Adv. Mater.* **2007**, *19*, 3308.
- (249) Pan, M.; Bao, Z.; Yu, L. *Macromolecules* **1995**, *28*, 5151.
- (250) Jayakannan, M.; van Hal, P. A.; Janssen, R. A. J. *J. Polym. Sci. A: Polym. Chem.* **2002**, *40*, 251.
- (251) Bundgaard, E.; Krebs, F. C. *Macromolecules* **2006**, *39*, 2823.
- (252) Chynwat, V.; Frank, H. A. *Chem. Phys.* **1995**, *194*, 237.
- (253) Englman, R.; Jortner, J. *Molecular Physics: An International Journal at the Interface Between Chemistry and Physics* **1970**, *18*, 145
- (254) Thompson, B. C.; Kim, Y. G.; McCarley, T. D.; Reynolds, J. R. *J. Am. Chem. Soc.* **2006**, *128*, 12714.
- (255) Wienk, M. M.; Turbiez, M. G. R.; Struijk, M. P.; Fonrodona, M.; Janssen, R. A. J. *Appl. Phys. Lett.* **2006**, *88*, 153511.
- (256) Wang, X.; Perzon, E.; Mammo, W.; Oswald, F.; Admassie, S.; Persson, N.-K.; Langa, F.; Andersson, M. R.; Inganäs, O. *Thin Solid Films* **2006**, *511-512*, 576.
- (257) Hagemann, O.; Jørgensen, M.; Krebs, F. C. *J. Org. Chem.* **2006**, *71*, 5546.
- (258) Roncali, J. *Acc. Chem. Res.* **2009**, *42*, 1719.
- (259) Qin, R.; Li, W.; Li, C.; Du, C.; Veit, C.; Schleiermacher, H.-F.; Andersson, M.; Bo, Z.; Liu, Z.; Inganäs, O.; Wuerfel, U.; Zhang, F. *J. Am. Chem. Soc.* **2009**, *131*, 14612.
- (260) Hou, J.; Chen, H.-Y.; Zhang, S.; Chen, R. I.; Yang, Y.; Wu, Y.; Li, G. *J. Am. Chem. Soc.* **2009**, *131*, 15586.
- (261) Lunt, R. R.; Benziger, J. B.; Forrest, S. R. *Adv. Mater.* **2009**, *22*, 1233.
- (262) Yang, H.; Shin, T. J.; Yang, L.; Cho, K.; Ryu, C. Y.; Bao, Z. *Adv. Funct. Mater.* **2005**, *15*, 671.
- (263) Mihailetti, V. D.; Koster, L. J. A.; Blom, P. W. M.; Melzer, C.; de Boer, B.; van Duren, J. K. J.; Janssen, R. A. J. *Adv. Funct. Mater.* **2005**, *15*, 795.
- (264) An, Z.; Yu, J.; Jones, S. C.; Barlow, S.; Yoo, S.; Domercq, B.; Prins, P.; Siebbeles, L. D. A.; Kippelen, B.; Marder, S. R. *Adv. Mater.* **2005**, *17*, 2580.
- (265) Stefan, M. L.; Sven, H.; Arnaud, C.; Mukundan, T.; Georg, K. *Angew. Chem. Int. Ed.* **2006**, *45*, 3364.
- (266) Sommer, M.; Lang, Andreas S.; Thelakkat, M. *Angew. Chem. Int. Ed.* **2008**, *47*, 7901.

- (267) Carrasco-Orozco, M.; Tsoi, W. C.; O'Neill, M.; Aldred, M. P.; Vlachos, P.; Kelly, S. M. *Adv. Mater.* **2006**, *18*, 1754.
- (268) Yagai, S.; Kubota, S.; Saito, H.; Unoike, K.; Karatsu, T.; Kitamura, A.; Ajayaghosh, A.; Kanesato, M.; Kikkawa, Y. *J. Am. Chem. Soc.* **2009**, *131*, 5408.
- (269) Percec, V.; Imam, M. R.; Peterca, M.; Wilson, D. A.; Graf, R.; Spiess, H. W.; Balagurusamy, V. S. K.; Heiney, P. A. *J. Am. Chem. Soc.* **2009**, *131*, 7662.
- (270) Feng, X.; Pisula, W.; Kudernac, T.; Wu, D.; Zhi, L.; De Feyter, S.; Müllen, K. *J. Am. Chem. Soc.* **2009**, *131*, 4439.
- (271) Jin, W.; Yamamoto, Y.; Fukushima, T.; Ishii, N.; Kim, J.; Kato, K.; Takata, M.; Aida, T. *J. Am. Chem. Soc.* **2008**, *130*, 9434.
- (272) Hill, J. P.; Jin, W.; Kosaka, A.; Fukushima, T.; Ichihara, H.; Shimomura, T.; Ito, K.; Hashizume, T.; Ishii, N.; Aida, T. *Science* **2004**, *304*, 1481.
- (273) Vijayakumar, C.; Praveen, V. K.; Ajayaghosh, A. *Adv. Mater.* **2009**, *21*, 2059.
- (274) Zhang, X.; Chen, Z.; Würthner, F. *J. Am. Chem. Soc.* **2007**, *129*, 4886.
- (275) Moon, K.-S.; Kim, H.-J.; Lee, E.; Lee, M. *Angew. Chem. Int. Ed.* **2007**, *46*, 6807.
- (276) Li, J. L.; Kastler, M.; Pisula, W.; Robertson, J. W. F.; Wasserfallen, D.; Grimsdale, A. C.; Wu, J. S.; Müllen, K. *Adv. Funct. Mater.* **2007**, *17*, 2528.
- (277) Yamamoto, Y.; Fukushima, T.; Suna, Y.; Ishii, N.; Saeki, A.; Seki, S.; Tagawa, S.; Taniguchi, M.; Kawai, T.; Aida, T. *Science* **2006**, *314*, 1761.
- (278) Schmidt-Mende, L.; Fechtenkotter, A.; Mullen, K.; Moons, E.; Friend, R. H.; MacKenzie, J. D. *Science* **2001**, *293*, 1119.
- (279) Li, W.-S.; Yamamoto, Y.; Fukushima, T.; Saeki, A.; Seki, S.; Tagawa, S.; Masunaga, H.; Sasaki, S.; Takata, M.; Aida, T. *J. Am. Chem. Soc.* **2008**, *130*, 8886.
- (280) Chambon, S.; Manceau, M.; Firon, M.; Cros, S.; Rivaton, A.; Gardette, J.-L. *Polymer* **2008**, *49*, 3288.
- (281) Manceau, M.; Rivaton, A.; Gardette, J.-L. *Macromol. Rapid Commun.* **2008**, *29*, 1823.
- (282) Lincke, G. *Dyes Pigm.* **2003**, *59*, 1.
- (283) Yu, C.-Y.; Chen, C.-P.; Chan, S.-H.; Hwang, G.-W.; Ting, C. *Chem. Mater.* **2009**, *21*, 3262.
- (284) Huo, L.; Hou, J.; Chen, H.-Y.; Zhang, S.; Jiang, Y.; Chen, T. L.; Yang, Y. *Macromolecules* **2009**, *42*, 6564.

- (285) Zhou, E.; Yamakawa, S.; Tajima, K.; Yang, C.; Hashimoto, K. *Chem. Mater.* **2009**, *21*, 4055.
- (286) Chan, W. K.; Chen, Y.; Peng, Z.; Yu, L. *J. Am. Chem. Soc.* **1993**, *115*, 11735.
- (287) Song, B.; Wang, Z.; Chen, S.; Zhang, X.; Fu, Y.; Smet, M.; Dehaen, W. *Angew. Chem.* **2005**, *117*, 4809.
- (288) Song, B.; Wei, H.; Wang, Z.; Zhang, X.; Smet, M.; Dehaen, W. *Adv. Mater.* **2007**, *19*, 416.
- (289) Rochat, A. C.; Cassar, L.; Iqbal, I. *US 4,579,949* **1986**.
- (290) Balakrishnan, K.; Datar, A.; Oitker, R.; Chen, H.; Zuo, J.; Zang, L. *J. Am. Chem. Soc.* **2005**, *127*, 10496.
- (291) Bushey, M. L.; Hwang, A.; Stephens, P. W.; Nuckolls, C. *J. Am. Chem. Soc.* **2001**, *123*, 8157.
- (292) Pisula, W.; Kastler, M.; Wasserfallen, D.; Mondeshki, M.; Piris, J.; Schnell, I.; Müllen, K. *Chem. Mater.* **2006**, *18*, 3634.
- (293) Simmerer, J.; Glüsen, B.; Paulus, W.; Kettner, A.; Schuhmacher, P.; Adam, D.; Etzbach, K.-H.; Siemensmeyer, K.; Wendorff, J. H.; Ringsdorf, H.; Haarer, D. *Adv. Mater.* **1996**, *8*, 815.
- (294) Marrocchi, A.; Seri, M.; Kim, C.; Facchetti, A.; Taticchi, A.; Marks, T. J. *Chem. Mater.* **2009**, *21*, 2592.
- (295) Tamayo, A. B.; Dang, X. D.; Walker, B.; Seo, J.; Kent, T.; Nguyen, T. Q. *Appl. Phys. Lett.* **2009**, *94*.
- (296) Lincker, F.; Bourgun, P.; Masson, P.; Didier, P.; Guidoni, L.; Bigot, J.-Y.; Nicoud, J.-F.; Donnio, B.; Guillon, D. *Org. Lett.* **2005**, *7*, 1505.
- (297) Ishiyama, T.; Takagi, J.; Ishida, K.; Miyaura, N.; Anastasi, N. R.; Hartwig, J. F. *J. Am. Chem. Soc.* **2001**, *124*, 390.
- (298) Reddy, M. S.; Narender, M.; Nageswar, Y. V. D.; Rao, K. R. *Synthesis* **2005**, *2005*, 714.
- (299) Aoki, K. i.; Kudo, M.; Tamaoki, N. *Org. Lett.* **2004**, *6*, 4009.
- (300) Egbe, D. A. M.; Ulbricht, C.; Orgis, T.; Carbonnier, B.; Kietzke, T.; Peip, M.; Metzner, M.; Gericke, M.; Birckner, E.; Pakula, T.; Neher, D.; Grummt, U.-W. *Chem. Mater.* **2005**, *17*, 6022.
- (301) Wunderlich, B. *J. Chem. Phys.* **1958**, *29*, 1395.
- (302) Chen, C.; Yu, P. H. F.; Cheung, M. K. *J. Appl. Polym. Sci.* **2005**, *98*, 736.

- (303) Helgesen, M.; Krebs, F. C. *Macromolecules* **2010**, *43*, 1253.
- (304) Petersen, M. H.; Gevorgyan, S. A.; Krebs, F. C. *Macromolecules* **2008**, *41*, 8986.
- (305) Zambounis, J. S.; Hao, Z.; Iqbal, A. *Nature* **1997**, *388*, 131.
- (306) Han, X.; Chen, X.; Holdcroft, S. *Chem. Mater.* **2009**, *21*, 4631.
- (307) Helgesen, M.; Gevorgyan, S. A.; Krebs, F. C.; Janssen, R. A. J. *Chem. Mater.* **2009**, *21*, 4669.
- (308) Tromholt, T.; Gevorgyan, S. A.; Jørgensen, M.; Krebs, F. C.; Sylvester-Hvid, K. O. *ACS Appl. Mater. Interfaces* **2009**, *1*, 2768.
- (309) Liu, J.; Kadnikova, E. N.; Liu, Y.; McGehee, M. D.; Fréchet, J. M. J. *J. Am. Chem. Soc.* **2004**, *126*, 9486.
- (310) Kim, J. S.; Lee, Y.; Lee, J. H.; Park, J. H.; Kim, J. K.; Cho, K. *Adv. Mater.* **2010**, *22*, 1355.
- (311) Wei, G.; Wang, S.; Renshaw, K.; Thompson, M. E.; Forrest, S. R. *ACS Nano* **2010**, *4*, 1927.
- (312) Zhang, Y.; Hau, S. K.; Yip, H.-L.; Sun, Y.; Acton, O.; Jen, A. K. Y. *Chem. Mater.* **2010**, *22*, 2696.
- (313) Mei, J.; Ogawa, K.; Kim, Y.-G.; Heston, N. C.; Arenas, D. J.; Nasrollahi, Z.; McCarley, T. D.; Tanner, D. B.; Reynolds, J. R.; Schanze, K. S. *ACS Appl. Mater. Interfaces* **2009**, *1*, 150.
- (314) Silva, J. F. M. d.; Garden, S. J.; Pinto, A. C. *J. Braz. Chem. Soc.*, **2001**, *12*, 273.
- (315) Bogdanov, A.; Mironov, V.; Musin, L.; Buzykin, B.; Konovalov, A. *Russ. J. Gen. Chem.* **2008**, *78*, 1977.
- (316) Minami, T.; Matsumoto, M.; Agawa, T. *J. Chem. Soc., Chem. Commun.* **1976**, 1053.
- (317) Mei, J.; Graham, K. R.; Stalder, R.; Reynolds, J. R. *Org. Lett.* **2010**, *12*, 660.
- (318) Moulé, A. J.; Meerholz, K. *Adv. Funct. Mater.* **2009**, *19*, 3028.
- (319) Ichino, Y.; Ni, J. P.; Ueda, Y.; Wang, D. K. *Synth. Met.* **2001**, *116*, 223.
- (320) Kooistra, F. B.; Mihailetti, V. D.; Popescu, L. M.; Kronholm, D.; Blom, P. W. M.; Hummelen, J. C. *Chem. Mater.* **2006**, *18*, 3068.
- (321) Sirringhaus, H.; Brown, P. J.; Friend, R. H.; Nielsen, M. M.; Bechgaard, K.; Langeveld-Voss, B. M. W.; Spiering, A. J. H.; Janssen, R. A. J.; Meijer, E. W.; Herwig, P.; de Leeuw, D. M. *Nature* **1999**, *401*, 685.

- (322) Tang, C.; Bang, J.; E. Stein, G.; Fredrickson, G. H.; Hawker, C. J.; Kramer, E. J.; Sprung, M.; Wang, J. *Macromolecules* **2008**, *41*, 4328.
- (323) Zhang, M.; Yang, L.; Yurt, S.; Misner, M. J.; Chen, J.-T.; Coughlin, E. B.; Venkataraman, D.; Russell, T. P. *Adv. Mater.* **2007**, *19*, 1571.
- (324) Kim, S. H.; Misner, M. J.; Russell, T. P. *Adv. Mater.* **2004**, *16*, 2119.
- (325) Beaujuge, P. M.; Pisula, W.; Tsao, H. N.; Ellinger, S.; Müllen, K.; Reynolds, J. R. *J. Am. Chem. Soc.* **2009**, *131*, 7514.
- (326) Izuhara, D.; Swager, T. M. *J. Am. Chem. Soc.* **2009**, *131*, 17724.
- (327) Wen, Y.; Liu, Y. *Adv. Mater.* **2010**, *22*, 1331.
- (328) Park, S. H.; Roy, A.; Beaupre, S.; Cho, S.; Coates, N.; Moon, J. S.; Moses, D.; Leclerc, M.; Lee, K.; Heeger, A. J. *Nat Photon* **2009**, *3*, 297.
- (329) Cates, N. C.; Gysel, R.; Dahl, J. E. P.; Sellinger, A.; McGehee, M. D. *Chem. Mater.* **2010**.
- (330) Guo, X.; Kim, F. S.; Jenekhe, S. A.; Watson, M. D. *J. Am. Chem. Soc.* **2009**, *131*, 7206.
- (331) Piliego, C.; Jarzab, D.; Gigli, G.; Chen, Z.; Facchetti, A.; Loi, M. A. *Adv. Mater.* **2009**, *21*, 1573.
- (332) Usta, H.; Facchetti, A.; Marks, T. J. *Org. Lett.* **2008**, *10*, 1385.
- (333) Ishiyama, T.; Murata, M.; Miyaura, N. *J. Org. Chem.* **1995**, *60*, 7508.

BIOGRAPHICAL SKETCH

Jianguo Mei, a native of China, received his college education from the Hefei University of Technology, and graduated with a bachelor's degree in engineering. He continued his post-graduate study there, worked on heterogeneous catalysis under the guidance of Professor Shaoming Yu, and obtained a master's degree in chemical engineering. After spending seven years in chemical engineering, he decided to pursue his career in science and engineering, attended the graduate school at the University of New Orleans, and started his practice in homogeneous catalysis under the guidance of Professor Steven P. Nolan. For family reasons, he moved to the University of Florida one year later, which coincidentally saved him being a victim of Hurricane Katrina. He joined the research group of Professor John R. Reynolds shortly after his arrival, and began his adventure in the field of organic pi-conjugated materials for optoelectronic applications. With the support from his advisor and colleagues, he exposed himself to many aspects of research in the Reynolds group, gained expertise in design, Synthesis and characterization of solution-processable organic electroactive materials for solar cells, electrochromics, field-effect transistors and light-emitting diodes. He was also briefly involved into the aspect of device fabrication through closely working with his collaborators. Jianguo earned his doctoral degree from the University of Florida in the summer of 2010. He will work with Professor Zhenan Bao as a postdoctoral fellow in Department of Chemical Engineering at Stanford University this fall.